

SAND REPORT

SAND2003-2813
Unlimited Release
Printed August 2003

2003 Research Briefs: Materials and Process Sciences Center

Michael J. Cieslak

Prepared by
Sandia National Laboratories
Albuquerque, New Mexico 87185 and Livermore, California 94550

Sandia is a multiprogram laboratory operated by Sandia Corporation,
a Lockheed Martin Company, for the United States Department of Energy's
National Nuclear Security Administration under Contract DE-AC04-94-AL85000.

Approved for public release; further dissemination unlimited.



Sandia National Laboratories

Issued by Sandia National Laboratories, operated for the United States Department of Energy by Sandia Corporation.

NOTICE: This report was prepared as an account of work sponsored by an agency of the United States Government. Neither the United States Government, nor any agency thereof, nor any of their employees, nor any of their contractors, subcontractors, or their employees, make any warranty, express or implied, or assume any legal liability or responsibility for the accuracy, completeness, or usefulness of any information, apparatus, product, or process disclosed, or represent that its use would not infringe privately owned rights. Reference herein to any specific commercial product, process, or service by trade name, trademark, manufacturer, or otherwise, does not necessarily constitute or imply its endorsement, recommendation, or favoring by the United States Government, any agency thereof, or any of their contractors or subcontractors. The views and opinions expressed herein do not necessarily state or reflect those of the United States Government, any agency thereof, or any of their contractors.

Printed in the United States of America. This report has been reproduced directly from the best available copy.

Available to DOE and DOE contractors from
U.S. Department of Energy
Office of Scientific and Technical Information
P.O. Box 62
Oak Ridge, TN 37831

Telephone: (865)576-8401
Facsimile: (865)576-5728
E-Mail: reports@adonis.osti.gov
Online ordering: <http://www.doe.gov/bridge>

Available to the public from
U.S. Department of Commerce
National Technical Information Service
5285 Port Royal Rd
Springfield, VA 22161

Telephone: (800)553-6847
Facsimile: (703)605-6900
E-Mail: orders@ntis.fedworld.gov
Online order: <http://www.ntis.gov/help/ordermethods.asp?loc=7-4-0#online>



SAND2003-2813
Unlimited Release
Printed August 2003

2003 Research Briefs: Materials and Process Sciences Center

Michael J. Cieslak
Materials and Process Sciences Center
Sandia National Laboratories
P.O. Box 5800
Albuquerque, NM 87185-0887

Abstract

This report is the latest in a continuing series that highlights the recent technical accomplishments associated with the work being performed within the Materials and Process Sciences Center. Our research and development activities primarily address the materials-engineering needs of Sandia's Nuclear-Weapons (NW) program. In addition, we have significant efforts that support programs managed by the other laboratory business units. Our wide range of activities occurs within six thematic areas: Materials Aging and Reliability, Scientifically Engineered Materials, Materials Processing, Materials Characterization, Materials for Microsystems and Materials Modeling and Computational Simulation. We believe these highlights collectively demonstrate the importance that a strong materials-science base has on the ultimate success of the NW program and the overall DOE technology portfolio.

Acknowledgment

First, we want to gratefully acknowledge the importance of our many customers who not only sponsor our work, but also provide valuable guidance, feedback, and programmatic motivation. In addition, we acknowledge the substantial and significant contributions of our co-workers from within many other organizations at Sandia, from universities, and from industry.

Editors:

C. L. Porter

J. W. Braithwaite

Introductory Message from the Center Director

The core responsibility of the Materials and Process Sciences Center is to provide materials-engineering support to Sandia's Nuclear-Weapons (NW) program. As a foundational Science and Technology organization for the Laboratories, the Center also performs R&D activities that are sponsored by the other laboratory business areas (Energy & Critical Resources, Nonproliferation and Assessments, Military Technologies & Applications, and Homeland Security). Importantly, our primary product is a science-based *knowledge* of material properties and behavior and the processes to more effectively produce, transform, and analyze them. Accordingly, our sponsors engage us in a broad range of research, development, and applications activities.



This report is the latest in a continuing series that contain highlights of recent specific accomplishments. These briefs are organized into sections that involve the Center's core capabilities: three prime thematic areas (Materials Aging and Reliability, Scientifically Engineered Materials, Materials Processing), and two of our three crosscutting areas (Materials Characterization and Materials for Microsystems). The goal of the work in *Materials Aging and Reliability* is to understand the chemical and physical mechanisms that cause materials properties to change and then develop mechanistic-based models to predict how these changes affect component reliability. Activities in the *Scientifically Engineered Materials* area focus on developing new and replacement materials with desired specific properties or performance characteristics through an understanding of how materials properties depend on composition, microstructure, and manufacturing processes. Within the *Materials Processing theme*, the knowledge base needed to understand, characterize, model, and ultimately control the materials fabrication technologies that are critical to hardware production is generated. Success with all of these activities requires the availability of effective tools and techniques to characterize materials. Thus, the focus of the crosscutting Materials Characterization area is to develop and apply analytical techniques to detect and measure chemical and structural information about materials at various temporal and spatial scales, down to the nanoscale. Our directed work to support Sandia's emerging microsystem initiative involves aspects of the other three thematic areas, but focused on the specific challenges associated with the inherently small-length scale of these devices. The third crosscutting Center capability involves the mathematical modeling and computational simulation of materials behavior and fabrication processes. Specific modeling accomplishments are described within each of the appropriate topical sections.

Consideration of this entire set of highlights in conjunction with the needs of the non-nuclear aspects of the NNSA's NW program provides a sense of the importance that a strong materials-science base has on the program's ultimate success. These briefs also demonstrate the connections between materials science and the breadth of the overall DOE technology portfolio.

We welcome your questions and comments on the work being performed in the Materials and Process Sciences Center. Contact information along with additional organizational and technical descriptions of what we do can be found by visiting our website at <http://www.sandia.gov/materials/science>.

Michael J. Cressler

TABLE OF CONTENTS

MATERIALS AGING

BRAZES

Solid State Interface Reactions Impact the Long Term Reliability of Braze Joints	10
--	----

CERAMICS & OXIDES

Aging and Reliability of Glass and Ceramics	12
---	----

Dynamics of Exchange at Gas-Zeolite Interfaces	14
--	----

CORROSION

Corrosion Mechanisms of Au-Al Wirebonds in Microelectronic Devices	16
--	----

Understanding Aluminum Corrosion	18
--	----

Kinetics of Atmospheric Copper Sulfidation	20
--	----

Corrosion Monitoring of Strategic Petroleum Reserve Brine Pipelines.....	22
--	----

POLYMERS

Hydrolytic Degradation of Estane® 5703: Chemistry and Morphology.....	24
---	----

Polymer Aging Studies	26
-----------------------------	----

Relationship Between Interfacial Interactions and Fracture Stress for Adhesive Joints in Mode II Loading	28
---	----

Using ¹⁷ O NMR Spectroscopy to Investigate Polymer Degradation.....	30
--	----

The Wear-out Approach for Predicting the Remaining Lifetime of Materials Applied to a Material with Induction-time Behavior.....	32
---	----

TRIBOLOGY

Aging and Degradation of Lubricant Materials – Assessing Performance and Aging Behavior	34
---	----

Aging and Degradation of Lubricant Materials – Assessing and Predicting Chemical Changes.....	36
---	----

MATERIALS CHARACTERIZATION

BATTERY & HAZARDOUS MATERIALS

Characterization of Hazardous Solids and Their Formation Process Resulting from Semiconductor Dichlorosilane Exhaust Flow	38
--	----

Gas Analysis for the Evaluation of Lithium Ion Cells	40
--	----

In-situ Neutron Diffraction of Commercial (Sony) Li-ion Battery	42
---	----

CERAMICS & OXIDES

Analysis of Multicomponent Adsorption on Type 3A Zeolites using TG-FTIR	44
---	----

Indentation Techniques Used as a Sensitive Microprobe for Stress	46
--	----

Multivariate Curve Resolution Improves Understanding of Zeolite Desiccants.....	48
---	----

TABLE OF CONTENTS

MATERIALS CHARACTERIZATION, cont.

MATERIALS SCIENCE

Discovery of New Orientation Relationship Between Body Centered Cubic and Face Centered Cubic Crystal Lattice Systems	50
Effects of Grain Orientation and Topology on Deformation	52
Excited State Interactions between Activators in Phosphors	54
Focused Ion Beam Applications in Materials Science	56

ORGANICS

Chemometric Analysis of NMR Spectroscopy Data.....	58
Characterizing Size Distribution of Core-Shell Spherical Particles.....	60
New Algorithms Improve Near-IR Spectrometer Calibrations.....	62
New Method to Determine Crosslink Density Gradients in Thermosetting Polymer Films	64
New Method to Probe Crosslink Density Profiles in Organosilane Films	66

SENSORS

Electrochemical and Spectroelectrochemical Detection of Trace Contaminants.....	68
Use of X-ray Diffraction as a Fatigue Sensor	70

MATERIALS FOR MICROSYSTEMS

Conformal Coatings for LIGA MEMS: Issues and Challenges	72
Evaluating Tools for Simulating Polysilicon CVD for MEMS Applications	74
Micromechanics Challenges for Modeling Polycrystalline Materials	76
Photoprogrammable Materials for Microsystems	78

MATERIALS SYNTHESIS

CERAMICS, OXIDES & SULFIDES

Barium Transport through Microminiature Thermionic Energy Converters.....	80
Controlled Assembly of Multi-Cationic Metal Alkoxides	82
Current Concentration at Defects in ZnO Varistor Material	84
ESP (Engineered Stress Profile) Glass – Unique Opportunities for Performance and Reliability	86
Growth and Morphology of Cadmium Chalcogenides	88
Influence of Precursor Nuclearity on ZnO Nanoparticle Morphology.....	90
Oxidized Metal Powders for Mechanical Shock Safety Enhancers	92

TABLE OF CONTENTS

MATERIALS SYNTHESIS, cont.

CERAMICS, OXIDES & SULFIDES, cont.	
Properties of Lanthanide Doped Lead Zirconium Titanate (PLnZT).....	94
Single-source Precursors to Nanoceramic Particles.....	96
Thin Film Dispenser Cathodes for Thermionic Micro-Devices.....	98
CATALYSTS	
Automotive Lean-Burn NO _x Catalysis.....	100
Homogeneous Catalysis Research at Sandia National Laboratories.....	102
Novel Monolithic Supports for Catalytic Combustion and Particulate Trapping.....	104
METALS	
Coinage Metal Nanoparticles from Mesityl Derivatives.....	106
Development of Low Temperature Conversion Silver Conductors for Deposition on Conformal Polymeric Surfaces.....	108
Stagnation of Grain Growth in Polycrystalline Thin Films.....	110
Superconducting Wires by Chemical Solution Deposition.....	112
ORGANICS	
Molecular Modeling of Polyolefins Using Theory and Simulation.....	114
Reformulated Sticky Foam for Non-lethal Deterrent and Access Delay Barriers.....	116
Removable Adhesives.....	118
SELF ASSEMBLY	
Colloidal Self-Assembly and Nanointeractions.....	120
Friction Between Self-Assembled Alkylsilane Monolayers.....	122

MATERIALS PROCESSING

CERAMICS	
Controlled Sintering of Ceramics.....	124
Freeform Fabrication of Photonic Band Gap Structures.....	126
JOINING	
Ceramic Joining.....	128
Elevated Temperature Properties of Braze Alloys.....	130
Linking Atomistic Computations with Phase Field Modeling.....	132
Molecular Dynamics Simulations of Reactive Wetting and Spreading.....	134

TABLE OF CONTENTS

MATERIALS PROCESSING, cont.

JOINING, cont.

Understanding Filler Metal Interactions Critical for Successful Use of Active Metal Braze Alloys in NT/NG Applications.....	136
Weld Visualization for Investigation of Solidification	138

METALS

An Investigation of Droplet Transfer Mechanisms for Micro-Wire Welding.....	140
Integrated Science-Based Understanding of Fundamental Brazing Reactions	142
Qualification of Processes to Clean Kovar Parts.....	144
Segregation of Alloying Elements to Grain Boundaries	146

LIQUID METALS

Control of Casting Rate during Vacuum Arc Remelting	148
Immersion Depth Control of the Electroslag Remelting Process at Shallower, More Consistent Levels	150

ORGANICS

Nonlinear Viscoelasticity of Curing Thermosets	152
--	-----

Solid-State Interface Reactions Impact the Long-Term Reliability of Braze Joints

P. Vianco, J. Stephens, F. Hosking, and P. Hlava

Motivation: Brazing is used to join structures earmarked for elevated temperature service – for example, jet engine components, fuel cell assemblies, heat exchangers, etc. The material discontinuity across interfaces in braze joints causes them to be susceptible to liquid-state reactions during processing and solid-state reactions during high temperature service. Interface reaction products can affect the performance of the braze joint (e.g., mechanical strength, corrosion resistance, etc.). The long-term reliability of braze joints is sensitive to microstructural changes that occur during service because of their impact on engineering properties.

Accomplishment: The effects of elevated temperature, solid-state reactions were examined for: (1) the *low-melting temperature 63.3Ag-35.1Cu-1.6Ti filler metal* on Thermo-Span™ and Inconel™718 substrate alloys and (2) the *high-melting temperature 81Au-17.5Ni-1.5Ti filler metal* on Thermo-Span™ and AISI Type 347 stainless steel. These particular filler metal/base alloy combinations represent a variety of advanced engineering applications. The Thermo-Span™/Cu-Ag-Ti couple interface developed a bi-layer structure in the as-fabricated condition. The two sub-layers had the same composition $90[(\text{Fe}, \text{Ni}, \text{Co}, \text{Cu})_2(\text{Nb}, \text{Ti}, \text{Si}, \text{Cr})]10\text{Ag}$, and were separated by a Ag-rich intermediate layer.

High-temperature, solid-state aging reduced the interface reaction zone to a single chemistry, $(\text{Fe}, \text{Ni}, \text{Co}, \text{Cu})_2(\text{Nb}, \text{Ti}, \text{Si}, \text{Cr})$. The interface of the as-fabricated Inconel™718/Cu-Ag-Ti couples contained two sub-layers having

compositions $(\text{Fe}, \text{Ni}, \text{Cu})_3(\text{Ti}, \text{Cr}, \text{Nb}, \text{Mo})_2$ and $(\text{Fe}, \text{Ni}, \text{Cu})_2(\text{Ti}, \text{Cr}, \text{Nb}, \text{Mo})$. Solid-state aging caused the overall reaction layer to thicken and the composition of the second sub-layer to change to $(\text{Fe}, \text{Ni}, \text{Cu})_7(\text{Ti}, \text{Cr}, \text{Nb}, \text{Mo})_3$. Bend bar fracture strengths determined that the Thermo-Span™/Cu-Ag-Ti and Inconel™718/Cu-Ag-Ti couples were not significantly affected by solid-state aging processes. The Thermo-Span™/Au-Ni-Ti and AISI Type 347 stainless steel/Au-Ni-Ti braze joints possessed a diffusion zone at the filler metal/base alloy interfaces. High-temperature, solid-state aging caused those diffusion zones to thicken slightly. The four-point bend strength tests, along with microstructural analysis, confirmed that the interface structure had little impact on mechanical properties. Rather, solid-state aging caused base alloy elements, which had dissolved into the filler metal during brazing, to precipitate. Therefore, bend test strength reflected the traditional precipitation hardening process in which mechanical strength is initially maximized by aging (coherent particles) at an intermediate temperature (460°C), but then decreases due to “over-aging” (particles becoming incoherent) at higher temperatures (700°C).

Significance: Technology-critical braze joints are susceptible to solid-state reactions during elevated temperature service. Interface reactions or those within a filler metal whose composition has been altered by base alloy dissolution, can affect joint mechanical properties.

Contact: Paul T. Vianco, Joining and Coating Dept., 1833
Phone: (505) 844-3429
Fax: (505) 844-9781
E-mail: ptvianc@sandia.gov

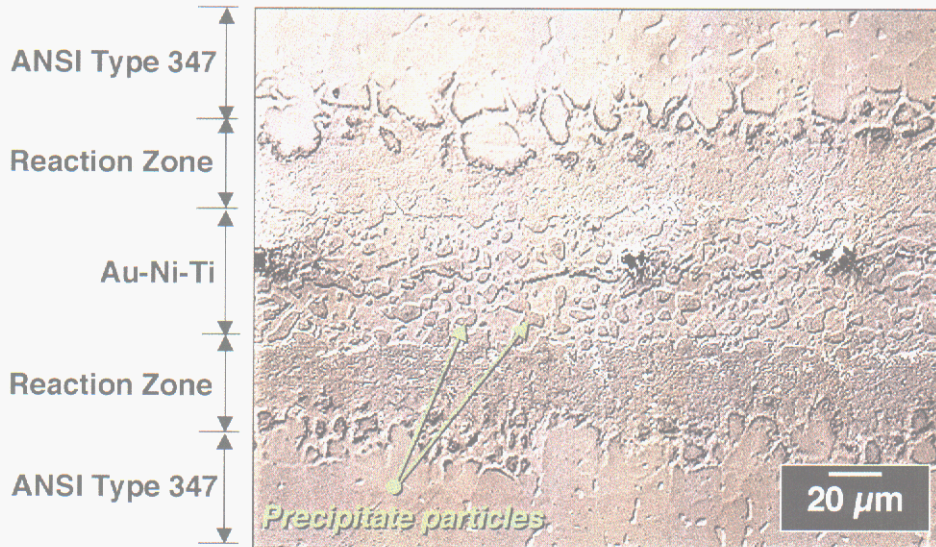


Figure 1. Optical micrograph (differential interference contrast) taken of the Type 347 stainless steel/Au-Ni-Ti sample aged at 700°C (1292°F) for 437 days.

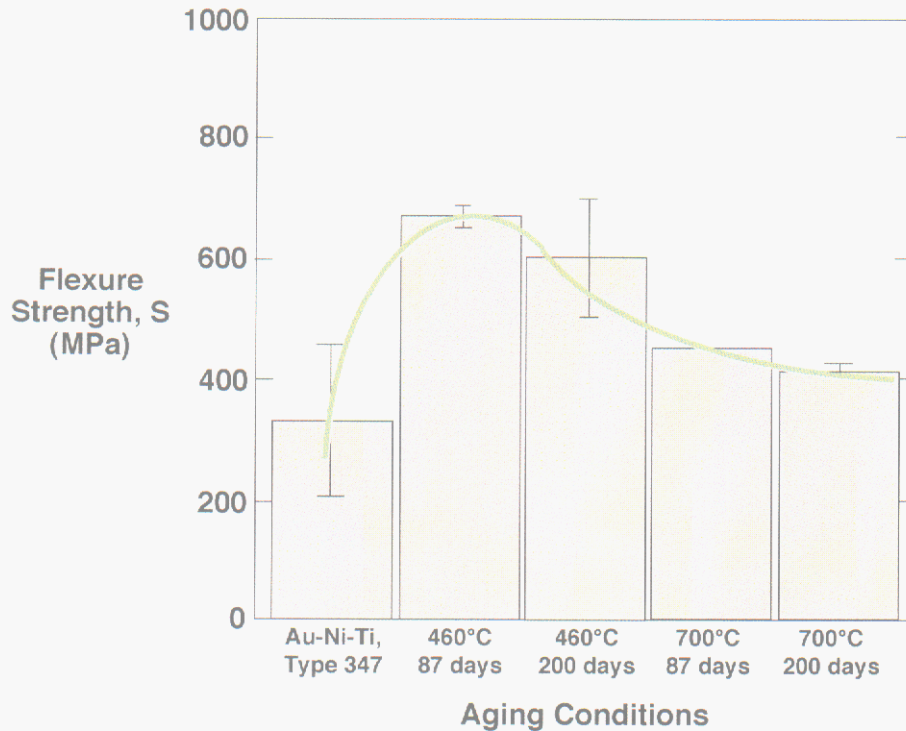


Figure 2. Bar chart of the four-point bend strength of the Type 347 stainless steel/Au-Ni-Ti joints after aging showing the traditional trend of precipitation hardening: a strength maximum (coherent particles) followed by “overaging” and a decline in strength (incoherent particles).

Aging and Reliability of Glass and Ceramics

S. Monroe, C. Newton, and J. Glass

Motivation: Ceramic and glass materials are used extensively in non-nuclear components in the weapons stockpile. The ceramic and glass members provide electrical insulation and/or hermetic-environmental barriers required for device function. The low fracture toughness and brittle nature of ceramics and glasses make their mechanical behavior highly sensitive to the presence of flaws. Large defects and the failures they produce are *usually* detected during processing and assembly, but sub-critical flaws exist in all ceramic and glass parts that are too small to be detected during initial testing and inspection. Residual stresses, thermal cycling and chemical attack (particularly by moisture) are the driving forces for sub-critical flaws to slowly grow to a critical size that may result in fracture and potentially compromise the function of components. A number of design methodologies now exist for predicting the probability of fracture (reliability) and lifetimes in brittle, ceramic materials based on time-independent and time-dependent fracture properties. With these properties, one can link the test data to components subjected to various environments and stress levels through structural reliability software, providing an engineering solution to lifetime prediction. However, this approach relies upon the accuracy and availability of materials response data and knowledge of the stress and environmental conditions encountered during the component's service life.

Accomplishment: We developed the test capability to measure the time-dependent and time-independent fracture properties, in controlled humidity environments, for any glass or ceramic of interest. Time-dependent and time-independent fracture properties were measured on 94% aluminum oxide, alkali-barium-silicate

sealing glass, and SB glass ceramic that are used to insulate electrical feed-throughs, and for 96% aluminum oxide (Figure 1) and Low Temperature Co-fired Ceramic (LTCC) ceramics that are the substrate or package housing materials for micro-electronic assemblies. Three simplified ceramic/metal and ceramic/ceramic test structures were designed and fabricated to evaluate/validate fracture prediction models. One ceramic/metal test structure, a 2-piece brazed four-point bend sample, is shown in Figure 2. These assemblies were tested to validate fracture prediction models that use Weibull strength statistics and finite element analysis of stresses in glass and ceramics as input. The brazed ceramic test sample had modest stress amplification in the joint. This gave a slightly higher predicted probability of fracture in this region and this was confirmed by the experimental results.

Significance: The capability to accurately predict fracture in glass and ceramic members of devices is key at several levels. In evaluating whether a fielded device may be at risk, we can select hardware for examination based on fracture predictions from computed stress and measured fracture properties. We use fracture prediction models to support failure analysis in current production environments. In this case we use observed fracture frequency during manufacture with predicted fracture probability to support/verify that calculated stress from finite element analyses are accurate. This allows confident decisions to correct deficiencies. In the case of new design concepts we use fracture prediction from measured fracture properties and stress models to refine design configurations and select alternative materials.

Contact: Sandy Monroe, Ceramic Materials Dept., 1843
Phone: (505) 845-8227
Fax: (505) 844-7910
E-mail: slmonro@sandia.gov

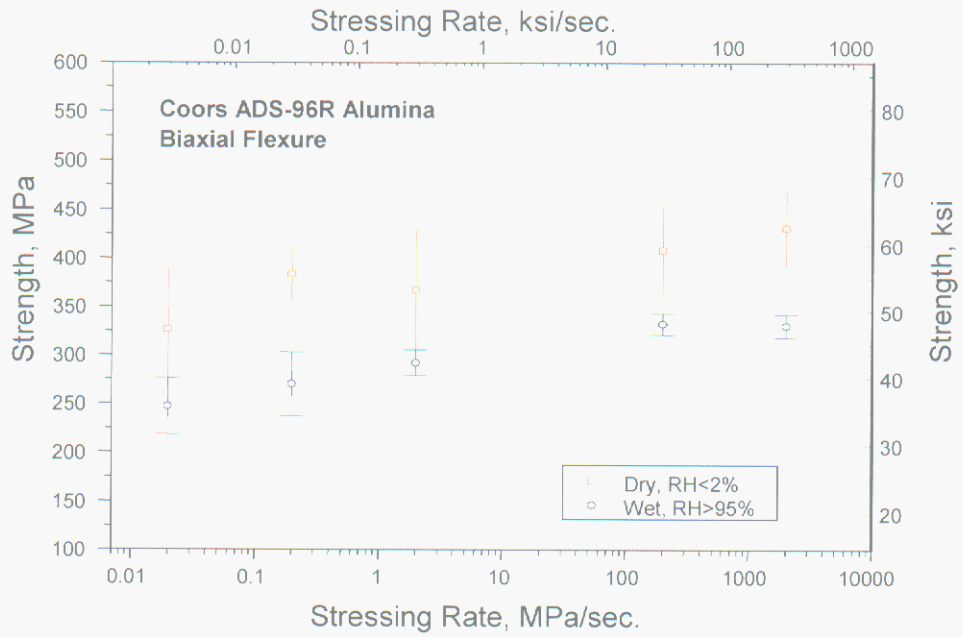


Figure 1. Time-dependent fracture properties measured on 96% aluminum oxide.

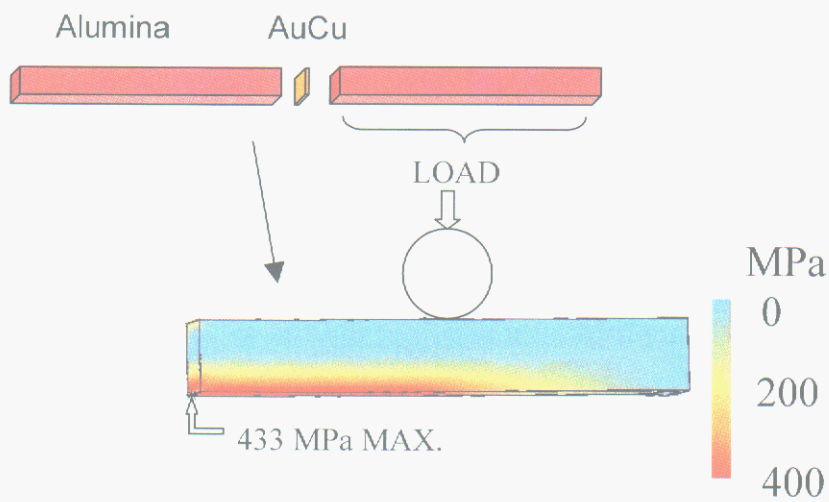


Figure 2. 2-piece brazed four-point bend bar test configuration for fracture prediction model validation.

Dynamics of Exchange at Gas-Zeolite Interfaces

M. E. Chandross, E. B. Webb III, and G. S. Grest

Motivation: Zeolites are microporous materials that are ideally suited to a number of industrial applications, such as catalytic cracking or hydroisomerization of hydrocarbon molecules as well as ion exchange in desiccant or purification applications. Zeolites with medium pore sizes, such as silicalite, are additionally useful for separations processes, as their openings are approximately the same size as the kinetic diameter of many small molecules.

Accomplishment: While the utility of zeolites for separations is well known, the actual mechanisms involved remain elusive. It is clear, however, that the fundamental underlying processes must be related to the relative diffusion rates and preferential adsorption of the molecules to be separated. To this end we have performed molecular dynamics (MD) simulations of interfaces between gases of small molecules (in particular, butane and isobutane) and silicalite. A representative snapshot of our butane simulations is shown in Figure 1. Molecules in the gas, adsorption layer and zeolite are colored red, yellow, and blue, respectively, while the zeolite itself is shown as purple bonds. Our simulations use periodic boundary conditions in all directions.

After verifying that our model and simulations accurately reproduce experimental bulk diffusion rates and adsorption isotherms, we studied the dynamics of exchange between molecules in the gas and in the zeolite. Our investigations centered on the role of the adsorption layer, and the origin of the “transport resistance” seen in many permeation and separations studies. One question we addressed in detail was as follows: given a molecule that is in the gas at some time t_0 and in the zeolite at

some later time t_z , how much time does this molecule spend in the adsorption layer for times $t_0 < t < t_z$?

A typical distribution of the adsorption layer lifetime is shown in Figure 2 for butane. This distribution is virtually unaffected by gas pressure, and only weakly affected by temperature. The distribution for molecules that begin in the zeolite and end up in the gas is identical. We also show in Figure 2 a fit to a binomial distribution. The fit is excellent, implying there are distinct adsorption sites on the surface, and that molecules hop between these sites until finding a pore mouth and entering the zeolite. This is confirmed in Figure 3, where we show a contour plot of the average density of molecules in the adsorption layer. The surface structure of silicalite is also shown. A number of distinct adsorption sites are clearly visible around each pore mouth.

Significance: Our results imply that there are identical transport resistances felt by molecules on the up and downstream side of permeation studies. The mean time spent in the adsorption layer is around 10 ps for both butane and isobutane. This time is only relevant when the zeolite is thin enough that the transport time through the membrane (around 1 ps per Angstrom) is comparable. Our simulations show excellent agreement with experiment for diffusion and adsorption measurements. These results, combined within a simple Langmuir model, also show excellent agreement with permeation experiments. Future work will consider competitive adsorption of mixtures and larger molecules.

Contact: Mike Chandross, Materials & Process Modeling & Computation Dept., 1834
Phone: (505) 844-5801
Fax: (505) 844-9781
E-mail: mechand@sandia.gov

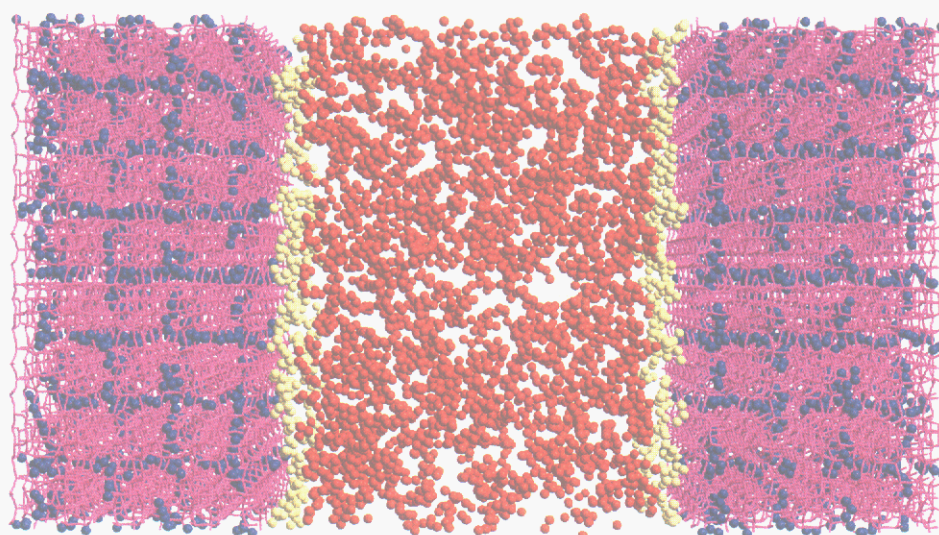


Figure 1. Snapshot of butane interface simulations. Molecules in the gas, adsorption layer, and zeolite are shown in red, yellow and blue, respectively. The zeolite is shown as purple bonds.

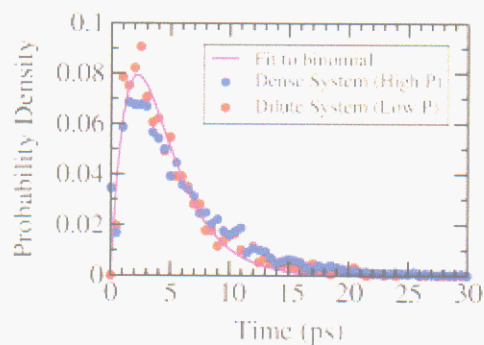


Figure 2. Distribution of adsorption layer lifetimes at 600 K. A fit to a binomial distribution is also shown.

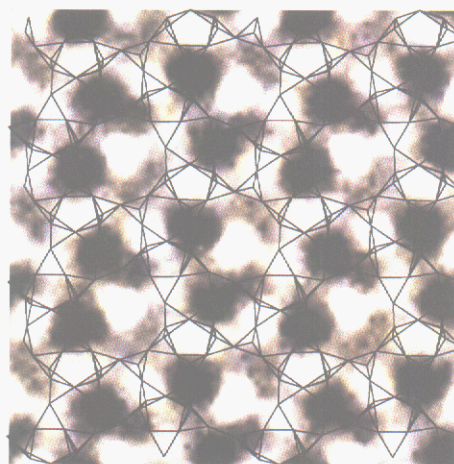


Figure 3. Contour plot of the average density of molecules in the adsorption layer. Areas of high (low) density are shown in white (black).

Corrosion Mechanisms of Au-Al Wirebonds in Microelectronic Devices

N. R. Sorensen, J. W. Braithwaite, J. R. Michael, and C. C. Battaile

Motivation: Atmospheric corrosion is an age-related degradation mode that has a high likelihood of occurrence and the potential to adversely impact the performance of electrical devices. We are in the process of developing a predictive capability that can be used to assess the effect of corrosion on the effective service life of such components. Most high-reliability military systems contain numerous microelectronic devices, typically housed in ceramic hermetic packages (CHP). However, the unavailability and high cost of CHP devices is already driving the insertion of plastic-encapsulated microelectronic (PEM) devices into electrical components. An important concern with the use of PEM devices is the uncharacterized effect corrosion can have on these devices during the long-term dormant storage conditions often associated with military systems. Effective predictions of microelectronic corrosion damage must be based on a physical understanding of the moisture-related phenomena relevant to metallization failure.

Accomplishment: Novel experimental techniques have been developed that are allowing us to characterize the corrosion process and directly image the corroding sites. A Sandia-developed Assembly Test Chip (ATC) was used to measure wirebond sheet resistance during atmospheric exposure. There is good correlation between the resistance response and the visible extent of corrosion (Figure 1). The included SEM images were taken after careful back-thinning of the ATC sample and show what the underside of the bondpad looks like following corrosion. As shown, there is significant variability in corrosion

rates between individual wirebonds, behavior that is at least partially related to the amount and distribution of Al-Au intermetallic compounds that form during chip fabrication. The intermetallic is visible as bright areas and the Al of the bondpads appears as the intermediate gray areas. The darker areas next to the Au and Au-Al intermetallic are voids where corrosion has removed the Al.

The shape of the resistance response consists of regions of gradual increases and several abrupt steps. This is suggestive of a system containing parallel resistance paths. This idea was explored using finite-element modeling of the bondpad (Figure 2). The intermetallics are modeled as a series of columns. Corrosion initiates at the Al/Al-Au intermetallic interface and grows into the Al matrix. The overall resistance of the resulting complex structure was calculated by solving Poisson's equation for each time step. The resulting predicted behavior is shown in Figure 2(c). The step indicated in this curve is the result of consuming the Al between two intermetallic islands and "pinching off" the more conductive path.

Significance: This study has provided significant physical-based insight into the corrosion mechanisms of Al-Au wirebonds. Specifically, the mechanistic understanding of the important role of the Al-Au intermetallic compounds is permitting us to explicitly describe and thus reduce a major source of uncertainty in the degradation kinetics.

Contact: Rob Sorensen, Corrosion, Electrochemistry and Cleaning Dept., 1832
Phone: (505) 844-5558
Fax: (505) 844-5558
E-mail: nrsoren@sandia.gov

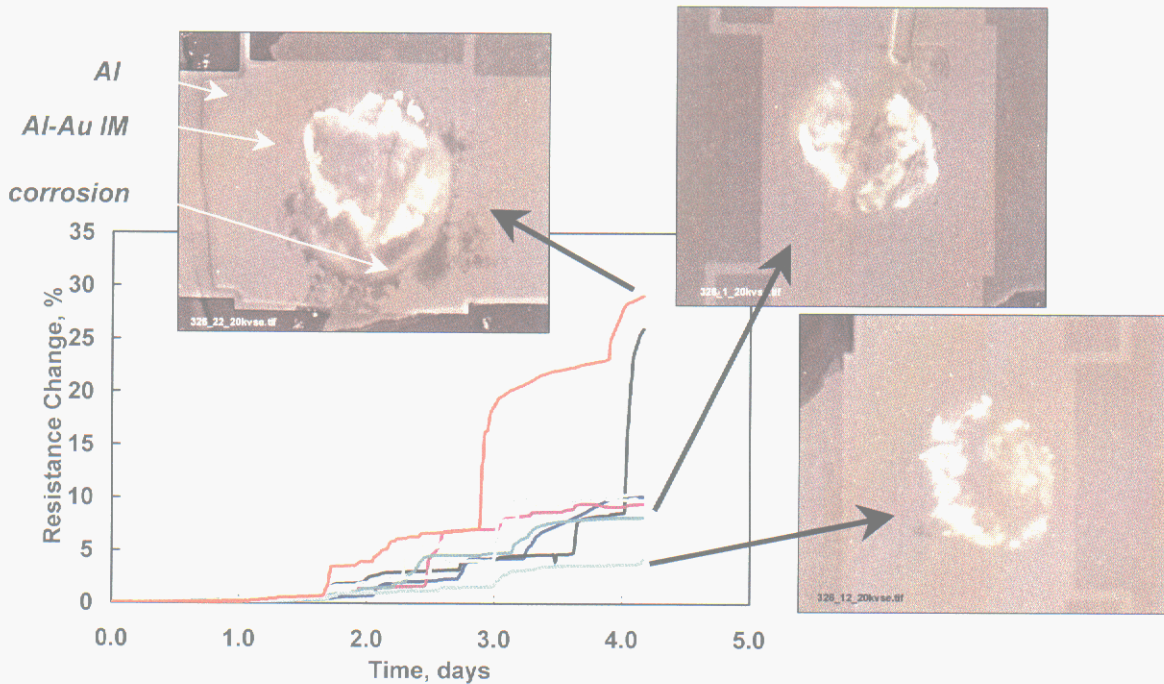


Figure 1. Resistance response for 8 Au-Al bondpads contained on a microelectronic corrosion test device that was exposed to air containing chlorine and water vapor. The inset images are views from the underside of the aluminum film (exposed by a novel back-thinning process) and show that the extent-of-corrosion (dark void regions) correlate with the observed resistance increase of the wirebond. The light regions are where the Au-Al intermetallic (IM) compounds exist and the medium gray areas are where unreacted aluminum exists.

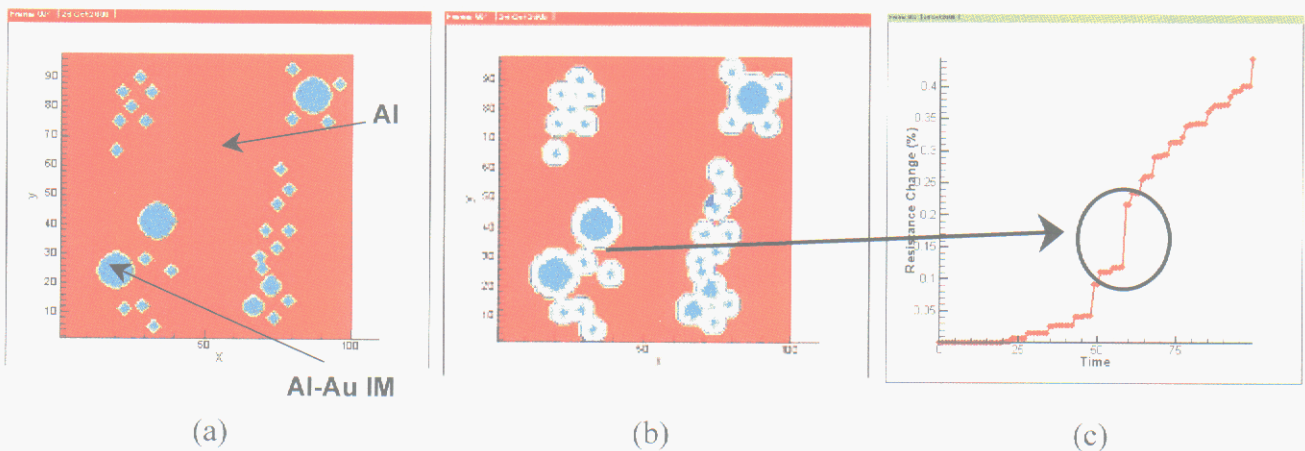


Figure 2. Progress and the result of corrosion around intermetallic compounds in the aluminum layer under a Au bondpad: (a) plan view map of intermetallic columns prior to corrosion, (b) voids formed around intermetallic particles due to corrosion (from finite-element simulation), and (c) calculated resistance change resulting from corrosion. The step in the resistance response occurred when two large-regions of corrosion joined, effectively removing a conduction pathway.

Understanding Aluminum Corrosion

C. C. Battaile, F. D. Wall, N. A. Missert, N. R. Sorensen, and J. W. Braithwaite

Motivation: Aluminum-based components are widely deployed in the stockpile, and their reliability is of prime concern to the surety and longevity of our weapon systems. Aluminum is vulnerable to various forms of corrosion in storage environments, and yet our understanding of the corrosion behavior of Al remains incomplete. Our goal is to develop physically based models of Al corrosion, in close collaboration with experimental efforts, to help broaden our understanding of the aging and reliability of Al-based weapons components.

Accomplishment: Our work to date has focused on two specific applications of Al corrosion: atmospheric pitting corrosion of oxide-passivated Al metal, and intermetallic formation and subsequent corrosion in Al-based plastic encapsulated microcircuits (PEMs) with Au bond pads. Both of these corrosion phenomena are modeled within the same basic theoretical framework, but require slightly different computational approaches.

Aluminum metal is susceptible to pitting attack when it is polarized to a sufficiently high potential, e.g. when galvanically coupled to Cu metal. Copper impurities in passivated Al components can lead to dissolution of the Al material near the impurity, and this can occur in both aqueous and humid atmospheric environments. To study the effects of geometry and environment on the corrosion behavior of Al/Cu systems in a well-controlled manner, we apply experimental and computational techniques to quantify the pitting susceptibility of microengineered Al/Cu structures. The polarization behavior of Al and Cu metal is measured independently, and this experimental data is supplied to a computer code that calculates the distributions of potential (see Fig.

1) and current as functions of Al/Cu geometry and environment. The susceptibility of various configurations to pitting attack is ascertained by introducing locally the polarization response for a pitting material and determining the capacity of the system to support the current required to sustain a pit.

Aluminum bonded to Au pads is common in PEM devices. When these components are stored in a humid environment, water can diffuse through the plastic encapsulant and corrode the Al metal in the microcircuit. Corrosion generally occurs in regions near the Au bondpad where intermetallic has formed. As the component's performance degrades, its resistance versus time shows a complex behavior that is related to the corrosion process but is not fully understood. The resistance "jumps" at specific times, and this behavior is presumably linked to some critical event in the corrosion process. By modeling the passage of current through the component as it corrodes, we are able to associate the discontinuous resistance increases with instances where separate insulating corroded regions impinge to "pinch off" a region of conductive Al (see Fig. 2).

Significance: The behavior of Al components as they corrode is often beyond the reach of our limited understanding of these complex phenomena. In order to quantify the effects of numerous geometrical and environmental variables on the corrosion process, and to establish cause and effect relationships that are critical to our fundamental understanding, we couple computational techniques with experimental input. In doing so, we acquire important new insights into the causes and mechanisms of Al corrosion, and thereby broaden our understanding of the reliability and surety of Al-based weapons components.

Contact: Corbett Battaile, Materials & Process Modeling & Computation Dept., 1834
Phone: (505) 844-7039
Fax: (505) 844-9781
E-Mail: ccbatta@sandia.gov

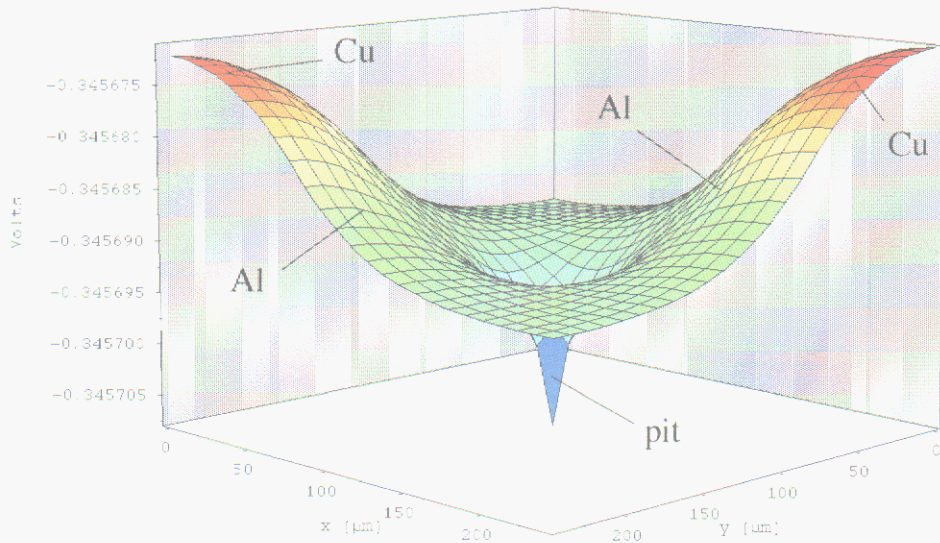


Figure 1. The distribution of potential around a corroding pit in an Al/Cu galvanic couple submerged in 50mM NaCl solution.

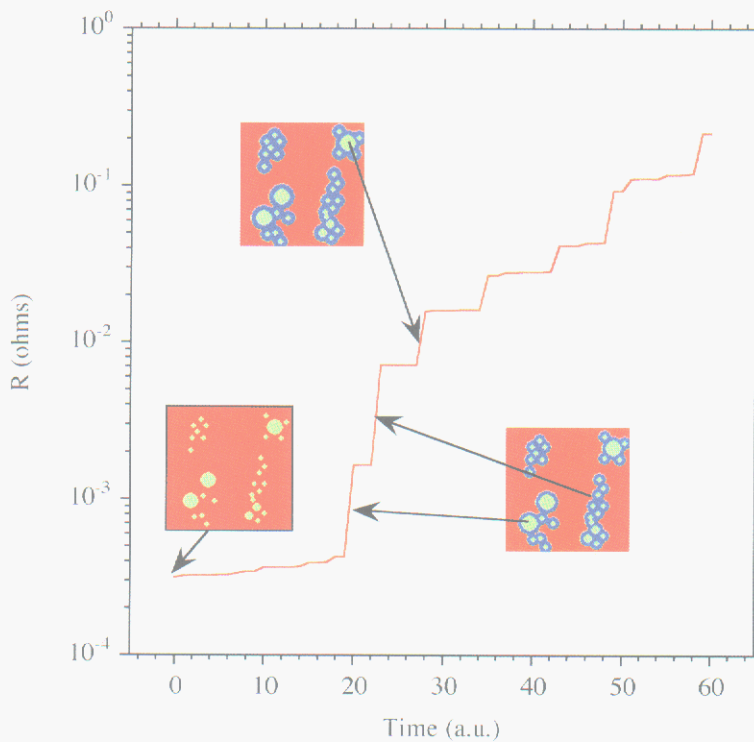


Figure 2. Resistance as a function of time in an Al-based PEM. Images show regions which are responsible for jumps in R. Red are Al, green is intermetallic, and blue is corroded.

Kinetics of Atmospheric Copper Sulfidation

J. W. Braithwaite, N. R. Sorensen, S. J. Lucero, and J. C. Barbour

Motivation: Atmospheric corrosion of copper is an important degradation process that can adversely impact the performance and reliability of electrical and electronic devices including connectors, contacts, printed circuit boards, diodes, and now even integrated circuits. An important part of mitigating or even predicting its effects is to understand how the environment influences the kinetics of the corrosion process. The work described in this brief involves our study of the prime environmental parameters (temperature, humidity, and contaminant concentration) on the rate of Cu₂S formation in very dilute sulfide containing atmospheres.

Accomplishment: As noted earlier by Graedel and co-workers at Bell Labs, copper sulfidizes in two distinct stages. In this investigation, several other significant characteristics of the sulfidation kinetics have been identified. A selection of the results are shown in Figure 1 and the main findings to date are as follows:

- Initial (Stage-I) kinetics is linear and first-order with respect to [H₂S]. If the humidity is low, an induction period exists that is related to the nature of the native copper-oxide layer. In the presence of light, the measured rate is affected by humidity with the rate being about 2 times higher at 80% RH than at 0.5% RH. At high RH, an adsorbed water layer probably enables faster electrochemical oxidation and reduction reactions to occur.
- The Stage-I rate is controlled primarily by gas-phase mass transport of H₂S at higher RH, whose contribution diminishes as the RH decreases. Nevertheless, the intrinsic surface sulfidation rate must be extremely fast. The measured activation energies for this stage are consistent with mixed kinetic

control (6-8 kcal/mole) at low RH and gas phase transport at high RH (< 4 kcal/mole).

- Stage II has a relatively parabolic shape and is observed only at mid to high humidity levels. Possibly, the presence of water affects the ionic diffusivity of the copper-sulfide product layer. That is, if the diffusivity is lower when the film is grown at high humidity (e.g., less defects present), then a transition from Stage-I to Stage-II will occur at thinner film levels. As determined by marker experiments (see corresponding brief on copper sulfidation mechanisms), the Stage-II kinetics are indeed controlled by Cu⁺ vacancy transport.

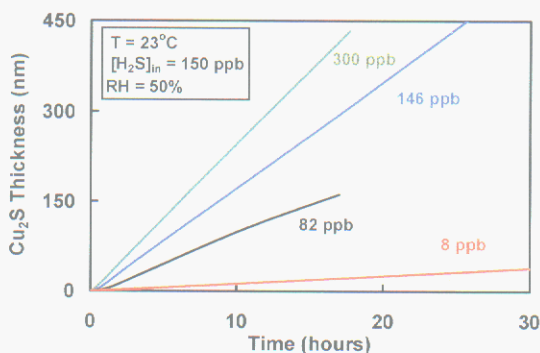
A phenomenological constitutive equation was formulated from these results that describes the rate of the surface reaction (J) at the moving Cu₂S / atmosphere interface as a function of contaminant (C_{H₂S}) and oxidant (C_{O₂}) concentration, temperature (T), and concentration of diffusing Cu holes and vacancies (C_{v-}, C_{h+}):

$$J = k_1 C_{H_2S} C_{O_2}^{\frac{1}{2}} e^{\left(-\frac{E_{k1}}{RT}\right)} - k_{-1} C_{v-} C_{h+} e^{\left(-\frac{E_{k-1}}{RT}\right)}$$

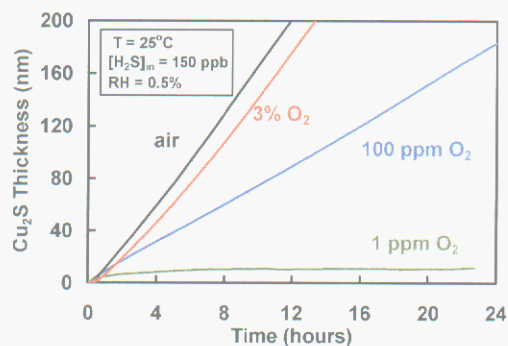
here, k_i=rate constants, E_{ki}=activation energies.

Significance: To assess the effects of corrosion on the performance and reliability of electrical devices, we are developing a comprehensive science-to-engineering tool-set. Computational considerations (e.g., multi-dimension device length scales, simulation time) require the core of the tool-set to be a deterministic, continuum-level mathematical model. The information from this work is providing the constitutive relationships and parameter quantification needed in such models.

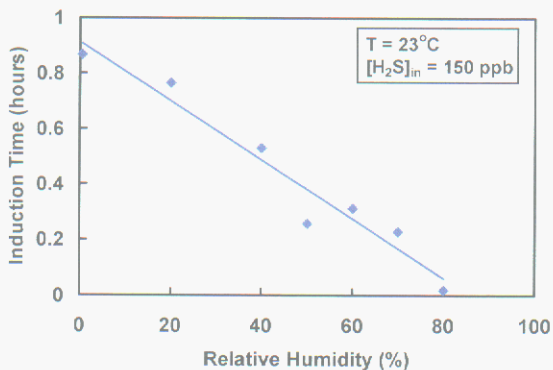
Contact: Jeff Braithwaite, Corrosion, Electrochemistry and Cleaning Dept., 1832
 Phone: (505) 844-7749
 Fax: (505) 844-6910
 E-mail: jwbrait@sandia.gov



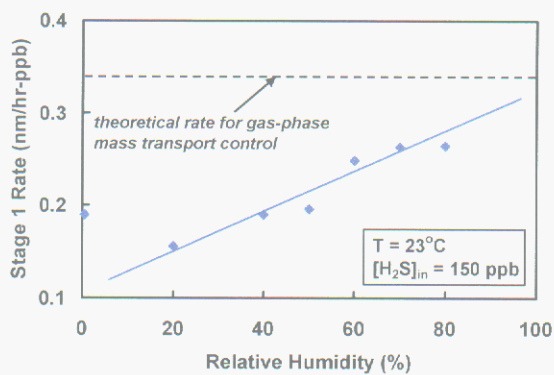
Effect of $[\text{H}_2\text{S}]$ on Stage-I kinetics



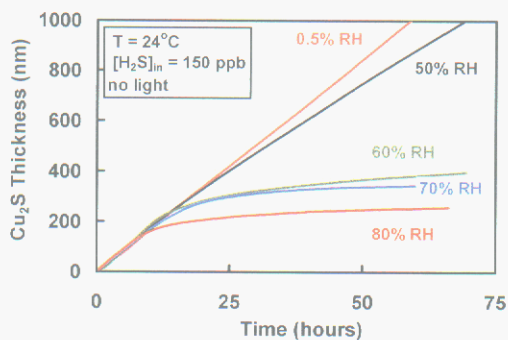
Effect of $[\text{O}_2]$ on Stage-I kinetics



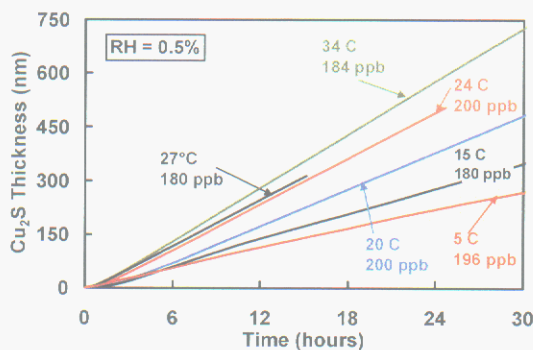
Stage-I induction time as f(RH)



Stage-I rate as f(RH)



Effect of RH on transition from Stage-I to II



Effect of temperature on Stage-I kinetics

Figure 1. Selected results from study of the effect of environmental parameters on the sulfidation kinetics of wrought copper.

Corrosion Monitoring of Strategic Petroleum Reserve Brine Pipelines

L.M. Serna and T.E. Hinkebein

Motivation: In the process of storing and retrieving crude oil in large underground salt caverns, the U.S. DOE Strategic Petroleum Reserve (SPR) transports brine (concentrated NaCl) via large diameter steel pipelines. For corrosion protection, these AISI 1020 pipelines have cement liners that provide a physical barrier and chemically passivate steel due to the localized alkalinity. The inherent passivity of the steel/cement interface can be compromised, however, by ingress of the chloride ion through the liner and subsequent corrosion.

The method of application for the liner is dependent on the geometry of the pipe section. Centrifugally spun liners are applied to straight pipe sections, while odd shapes, such as joints and flanges, receive a hand-trowelled liner. Spun liners form very dense and adherent barriers that provide excellent corrosion protection. Hand-trowelled liners, due to their lower density and adhesion, are more susceptible to solution penetration, corrosion and eventual spalling.

Electrochemical sensors were installed during the construction phase of the pipelines to allow in-situ monitoring of corrosion. These probes are seated flush with the internal surface of the pipe, under the cement lining (Figure 1). Primarily, linear polarization (LP) is used for routine field measurements because it provides a portable, fast, and easy way to collect corrosion rate data and site personnel can utilize it. The LP technique, however, is really limited to characterizing corrosion when the kinetics are controlled by an electrochemical charge-transfer process. When the steel is passivated or when diffusion of reactants dominates the corrosion rate (both possible), the LP technique will predict corrosion rates that are higher than actual. To address this deficiency, electrochemical

impedance spectroscopy (EIS) is also used to periodically monitor corrosion rates in the field (Figure 2). With EIS, it is possible to measure solution resistance, as well as distinguish between passive, diffusion-limited and active corrosion (Figure 3). The LP and EIS techniques are used in combination to provide a complete corrosion-monitoring plan. The LP measurements provide routine data needed for lifetime assessment and EIS allows in-depth analysis of unusual indications ("red flags") identified by LP.

Accomplishment: Historical corrosion rates for bare steel exposed to brine at SPR sites are 10-15 mils/year (mpy). Since the application of cement liners, corrosion rates have been reduced to acceptable levels of ≤ 1 mpy. Using LP and EIS techniques, monitoring at the West Hackberry, LA SPR site between 1994 and 1998 showed hand-trowelled sections had slightly higher corrosion rates (≈ 1 mpy) than sections with a spun liner (≈ 0 mpy). These results illustrate the ability of both LP and EIS to differentiate the corrosion rates of hand-trowelled and spun liners, even at very low values. The Sandia experimental program has now been established as a field-deployed tool for long term monitoring.

Significance: Periodic monitoring of corrosion rates of SPR brine pipelines is necessary to identify potential problem areas. This important part of the ongoing maintenance program will assure that the pipelines function properly over their design service life.

Contact: Lysle Serna, Corrosion, Electrochemistry and Cleaning Dept., (1832)
Phone: (505) 284-4495
Fax: (505) 844-9624
E-mail: lmserna@sandia.gov

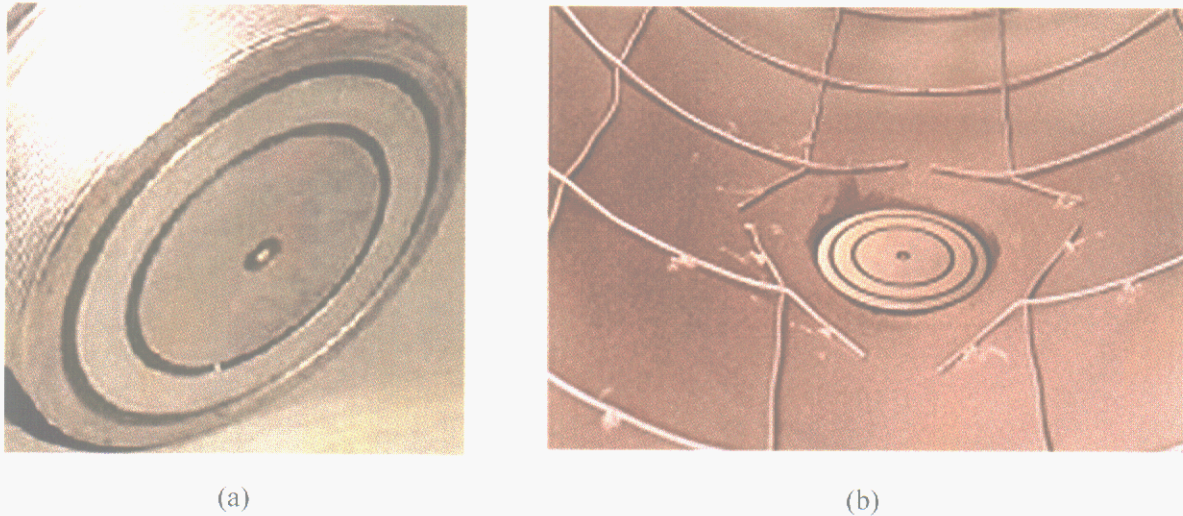


Figure 1. Corrosion monitoring probe with gold-pin pseudo-reference electrode, steel working electrode, and Hastelloy C276 counter electrode (a). Electrodes are electrically isolated from each other and the pipeline by an insulating epoxy. Corrosion probe flush in internal pipe wall, prior to application of a hand-trowelled cement liner (b).

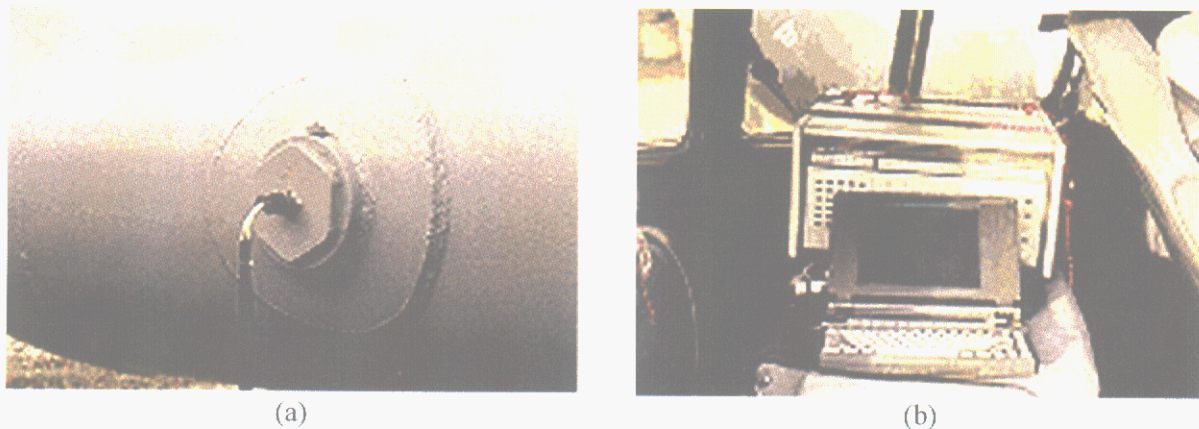


Figure 2. (a) Corrosion monitoring probe and test cable on brine pipeline and (b) electrochemical equipment in mini-van during field testing at West Hackberry, LA.

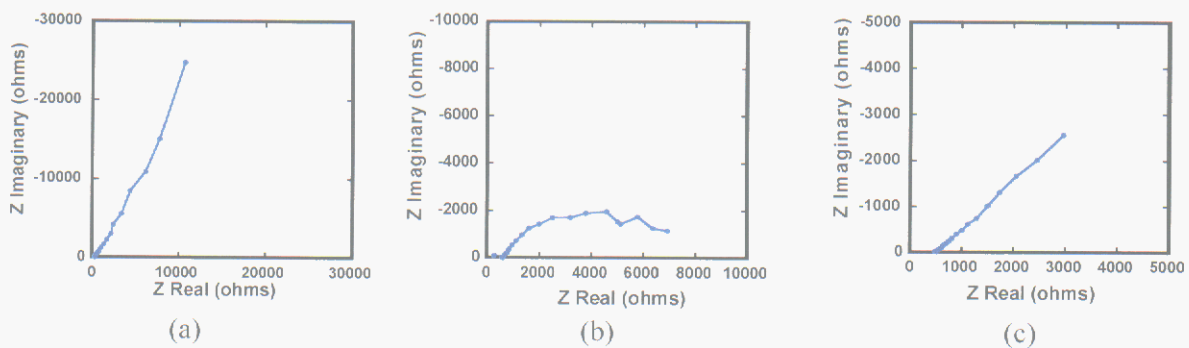


Figure 3. EIS complex plane (Nyquist) plots from field data for corrosion probes, indicating (a) passive behavior on a probe under a spun cement liner, (b) charge transfer behavior on a probe under a hand-trowelled cement liner and (c) diffusion behavior (a Warburg impedance) on a corrosion probe under a separate hand-trowelled cement liner.

Hydrolytic Degradation of Estane®5703: Chemistry and Morphology

R. A. Assink

Motivation: Estane®5703 is a polyurethane binder used in many composite energetic materials. The chemical and physical integrity of the binder often determines the mechanical properties of the composite, which in turn affect its safety and performance. Estane is a copolymer with chemically incompatible segments that segregate to form hard and soft micro-domains at room temperature. The primary degradation mechanism is believed to be hydrolysis of the ester group in the soft segment. We wish to develop a mathematical description of the chemical kinetics of hydrolytic degradation, characterize the effect of hydrolysis on the domain structure and relate these chemical and morphological changes to the mechanical properties of the composite.

Accomplishment: Estane has been aged under humid conditions at temperatures ranging from 37 to 95°C. ¹³C NMR spectroscopy has been used to investigate the chemical changes. Figure 1 shows ¹³C NMR spectra as a function of aging time. The spectra of the aged samples include additional peaks at 28, 62 and 176 ppm that can be assigned to products formed by hydrolysis of the ester linkage. The peaks were deconvoluted to provide a quantitative description of the chemical kinetics.

The hydrolysis reaction can be divided into three phases: an induction period, rapid hydrolysis and finally equilibrium. The induction period is attributed to the autocatalytic behavior of the acidic product. After the induction phase, the reaction proceeds rapidly to approximately 30% completion. At this time, the hydrolysis reaction has come to equilibrium with the reverse reaction. The extent of hydrolysis at equilibrium

depends on the ratio of the forward and reverse reactions. We were able to measure the reverse reaction rate in isolation by aging hydrolyzed Estane in a desiccated atmosphere. Modelers from LANL have developed a mathematical description of the chemical kinetics.

Hydrolytic degradation may affect both the integrity and chemistry of the hard and soft micro-domains. Earlier work has shown that the chain dynamics of the hard and soft micro-domains have very different characteristics. We are able to use the relaxation properties of ¹H NMR, which are sensitive to chain dynamics, to study domain structure. Figure 2 shows that the ¹H spectrum of Estane is composed of narrow and broad lines that correspond to the soft and hard phases, respectively. These spectra enable us to measure the phase content of the polyurethane versus extent of hydrolysis. Preliminary results suggest that the amount of hard phase increases during hydrolysis. This behavior is similar to chemi-crystallization, an increase in the crystalline fraction during aging, of partially crystalline polymers. A variation of a 2-dimensional experiment enables us to determine the chemical composition of each phase. As expected, the soft phase is composed primarily of the ester groups while the aromatic units are in the hard phase.

Significance: The performance of organic materials in humid conditions is important for many applications both within and outside of the DOE complex. These experiments are assisting in the development of quantitative models for the hydrolytic degradation of materials.

Contact: Roger Assink, Organic Materials Dept., 1811
Phone: (505) 844-6372
Fax: (505) 844-9624
E-mail: raassin@sandia.gov

Figure 1. The ^1H NMR spectra of Estane® 5703 exposed to 100 % relative humidity at 95 °C for the times indicated. The appearance of peaks corresponding to carboxylic acid and alcohol confirms that hydrolysis is the primary degradation pathway under these humid conditions. Deconvolution of the overlapping peaks enables us to quantitatively measure the extent of reaction as a function of aging time.

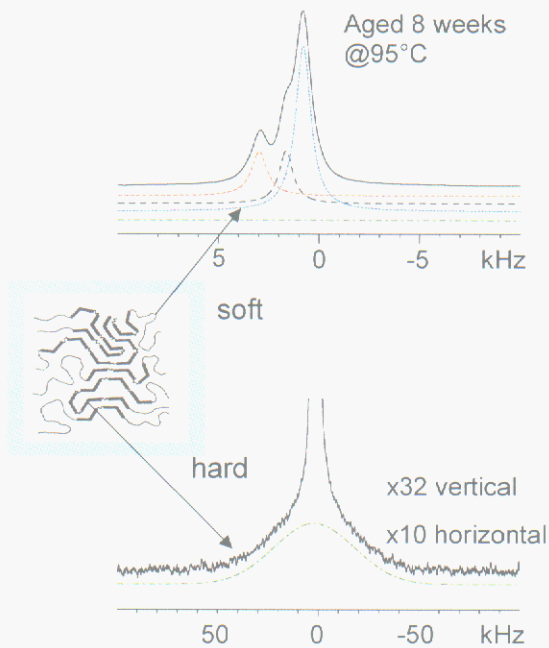
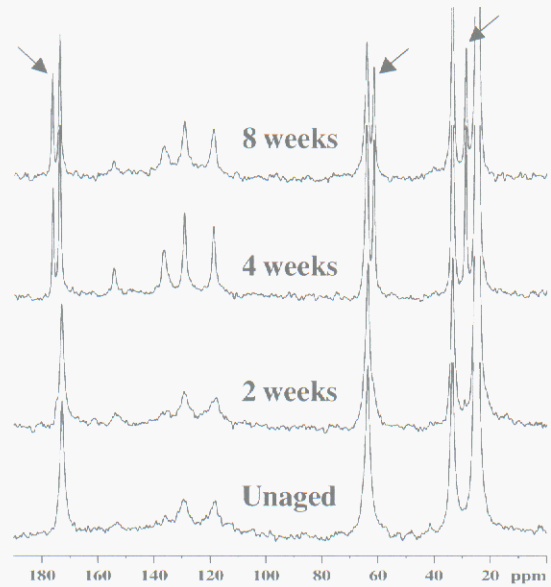


Figure 2. The upper spectrum is a normal high-resolution ^1H NMR spectrum that shows the chemical structure of the soft phase. If we expand the spectral window (lower spectrum), we observe the contribution from the hard phase.

Polymer Aging Studies

R. Bernstein and K. T. Gillen

Motivation: Organic materials, more specifically polymers, are often the 'weakest' part of any component. Like all materials, devices made of polymers age, thus time may have a dramatic effect on the chemical and therefore physical properties. Understanding how these polymers age, along with predictions of 'lifetimes' and real world analysis of aged polymers are important aspects in the determination of the reliability and life expectancy of any system.

Accomplishment: Utilization of our radiation and thermal aging facilities allows us the ability to better extrapolate lifetimes by performing accelerated aging under various aging conditions over extended time periods. This ranges in time from days to months/years. The ability to cover many temperatures for long times allows dramatically enhanced lifetime predictions. The classical application of the Arrhenius equation involving a few high temperature short time experiments can lead to disastrous predictions of room temperature real world aging.

We use classical as well as highly specialized techniques to measure both bulk and localized properties of the polymer. New techniques/approaches are constantly being sought to monitor/predict polymer aging behaviors that are applicable to a variety of different polymers, and/or broaden our current techniques to examine polymers previously not amenable to analysis.

Our research involves examining polymers from various components/devices. Current projects are examining Nylon and Kevlar from parachutes, wire insulation from nuclear power

plants, and o-ring/seals from weapons and equipment.

A specific example focuses on the degradation of Nylon used in parachutes. Thermal accelerated aging studies as well as innovative humidity studies are being performed to better understand and separate the role of thermal oxidation and hydrolysis mechanisms in the degradation of nylon. This will lead to a quantitative understanding of the importance of relative humidity on long-term degradation of Nylon. Physical properties (tensile strength) are monitored, as well as chemical properties (UV-Vis spectroscopy). A correlation will be sought between these properties with the goal of this project to predict the service lifetime of the Nylon, and to perform condition monitoring of the Nylon in the field. The latter involves removal and testing of small samples of Nylon from parachutes to determine the overall condition and remaining lifetime.

Significance: Parachute materials lifetimes as well as physical property changes with respect to aging will be determined. This will lead to predictions as to how long a parachute can remain in the weapon stockpile before it needs to be replaced. Condition monitoring techniques in development will provide a method to validate these predictions by examining parachutes throughout the stockpile.

Contact: Robert Bernstein, Organic Materials Dept., 1811
Phone: (505) 284-3690
FAX: (505) 844-9781
E-mail: rbernst@sandia.gov

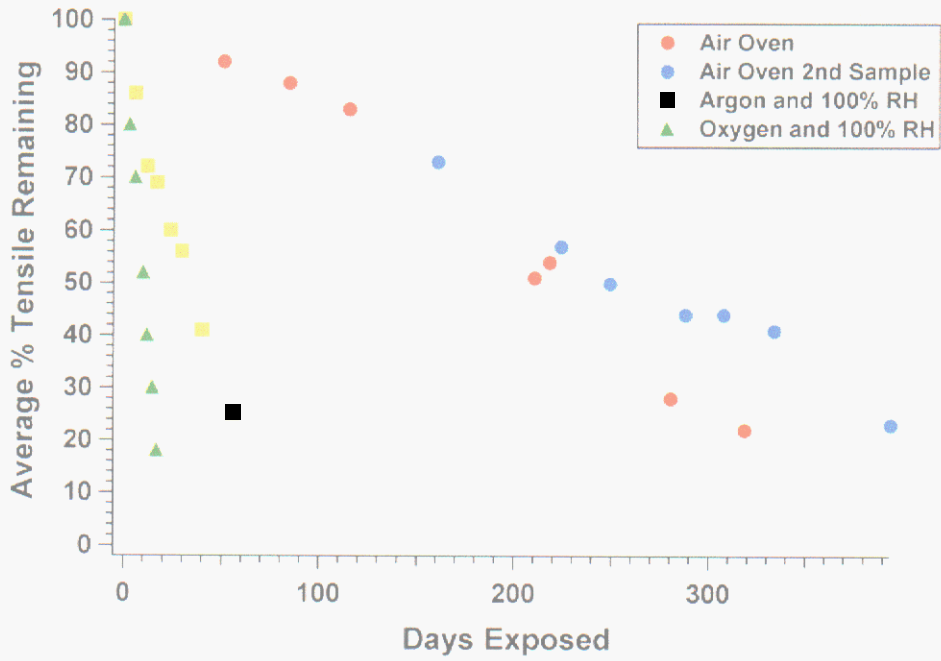


Figure 1. Nylon percent tensile strength remaining as a function of days exposed to 125°C: Air (circles), Argon and 100% RH (squares), and Oxygen and 100% RH (triangles).

Relationship Between Interfacial Interactions and Fracture Stress for Adhesive Joints in Mode II Loading

M. S. Kent, H. Yim, E. D. Reedy

Motivation: Much effort in adhesion science has been devoted toward understanding the relationship between fundamental interfacial interactions and engineering fracture quantities such as joint strength or fracture energy. These relationships are important from the standpoint of designing interfacial chemistry sufficient to provide the level of mechanical strength required for a particular application. In addition, such relationships are also important for understanding the effects of contamination and the effects of aging. If the areal density of interfacial chemical bonds decreases over time due to the presence of a contaminant such as water, or exposure to UV or other radiation, etc, the relationships between joint strength or fracture energy and interface strength are important for lifetime prediction.

Accomplishment: Through the use of self-assembling monolayers we have determined the relationship between the proportion of chemical and physical interactions at the epoxy/silicon interface and the fracture stress for nominally pure shear loading (Journal of Adhesives, 2001, 75, 267.). The model system was an epoxy adhesive on a polished silicon wafer containing its native oxide. The interfacial interactions were varied systematically over a wide range using self-assembling monolayers (SAMs) of octadecyltrichlorosilane (ODTS). This is illustrated in Figure 1. The epoxy interacted strongly with the bare silicon oxide surface through H-bonding interactions involving the acidic silanol groups on the silicon oxide surface and the basic amine groups of the crosslinker. However, the epoxy interacted with the methylated tails of the ODTS chains through only very weak van der Waals interactions. We examined the fracture behavior of such joints as a

function of the ODTS coverage, thereby systematically varying the proportions of H-bonding and van der Waals interactions acting across the interface. By varying the deposition temperature, the deposition can occur either by island growth or single chain growth. Both cases were examined in this work.

The relationship between the surface density of specific interaction sites and fracture stress was found to be highly nonlinear (shown in Figure 2), with a sharp increase in fracture stress occurring over a small increase in the density of specific interaction sites. The rise in the fracture stress coincides with the onset of deformation in the epoxy rather than a transition from adhesive-to-cohesive failure, although the latter transition follows closely after the onset of deformation in the epoxy. The results are independent of whether the ODTS deposition occurs by island growth ($T_{\text{dep}} = 10\text{ }^{\circ}\text{C}$) or by homogeneous growth ($T_{\text{dep}} = 24\text{ }^{\circ}\text{C}$). We postulate that an adhesive-brittle to adhesive-ductile transition occurs when the interface can support local stresses that are comparable to the macroscopic yield stress.

Significance: This work suggests a new criterion for strength in adhesive joints in pure shear loading. The criterion is that the interface strength must be sufficient to promote yielding in the adhesive. Since this criterion involves fundamental interfacial interactions which can be calculated from first principles or measured directly with scanning force probes, and an easily measured mechanical property of the adhesive, reliability predictions can be made for a wide range of adhesive joints loaded in pure shear.

Contact: Mike Kent, Microsystem Materials, Tribology & Technologies Dept., 1851
Phone: (505) 845-8178
Fax: (505) 844-9624
E-mail: mskent@sandia.gov

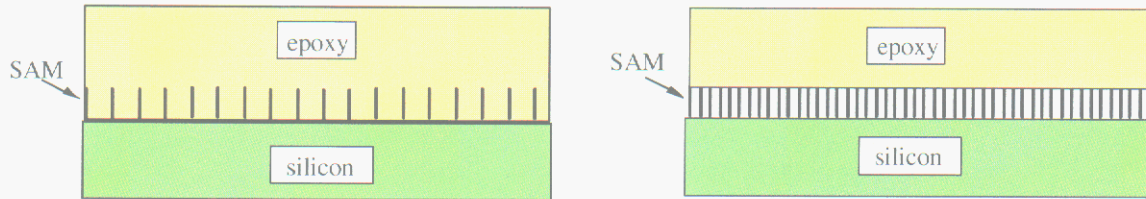


Figure 1. Illustration of the use of self-assembling monolayers to control interfacial interactions by varying coverage. The SAM is composed of methyl-terminated alkyltrichlorosilane chains roughly 25 Å in length. The epoxy interacts strongly with the silicon oxide through H-bonding of the amine groups on the crosslinker and the acidic silanol groups of the native oxide.

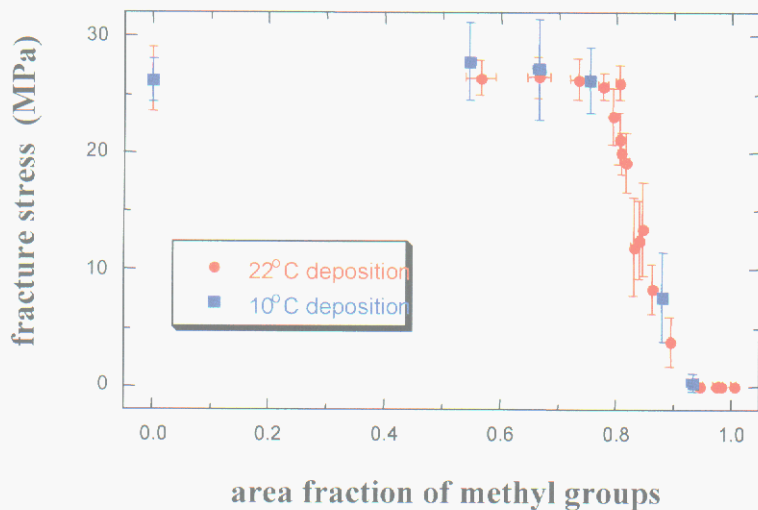


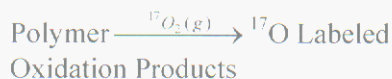
Figure 2. Fracture stress data from the napkin-ring pure shear test geometry as a function of the area fraction of methyl groups. The latter is varied using SAMs as in Figure 1. These data demonstrate a sharp increase in engineering fracture stress over a narrow range of the density of specific interaction sites.

Using ^{17}O NMR Spectroscopy to Investigate Polymer Degradation

T. M. Alam

Motivation: Understanding polymer aging and degradation is crucial for accurate prediction of polymer lifetime, durability and reliability. The elucidation of the chemical and physical mechanisms at the molecular level leading to polymer degradation is an important objective in achieving this goal. This laboratory has recently demonstrated that by using ^{17}O nuclear magnetic resonance (NMR) spectroscopy, molecular level details of the degradation can be obtained.

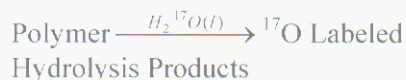
Accomplishment: By utilizing ^{17}O NMR and isotopic enrichment the difficulty of distinguishing the degradation species signal from the dominant unaged polymer signal can be eliminated, thus providing a powerful tool for the investigation of degradation in polymer systems. For example, oxidative degradation can be directly probed by utilizing $^{17}\text{O}_2$ during the aging process.



We recently reported the ^{17}O NMR study of the thermal oxidation of the homopolymer polyisoprene and the long chain alkane pentacontane. Figure 1a shows the ^{17}O NMR spectra for the thermal oxidation of pentacontane. A wide range of degradation species can be quantitatively measured, allowing the distribution of degradation species as a function of aging time to be accessed as shown in Figure 1b. The oxidative degradation of polymers under γ -irradiation has also been studied using ^{17}O NMR, allowing differences in the chemical mechanisms

of oxidative degradation in the presence or absence of radiation to be directly assessed.

This laboratory has also demonstrated that hydrolysis of polymer systems can be investigated by utilizing ^{17}O labeled water during the aging process.



Hydrolysis in the polyurethane Estane and in polydimethylsiloxane (PDMS) have been investigated. Figure 2 shows the ^{17}O NMR spectrum for a PDMS that has undergone hydrolysis in the presence of γ -irradiation. Several different type of alcohol species are clearly resolved

Significance: These studies demonstrate the potential of using ^{17}O NMR to probe oxidation and hydrolysis in polymer systems. This novel and promising technique allows elucidation of detailed aspects of the degradation mechanism, along with the determination of individual oxidation product yields.

Contact: Todd Alam, Organic Materials Dept., 1811
Phone: (505) 844-1225,
Fax: (505) 844-2974
E-mail: tmalam@sandia.gov

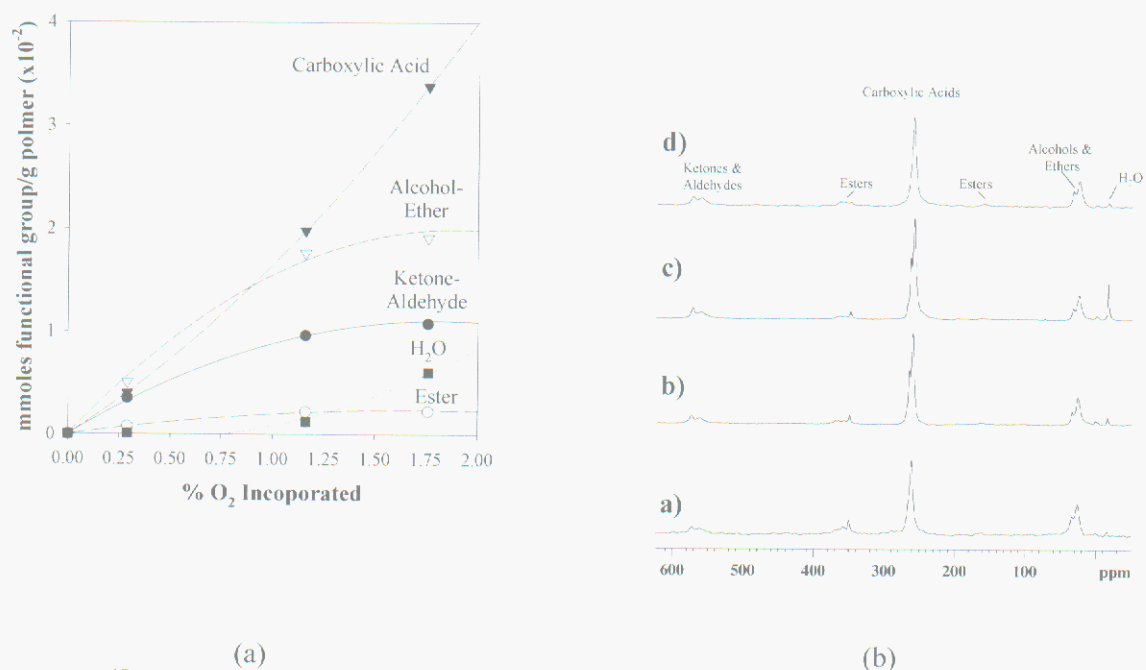


Figure 1. (a) ¹⁷O NMR spectra of γ -irradiated oxidatively aged pentacontane for different O₂ incorporation levels. (b) Distribution of degradation species in radiolytically oxidized pentacontane.

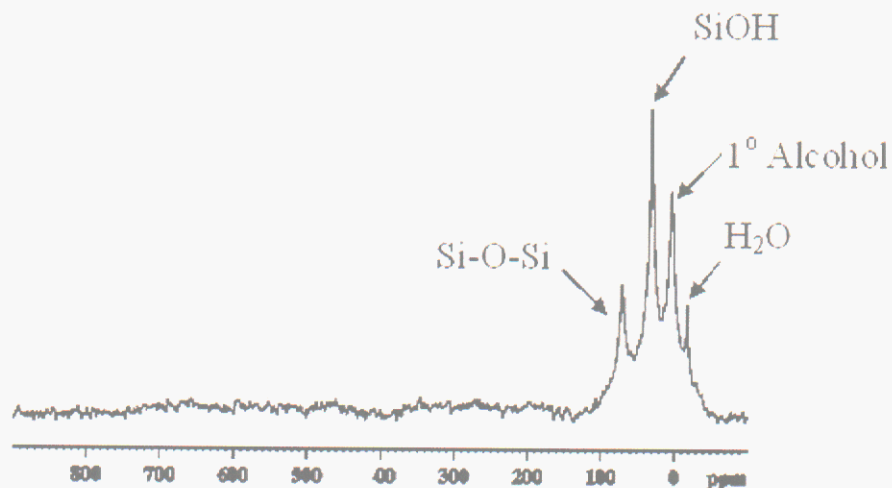


Figure 2. ¹⁷O NMR spectra of hydrolyzed PDMS aged under γ -irradiation.

The Wear-out Approach for Predicting the Remaining Lifetime of Materials Applied to a Material with Induction-time Behavior

K. T. Gillen, M. Celina and R. Bernstein

Motivation: Extrapolations of accelerated aging data are often used to predict the lifetime of materials under their ambient aging condition. Such extrapolations involve a certain amount of uncertainty. For critical applications (e.g., nuclear weapons, aircraft, nuclear power plants), the presence of confirmatory approaches would add confidence to such predictions.

Accomplishment: A new method (the “Wear-out” approach) was developed to allow better predictions of residual lifetimes for polymer materials. The method is a generalization of cumulative damage failure models that have been used mainly for fatigue life predictions for metals and composite materials. The aging time to reach failure takes the place of the number of fatigue cycles necessary to reach failure. For thermal aging of polymers, the usual accelerated aging assumption is that an increase in temperature will lead to a constant increase in the reaction rate driving degradation. This implies that degradation curves at two different temperatures (T and T_{ref}) superimpose when the times at temperature T are multiplied by a_T ; this is referred to as time-temperature (t - T) superposition. For a step change in T after damage has occurred at T_{ref} , t - T superposition implies that the remaining lifetime at the second T should be linearly related to the aging time prior to the step. It should therefore be possible to estimate the remaining lifetime and therefore the service lifetime of polymers by completing the aging at an accelerated T (the “Wear-out” T). For many materials, degradation will approximate so-called “induction-time behavior, where the

degradation property being followed changes very little until large changes occur at failure. Following properties versus time therefore offers little warning of impending failure. One tremendous advantage of the Wear-out approach comes from its potential for converting such non-predictive results to linear predictive behavior. Figure 1 shows density results (a typically sensitive degradation monitor) versus aging time for an EPR material aged at four different temperatures. At each temperature, the point where the density abruptly increases corresponds to the time where the tensile elongation quickly plummets to zero. To test the Wear-out approach, we took samples that had aged for various times at 110°C and switched them to a 140°C oven until their densities reached 1.45 g/cc (“failure”). The times to reach 1.45 g/cc at 140°C are plotted versus the times at 110°C in Figure 2 (squares); also plotted are the density results versus aging time at 110°C (diamonds). As anticipated, the Wear-out approach transforms totally non-predictive “induction-time” behavior into linear predictive results.

Significance: A new, general approach (the Wear-out method) for predicting residual polymer lifetimes has been developed. This method should be especially valuable for so-called “induction-time” behavior (little degradation occurs until just before failure) since such non-linear behavior can be transformed into linear predictive behavior.

Contact: Ken Gillen, Organic Materials Dept., 1811
Phone: (505) 844-7494
Fax: (505) 844-9781
E-mail: ktgille@sandia.gov

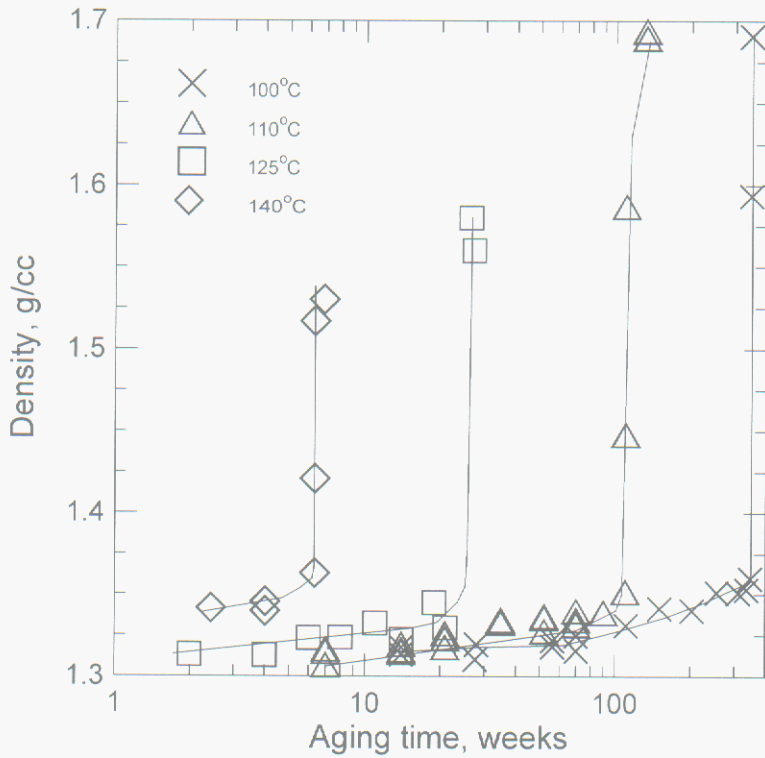
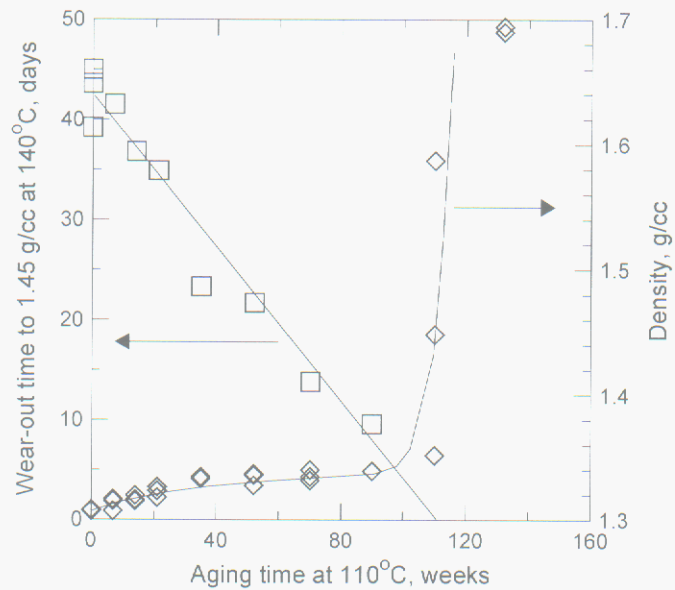


Figure 1. Density versus aging time at the four indicated aging temperatures for an ethylene propylene rubber (EPR) material.

Figure 2. Diamonds show density results versus aging time at 110°C (right-hand y-axis). Squares show Wear-out results representing the subsequent times required at 140°C for the 110°C samples to reach a density of 1.45 g/cc plotted against the aging times at 110°C



Aging and Degradation of Lubricant Materials –Assessing Performance and Aging Behavior

M.T. Dugger and D.E. Peebles

Motivation: Several categories of electromechanical devices are used in weapon systems for controlling the arming of the weapon, including access control devices and those that sense the environment. These devices employ mechanical actuation to perform their intended functions, and use several general types of lubricant coatings and self-lubricating materials to control friction and wear. Design of these components incorporates chemically stable materials in a carefully controlled environment, but outgassing of materials inside the component or unintended exchange of gases with the outside atmosphere can result in reactive species being present with the lubricants. Changes in lubricant composition can alter its friction and wear behavior. Oxygen and water vapor may be present inside electromechanical devices, and the performance of solid lubricants that contain MoS₂ is known to change due to oxidation. Prediction of the operating characteristics of electromechanical devices as a function of age requires an understanding of the aging mechanisms, kinetics, and performance impact for these lubricant materials. At some contact points, several lubricant materials may be used in combination, which can produce different aging behavior than observed for the individual materials.

Accomplishment: Our work to date has focused on predicting the impact of aging in a stronglink. Gas sampling of hardware returned from the stockpile has shown that oxygen and/or water vapor may be present inside these devices. The device in question employs three major types of lubricants. Electrofilm is a sprayed-on film consisting of MoS₂ particles in a phenolic resin binder, and is cured and mechanically burnished

after deposition. Vespel is a bulk composite containing 15 wt.% MoS₂ particles in a polyimide matrix, which is machined to the desired final shape of the part. Vydax consists of fragments of fluorocarbon molecules similar to Teflon, below about 800 amu, and is deposited from solution in a fluorinated solvent such as Freon-TF.

Figure 1(a) shows the performance of the Vespel composite related to the amount of oxidation that has taken place in several different environments. Combination of the friction data on as-fabricated as well as aged Vespel surfaces with the oxidation kinetics data results in the predicted friction performance shown in Figure 1(b). This performance data may be used to predict the friction behavior of Vespel composite in contact with unlubricated stainless steel as a function of age. Our present work is focused on establishing performance models for more complex interfaces, where multiple lubricating materials are present together. Figure 2 shows the variation in steady-state friction data as a function of oxidation time for interfaces where electrofilm, Vespel and Vydax are all-present.

Significance: We can now construct age-aware performance models for the individual lubricant materials in the stronglink under study. These results are also applicable to many more electromechanical devices used in weapons that employ the same lubricants. These models can be used in dynamic models of device performance to determine the impact of lubricant degradation on device performance. These relationships can be used in dynamic models of device performance to determine at what age the device may operate outside of specifications.

Contact: Mike Dugger, Microsystem Materials, Tribology, & Technologies Dept., 1851
Phone: (505) 844-1091
Fax: (505) 844-4816
E-mail: mtdugge@sandia.gov

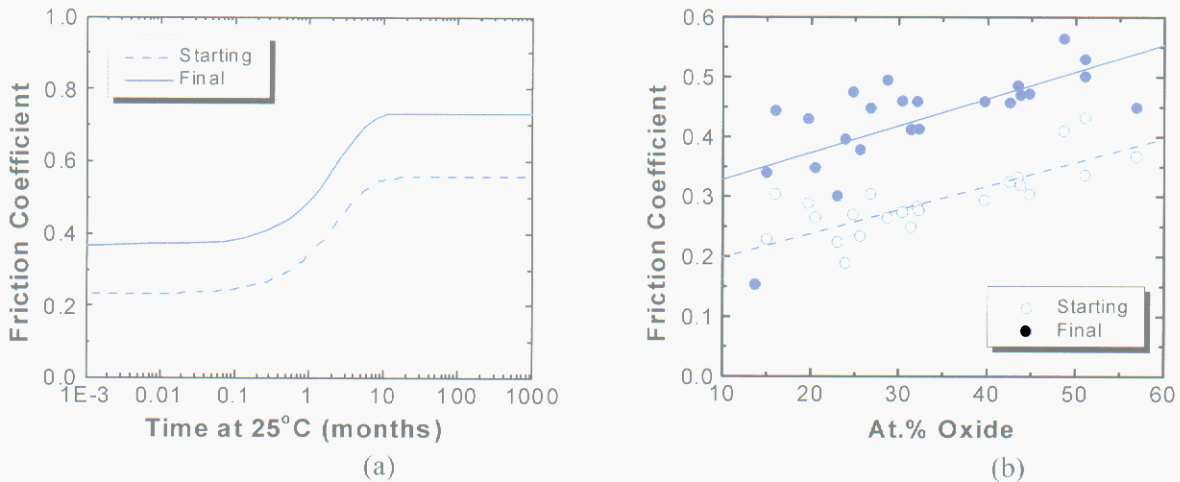


Figure 1. Friction coefficient exhibited by Vespel self-lubricating composite as a function of the amount of MoS₂ converted to oxide (a) during controlled oxidation exposures, and the predicted friction coefficient as a function of age in air at 25°C (b) based on the oxidation kinetics data.

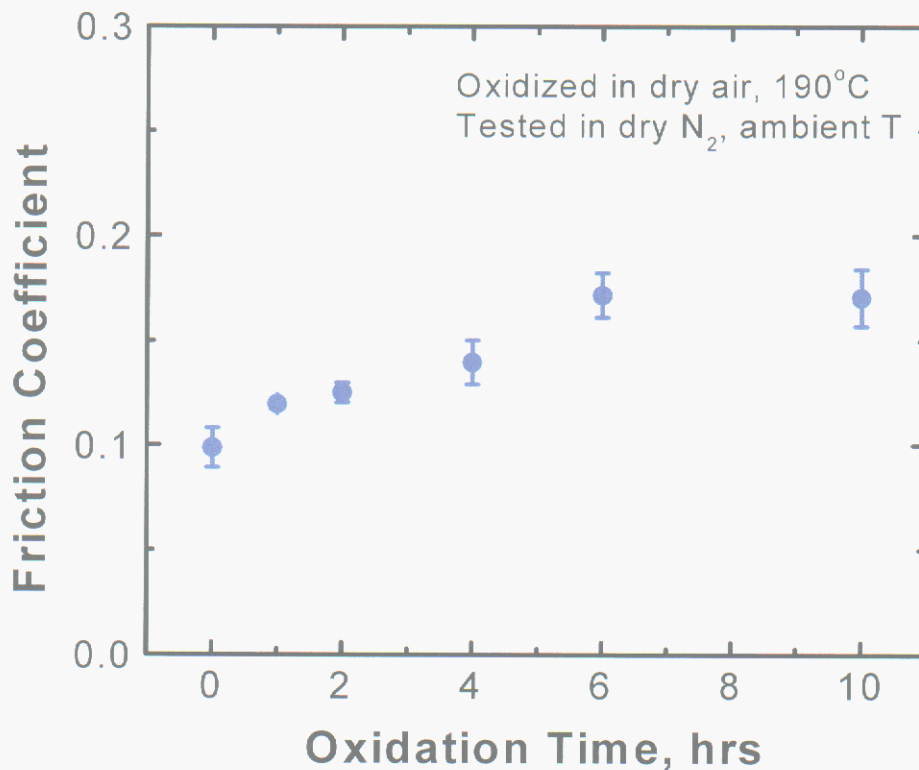


Figure 2. Measured friction coefficient as a function of the exposure time (to air at 190°C) for a tribosystem containing stainless steel coated with electrofilm and then coated with Vydax, in contact with Vespel. The data at each time increment includes the mean value and an error bar equivalent to one standard deviation.

Aging and Degradation of Lubricant Materials – Assessing and Predicting Chemical Changes

D. E. Peebles and M. T. Dugger

Motivation: Electromechanical devices are utilized in the stockpile for use and safing controls. Several general classes of lubricant coatings and self-lubricating materials are commonly used in these devices for control of friction and wear. In order to predict performance as a function of time, the aging behavior of these lubricant materials must be understood. In many of the common electromechanical devices, the lubricant materials are often used in combination at critical device interfaces. The aging behavior of the lubricants used in combination can be quite different from the aging behavior of the isolated lubricant materials.

Accomplishment: Previously, we have assessed the aging of each of three common lubricant materials individually in the expected device atmospheres and conditions. The newest challenge was to understand the lubricant aging when all three lubricant materials were present at the same critical interface. The lubricants involved include Electrofilm, Vydax AR and Vespel SP-3. Electrofilm is a composite coating with particles of MoS₂ and graphite dispersed in a vinyl phenolic resin matrix. Vydax AR is a waxy fluorocarbon material derived as a byproduct from Teflon production. Vespel SP-3 is a composite consisting of 15 wt.% MoS₂ dispersed in a polyimide matrix. The critical interface of interest involves a part that is coated with Electrofilm on stainless steel, and then overcoated with Vydax AR, in contact with a part made of Vespel SP-3 that is overcoated with Vydax AR.

Since the surfaces play the largest role in the interactions at the interface, the extent of oxidation of the lubricant materials is assessed by the use of x-ray photoelectron spectroscopy (XPS), which can differentiate chemical states in the near surface region. Two different assessments of surface oxidation are used – the

amount of molybdenum that has been converted from the sulfide to the oxide, and the amount of sulfur that has been converted from the sulfide to a sulfate. Figures 1 and 2 show how each of these quantities change for each of the component parts of the critical interface for two ambient atmospheres at 150°C. The ambient environments used for controlled oxidation include dry air (79% N₂, 21% O₂, 0% H₂O) and wet N₂ (97% N₂, 0% O₂, 3% H₂O).

As seen in the figures below, the lubricant materials show different responses to the Vydax overcoat, and the ambient oxidizing species has a significant affect of the oxidation rates. For Vespel, the presence of Vydax has very little affect on the oxidation rates for production of either molybdenum oxide or surface sulfate species. In addition, the oxidation rates for Vespel are essentially independent of the oxidizing species (O₂ versus H₂O). The observed differences in rate are attributed to part geometries. For Electrofilm, there is a larger affect of oxidizing species, especially in the presence of Vydax, where oxidation in dry air (by O₂) is significantly slowed down.

Significance: We now have sufficient information on how lubricant aging is affected by the presence of additional lubricant materials to construct an accurate aging model for this critical interface where multiple lubricants are used. By knowing how the oxidation rates are affected by the concentrations of O₂ and H₂O present and the temperature, we can use the information to predict oxidation as a function of time, temperature and ambient environment under actual use conditions. This is one piece of the puzzle needed to determine the performance of the electromechanical device as a function of age. The friction coefficient of the component parts as a function of oxidation level have determined in another part of the project.

Contact: Diane Peebles, Materials Characterization Dept., 1822
Phone: (505) 845-8087
Fax: (505) 844-7425
E-mail: depeebl@sandia.gov

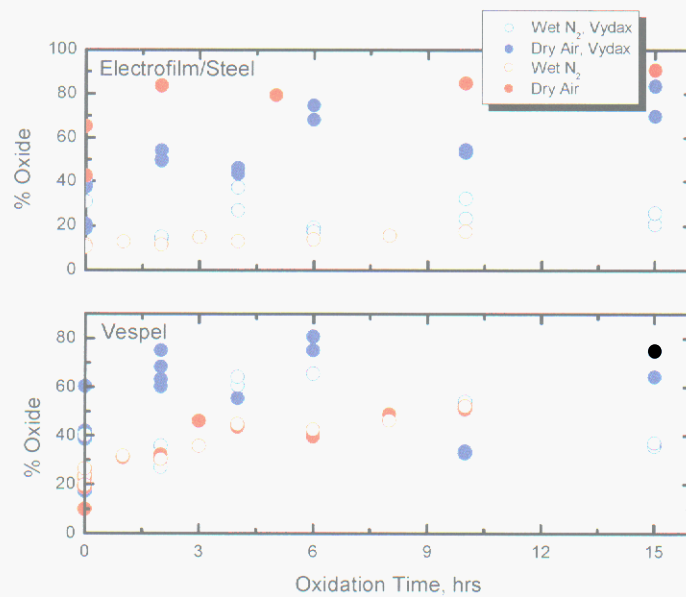


Figure 1. Amount of molybdenum that has been converted from the sulfide to the oxide as a result of surface oxidation in different atmospheres at 150°C for the two component parts of the critical interface (blue symbols). Red symbols show the comparison to coupon oxidation studies of Electrofilm and Vespel without Vydax present in the same atmospheres.

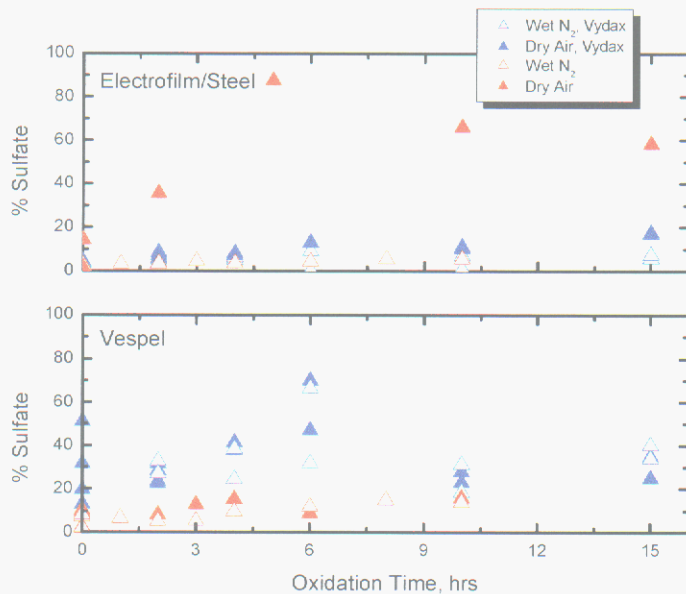


Figure 2. Amount of sulfur that has been converted from the sulfide to a sulfate as a result of surface oxidation in different atmospheres at 150°C for the two component parts of the critical interface (blue symbols). Red symbols show the comparison to coupon oxidation studies of Electrofilm and Vespel without Vydax present in the same atmospheres.

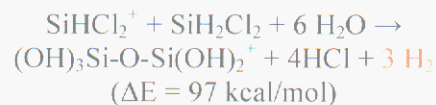
Characterization of Hazardous Solids and Their Formation Process Resulting from Semiconductor Dichlorosilane Exhaust Flow

S. M. Thornberg and R. L. Jarek

Motivation: Intel approached Sandia to investigate the cause of several fires that had occurred during maintenance of exhaust tubing. High-temperature oxide (HTO) processes using dichlorosilane (DCS) gas result in a buildup of pyrophoric solid deposits that sometimes react violently with air or water. This problem is not isolated to just this one process, but can occur whenever low amounts of unreacted DCS are exhausted for long periods of time making hazardous buildup prevention of interest to all semiconductor manufacturers.

Accomplishment: Initially, the solid deposits were analyzed using NMR, FTIR and differential scanning calorimetry. A strong correlation was found between the flammability of the sample and the content of Si–O–Si (siloxane) bonds present, however, chemical mechanisms remained unknown. Detailed chemical investigations were carried out using high-resolution Fourier-transform ion cyclotron resonance mass spectrometry (FT-ICR/MS). Gas samples from the process exhaust flow were analyzed using FT-ICR/MS and over 35 different chlorosiloxane fragments and their isotopes were identified. Figure 1 shows a resulting FT-ICR/MS spectrum and the identification of the larger mass peaks. FT-ICR/MS ion-molecule reaction studies of the dichlorosilyl cation (DCS^+) elucidated the origin of chlorosiloxanes. While no reaction was found between DCS^+ and nitrogen, oxygen or nitrous oxide, a significant reaction was found with water. This DCS^+ /water reaction, in the presence of neutral DCS, leads to the formation of chlorosiloxane cations,

precursors to formation of the larger, pyrophoric chlorosiloxanes found deposited in exhaust tubing. Kinetic studies determined the rates of reaction for the formation of chlorodisiloxane species. Figure 2 shows two examples of the DCS^+ reaction kinetics recorded (points) and the resulting fit (solid lines). It was found that after reaction with water, DCS^+ polymerizes quickly with available DCS. The thermodynamics of the reactions and proposed products were modeled using high-level *ab-initio* calculations confirming that all observed reactions were exothermic and corresponding neutral DCS reactions have similar energies. For the complete hydration of DCS^+ with DCS and water there is significant heat released as well as hydrogen gas:



Significance: Since DCS/water reaction was found to cause of the exhaust deposit formation, solutions to the problem were devised. To minimize buildup the exhaust manifold must be airtight for as long as the DCS in the exhaust is concentrated. It also followed that the most effective scrubbing unit would utilize water. A water scrubber has been installed and found to eliminate >99.7% of the DCS from the exhaust plume, effectively eliminating buildup problems. (IEEE Trans. Semicond. Manuf. 2001, 14 (1), 20-25.)

Contact: Steve Thornberg, Chemical & Biological Sensing, Imaging & Analysis Dept., 1812
Phone: (505) 844-8700
Fax: (505) 844-2974
E-mail: smthorn@sandia.gov

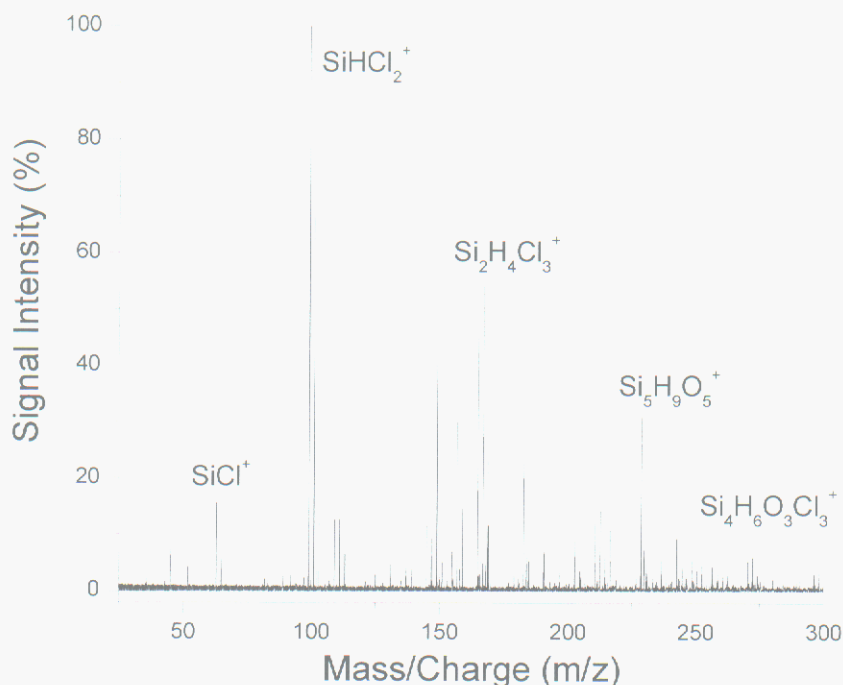


Figure 1. FT-ICR/MS spectrum of the HTO exhaust. The spectrum is from a delayed detection experiment performed to enhance ion signals from low hydride affinity and ionization potential molecules.

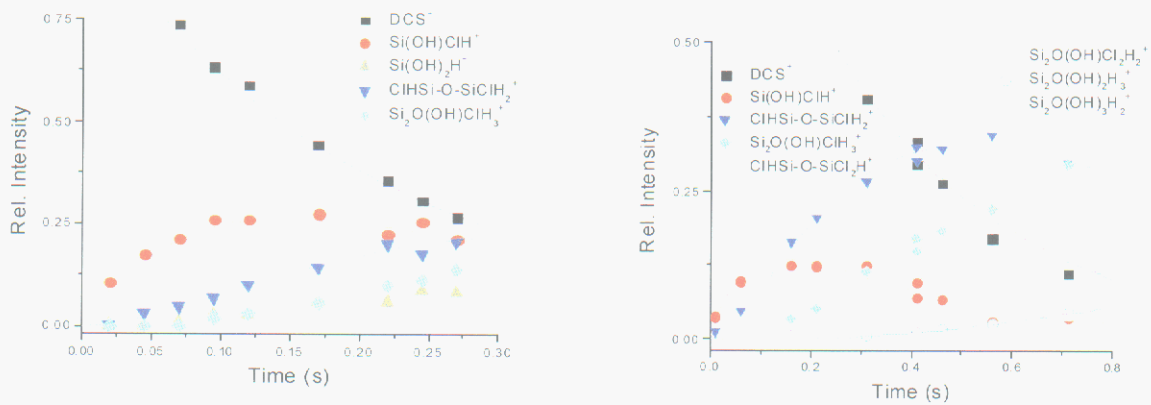


Figure 2. Plot of ion populations vs. time, demonstrating the kinetics of the reactions forming chlorodisiloxane species. These two plots differ only in the pressure of H_2O and DCS, where the right one has more DCS present. Reaction rates are determined by least squares fitting and modeled by the straight lines shown.

Gas Analysis for the Evaluation of Lithium Ion Cells

T. T. Borek

Motivation: Part of the evaluation of lithium ion cells for various mobile applications concerns the safety of these systems deployed in the field. This is especially true for systems such as hybrid electric vehicles that may contain many of these cells to provide power. The generation of toxic gas in regular and abuse conditions is a main concern of manufacturers of vehicles. Also, an understanding of solvent decomposition mechanism can permit intelligent selection of additives to minimize loss of cell performance.

Accomplishment: A gas chromatograph that can analyze fixed and organic gases was equipped with a flow-through gas-sampling manifold. The manifold monitors the gas sample pressure and will control the flow of helium purge gas through the system. The fixed gases that this system can monitor are nitrogen, oxygen, argon, carbon monoxide, carbon dioxide, methane, and other C2 and C3 organic gases. The organic gas system will also detect methane, C2, C3, and higher molecular weight organic gases.

This analytical system is coupled with an Accelerating Rate Calorimeter (ARC). The ARC will heat a sample to a set temperature under precise thermal conditions. For the experiments discussed here, a typical lithium ion cell electrolyte solution consisting of ethyl methyl carbonate, ethylene carbonate, and lithium hexafluorophosphate is placed in a small spherical sample bomb for heating. The ARC is purged with helium, and heating commences at a slow rate to 210°C. The experiment shown lasted for 17 hours. As may be seen in contour plots,

much gas is evolved at higher (~170°C) temperatures.

Figure 1 is a contour plot of the fixed gas analysis. The largest peak is due to carbon dioxide; the other peaks present are light organic gases, carbon monoxide, and nitrogen, oxygen, or argon. Figure 2 is a contour plot of the organic gases. Organic gases such as ethylene, ethyl fluoride, and other species are observed, in addition to solvent molecules. Note that these contour plots represent 17 hours of data collection.

Significance: We are able to detect and identify fixed and organic gases in electrolyte samples heated in an ARC under controlled conditions. This proof-of-concept test will be expanded to analyze lithium ion cell cathode and anode materials immersed in electrolyte, and eventually, full cells. Cells may also be tested as a function of applied voltages and thermal conditions.

This project is a joint effort between Organization 1822 and Organization 2521, Lithium Battery Research and Development Department.

Contact: Ted Borek, Materials Characterization Dept., 1822
Phone: (505) 844-7758
Fax: (505) 844-2974
E-mail: tborek@sandia.gov

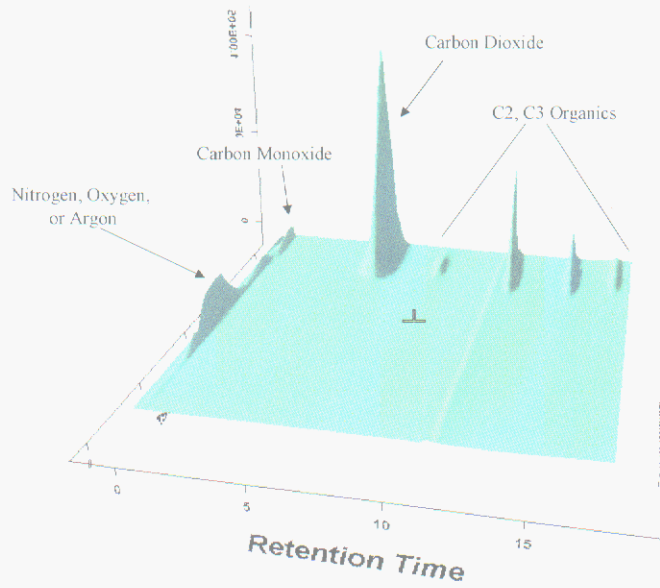


Figure 1. Contour Plot of Fixed Gas Response for Electrolyte Heating

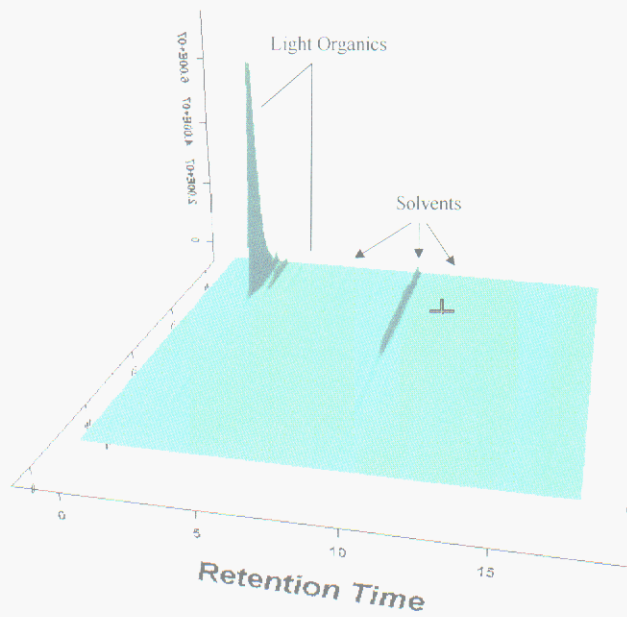


Figure 2. Contour Plot of Organic Gas Response for Electrolyte Heating

In-situ Neutron Diffraction of Commercial (Sony) Li-ion Batteries

M. A. Rodriguez and D. Ingersoll

Motivation: In-situ measurements yield the best information about the function of battery materials because the data is collected on an actual functioning cell as it undergoes charge/discharge. We, as well as other groups, have recognized the utility of these in-situ measurements, and have studied a wide variety of materials in experimental cell designs. We were interested in performing in-situ structural studies via neutron diffraction for a couple of reasons. First, neutrons have a high penetration, and therefore, can monitor full battery assemblies (i.e. commercially available cells). Secondly, the stronger relative scattering of lithium by neutrons makes neutron diffraction a good probe for lithium occupancy in the structure.

Accomplishment: Our experimental setup was straightforward. An electroded Sony Li-ion cell was placed on the HIPD neutron spectrometer at LANSCE for data collection in the uncharged state. Data was collected overnight to obtain the best possible pattern. Next the cell was charged up to ~4.1 V and allowed to equilibrate (~ 1 hour) before a second set of spectra were collected (again overnight for the best possible signal). Although the diffraction peaks from the cathode (LiCoO_2) were small, it was possible to see a structural difference in the diffraction peak locations. Figure 1 shows a zoomed region of the diffraction data from the charged and uncharged cell. The LiCoO_2 (017) and (018) peaks are very sensitive to c-axis changes while the (110) senses only changes in the a-axis and the (113) is sensitive to both a- and c-axis changes, making it a good gauge for total volume change. The large

shift in the (017) and slight change in the (110) peak indicates a large c-axis expansion and slight a-axis contraction. Refined lattice parameters based on these peak positions confirmed the expansion of the c-axis along with a slight contraction of the a-axis. These results are completely consistent with the expected behavior of the cell during Li de-intercalation as observed in our original XRD experiments. Interestingly, the iron peak from the outside canister showed no change in peak position, making it a good internal standard for the experiment.

Significance: This in-situ experiment demonstrates the feasibility of investigating actual commercial cells via neutron diffraction. Clear structural changes were observed between the charged and uncharged states of the cathode. Past XRD work required fabrication of in-situ cells that were similar but not exact replicas of commercially-available batteries. In this study, we have shown that we can now obtain similar results as with our XRD analysis but on the exact configuration of the functioning cell. With this technique, we have a way to perform non-destructive structural analysis of fully assembled/functioning Li-ion cells and directly correlate this information to properties and performance, all in the same experiment. Additional experiments are planned on the new HIPPO neutron spectrometer to improve counting statistics via the large detector array.

Contact: Mark Rodriguez, Materials Characterization Dept., 1822
Phone: (505) 844-3583
Fax: (505) 844-9781
E-mail: marodri@sandia.gov

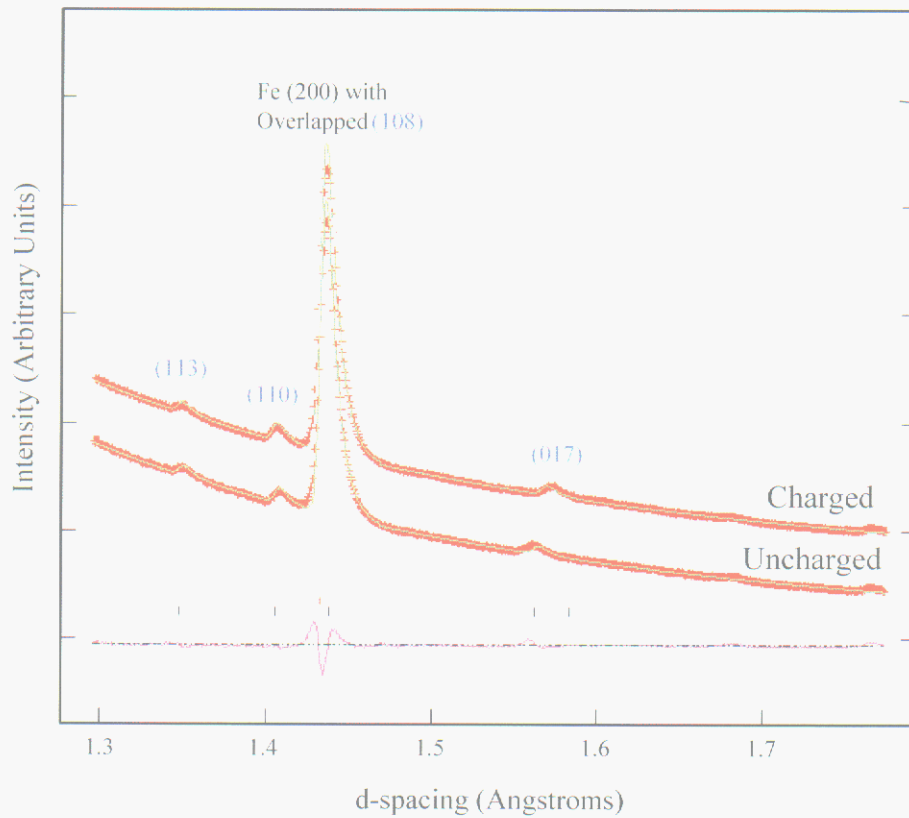


Figure 1. Zoomed region of neutron diffraction patterns from Sony Li-ion cell in uncharged and charged states. Blue labels are LiCoO_2 hkl 's.

Analysis of Multicomponent Adsorption on Type 3A Zeolites Using TG-FTIR

M. K. Alam and L. E. Martin

Motivation: Type A zeolites are commonly used as desiccants in many applications from manufacturing to storage. For critical storage applications, models based on weight gain are often used to estimate when the zeolite has become saturated. The model used must account for other possible adsorbates and the competition between the other adsorbates and water. Unfortunately, many models do not account for adsorbate competition.

The adsorption characteristics of zeolites in the presence of single component adsorbates have been well documented, using isothermal methods. Typically, these experiments are performed by monitoring the pressure change after the zeolite is exposed to a known pressure of the gas under study. In the case of more than one gas, GC (gas chromatographic) analysis or some other method must be used to determine the composition of atmosphere surrounding the zeolite. Infrared (IR) spectroscopy has also been used to examine the characteristics of adsorbates on the surface of type A zeolites. IR has the advantage that several species may be studied directly and concurrently. However, quantitation of each species on the zeolite surface has been difficult, due to lack of an appropriate calibration.

Accomplishment: A promising method of analysis for adsorbate competition on zeolites is thermogravimetric (TG) analysis combined with Fourier Transform IR, or TG-FTIR. Weight gain and weight loss can be monitored using TG, providing quantitative information regarding the amount of adsorbate on the zeolite. The infrared

spectra collected during desorption of the zeolite also indicate the amount of each analyte desorbed. A system has been developed allowing known amounts of water and other gases to be adsorbed by a desiccant contained within the TGA.

Data from the adsorption of CO₂, water and nitrogen on a type 3A zeolite has been collected. Infrared data was examined using the generalized rank annihilation method (GRAM) as well as a direct spectral fitting method. GRAM allowed the estimation of the amount of water desorbed from the samples, which provided an estimation of CO₂ by difference. A direct estimation of both CO₂ and water desorbed was done using a Classical Least Squares (CLS) calibration. Synthetic data, used for the calibration, was created using the MALT software package. Analyses indicate that the amount of CO₂ adsorbed on the Type 3A zeolite is dependent on the amount of water present (see Figure 1).

Significance: Prior determinations of multicomponent adsorption on zeolites have relied on analysis of the gas mixture after adsorption had occurred. Using the TGA/IR method direct analysis of desorption is possible, along with the kinetics of desorption.

Contact: Kathy Alam, Chemical and Biological Sensing, Imaging and Analysis Dept., 1812
Phone: (505) 845-9621
Fax: (505) 844-2974
Email: mkalam@sandia.gov

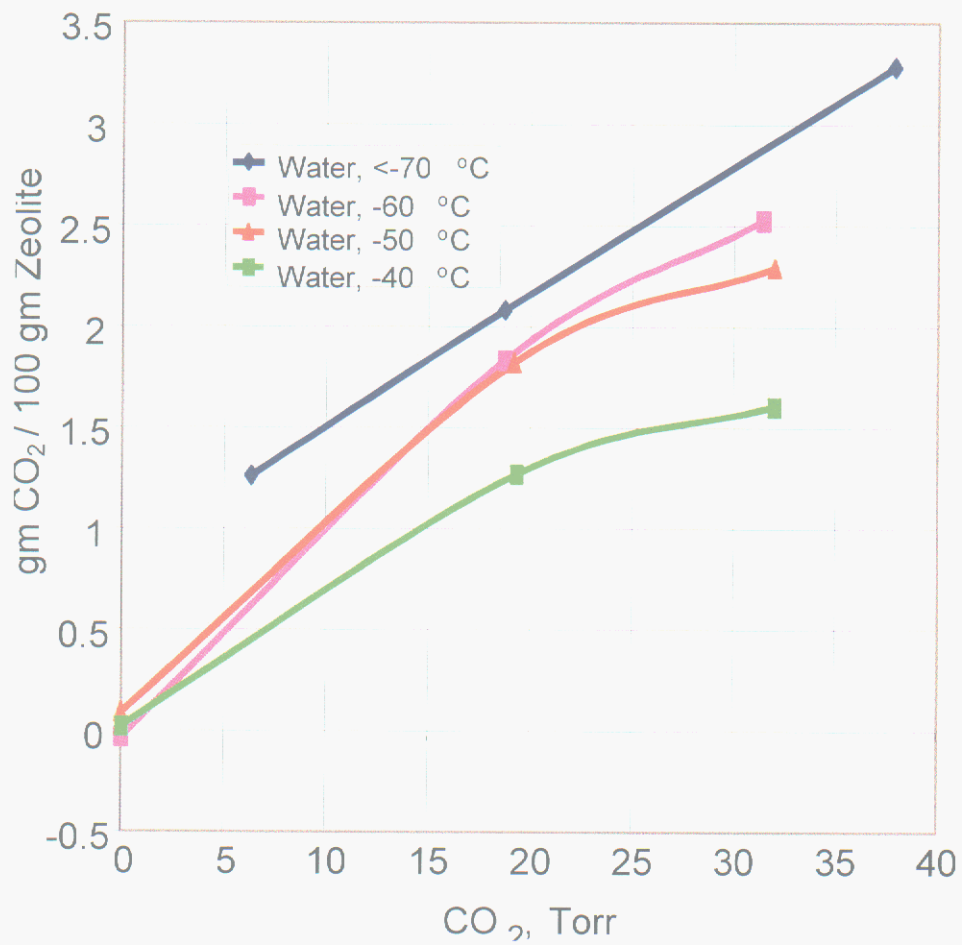


Figure 1. Results of TG-IR analysis, showing increased CO₂ adsorption with decreased water adsorption.

Indentation Techniques used as a Sensitive Microprobe for Stress

R. Tandon

Motivation: Residual stresses are ubiquitous in brittle materials, their composites, and at and around an interface where one or more brittle material is present. In polycrystalline materials, residual stresses exist at the grain boundary level due to a thermal expansion mismatch, and crack path selection through or around the grain is influenced by this stress. In particulate, whisker or fiber composites residual stresses, over ten to hundreds of grains, play a significant role in determining the effectiveness of the reinforcement. At interfaces, stresses may occur over thousands of grains due to elastic and thermal mismatches, and are crucial in determining the practical work of adhesion of the interface, and the strength of the adhered layers. Residual stresses are sometimes deliberately introduced to strengthen the material and suppress crack initiation. Therefore residual stress characterization is crucial in understanding the mechanical response of the material, and assessing system reliability.

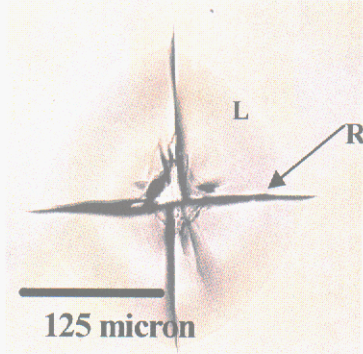
Accomplishment: We are utilizing indentation with a sharp Vickers indenter to ascertain the magnitude and extent of the stress profiles in materials. In the validation stages, we have conducted experiments on glass with a compressive stress profile introduced using ion-exchange treatment. The load range used in the indentation tests was from 0.001N to 20N. The smallest load used provides information about the aggregated stress in the top 0.25 micron of the material, whereas the largest load probes ~40 micron deep layer. Current models for stress determination utilize a change in the crack length

at the indentation site to estimate the stress. These models have been found to be inaccurate for our systems. A new approach based on deconvolution of load-displacement data appears to be more promising. Figure. 1 shows the crack patterns obtained for 20N load on the as-received, 12 hour and 96 hour exchanged samples. Stress analysis around the indentation and the observed crack patterns are used to deduce the stress profiles in the material. Figure. 2 shows indentations placed at different distances from the center of a metallic via in a LTCC substrate. Cracks close to the via interact strongly with the thermal expansion mismatch stress field, and changes in crack trajectories help map the stress fields around the via.

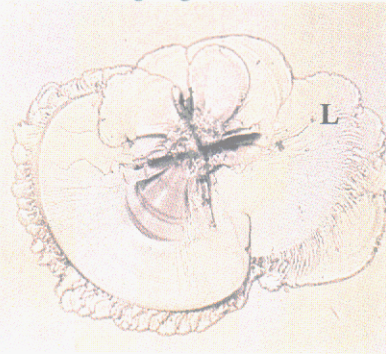
Significance: A complete understanding of the stress fields around a sharp indentation in a brittle material allows us to predict the mode of cracking around the site, and the crack trajectories. When the indentation is placed in a material with a prior stress field, either on a surface that possesses a residual stress, or near a dissimilar microstructural feature, the crack patterns are altered. This alteration can be used to map the prior stress state. This stress state along with other material properties serves to validate FEA calculations, as a measure of the impact of processing changes, and as input into reliability analyses.

Contact: Rajan Tandon, Ceramic Materials Dept., 1843
Phone: (505) 844-1187
Fax: (505) 844-9781
E-mail: rtandon@sandia.gov

Ion-Exchanged glass: 12 hr.



Ion-Exchanged glass: 12 hr.



Ion-Exchanged glass: 96 hr.

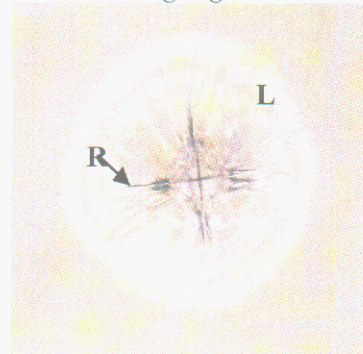


Figure 1. As-received glass subjected to an indentation load of 20N shows surface radial (R) cracks emanating from the corners of the Vickers indenter and subsurface lateral (L) cracks (seen as a diffuse circular band). The 12 hr. ion-exchange treatment reduces the radial cracks but exacerbates lateral cracking at the same load. For the 96 hour ion-exchange treatment, lateral cracks remain sub-surface while the radials are resurgent. These crack patterns provide clues to the distribution of the stress profile under the surface.

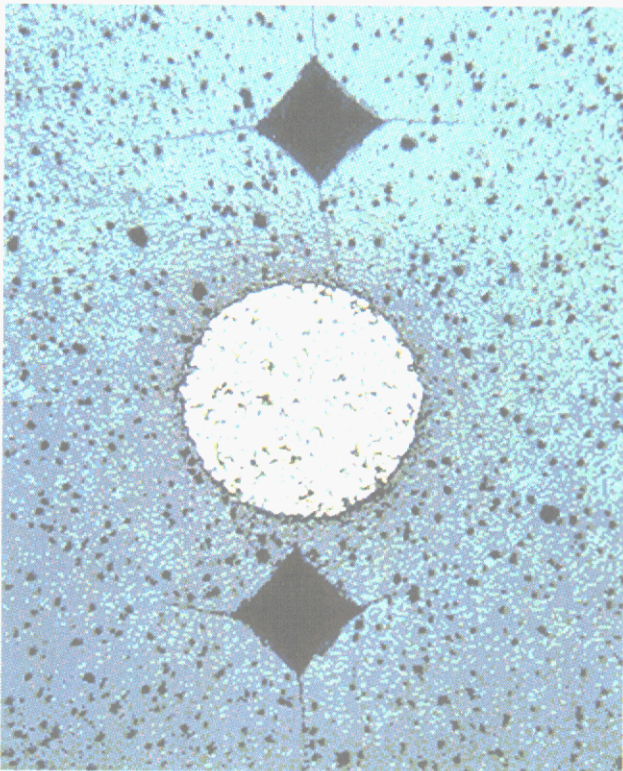


Figure 2. Indentation cracks in a LTCC substrate (blue) interact with the stress field around the metallic via (diameter~ 200 microns). The stress state influences the crack initiation, and three (instead of one) cracks initiate closer to the via (bottom indent, top vertex). Crack trajectories at the two vertices below are slightly affected, whereas the bottom vertex is unaffected. Only the crack emanating from the bottom vertex of the indent further from the via (top) is affected by the stress field.

Multivariate Curve Resolution Improves Understanding of Zeolite Desiccants

M. R. Keenan

Motivation: Zeolite molecular-sieve desiccants are used extensively in military systems to maintain the internal humidity at acceptably low levels. Recent aging studies have shown that these materials can become a life-limiting component in some applications. A proper assessment of the impact of desiccant degradation requires an in-depth, fundamental understanding of their water adsorption characteristics and specifically how co-adsorbed species (e.g., CO₂ and NH₃) affect performance.

Accomplishment: Sandia, in collaboration with the University of New Mexico, has developed an IR spectroscopic method to characterize the adsorption in situ and in real-time of water and other gases onto zeolites. The resulting IR spectrum is monitored as a function of time. Even for the relatively simple case of water alone onto a commonly used zeolite (Type 3A), complicated changes in the spectrum are observed (Figure 1). Several distinct but overlapping spectral features are seen to grow in and/or decay as adsorption progresses.

To extract the maximum amount of information from these types of very large data sets, several new analytical techniques have been developed. One of these, multivariate curve resolution (MCR), describes a family of algorithms whose purpose is to separate mixed, overlapping spectral signatures (such as shown in Figure 1) into pure spectral components and their spatially and/or time-varying concentrations. Recently, MCR was applied to the IR spectra for these desiccants and new insight into how water is adsorbed has been gained. As shown in the Figure 2 inset, MCR analysis resolved at least

four distinct spectral features. One feature is probably associated with the spectrum of dry zeolite as it rapidly goes away with the introduction of water. The three remaining features appear to be directly related to water adsorption. Also shown in Figure 2 is how the abundance of each of these components varies with time. While the exact physical or chemical cause of these spectral changes is not presently known, the results suggest that water can exist in a number of different states in the zeolite. For example, several different types of adsorption sites may exist in the zeolite or water may adsorb in multiple layers.

Significance: Adsorption behavior is typically described in terms of an adsorption isotherm. A variety of isotherm models are available in the literature, but these typically apply only over a limited range of exposures. Using the insights gained through our adsorption experiments and MCR analyses, a multi-site/layer Langmuir-like isotherm was devised that can adequately describe the adsorption behavior of desiccant materials over a dew point range exceeding 100°C (or a factor > 105 in water vapor partial pressure). These newly developed spectroscopic and data analysis tools have already improved our desiccant engineering ability and promise to be indispensable for understanding the more complex behavior expected when multiple, strongly adsorbing, species are present.

Contact: Mike Keenan, Chemical & Biological Sensing, Imaging & Analysis Dept., 1812
Phone: (505) 844-2190
Fax: (505) 844-7910
E-mail: mrkeena@sandia.gov

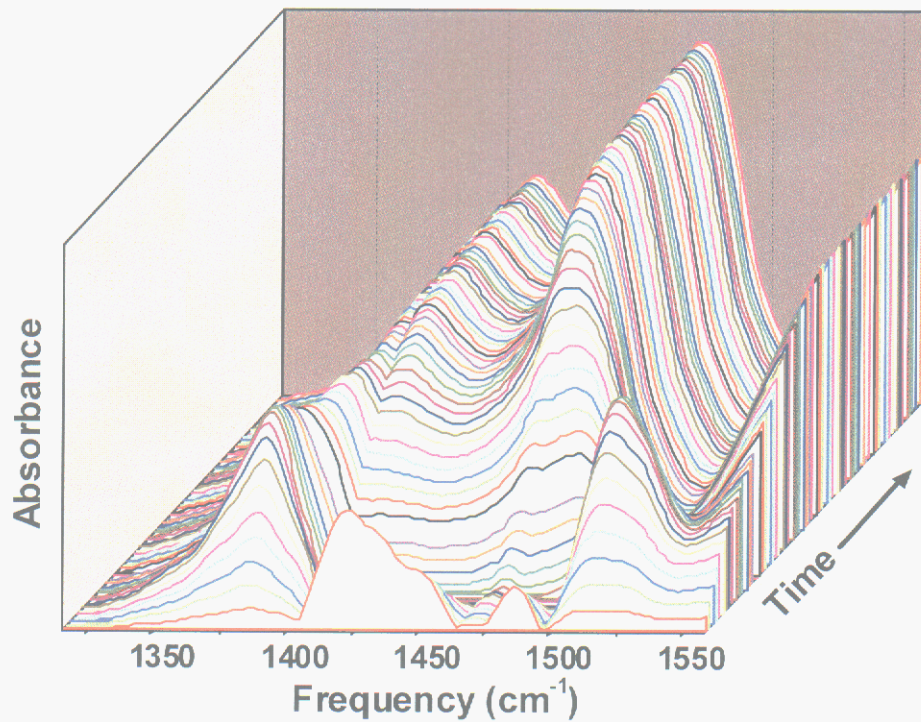


Figure 1. The infrared spectrum of Type 3A zeolite changes with time as water is adsorbed in a -20°C dew point environment.

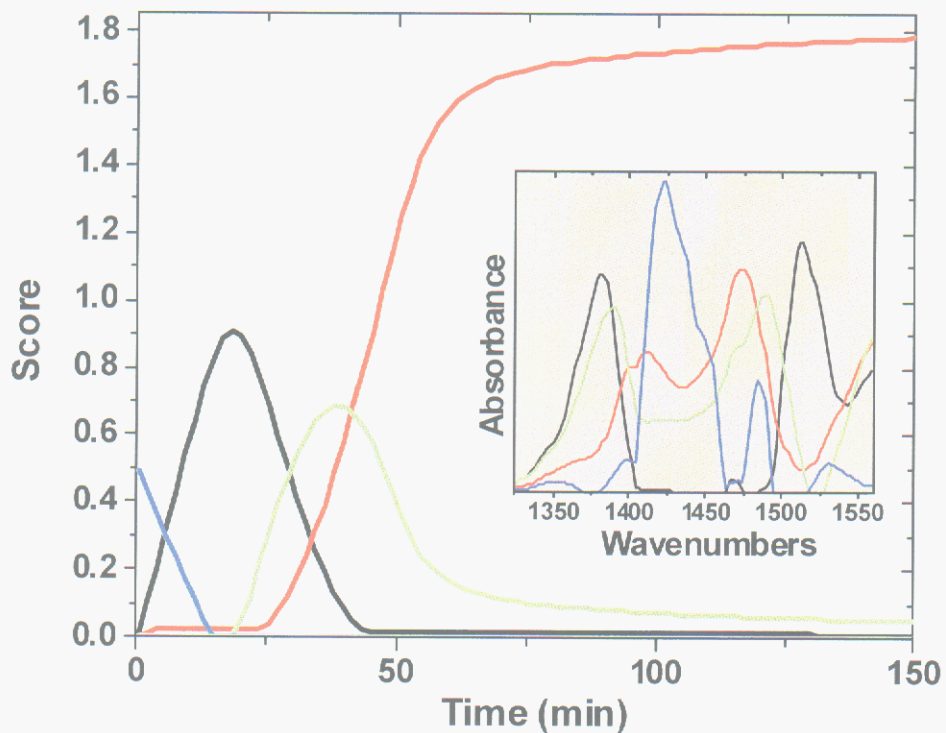


Figure 2. Multivariate curve resolution is used to extract pure spectral components (inset) and their time-varying abundances from the raw spectral data.

Discovery of a New Orientation Relationship between Body Centered Cubic and Face Centered Cubic Crystal Lattice Systems

T. J. Headley and J. A. Brooks

Motivation: Knowledge of the crystallographic orientation relationship (OR) between two phases with different crystal structure is crucial to understanding microstructure/property relationships in important processes such as solid-state precipitation, martensitic transformation, epitaxial growth, and solidification. Historically, only a small number of ORs has been known to exist between the common crystal lattice systems, e.g. only five have ever been reported for the bcc-fcc system. While investigating ORs in solidification structures of several steels, we discovered a new OR between delta-ferrite (bcc) and austenite (fcc) that has not been previously reported for bcc-fcc lattices.

Accomplishment: The new OR was found in solidification microstructures of type 304L and 309S austenitic stainless steels and a ternary Fe-Cr-Ni alloy. These solidification structures were produced by laser-engineered-net-shaping (LENS) of the 304L alloy, and by gas-tungsten-arc (GTA) welding of the 309S and Fe-Cr-Ni alloys. Evidence for the new OR was obtained from electron diffraction patterns in transmission electron microscopy. The new OR is: $(111)_{\text{fcc}} // (110)_{\text{bcc}}$ and $[-110]_{\text{fcc}} // [-110]_{\text{bcc}}$. The $\langle 110 \rangle_{\text{fcc}} // \langle 110 \rangle_{\text{bcc}}$ alignment is distinctive among known bcc-fcc ORs. Because a set of close-packed planes is parallel between the ferrite and austenite lattices in the new OR, it is related to the well-known Kurdjumov-Sachs (K-S) and Nishiyama-Wassermann (N-W) ORs by relative rotations about the normal to the parallel close-packed planes. Rotations of 35.26° and 30° bring

the new OR into coincidence with the K-S and N-W ORs, respectively.

In LENS-fabricated 304L, delta-ferrite with the new OR was found to coexist with other ferrite having both K-S and N-W ORs, but in separate grains and with less frequent occurrence, indicating that it was less favorable energetically than K-S or N-W for the LENS solidification conditions. In the 309S and Fe-Cr-Ni GTA welds, the new OR was the only one to form within a few grains, whereas ferrite in the other austenite grains did not establish an OR.

Figure 1 shows TEM micrographs of delta-ferrite with the new OR residing in dendrite cores within an austenite grain in the LENS-fabricated 304L alloy. Figure 2 shows experimental and matching computed electron diffraction patterns of the ferrite and austenite in Figure 1 from which the new OR can be derived directly.

Significance: Knowledge of this new OR and its relationship to the K-S and N-W ORs will help us to better understand the complex nature of ferrite/austenite morphologies and their relationship to solidification sequences in steels. This work broadens the spectrum of known ORs for bcc-fcc systems that has not changed since the 1950s.

Contact: Tom Headley, Materials Characterization Dept., 1822
Phone: (505) 845-0191
Fax: (505) 844-9781
E-mail: tjheadl@sandia.gov

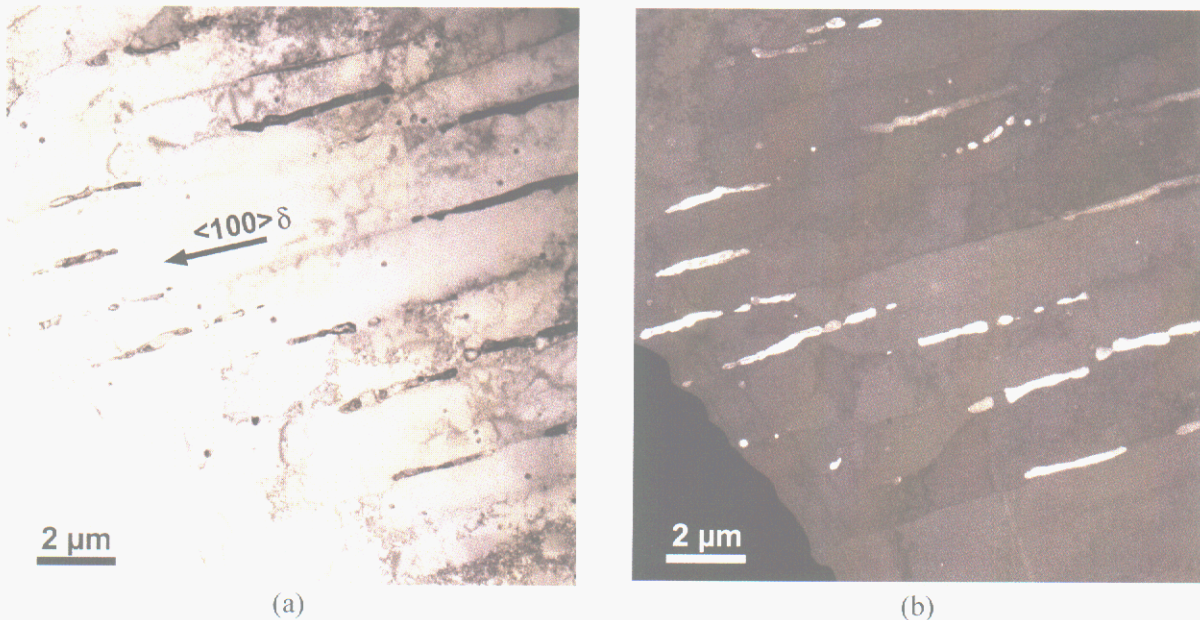


Figure 1. TEM micrographs of delta-ferrite particles with the new OR aligned in dendrite cores within an austenite grain in LENS-fabricated 304L alloy: (a) bright field image, and (b) dark field image from a ferrite reflection confirming all ferrite within the grain has the same orientation.

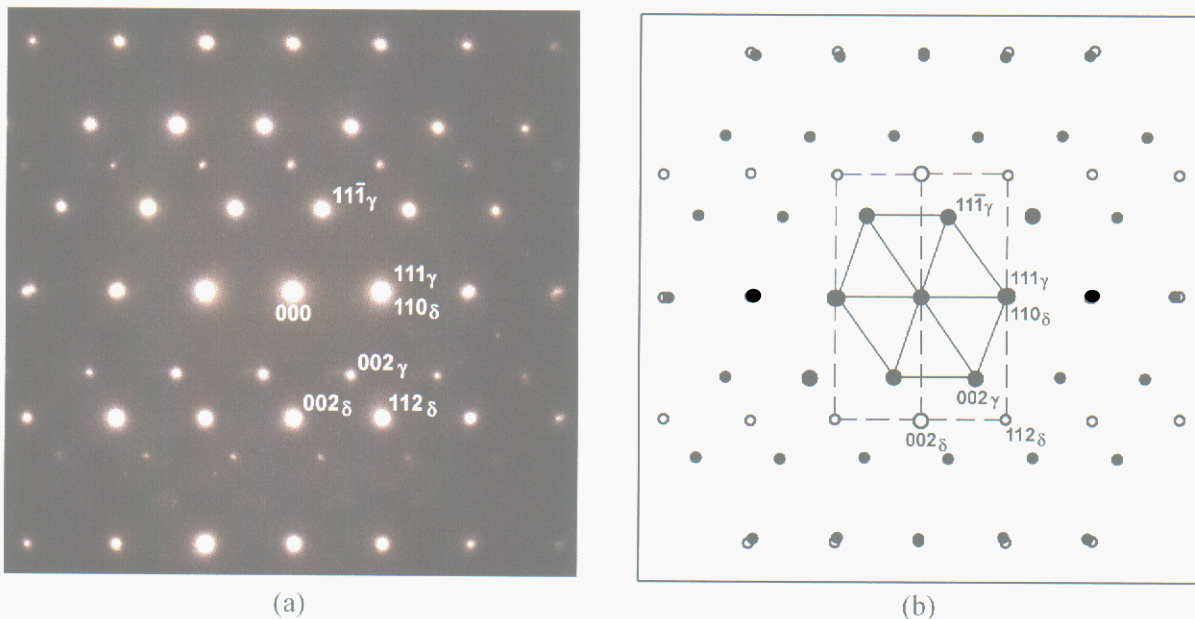


Figure 2. (a) Experimental, and (b) computed SAED patterns for the ferrite/austenite in Figure 1. The $[-110]$ -austenite and $[-110]$ -ferrite zone-axes patterns are superimposed indicating $[-110]$ -austenite and $[-110]$ -ferrite directions are parallel normal to the pattern. The 111 -austenite and 110 -ferrite diffraction spots are superimposed within the pattern indicating (111) -austenite planes are parallel to (110) -ferrite planes.

Effects of Grain Orientation and Topology on Deformation

C. C. Battaile, T. E. Buchheit, G. W. Wellman, W. A. Counts, and E. A. Holm

Motivation: Microstructure and deformation interact in many ways. Deformation can create microstructural features (e.g. subgrains and twins) and microstructural evolution can change a material's mechanical state (e.g. when a material recrystallizes). This complex coupling is the basis for a wide variety of thermomechanical processing techniques like cold working and annealing. While these techniques are well established and backed by a wealth of engineering knowledge, little is known fundamentally about how microstructure and deformation interact. The goal of this work is to develop and test a computational framework for modeling coupled mechanical deformation and microstructural evolution. This report outlines preliminary results from this approach that clarify the roles of grain topology and orientation in determining local stress distributions.

Accomplishment: Grain growth is modeled by an interface tracking method where each grain boundary is represented by a series of points in space, as depicted in Figure 1a. The simulation is dynamic, and velocity of each boundary point is proportional to its curvature. Sandia's JAS3D finite element analysis (FEA) code is used in this study to perform deformation simulations, with a strain-hardening polycrystal plasticity material model, on two-dimensional grain microstructures at various stages of grain growth. The finite element mesh is generated directly from the interface tracking structure to produce a two-dimensional hexahedral mesh like the one in Figure 1b. Random crystallographic orientations are assigned to each grain, and the mesh is

elongated by 1%. Figure 2 shows the resulting von Mises stress distribution at various stages of grain growth. Even when the local grain topology changes, regions of high local stress tend to stay high, and vice versa. Figure 3 shows the von Mises stress in the same microstructure as Figure 2d, but with a different random assignment of grain orientations. Clearly the stress distribution in Figure 3 is very different from that in Figure 2d, indicating that grain orientation, and not local grain topology, controls local stress distribution.

Significance: Modeling the complex coupling between microstructure and deformation requires not only sophisticated computer models, but also robust methods to couple them. We are working to develop a fully coupled computational framework wherein evolution and deformation are interdependent. This report contains preliminary results on the path toward that goal. These results demonstrate that the stress distribution in a simulated polycrystal is dominated by individual grain orientations rather than local grain topologies. This fundamental piece of information will provide valuable guidance as we develop more complex approaches to solving the fully coupled problem of interdependent deformation and microstructural evolution.

Contact: Corbett Battaile, Materials & Process Modeling & Computation Dept., 1834
Phone: (505) 844-7039
Fax: (505) 844-9781
E-mail: ccbatta@sandia.gov

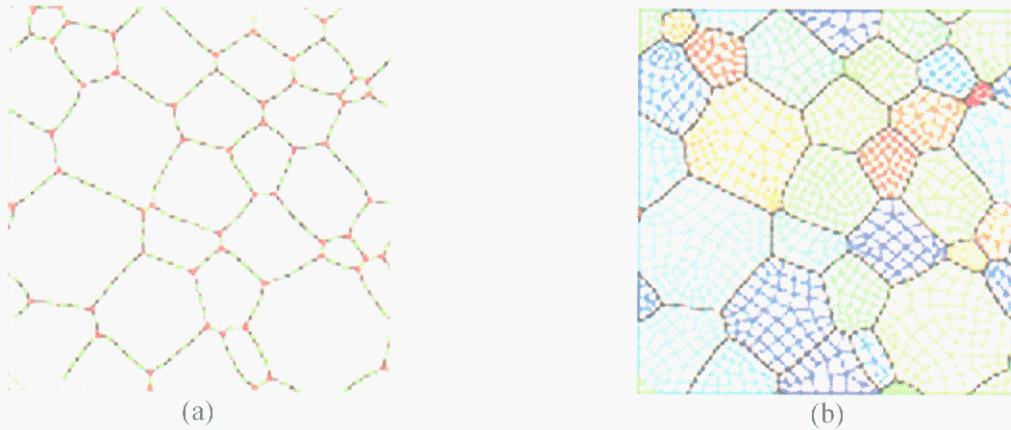


Figure 1. Grain microstructures represented as (a) grain boundary points for the interface tracking model, and (b) quadrilateral finite elements for the finite element model.

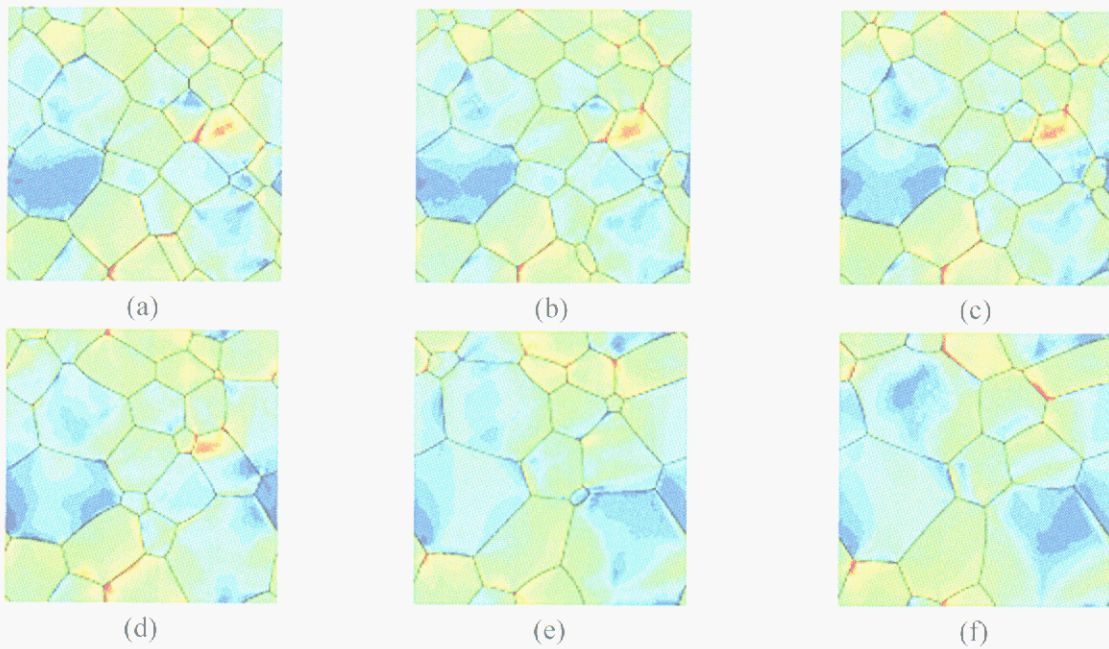


Figure 2. Von Mises stress at various stages of grain growth. Dark blue is 30 MPa and red is 70 MPa.

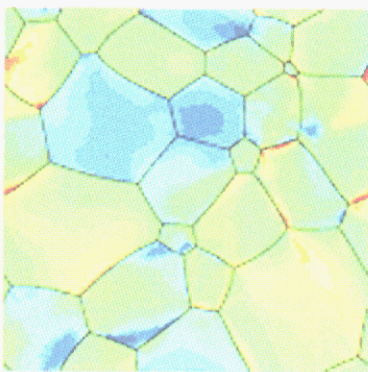


Figure 3. Von Mises stress in the microstructure from Figure 1d, but with a different random assignment of grain orientations. Dark blue is 30 MPa and red is 70 MPa.

Excited State Interactions between Activators in Phosphors

D. R. Tallant and C. H. Seager

Motivation: Improving the efficiency of phosphors for everything from general lighting applications to flat panel displays leads to potential improvements in energy efficiency. New flat panel display technologies may replace liquid crystal technology with electroluminescent, cathodoluminescent or plasma-source excitation of phosphors. The lack of high-efficiency phosphors compatible with these excitation sources has hindered the development of new display technologies. Our DARPA-funded work was initially directed at improving phosphor cathode-luminescence in low-voltage field emission displays.

Accomplishment: The intrinsic thinness of flat panel field emission displays constrains them to operate at kilovolt, rather than the tens of kilovolt electron accelerating voltages present in cathode ray tubes used in televisions and computer monitors. Phosphor efficiency is known to be much lower at kilovolt (compared to tens of kilovolt) accelerating voltages. This reduction in phosphor efficiency was believed to be from a combination of decreased electron penetration of the phosphor at low voltages and relatively high exciton recombination at surface defect sites.

A more general issue is “concentration quenching” in phosphors. As the activator (the emissive element in a phosphor) concentration increases above approximately one atomic %, phosphor efficiency decreases. This concentration quenching was believed to be due to defect sites.

We have proposed a different type of mechanism that explains the dependence of phosphor efficiency on activator concentration

and electron accelerating voltage. This mechanism involves an interaction between two activators in excited states (Figure 1). This interaction differs from traditional concepts of relaxation in that it involves two excited states (second-order kinetics) versus one (first-order kinetics). At low activator concentrations and low excitation densities, first-order kinetics dominates the relaxation of the phosphor, resulting in linear persistence behavior (Figure 2). At high activator concentrations and high excitation densities, the second-order interaction dominates, and the persistence becomes nonlinear. Strong second-order effects are caused by electron-stimulated cathodoluminescence that achieves extremely high excitation densities. The dependence of persistence curve shape on excitation density has been demonstrated for $Zn_2SiO_4:Mn$ (Figure 2), $Y_2O_3:Eu$ and $Y_2SiO_5:Tb$ phosphors and is confirmation of the excited state interaction mechanism.

Significance: Attempts to improve phosphor efficiency by annealing and surface treatment have been largely unsuccessful. Synthesis techniques in which the activators are dispersed at the atomic level (spray pyrolysis, hydrothermal synthesis and homogeneous precipitation) may achieve improved efficiencies because they minimize activator aggregation and, hence, their interaction.

Contact: Dave Tallant, Materials Characterization Dept., 1822
Phone: (505) 844-3629
Fax: (505) 844-9781
E-mail: drtallal@sandia.gov

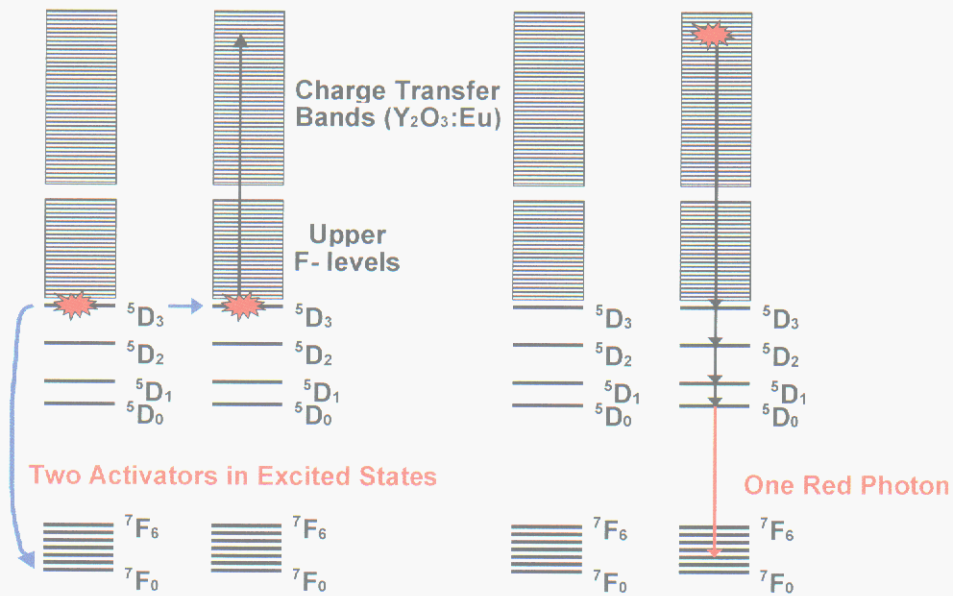


Figure 1. Excited state interactions in $Y_2O_3:Eu$. One Eu activator transfers its excitation to the other. The added energy relaxes nonradiatively through closely packed energy levels in the second Eu activator. Emission efficiency decreases because the first state has the potential of emitting two red photons, whereas the second state can emit only one.

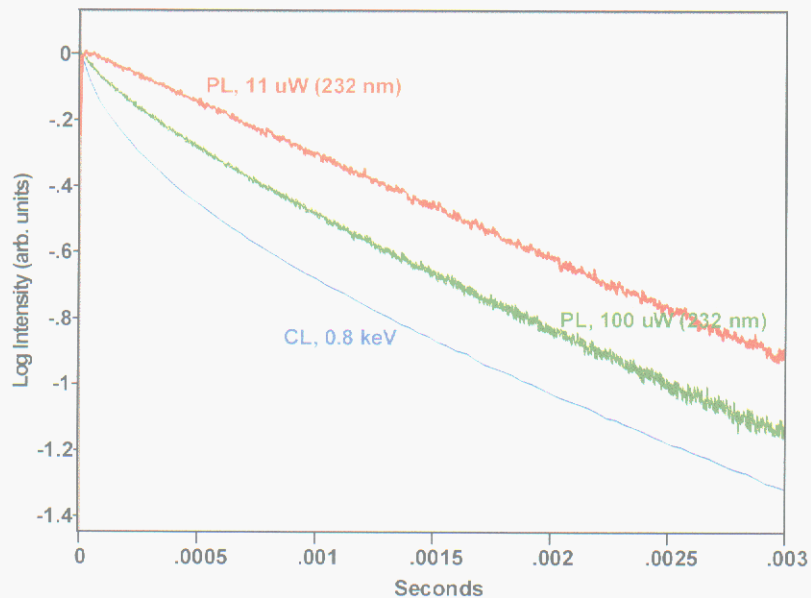


Figure 2. Persistence (log emission intensity versus time) for Zn_2SiO_4 with 10 at% Mn activator for photon-stimulated emission (PL) at low and high excitation intensity and electron-stimulated emission (CL) at low excitation voltage. The persistence becomes more nonlinear as (second-order) excited state interactions are enhanced.

Focused Ion Beam Applications in Materials Science

J. R. Michael

Motivation: Focused ion beam (FIB) micromachining or milling has been most extensively utilized as a diagnostic tool in the integrated circuit manufacturing industry. The recent development of lower cost dual-beam (FIB and scanning electron microscope (SEM) columns combined in one instrument) has made this tool more available to the materials science community. The dual beam systems make the preparation of cross sections for SEM and thin samples for transmission electron microscopy from precisely located areas of the sample possible.

FIB systems consist of a liquid metal ion source and a electrostatic focusing column that is used to produce a finely focused beam of 30 kV Ga⁺ ions. The interaction of the ions with the sample results in the sputtering of atoms from the surface of the sample. Sputtering occurs only in the immediate vicinity of the beam impact point. Thus, cross sections can be produced from very specific areas of the sample. These cross sections can then be viewed at high resolution in the same instrument when a dual beam system is used. The unique combination of the FIB and SEM allows previously impossible samples to be easily and efficiently produced. TEM samples are produced by milling trenches on either side of the desired region followed by slowly thinning the resulting membrane to electron transparency.

Accomplishment: The dual beam FIB system has now been applied to a wide range of materials of interest to researchers at Sandia National Laboratories. We have now developed techniques for the preparation of both TEM and SEM samples.

The growth of copper sulfide on gold plated copper contacts in electrical switches can cause high electrical contact resistance and can result in switch failure. Previously, it was believed that large defects in the gold plating were responsible for the formation of these nodules. Figure 1 is an example of serial FIB cross sectioning through a copper sulfide nodule that has formed on a gold-plated copper substrate. Careful sectioning through the nodule and the substrate revealed the small defect in the gold plating that permitted the nodule to grow. The defect in the gold plating is as small as 1 μm in diameter and the loss of copper from the substrate is also apparent.

The preparation of TEM samples of metal to ceramic brazes using traditional techniques has been very difficult. Figure 2 is a TEM micrograph of a braze joint between a metal braze and alumina. The results of the chemical reactions responsible for the braze performance are visible at the interface between the alumina and the braze material.

Significance: We have now developed the expertise in the use of the FIB to prepare cross sections for SEM and thin samples for TEM from a wide range of materials. This technique now allows previously impossible samples to now be prepared in a fast and efficient manner from precise locations within a sample.

Contact: Joe Michael, Materials Characterization Dept., 1822
Phone: (505) 844-9115,
Fax: (505) 844-2974
E-mail: jrmicha@sandia.gov

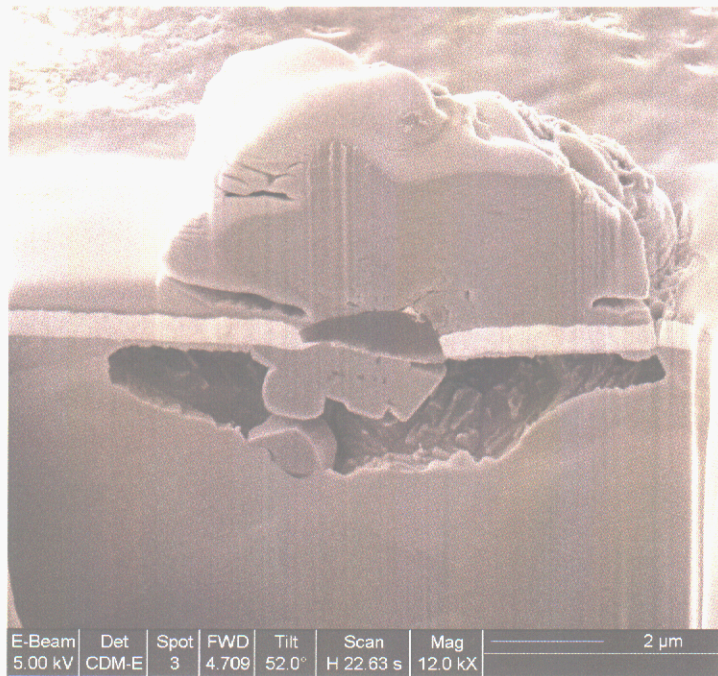


Figure 1. FIB prepared cross section through a Au plated substrate that has been exposed to a sulfidizing atmosphere.

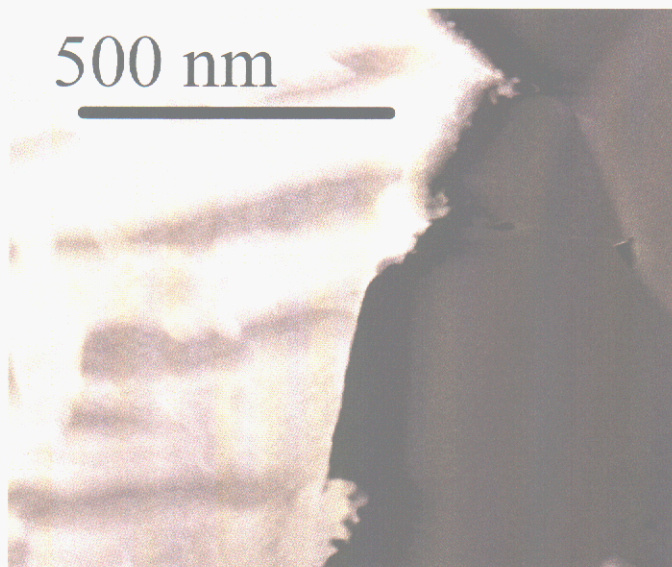


Figure 2. FIB prepared TEM sample of a braze joint to alumina.

Chemometric Analysis of NMR Spectroscopy Data

T. M. Alam and M. K. Alam

Motivation: The analysis of complex mixtures using nuclear magnetic resonance (NMR) spectroscopy continues to affect a variety of different fields including agriculture, industry, medicine, materials, biotechnology and chemistry. Although the use of numerical techniques is well founded in the analysis of NMR data, the use of multivariate techniques for NMR has been rather limited in comparison to other spectroscopies. With the increased use of NMR spectroscopy to investigate a variety of complex problems, advanced chemometric techniques for NMR data analysis will become an important part of the analysis arsenal. This laboratory has recently investigated the development of NMR chemometric techniques to help in the analysis of a variety of materials. ("Chemometric Analysis of Nuclear Magnetic Resonance Spectroscopy Data", *Spectroscopy*, 16(1), 18-27 (2001)).

Accomplishment: By utilizing chemometric techniques, additional information can be obtained from the NMR spectra that would not be readily apparent. In situations where one is interested in very small signals (as encountered in the analysis of degradation species during material aging) or in situations where spectral overlap may result in an incorrect interpretation; chemometrics has proven beneficial. A major accomplishment has been the implementation of self-modeling and three-way techniques to obtain unique or pure-component spectra and concentration profiles from the abstract eigenvectors and eigen values commonly encountered during principal component analysis

(PCA). For example, a method that uses the direct exponential curve resolution algorithm (DECRA) has been used to analyze a variety of data types, including spin-lattice relaxation and pulse field gradient (PFG) experiments. DECRA relies on the creation of two data sets (A and B) that are proportional, and can be expressed in matrix form as:

$$\begin{aligned} A &= CP \\ B &= \alpha CP \end{aligned}$$

where C is the concentration matrix, P is the pure component spectra, and α is the proportionality matrix. DECRA has been used to analyze the changes in the concentration and spin dynamics for intermediate and amorphous polymer phases in irradiated insulating cables followed by annealing. Figure 1 shows an example of the DECRA analysis of these aged polymer cables. This laboratory has also demonstrated the use of partial least squares (PLS) and net analyte signal (NAS) analysis to probe interference-effects in ^{17}O NMR mixtures.

Significance: These studies demonstrate the potential of using chemometric techniques for the analysis of NMR spectroscopy data, including the application to both ^{17}O and ^{13}C data sets. The use of chemometrics has allowed additional insight into material changes as a function of aging.

Contact: Todd Alam, Organic Materials Dept., 1811
Phone: (505) 844-1225
Fax: (505) 844-9624
E-mail: tmalam@sandia.gov

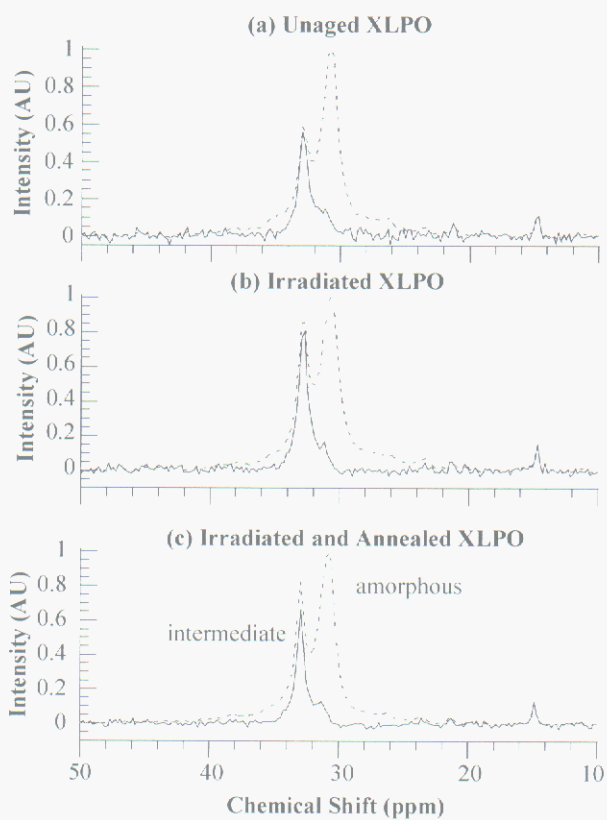


Figure 1. DECRA resolved ^{13}C MAS NMR spectra showing the intermediate and amorphous components in unaged, irradiated and irradiated+annealed XLPO samples. The dashed lines show the sums of the components. (Harris and Alam, 2002).

Characterizing Size Distribution of Core-Shell Spherical Particles

R. R. Lagasse and D.W. Richards

Motivation: Research performed in collaboration with R. A. Anderson has determined the mechanism causing dielectric breakdown of epoxy composites containing 50 volume % of hollow glass spherical balloons. Dielectric breakdown of the composite is initiated by gas discharges inside the microballoons. The mechanism involves a “weakest-link” concept, in which a spontaneous discharge inside a single balloon within the composite launches a chain reaction of discharges, which culminates in breakdown of the composite. Theory and experiment show that the largest balloons are most prone to the gas discharges that initiate breakdown. For that reason, it is important to characterize the size distribution of the microballoons.

Laser diffraction is a popular method for determining size distribution of powders. Measurements of angularly dependent light scattering are analyzed, usually with software supplied with commercial instrumentation. Since this proprietary software assumes that the particles are spheres having spatially homogeneous optical properties, it is not strictly applicable to the hollow glass spheres. To determine their size distribution, we have developed a method to analyze scattering from particles consisting of a spherical core surrounded by a concentric shell.

Accomplishment: We determined the size distribution of a microballoon powder having 6 micron average radius and an average shell thickness equal to 18% of that value. The unknown size distribution was represented as a linear combination of cubic B-splines (Figure 1).

The intensity scattered by each of those B-spline distributions was computed with a code appropriate for two-layer core-shell spherical particles (Figure 2). This code was developed starting with the Aden-Kerker equations for scattering from core-shell particles. A set of coefficients multiplying each curve in Figure 2 was determined to produce a good fit to the measured angularly dependent scattering (Figure 3.) Then those coefficients were multiplied by the corresponding B-spline distributions in Figure 1 to produce the size distribution shown in Figure 4. To determine the coefficients, a *linear regularization* method was employed because it produced both a good fit to the measured intensity as well as a smooth, physically realistic size distribution. In contrast, simple, linear least squares regression produced an unacceptable distribution having unrealistic oscillations. The size distribution produced by the core-shell analysis is compared in Figure 4 with that produced by the conventional homogeneous sphere analysis. The latter produces considerable error below particle radii of 10 μm . This finding is completely consistent with Mie and Fraunhofer light scattering theories, which show that core-shell and homogeneous spheres should scatter the same for particle radii larger than 10 μm .

Significance: The analysis method developed here can be applied to determine via light scattering the size distribution of other kinds of particles that are more complex than homogeneous spheres, as long as their scattering curves can be computed. One class of particles amenable to this analysis is cylindrical rods.

Contact: Bob Lagasse, Organic Materials Dept., 1811
Phone: (505) 845-8333
Fax: (505) 844-9781
E-mail: rrlagas@sandia.gov

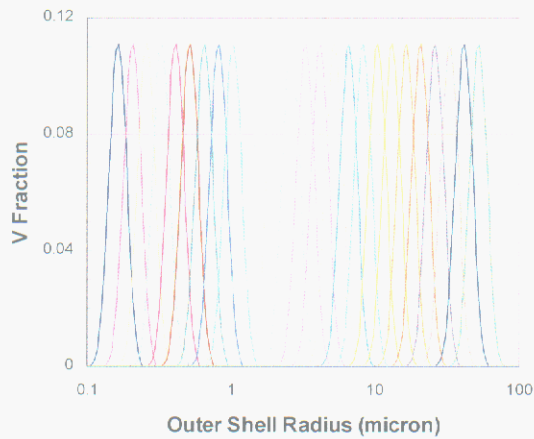


Figure 1. Cubic B-spline distributions used as basis functions to represent the unknown size distribution. Each of these is multiplied by a coefficient to construct the size distribution.

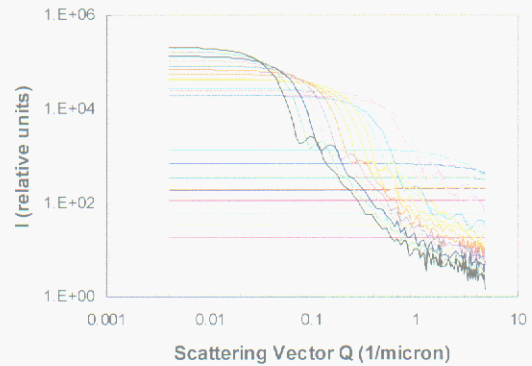


Figure 2. Angularly dependent scattering curves corresponding to each of the cubic B-spline distributions in Figure 1.

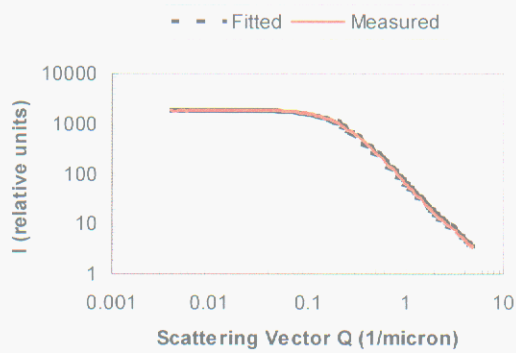


Figure 3. Fitting of the measured scattering curve to determine the coefficients multiplying each of the curves in Figure 2.

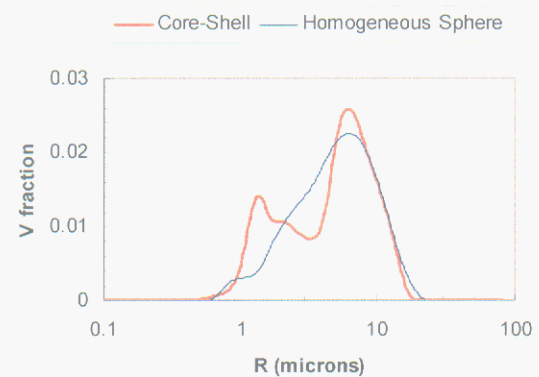


Figure 4. Size distribution produced by the accurate core-shell analysis and by the approximate homogeneous sphere analysis.

New Algorithms Improve Near-IR Spectrometer Calibrations

C. M. Wehlburg, D. M. Haaland and D. H. Melgaard

Motivation: Transfer of calibration and instrument stability over time are major problems in quantitative IR spectroscopy. A large number of calibration samples are necessary to develop a model with reasonable predictive ability. As the instrument response changes significantly over time (or a different instrument is used to collect data), the calibration spectra must be recollected and a new model built.

Accomplishment: Our group has been involved in the development of a novel chemometric hybrid algorithm termed Prediction Augmented Classical Least Squares/Partial Least Squares (PACLS/PLS). The spectral interferences or spectral "shapes" of unmodeled components such as instrument drift and instrument response changes are explicitly added to the algorithm during calibration. By combining improved experimental designs and this new algorithm, we have developed near-IR calibration models that require fewer samples, are stable over time and can be transferred to secondary spectrometers.

In the analysis of dilute aqueous solutions containing glucose, ethanol and urea, we used a midpoint sample to model instrument drift. Repeat spectra of the midpoint sample collected when running calibration and prediction samples, captures both short- and long-term instrument drift. By utilizing the explicit modeling of the shape of instrument drift, Figure 1 shows the predictive ability of the PACLS/PLS model proved better than that of PLS in maintaining the calibration of a spectrometer.

We have also been able to minimize the size of the calibration sample set by realizing that the historically large calibration sample sets were

actually required to model short-term instrument drift. We decreased the number of calibration samples from 27 to 3 and again collected the midpoint sample spectrum repeatedly during the measurement of the calibration and unknown prediction spectra. As Figure 2 shows, the prediction results using only 3 calibration samples for the model were as good as using 27 calibration samples and the new PACLS/PLS model again outperformed PLS, especially for the glucose component.

Finally, the algorithm's utility in the transfer of calibration among spectrometers was ascertained. For a 3 component organic system, a subset of samples was used to determine the "spectral shapes" of instrument differences between the primary and secondary spectrometers. With the explicit shapes added to the PACLS/PLS model, the new algorithm outperformed the implicit modeling of PLS in predicting sample spectra on the secondary instruments.

Significance: Reducing the number of calibration samples, and maintaining and transferring multivariate calibrations will greatly decrease the cost and increase the reliability of quantitative spectroscopic results. These methods are not limited to near-IR instrumentation. Contaminant analytes, temperature variations and detector variations are all possible spectral "shapes" that could be ascertained and explicitly included in these new algorithms in order to develop more stable and parsimonious calibration models.

Contact: Christine Wehlburg, Chemical & Biological Sensing, Imaging & Analysis Dept., 1812
Phone: (505) 845-8283
Fax: (505) 844-2974
E-mail: cmwehlb@sandia.gov

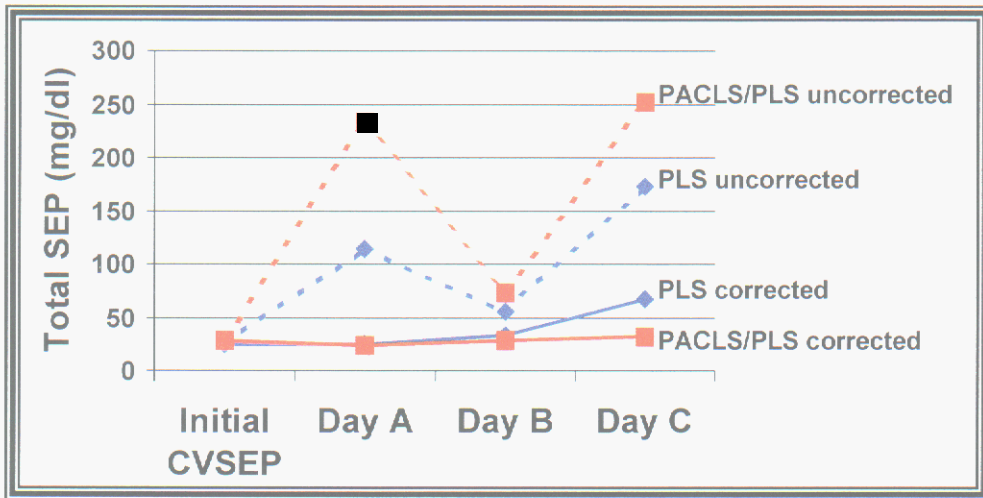


Figure 1. Maintenance of calibration prediction results using the Standard Errors of Prediction (SEP's) for both uncorrected (no repeat spectra) and corrected models. The use of repeats for both short- and long-term drift improves both PLS and PACLS/PLS predictive abilities relative to the original cross-validated SEP's. The new PACLS/PLS algorithm outperforms PLS over time.

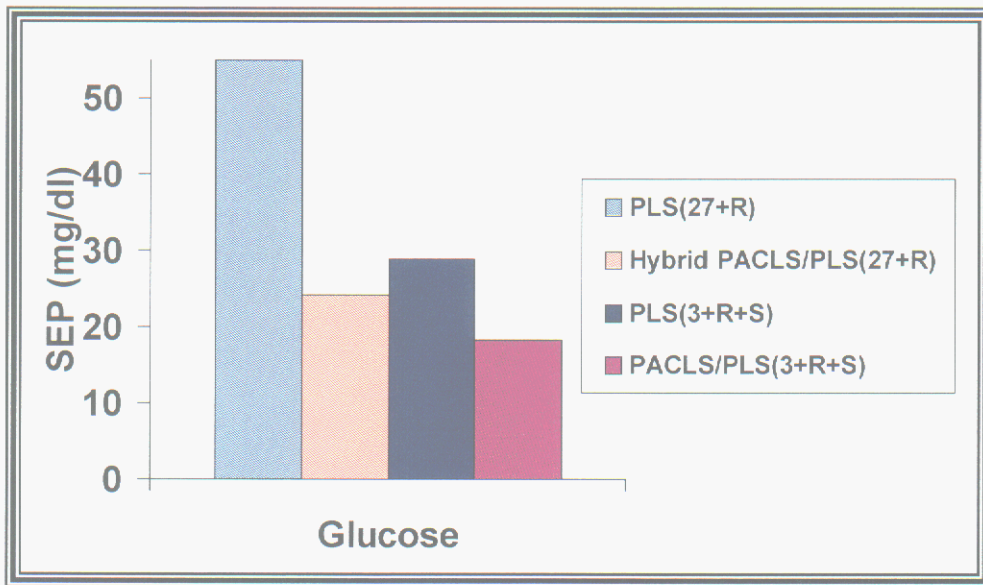


Figure 2. Standard Errors of Prediction (SEP's) for glucose using 27 calibration samples versus 3 calibration samples plus repeat (R) and saline (S) solution in the original model. The prediction samples are those collected on Day C in Figure 1. The PLS model's predictive ability is already degraded for glucose. Decreasing the sample set size actually improves the PLS results, but the new PACLS/PLS algorithm consistently outperforms PLS.

New Method to Determine Crosslink Density Gradients in Thermosetting Polymer Films

M. S. Kent, H. Yim, W. F. McNamara

Motivation: The density and crosslink density within thermosetting polymer films near a substrate surface is important for stress transfer, mechanical properties, aging and fracture mechanisms, and diffusion of penetrants, among others. Structure at the air surface can impact surface reconstruction, surface free energy, wettability, and reactivity. In addition, structural gradients at air interfaces can impact the interfacial strength that develops when contacted with a second polymer. Below we describe a new method that allows for the first time a detailed characterization of crosslink density gradients in thin thermosetting films.

Accomplishment: Variation in the crosslink density within thin (600-1200 Å) epoxy films on silicon substrates was examined by solvent swelling and neutron reflection (*Macromolecules* 32, 7932, 1999). The method, illustrated in Figure 1, is based on the fact that the equilibrium volume fraction of a swelling solvent is strongly dependent upon the local crosslink density. Volume fraction profiles of the good solvent *d*-nitrobenzene through the epoxy films were determined by neutron reflection. The solvent was deuterated in order to provide scattering contrast with the epoxy matrix. Swelling is a method that has been employed for many years to determine the average crosslink density in macroscopic bulk samples. Structure within the thin epoxy films was investigated as a function of resin/crosslinker composition and cure temperature. The epoxy resin was a research grade DGEBA-based resin (RSL 1462) obtained from Shell Chemical Co. cured with an aliphatic

polyethertriamine (T403, Huntsman Chemical). The experimental data demonstrate good sensitivity to the concentration profile of the swelling solvent. An example is shown in Figure 2. The principle observation is a large excess of solvent near the air surface. This is not a wetting layer, but rather indicates a lower crosslink density in the near-surface region. This effect is due to preferential segregation of the crosslinker to the air surface, driven by the lower surface tension of the crosslinker relative to the epoxide oligomers. The magnitude of the effect is a function of composition and cure temperature. Exclusion of *d*-nitrobenzene from the region immediately adjacent to the substrate surface was also observed in certain cases, possibly indicating a tightly bound layer of epoxy. Regarding swelling in the bulk of the films, the behavior is non-symmetric with departure from the stoichiometric ratio. The films deficient in curing agent show greater equilibrium swelling and faster swelling kinetics than the films with an excess of curing agent.

Significance: This new method can be used to determine gradients in crosslink density within thin thermosetting films, and the variations in structure that occur with processing conditions. This information is related to important properties such as interfacial toughness in adhesives and the mechanical properties of composites.

Contact: Mike Kent, Microsystem Materials, Tribology & Technologies Dept., 1851
Phone: (505) 845-8178
Fax: (505) 844-9624
E-mail: mskent@sandia.gov

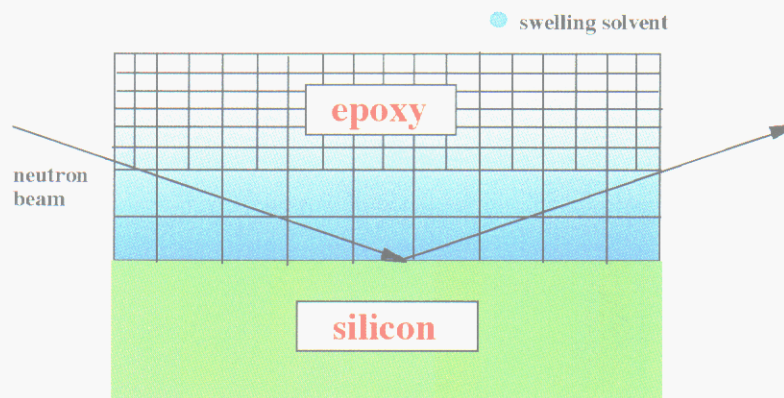


Figure 1. Illustration of the method. Greater local swelling occurs for lower crosslink density. The concentration profile of the swelling solvent is determined by neutron reflection.

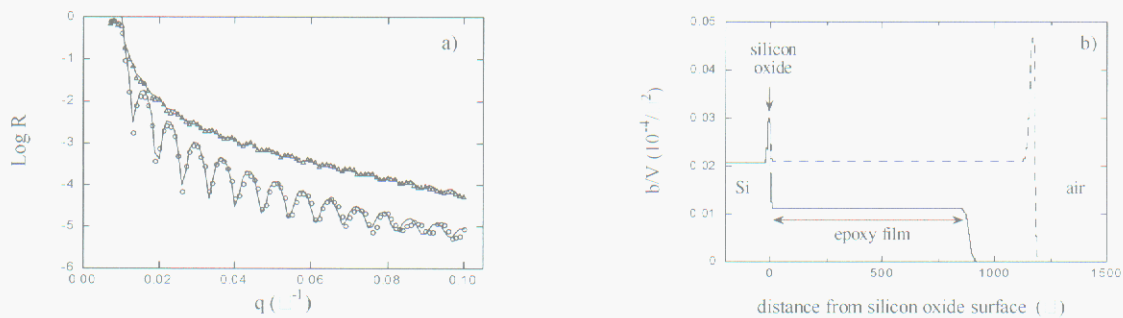


Figure 2. Neutron reflectivity data and corresponding scattering length density profiles for as-prepared and swelled films indicating a large excess of swelling solvent, and therefore a low crosslink density, at the air surface for 46 parts crosslinker per hundred parts resin.

New Method to Probe Crosslink Density Profiles in Organosilane Films

M. S. Kent, H. Yim, J. Hall

Motivation: Thin films of organosilanes are widely used for providing adhesion promotion, durability, and corrosion resistance. Although the crosslink density profile within such films is likely to affect their performance, no reliable assay has been available to characterize this distribution. In this work we used solvent swelling combined with neutron and X-ray reflection to study the crosslink density distribution within ultrathin films of (3-glycidoxypropyl) trimethoxysilane (GPS) and bis(triethoxysilyl)ethane (BTSE) on silicon. Due to the chemical differences, the network structures of these films are dramatically different.

Accomplishment: Variation in the crosslink density within thin (10 – 400 Å) organosilane films on silicon substrates was examined by solvent swelling and neutron reflection (*J. Phys. Chem. B* 106, 2002, 2474). The method, illustrated in Figure 1, is based on the fact that the equilibrium volume fraction of a swelling solvent is strongly dependent upon the local crosslink density. Volume fraction profiles of the good solvent d-nitrobenzene through the organosilane films were determined by neutron reflection. Swelling has been employed for many years to determine the average crosslink density in bulk samples. Structure within the thin organosilane films was investigated as a function of thickness for GPS and BTSE films. GPS has been widely used as an epoxy-compatible adhesion promoter in glass-fiber reinforced composite materials. On the other hand, bis(triethoxysilyl)ethane (BTSE) films have been known to impart corrosion resistance to metal

surfaces under appropriate conditions. BTSE is believed to form highly crosslinked films due to the fact that it possesses six reaction sites per molecule. It has been proposed that this high crosslink density provides an impenetrable barrier to water.

The experimental data demonstrate good sensitivity to the concentration profile of the swelling solvent. An example is shown in Figure 2 for a GPS film. For the GPS films, we conclude that a high crosslink density exists near the silicon surface as well as near the surface of the film but with a much lower crosslink density in the center of the film. The amount of swelling in the bulk of the thin GPS films and the fractional increase in thickness is more like that of an elastomeric material than a highly crosslinked material. The fractional increase in thickness obtained by neutron reflectivity, X-ray reflectivity, and ellipsometry were in good agreement. In contrast to the GPS films, BTSE films do not swell with d-NB, consistent with the notion that they have a much higher crosslink density.

Significance: This new method allows determination of the crosslink density and crosslink density gradients within thin organosilane films. This information impacts the optimization of such films for adhesion, corrosion resistance, and mechanical properties of composites.

Contact: Mike Kent, Microsystem Materials, Tribology & Technologies Dept., 1851
Phone: (505) 845-8178
Fax: (505) 844-9624
E-mail: [mskent@sandia.gov](mailto:m Kent@ sandia.gov)

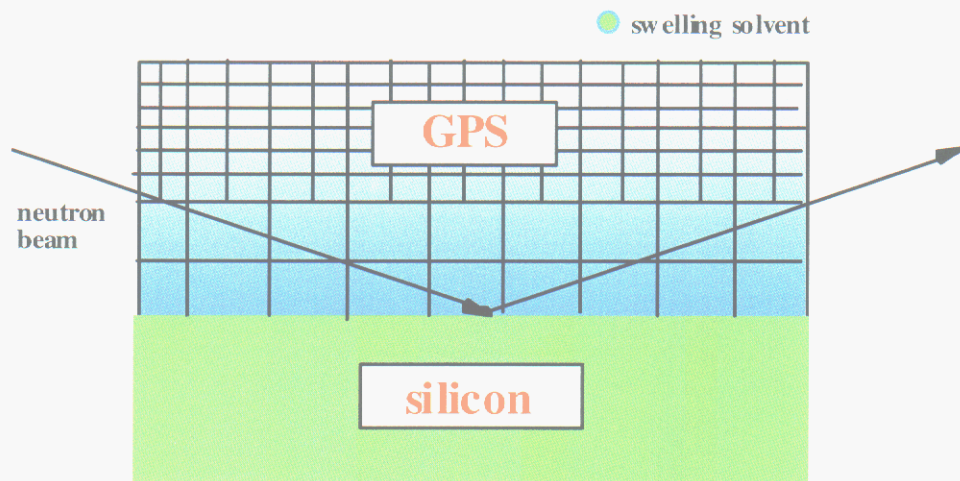


Figure 1. Illustration of the method. Greater local swelling occurs for lower crosslink density. The concentration profile of the swelling solvent is determined by neutron reflection.

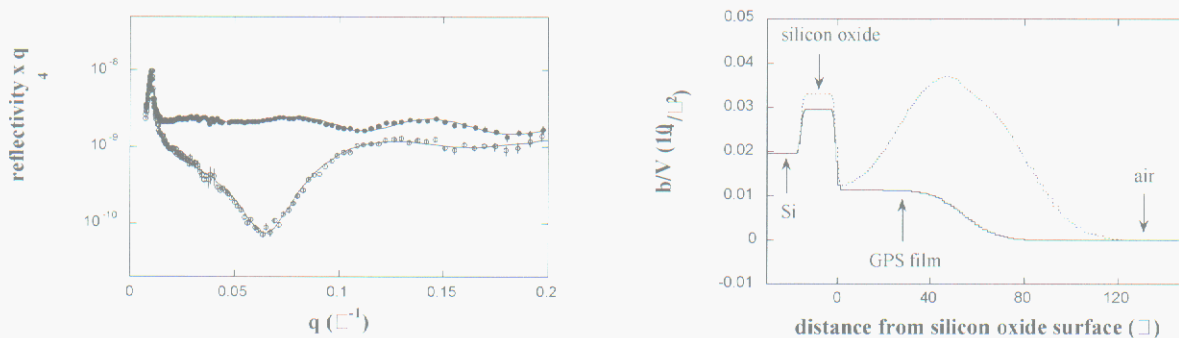


Figure 2. Neutron reflectivity data and corresponding scattering length density profiles for as-prepared and swelled films indicating a large excess of swelling solvent, and therefore a low crosslink density, in the center of the film.

Electrochemical and Spectroelectrochemical Detection of Trace Contaminants

M. J. Kelly

Motivation: Electrochemical methods are widely used to investigate the thermodynamics and kinetics of reactions occurring at metal or semiconductor electrodes. In a common suite of techniques, the potential of the working electrode (the substrate of interest) is controlled in a static or dynamic manner with respect to a reference electrode. This control allows the study of selected electrode processes because only certain reactions are thermodynamically accessible at a given potential. Simultaneously, the working electrode current and/or an optical property of the electroactive species are measured to determine the kinetics of the electrode reaction and the concentration of the species. The versatility, sensitivity, and relative simplicity of electrochemical techniques have led to widespread use in analytical chemistry (e.g., measurement of trace levels of organic and inorganic species in solution), materials processing (e.g., electroplating of functional coatings on metals, semiconductors, and ceramics), and corrosion studies (e.g., in studies of anode and cathode reactions).

Accomplishment: Electrochemical methods are widely used to investigate the thermodynamics and kinetics of reactions occurring at metal or semiconductor electrodes. In a common suite of techniques, the potential of the working electrode (the substrate of interest) is controlled in a static or dynamic manner with respect to a reference electrode. This control allows the study of selected electrode processes because only certain reactions are thermodynamically accessible at a given potential. Simultaneously, the working electrode current and/or an optical property of the

electroactive species are measured to determine the kinetics of the electrode reaction and the concentration of the species. The versatility, sensitivity, and relative simplicity of electrochemical techniques have led to widespread use in analytical chemistry (e.g., measurement of trace levels of organic and inorganic species in solution), materials processing (e.g., electroplating of functional coatings on metals, semiconductors, and ceramics), and corrosion studies (e.g., in studies of anode and cathode reactions).

Significance: Electrochemical methods have also been used to measure metal ion contaminants (at concentrations as low as 40 ppb) in high-purity acids and etchants used at Sandia in the fabrication of integrated circuits and microelectromechanical systems (MEMS). Further, these methods are integral to a new FY02-FY04 LDRD project that seeks to overcome certain limitations of current working electrode designs via an integrated array of nanoelectrode elements. These advances should enable portable, battery-powered field-testing and continuous remote system monitoring (e.g., for arsenic in municipal or rural water supplies).

Contact: Mike Kelly, Materials Characterization Dept., 1822
Phone: (505) 844-4031
Fax: (505) 844-2974
E-mail: mjkelly@sandia.gov

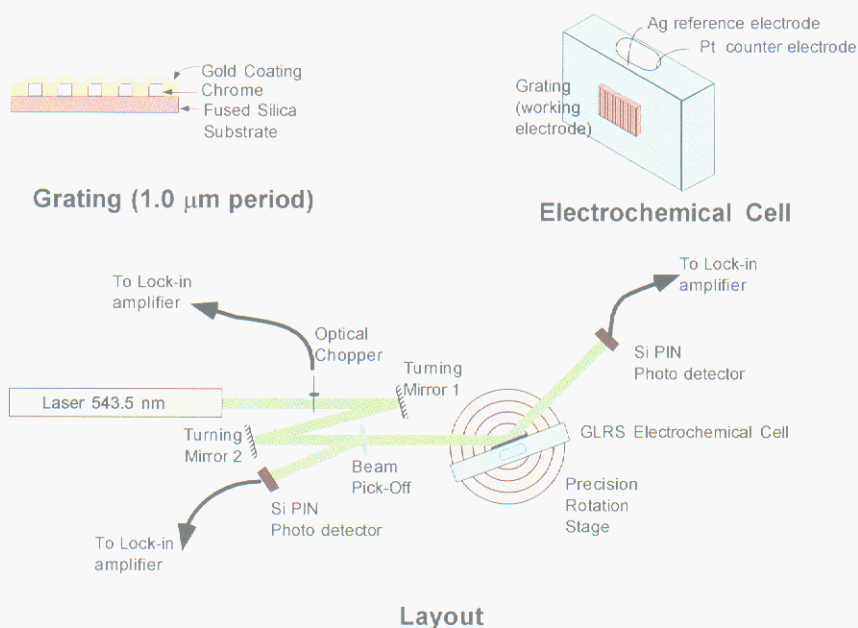


Figure 1. Grating Light Reflection Spectroelectrochemistry experiment. *Upper left* - Diffraction grating, 1.0 μm period, chromium on fused silica. A semi-conformal gold layer, approximately 200 nm thick, was deposited over the grating to improve electrochemical performance. *Upper right* - Three-electrode electrochemical cell. A liquid-tight seal between the grating and the high-density polyethylene cell body was achieved with an o-ring gasket. *Bottom* - Optical layout (see text).

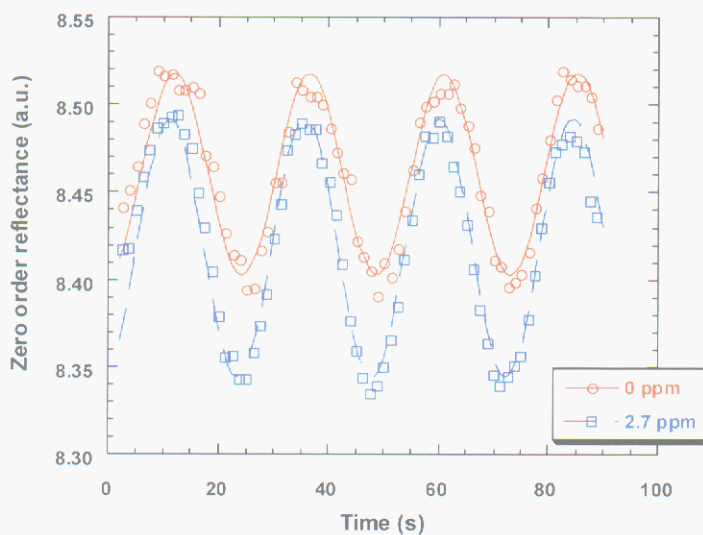


Figure 2. Zero order reflectance as a function of time for cyclic voltammetry experiments on a 2.7 ppm solution of 7-dimethylamino-1,2-benzophenoxazine in water (blue squares), as well as for pure water (red circles). Working electrode (grating) was scanned between +3 and -3 volts (vs. silver wire pseudo reference electrode), scan rate = 500 mV/s, approximately 4 cycles. Experimental data are shown by symbols, mathematical curve fits are shown by solid or dashed curves.

Use of X-Ray Diffraction as a Fatigue Sensor

M. O. Eatough and R.G. Tissot

Motivation: The fact that cold work will broaden a diffraction ring due to small particle size and strain is well known, however, no published reports have quantified the amount of broadening that will occur at the various steps of “work” leading to failure; in essence, developing a fatigue sensor that will predict failure.

Accomplishment: We have observed how x-ray diffraction rings change as a function of “cold work” for various materials. For example an as drawn wire will have fairly large crystallites of a given material. These crystallites will also be textured about the diameter of the wire. Diffraction rings taken of the wire using a two dimensional detector will show a spotty diffraction ring. As the wire is fatigued toward its elastic limit the crystallites will become smaller and less textured. Also defects will be developed in the metal. These will in turn cause the diffraction ring to broaden and become less spotty. Earlier work using film techniques have measured mean particle size and grain misorientation from the number and shapes of the diffraction “spots” respectively.

A microdiffractometer utilizing capillary optics is used to analyze small areas and an area detector enables us to collect the data in two-dimensions. Also Residual stress is increased near the break, which will cause the shape of the diffraction ring to change. The degree that the diffraction ring changes as a function of cold

work leading to failure can be determined for several materials. Models can be developed for each material type. In turn these models can be used to determine how close to failure a material is by simply collecting diffraction rings and comparing to the model.

Significance: Current technology will not detect failure until small cracks occur. In essence the failure has already occurred. We will demonstrate how failure can be predicted prior to actual failure of a given material such as copper and aluminum. If our predictions are correct then we will have in essence the first method for predicting failure in metals.

Contact: Mike Eatough, Materials Characterization Dept., 1822
Phone: (505) 844-7761
Fax: (505) 844-9781
E-mail: moeatou@sandia.gov

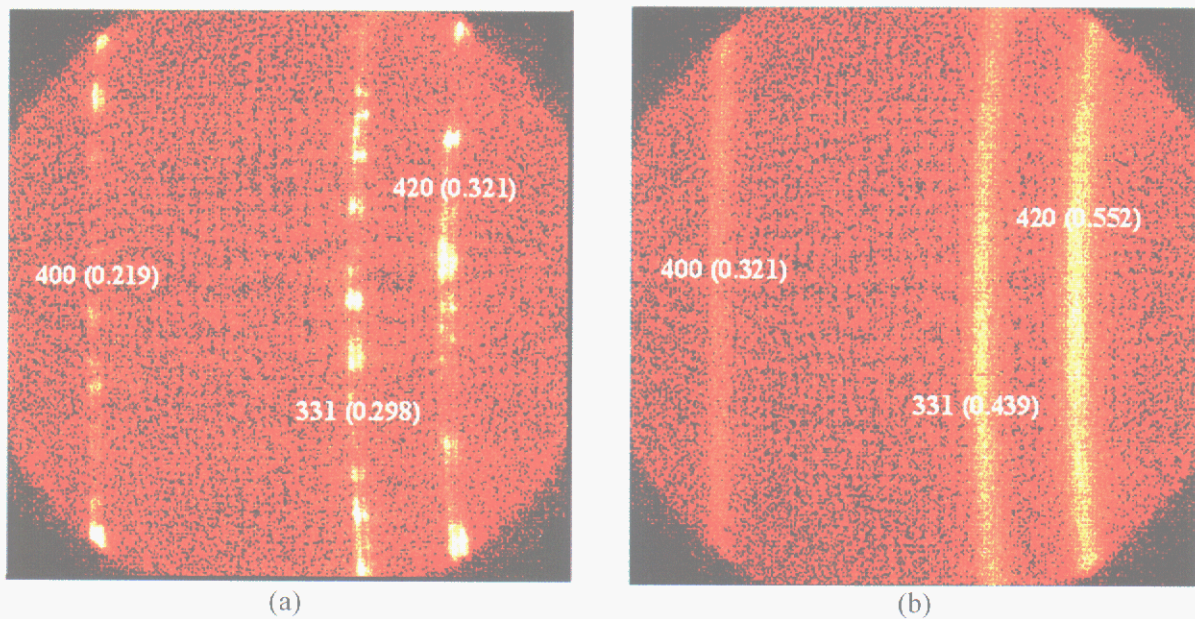


Figure 1. Frame (a) shows a section of the Debye ring of the 400, 331 and 420 hkl reflections for an Aluminum bar. The numbers in parenthesis are the FWHM for the Ka1. Note the spottiness of the pattern and the well resolved Ka1 and Ka2. Frame (b) is the same bar that has undergone low cycle fatigue. The pattern was taken near the crack produced from failure. Note the uniformity of the lines and the unresolved Ka1 and Ka2 as well as the increase in the FWHM of the Ka1.

Conformal Coatings for LIGA MEMS: Issues and Challenges

S. V. Prasad and T. R. Christenson and P.G. Kotula

Motivation: Many microelectromechanical systems (MEMS) fabricated by LIGA utilize electrodeposited metals such as nickel and Ni alloys. While Ni alloys may meet the structural requirements for MEMS, their tribological behavior remains somewhat undefined. For instance, the friction coefficient of pure Ni in dry sliding conditions is high ($\mu = 0.6 - 1.2$), and the stick-slip behavior could interfere with the performance and reliability. In a number of microsystems applications such as gear trains, comb drives and transmission linkages, tribological considerations, particularly sliding contacts amongst sidewalls, is of paramount importance. With the increasing number of MEMS fabricated by LIGA and other thick resist electroforming processes, there exists a need for the development of suitable coatings to combat the tribological problems.

Accomplishment: There is a variety of techniques (e.g., burnishing, resin bonding, physical vapor deposition, chemical vapor deposition) to deposit friction-reducing coatings on conventional machine elements. However, the miniature nature of LIGA MEMS elements--several hundred microns to millimeters in size--poses a tough challenge to the coating technology. Handling of individual LIGA MEMS elements is extremely difficult, and applying such techniques as resin bonding and burnishing can be ruled out. Physical vapor deposition is typically a line-of-sight process, whereas coatings are most needed on the sidewalls. Chemical vapor deposition, though conformal in nature, is a high temperature process that could potentially alter the microstructure of the base Ni alloy. So, we have devised a novel strategy to overcome these difficulties. Instead of handling the individual LIGA MEMS elements, we coated

the entire wafer before releasing the parts, i.e. after electroforming, lapping and dissolving the PMMA mold material. We opted for a commercially available plasma enhanced CVD process, in which ionized species are deposited onto biased substrates, thereby limiting the substrate temperatures to below 200°C. As a first step in this direction, we obtained a 100 nm thick commercial PECVD diamond like nanocomposite (DLN) coating on a LIGA wafer with MEMS elements on it, Figure 1a. The coated wafer was backsputtered to remove the coating material from the planar surfaces of the MEMS elements and from the rest of the wafer. The parts were subsequently released per standard LIGA process, Figure 1b. Simultaneously, techniques were developed to characterize the coated parts. A focused ion beam (FIB) section taken from the sidewall of a LIGA gear along with a bright field TEM image of the DLN coating, are shown in Figure 2a. Spectral imaging by automated X-ray spectral image analysis confirmed the presence of all the elements of DLN coating (e.g. C, O, Si) in the right proportions, Figure 2b. Parallel tribological measurements of DLN coatings on test coupons showed much improved tribological behavior with friction coefficient of 0.1 (or less) and practically no signs of debris generation or stick-slip behavior.

Significance: We have demonstrated a novel coating strategy that can be integrated into the mainstream LIGA technology to coat the sidewalls of intricate LIGA MEMS elements. This technique can be easily adapted to apply a variety of other friction-reducing coatings for improved performance and reliability of LIGA Microsystems.

Contact: Somuri Prasad, Microsystem Materials, Tribology and Technology Dept., 1851
Phone: (505) 844-6966
Fax: (505) 844-7910
E-mail: svprasa@sandia.gov

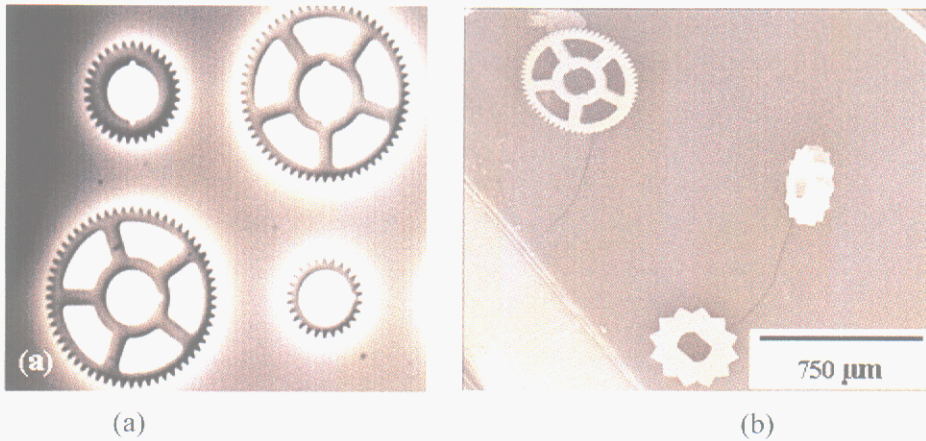


Figure 1. (a) Part of a wafer containing LIGA fabricated parts coated with a 100 nm thick Diamond-Like Nanocomposite by plasma enhanced CVD. (b) shows the SEM images of released parts after backsputtering.

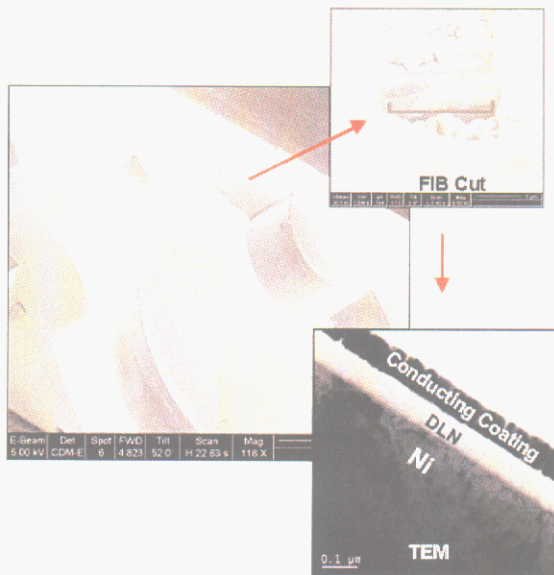
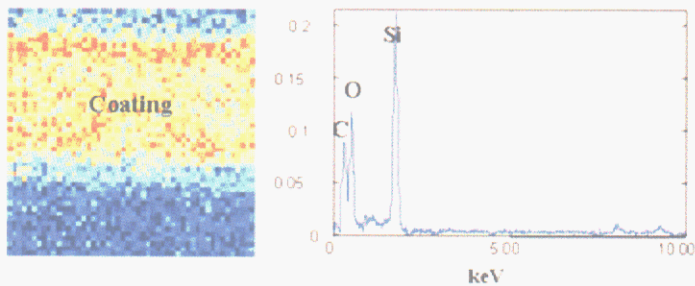


Figure 2. (a) A FIB section from the sidewall of a LIGA part along with a bright field TEM image showing a 100 nm thick DLN coating, (b) Results of the automated X-ray spectral image analysis showing the DLN coating component consisting of C, O, and Si and its location. Not shown from the automated analysis is the substrate component consisting of Ni.



(b)

Evaluating Tools for Simulating Polysilicon CVD for MEMS Applications

C.C. Battaile, P. Ho, and C.C. Wong

Motivation: Meaningful prediction of properties and performance of MEMS devices requires an accurate description of the morphologies and properties of the processed materials. In surface micromachining (SMM), these materials are deposited by thin film chemical vapor deposition (CVD) and etched by wet and plasma processes. Virtual prototyping for visualization and analysis requires “process geometry rules” that tell solid modeling codes how to generate realistic structures, and that inform analysis codes about the properties of the various materials. These process rules are obtained from a suite of detailed physical calculations. This report focuses on the evaluation of two candidate methods for microstructure-level modeling of polysilicon CVD: Los Alamos National Laboratory’s (LANL) Toposim3D moving mesh code, and a kinetic Monte Carlo approach developed at Sandia. (The level set technique is another powerful tool currently being implemented at Sandia for this application, but it will not be addressed here.)

Accomplishment: LANL’s Toposim3D code meshes the substrate, the growing film, and the vapor, as shown in Figure 1a. The local growth rates at the film/vapor interface are calculated using CHEMKIN. At each time step in a growth simulation, Toposim3D moves the interface according to the growth rates, and at specified intervals performs mesh maintenance (by adaptive remeshing with LANL’s LaGriT package) which is not guaranteed to succeed. In Figure 1b, growth on the seven-grain film was aborted in the depicted state due to mesh

maintenance failure, and the growth behavior at the grain boundaries relies on the mesh maintenance rather than the physics.

The kinetic Monte Carlo (kMC) method automatically handles the topology. Deposition fluxes, chemical reaction rates, diffusion rates, and bonding energies can be specified with arbitrary complexity to ensure the appropriate level of physical detail. An example of the growth of a polycrystalline film by kMC is shown in Figure 2. The method accounts for nucleation, island coalescence, and film growth in a straightforward manner, and unlike with moving mesh methods, the growth of very high aspect ratio, complex films can be modeled.

Significance: Computer-aided design and analysis of MEMS devices will eventually require models that faithfully predict the morphologies and properties of the processed materials. Moving-mesh techniques powerful and convenient for coupling to other mesh-based methods, but suffer from the complications of mesh maintenance. The kMC approach is flexible and provides a realistic treatment of the formation and development of complex microstructures.

Contact: Corbett Battaile, Materials & Process Modeling & Computation Dept., 1834

Phone: (505) 844-7039

Fax: (505) 844-9781

E-mail: ccbatta@sandia.gov

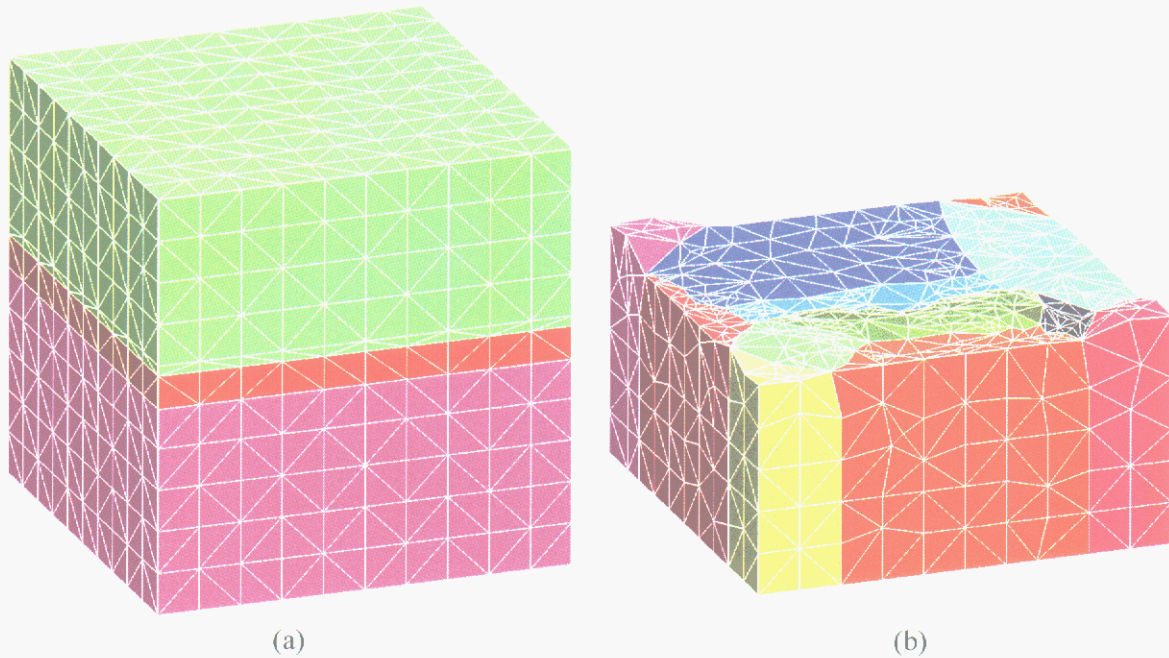


Figure 1. Toposim3D wafers showing (a) a simple planar film (red) growing on a substrate (purple) into a vapor (green); and (b) a seven-grain columnar polycrystal grown to the limits of the adaptive meshing capability.



Figure 2. Toposim3D wafers showing (a) a simple planar film (red) growing on a substrate (purple) into a vapor (green); and (b) a seven-grain columnar polycrystal grown to the limits of the adaptive meshing capability.

Micromechanics Challenges for Modeling Polycrystalline Materials

T.E. Buchheit, C.C. Bataille, and G.W. Wellman

Motivation: The need for a fundamental understanding of the mechanical response of polycrystalline materials lies within properties characterization of many materials critical to Sandia's mission, such as LIGA fabricated MEMS, solder, and braze alloys. This understanding can best be addressed through a complementary blend of microscale and nanoscale modeling and experimentation. An important part of developing a useful micromechanics modeling tool is to validate that model through experimentation at the appropriately small size scale.

Accomplishment: A 3-D finite element model composed of as many as 64,000 elements that can simulate the deformation response of 200 or more grains within a polycrystal has been developed and implemented into JAS-3D, Sandia's non-linear quasistatic finite element code. The simulated deformation response of grains in the polycrystal depends on their crystallographic orientation, which is tracked within each finite element of every grain. Consequently, the microstructure can evolve at a subgrain scale within the polycrystal and a large amount of information about the deformation of a polycrystalline material may be divulged at a micro- (and in some cases nano-) size scale. An example of a simulated result, a tension test, using this model is given in Figure 1.

As barriers to dislocation motion, grain boundaries play a very important role in dictating both the local and global mechanical response of a polycrystal. In a quasi-continuum context, more equivalent to that captured by a crystal plasticity

formulation, they impart strengthening to the polycrystal via the well-known Hall-Petch relation. A standard crystal plasticity model treats grain boundaries simply as orientation changes within a polycrystal, neglecting a critical part of their true role in polycrystalline materials. As a result, grain size (an important length scale) cannot be defined within a standard polycrystal plasticity model, compromising the capability of these models to make accurate local mechanical response predictions. A very recently developed modification to the JAS-3D finite element model captures the influence of grain boundaries and successfully captures experimentally observed polycrystal strengthening due to grain size. A comparison of simulated and experimental stress strain curves is given in Figure 2.

Significance: Developing a modeling capability, which provides quantitative insight into the micromechanical deformation response of materials, provides Sandia National Laboratories with a tool critical to accomplishing its mission, nuclear weapons stockpile reliability and stewardship. In this specific case, capturing grain size as a length scale in microstructure-based deformation modeling greatly improves its ability to accurately predict microstructure deformation evolution during deformation. Figure 3 illustrates deformation substructure representative of bands which occur in real material deformation. Substructure deformation evolution is captured in this model because it uses grain size as a length scale.

Contact: Tom Buchheit, Microsystem Materials, Tribology & Technologies Dept., 1851
Phone: (505) 845-0298
Fax: (505) 844-4816
E-mail: tebuchh@sandia.gov

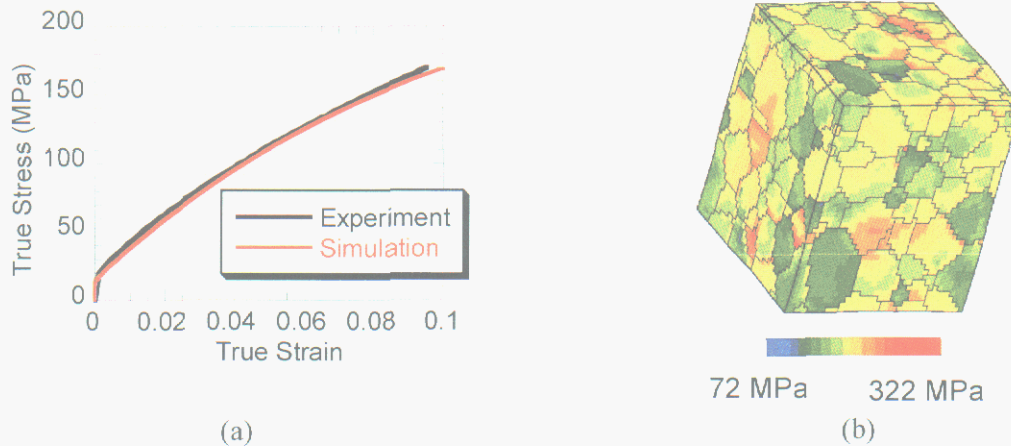


Figure 1. Simulation of a tension test using the 3-D polycrystal plasticity model. The simulation consists of 200 grains with imposed periodic boundary conditions designed to replicate a tension test within a polycrystal. (a) Stress-strain curve -comparison between simulation and experiment. (b) Predicted von-mises stress distribution within simulated result.

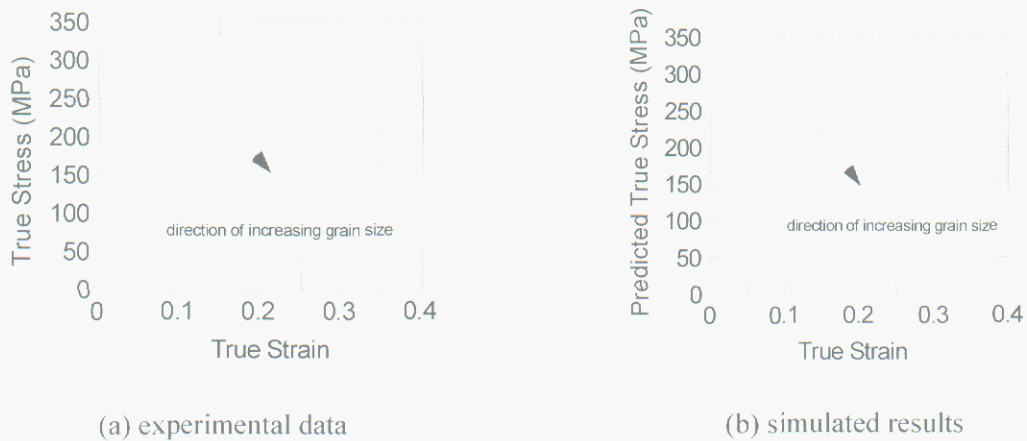


Figure 2. Tensile stress-strain curves of copper polycrystals with various grain sizes ranging from 15 μm to 350 μm .

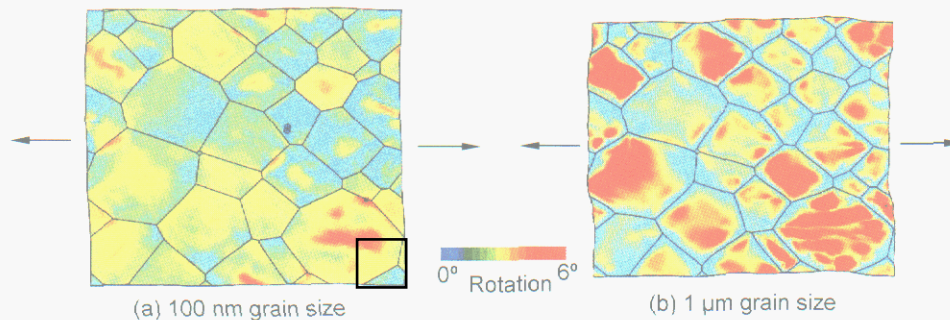


Figure 3. Graphical representation of substructure deformation evolution after 10% tensile strain (indicated by arrows) using grain size as a length scale in a polycrystal plasticity model.

Photoprogrammable Materials for Microsystems

G. Jamison

Motivation: Photoactive materials offer the opportunity for rapid, non-contact manipulation of material properties (i.e. optical, mechanical, structural, electronic) with direct impact on DOE/DP microsystems for nuclear safety and security. A fundamental understanding of photosensitive mechanisms will allow us to engineer tailored materials at the molecular level to provide optimal photoinduced refractive index changes. The results will be tailored environmental stability for optical beam manipulation and microscale physical state sensing. This project focuses on the preparation of requisite materials and the subsequent photopatterning of refractive index structures through the material's photosensitive response, to form integrated photonic devices possessing unique optical and physical properties.

Accomplishment: Hybrid organic-inorganic materials with high photoresponse to accessible ultraviolet wavelengths ($\Delta n = -0.14$ as determined by ellipsometry at 632 nm) have been prepared and processed into homogeneous films. Next generation materials have also been prepared with absorption maxima coinciding with UV wavelengths consistent with microscale solid-state UV sources, making them suitable for integration into microsystem devices. These polymeric materials' optical properties can be tailored through rational design, selection and manipulation of backbone composition, degree of connectivity and pendant organic side group functionality.

High contrast optical structures (gratings and curved waveguides) have been fabricated via exposure to high intensity UV light and their photoresponses quantified, in order to

demonstrate the potential utility of these materials as write-once substrates in optical microscale devices.

Preliminary demonstrations of secondary, low energy incident beam refraction and diffraction (incident beam normal to grating plane, Figure 1) as well as real-time guide writing and guiding of prism-coupled light into planar multimodal waveguides have been conducted (Figure 2). Current efforts include evaluation of thermal and optical thresholds for inclusion in microscale devices relevant to DOE/DP weapon and security applications.

Significance: An established emphasis on photonic, electronic, electromechanical and fluidic microsystems to support DOE/DP and other SNL customer needs requires the design and development of new materials with tailored structures and nanoscale behavior. The significant dependence of microsystem performance and reliability on nanostructure provides an opportunity to pursue new material processing strategies and material functionality with the possibility of improving manufacturing options and operational capabilities of a given microsystem. Therefore, these materials' photoactivated changes in properties including local electrostatic behavior; polarizability or even structural characteristics can form the basis for an inherently new materials strategy allowing for real-time photoactivation of material properties directly impacting microsystem function. The unique optical, thermal and ionizing radiation properties of these photopatterned devices can be exploited to contribute to weapon system safety under abnormal conditions, for example.

Contact: Greg Jamison, Chemical Synthesis and Nanomaterials Dept., 1846
Phone: (505) 844-8281
Fax: (505) 844-9624
E-mail: gmjamis@sandia.gov

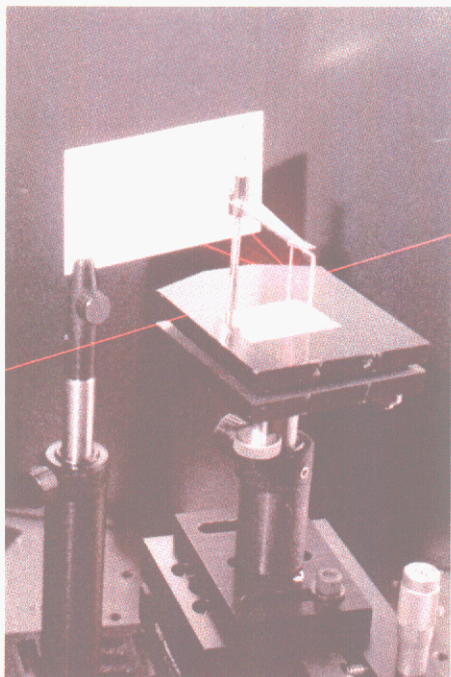
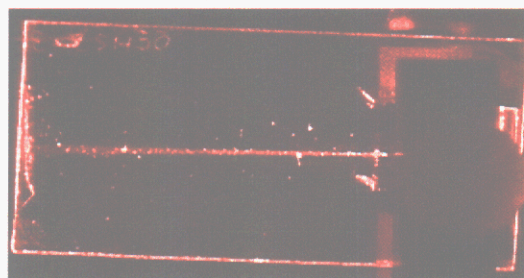
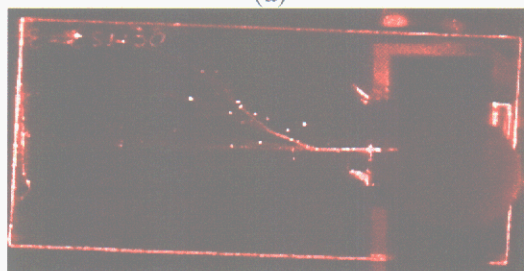


Figure 1. Diversion of incident secondary beam normal to photoimprinted grating, defined by exposure of photosensitive hybrid material through photomask.

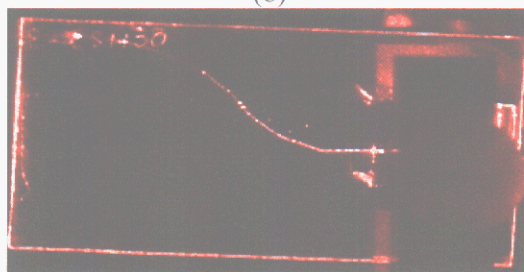
Figure 2. Writing of embedded strip waveguide: (a) Coupling into 700nm thick unexposed planar film; (b) Partial coupling into photo-written 250 nm- wide curved strip; (c) Light fully coupled into photowritten S-shaped strip guide (total exposure 3 min. @ 248 nm, 2 mJ/cm²). (total exposure 3 min. @ 248 nm, 2 mJ/cm²).



(a)



(b)



(c)

Barium Transport through Microminiature Thermionic Energy Converters

C. C. Battaile, D. B. King, and K. R. Zavadil

Motivation: The technological drive toward miniaturization demands new approaches to a wide variety of age-old engineering problems. Microminiature thermionic converters (MTCs) have demonstrated the potential for high-energy conversion efficiency in a tiny package, but predicted performance levels have not been achieved because materials optimization is not yet understood. The MTCs being developed at Sandia utilize Ba transport to the surface to achieve a low work function. The goal of this study is to develop a complete model of Ba transport to the surface, Ba surface diffusion and reaction, and Ba desorption. This report focuses on modeling transport through a porous polycrystalline matrix.

Accomplishment: The computational domain is generated from Monte Carlo Potts model (grain growth) results. A finite difference (FD) mesh is constructed by creating nodes at the vertices of the Potts lattice sites. Thus, the edges connecting each FD node lie either: 1) in a grain interior, 2) in a pore interior, 3) on a grain boundary, or 4) on a pore surface. Diffusivity values are assigned to each of the four possible transport paths, and the flux of material through the microstructure is calculated by solving the Laplace equation for steady-state diffusion,

$$\frac{\partial C}{\partial t} = -\nabla J = \nabla(D\nabla C) \quad (1)$$

where C is the concentration, t is time, J is the flux, and D is the (spatially nonuniform) diffusivity.

Figure 1 shows a porous polycrystalline microstructure on a million-site lattice, and the corresponding map of the total flux through each FD node. Diffusion was allowed along grain boundaries at an arbitrary reference diffusion rate, and at pore surfaces at ten times that rate. The flux is only high at the grain boundaries and pore surfaces, as expected. Figure 2 contains data from many calculations of single crystals with randomly distributed, single-site pores in varying densities. Diffusion is only allowed along the pore walls in these calculations. Since efficient transport relies on the percolation of high-diffusivity paths, and these paths are pore surfaces rather than pore interiors, the optimum pore density is 50% where the cross-section of high diffusivity paths is maximized.

Significance: The fabrication of efficient MTCs depends in part on the optimization of porous microstructures. By developing models of diffusion through these complex materials, we will be able to identify ideal combinations of microstructural features to optimize bulk transport and surface delivery of species that will reduce the work function and improve converter efficiency.

Contact: Corbett Battaile, Materials & Process Modeling & Computation Dept., 1834
Phone: (505) 844-7039
Fax: (505) 844-9781
E-mail: ccbatta@sandia.gov

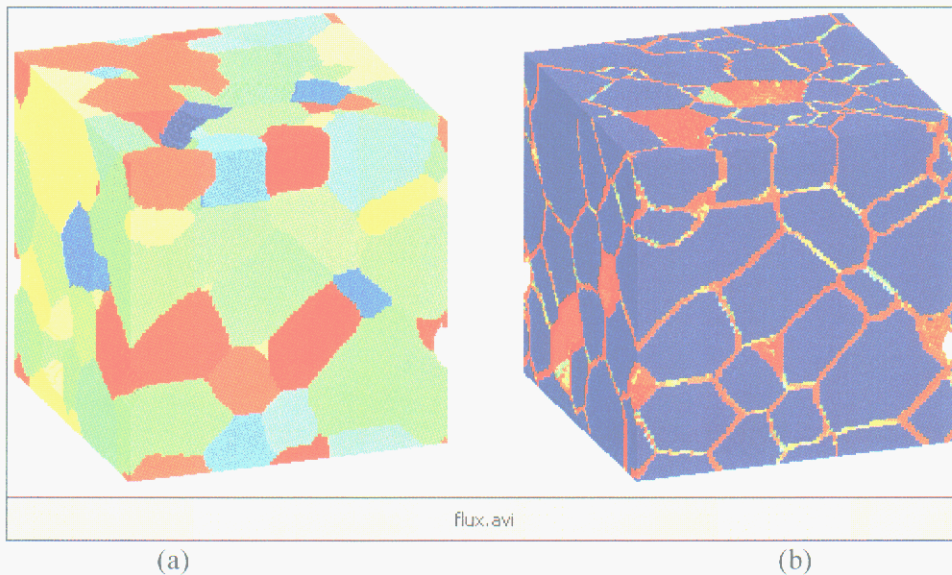


Figure 1. Images of a) a million-site porous polycrystal, and b) a map of the total flux at each node in it. The colors in a) simply distinguish different grains, and in b) represent an arbitrary logarithmic flux scale where blue is low and red is high.

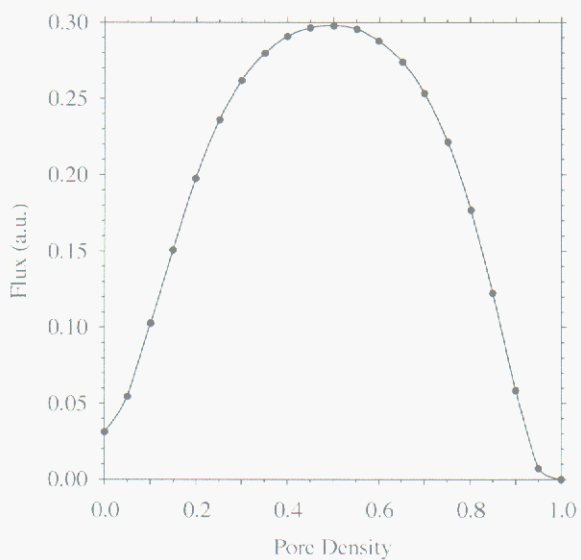


Figure 2. Average flux at the surface of randomly pored single crystals as a function of the pore density. Error bars are the standard deviations over 21 calculations with different random pore distributions.

Controlled Assembly of Multi-Cationic Metal Alkoxides

T. J. Boyle, T. M. Alam, M. A. Rodriguez

Motivation: Metal alkoxides are excellent precursors to ceramic materials. These precursors are easily modified to tailor their hydrolysis and condensation rates yielding control over the properties of the final ceramic material of interest. Even though metal alkoxides have been known for more than 60 years, the ability to construct multi-cationic metal alkoxide precursors, in a rational manner, has not been realized. We have undertaken the synthesis of mixed metal alkoxide compounds to generate "single-source" precursors for both MOCVD and sol-gel routes to thin films.

Accomplishment: Three synthetic approaches were undertaken to generate single-source metal alkoxide compounds.

1) Metathesis, or exchange reactions are classically used to generate mixed metal alkoxide species (i.e., an alkali metal is introduced to the parent alkoxide followed by removal through complexation with a metal halide). Unfortunately, this often results in no reaction or products that retain either the alkali metal or the halide. We found through a structural study, and solution characterization, that the alkali metals were not accessible in these compounds for metathesis. We then investigated thallium-containing species due to the halophilicity of this metal. By altering the steric bulk of the TI and the co-metal Ti's ligands, we isolated the first fully ionic metal alkoxide, $[Tl^+][Ti(OAr)_5]$ (Figure 1) which is an ideal metathesis reagent. Subsequent reactions led to phase separated species, demonstrating the futility of the metathesis approach.

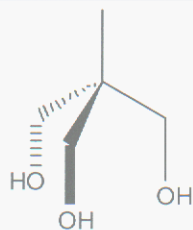
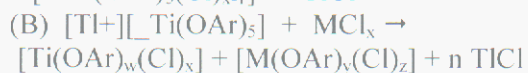
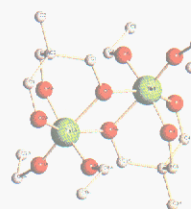
2) Hyper-oligomerization relies on the small charge to large cation size to allow metal alkoxides to oligomerize. This method often fails, due to preferential crystallization of one component. Inclusion of a polydentate ligand (THME-H3) prevents separation, which has allowed us to systematically generate a series of mixed-metal alkoxides. The first example of THME modified mixed metal alkoxides are shown in Figure 2.

3) The use of an internal chemical reaction to hold a metal alkoxide together is a unique approach to generating single source metal alkoxides. This was realized using carboxylic acids in the presence of a metal alkoxides, which induces esterification. We have successfully established this process as a viable route to a number of mixed metal Ti species including early, late, and main group metals. Some examples are shown in Figure 3.

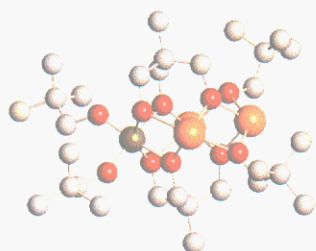
Significance: We have demonstrated with an ideal molecule that the metathesis routes are not a viable means for production of mixed metal species. For the first time we have two routes using polydentate ligands that will consistently yield polymetallic species. This will lead to the controlled construction of "single-source" precursors. These compounds will have uniform solubilities, volatilities, and decomposition temperatures thus increasing the utility while maintaining cation stoichiometry.

Contact: Tim Boyle, Ceramic Materials Dept., 1843
Phone: (505) 272-7625
Fax: (505) 272-7336
E-mail: tjboyle@sandia.gov

Figure 1. The first unsupported ionic metal alkoxide, (a)[Ti+][$\text{Ti}(\text{OAr})_5$] was used for a metathesis (eq A) reaction but did not yield the mixed metal species instead phase separation occurred (eq B).

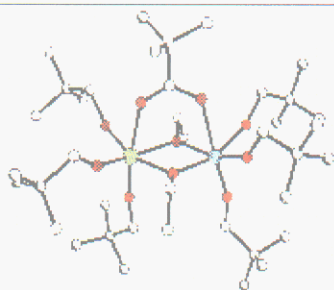
2(a) THME-H₃

2(b)

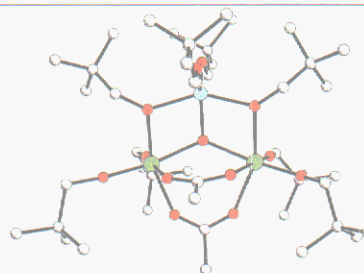


2(c)

Figure 2. The use of the (a) THME ligand allows for synthesis of polymetallic species: (b) [(μ -THME)NbTa(OEt)₂] and (c) [(μ -THME)Sn₃Ti(μ -ONep)₂(ONep)₂]

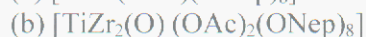


3(a)



3(b)

Figure 3. Using carboxylate ligands that can undergo in situ esterification, multi-cationic metal alkoxides were isolated as:



3(c)

Current Concentration at Defects in ZnO Varistor Material

R. A. Anderson and G. E. Pike

Motivation: Varistors are electrical devices that regulate voltage and arrest damaging voltage surges. Most applications exploit the nonlinear conductivity of polycrystalline, semiconducting zinc oxide (ZnO). Electric current in a ZnO varistor increases steeply with increasing voltage (e.g., a power-law exponent >20) above a threshold voltage, but a varistor sometimes fails by a progressive decline in the regulation voltage under repeated high-power electrical pulses. A failed varistor typically reveals a small-diameter hollow filament, with thermally altered ZnO at its surface, extending partway along the varistor length. Data acquired during a degradation process can be accounted for by assuming that the filament is conductive and lengthens each pulse.

Various types of inclusions, much larger than ZnO grains, are often observed and some of these defects were suspected to trigger electrical degradation. For example, thin disk-like bodies of presumably non-conductive material are commonplace. Inclusions that perturb the current flow will cause local current concentration, but the nonlinear response of the varistor interferes with intuitive estimation of the magnitude of such effects. Our quantitative computations were undertaken to resolve this issue.

Accomplishment: We investigated non-conductive inclusions of simple shapes, from rounded-edge disks to spheres, and perfectly conductive shapes from spheres to cylindrical rods with domed ends. Conductive spheres represent metal-filled voids intersected by electroded surfaces and conductive rods may simulate high-conductivity filaments that

accompany pulsed electrical degradation. We developed a computational technique that treated the varistor medium as a nonlinear, although isotropic, electrical conductor and self-consistent electric fields and current densities were obtained. Our method eliminated a severe mesh-imprinting artifact in conventional resistor-network simulations.

The main findings are: Electric current is diverted by a non-conductive inclusion and becomes crowded at the inclusion equator. The current concentration is larger when the surrounding medium has varistor, rather than Ohmic, conductivity, although enhancement factors remain modest. Highly conductive inclusions cause a greater effect. Figure 1 shows a 75x boost in current density in the model varistor material, compared with 3x in Ohmic material. Power-density ratios in the two media are 90x and 9x. With rods of aspect ratio 6 (see Figure 2) the rod-tip current concentration exceeds 700x. Enhancements this large would lead to severe local heating during a high-power voltage pulse, sufficient to elongate the region of altered material.

Significance: This work revealed how inclusion defects perturb the electric current in a ZnO varistor. Non-conductive inclusions are unlikely to trigger electrical degradation, but the extreme current concentration found with elongated high-conductivity regions shows that a filamentary breakdown process can readily lengthen, and it may explain the stepwise nature of the degradation process.

Contact: Bob Anderson, Ceramic Materials Dept., 1843
Phone: (505) 844-7676
E-mail: raander@sandia.gov

Figure 1. Normalized current densities in varistor medium containing a perfectly conductive sphere, as a function of dimensionless radial distance from the symmetry (z) axis. J_0 is the uniform current density far from the inclusion. Maximal current concentration is found at the poles of the sphere, and the results for the varistor medium are compared with those for an Ohmic medium in the case of a plane tangent to the sphere pole. Current densities in the varistor medium at two other planes normal to the z axis are also plotted; current baselines (dotted lines) are drawn at the vertical positions of those planes. The very high currents are limited to the near vicinity of the sphere poles.

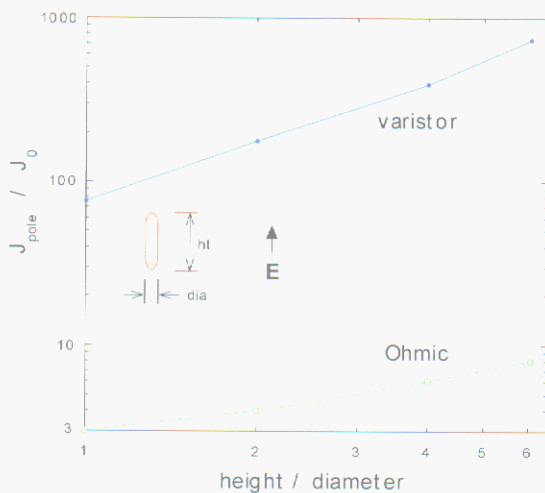
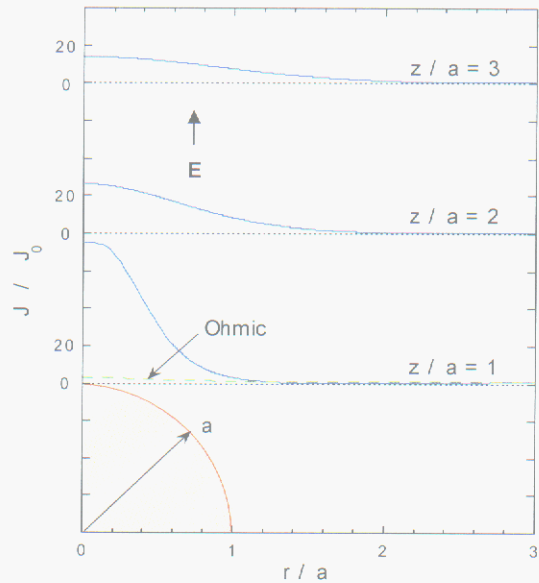


Figure 2. Normalized current densities at the poles of perfectly conductive rods immersed in varistor and Ohmic media. The varistor medium causes substantially greater current concentration than Ohmic medium, and it also gives rise to a steeper increase in current density with increasing rod aspect ratio (unity aspect ratio denotes a sphere). These results show a 700x local current density boost in the varistor from a rod six times as long as its diameter.

ESP (Engineered Stress Profile) Glass - Unique Opportunities for Performance and Reliability

S. J. Glass, E. K. Beauchamp, C. Newton, and R. Stone

Motivation: Glass is extremely sensitive to the presence of surface flaws. A wide flaw size distribution leads to low strengths and a wide strength distribution. As a result glass is rarely considered for structural applications and large safety factors are built into any design where reliability is critical. The introduction of residual surface compression is commonly used to increase the glass strength and to cause it to fracture into small pieces. Unfortunately the traditional approaches for pre-stressing glass often increase the strength scatter.

Accomplishment: A new approach for strengthening glass and dramatically increasing its reliability has been developed for both specialty compositions and for soda lime silicate glass. Regular ion-exchanged glass and thermally tempered glass have the compressive stress maximum right at the surface. The Engineered Stress Profile (ESP) process uses a two-step ion exchange that results in the compressive stress maximum being below the surface. At significant levels of the applied stress (relative to the fracture strength) a single surface crack starts to grow into the glass. As the crack grows perpendicular to the surface it encounters increasing resistance to propagation. Finally the crack turns away from its initial trajectory and it arrests. As the applied stress is further increased another surface crack begins to propagate and is then arrested in the same manner. Figure 1 shows ESP glass that contains an array of arrested

cracks. The cracking process is repeated until a critical value of the applied stress is reached. The failure strength is not dependent on the size of the worst flaw, but on the details of the stress profile. Thus the strength distribution is not dependent on the flaw size distribution and is very narrow compared to that of regular glasses and ceramics. A typical glass has a low Weibull modulus, e.g., $m=5-10$. ESP glass has Weibull moduli as high as 60. The two-step ion exchange and other processes provide broad flexibility in terms of engineering the stress profile to optimize strength, reliability, and fragmentation behavior for different glasses.

Significance: For the first time we have a glass that is both strong and dependable, cracks non-catastrophically, and fractures into small fragments. A designer's confidence in the glass's ability to survive or fail at a given stress is increased significantly as shown in Figure 2. In an application where the glass must sustain 80% of the average failure stress, ESP glass with $m=60$ has an only one two in one million chance of failing. In contrast regular annealed glass has a failure probability of about 30%. Engineered stress profiles can be produced with processes that allow great flexibility with respect to the glass composition and performance optimization. We are continuing to improve our ability to engineer stress profiles and glass behavior and to test ESP glass in adverse environments to satisfy new application requirements.

Contact: S. Jill Glass, Ceramic Materials Dept., 1843
Phone: (505) 845-8050,
Fax: (505) 844-4816
E-mail: sjglass@sandia.gov

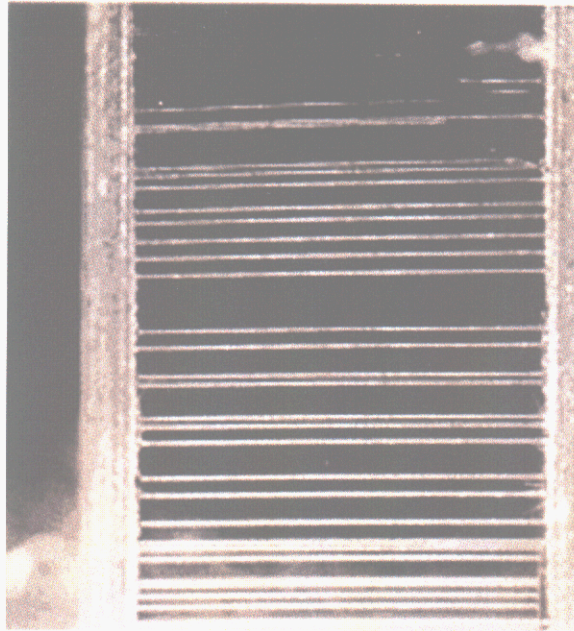


Figure 1. Soda lime silicate glass with non-catastrophic surface cracks formed prior to failure.

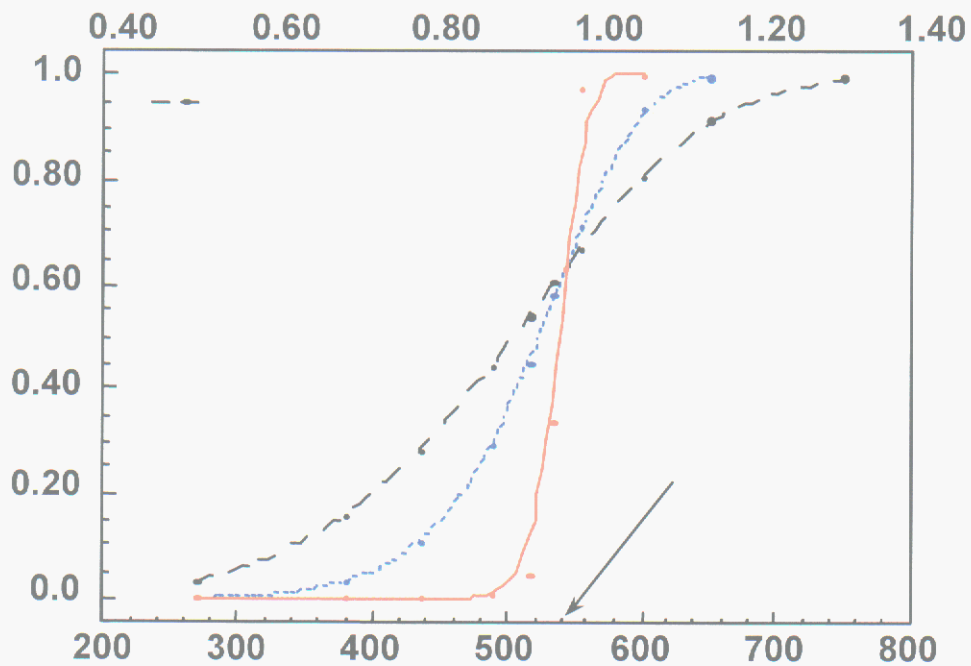
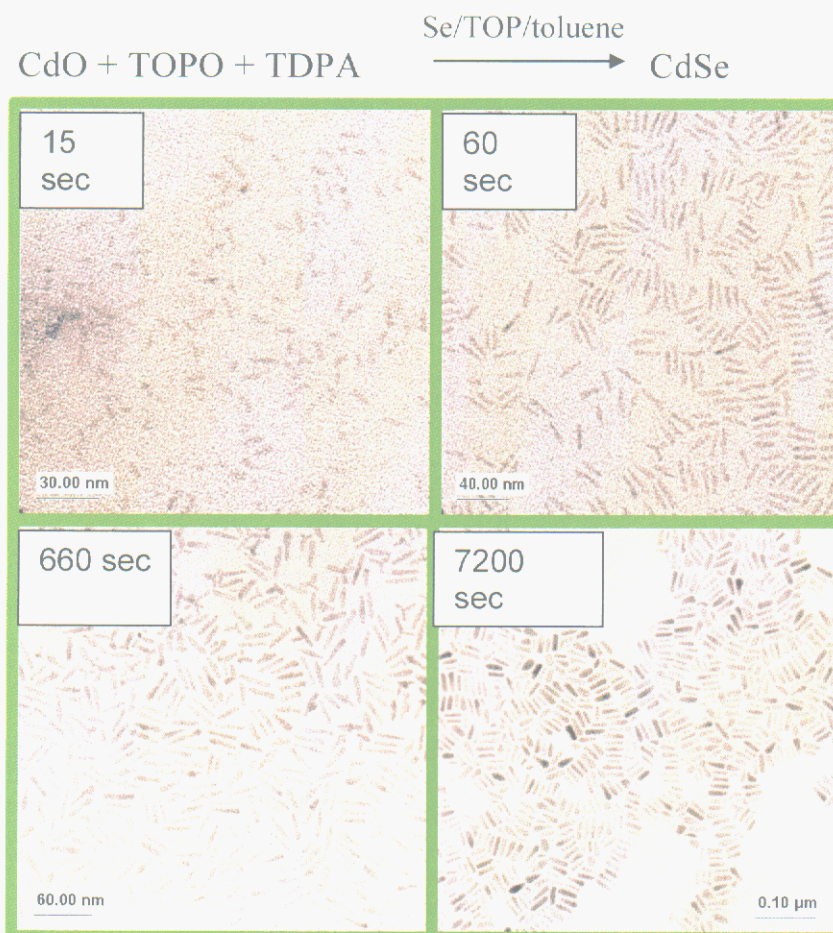
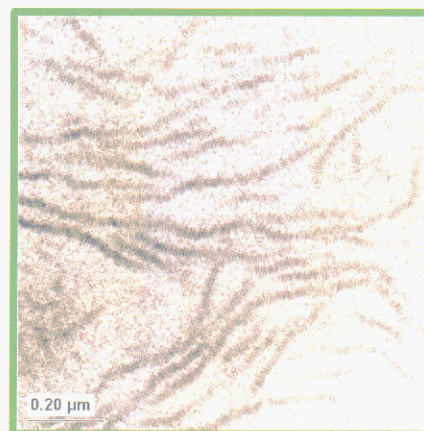


Figure 2. Failure probability vs. applied stress for various Weibull moduli, m . ESP glass, with $m=60$, has a dramatic increase in failure probability only at the average failure stress, in contrast to regular glass ($m=5-10$), which has a high failure probability at stresses below the failure stress.

Figure 1. The temporal growth of CdSe material from CdO (shown) or Cd(OAc)₂ was found to yield rod-like morphologies. The UV-Vis spectral data (metrically listed) shows the changes that occur in the exciton peaks. Based on the time of reaction, the size of the rods grows but the aspect ratio does not change. For select times, a 24 nm CdSe nanorods self-assembles into tracks over 1 μm long (lower figure).



Rxn Time	Length (nm)	λ_{max} (nm)
15 sec	10	549
60 sec	18	587
11 min	30	624
2hr	30	~650



Influence of Precursor Nuclearity on ZnO Nanoparticle Morphology

N.L. Andrews, T.J. Boyle, M.A. Rodriguez, S.D. Bunge, T.J. Headley

Motivation: Recently, there has been a great deal of interest in producing materials on the nanoscale due to the expected unique physical properties of materials in this size regime. At this scale, the properties of the material will be dominated by surface phenomenon dictated by individual particle composition, morphology, crystallinity and interparticulate interactions. Of these factors, the ability to control nanoparticle morphology will be key in the production of functional nanodevices. In order to manipulate the morphology of nanoparticles, a fundamental understanding of the precursors' effects on nanoparticle size and shape is necessary.

Zinc oxide (ZnO) has a diverse number of applications, such as sensors, catalysts, varistors, surface acoustic wave devices, electrooptic devices, photo-, and electro-luminescent devices, dental implants, and semi-conductors. Because of its wide variety of uses, ZnO is an ideal candidate for preliminary studies examining the relationship between precursor structure and nanoparticle morphology. For sol-gel systems, a strong connection between the precursor nuclearity and arrangement to the final thin film properties has been firmly established.

Accomplishment: Due to the limited number of diverse structured ZnO precursors, we have synthesized and fully characterized a variety of structurally diverse zinc alkyl alkoxide compounds. The resulting molecules include monomers, dimers, tetramers, and heptamers of

Zinc. This variation afforded us the opportunity to examine the role of precursor nuclearity in dictating nanoparticle morphology. Toward this end, four representative nuclearities (monomer, dimer, tetramer, and heptamer) were chosen from the structurally characterized species and used to generate nanoparticles of ZnO. The nanoparticles generated from each precursor were essentially identical, nanorods with average dimensions of approximately 35 x 7 nm. Based on these studies, it appears that precursor nuclearity does not play as strong a role in the synthesis of nanoparticles as compared to the strong influence noted for the precursor effects observed in sol-gel systems.

Significance: This work shows that control of nanoparticulate morphology requires an understanding of the more fundamental molecular conversions during processing. There appears to be no major correlation between the nuclearity of the precursor and the final particulate morphology. However, another consequence of this work is that the route to a specific particulate morphology may be optimized independent of precursor selection.

Contact: Tim Boyle Chemical Synthesis and Nanomaterials Dept., 1846
Phone: (505) 272-7625
Fax: (505) 272-7336,
E-mail: tjboyle@sandia.gov

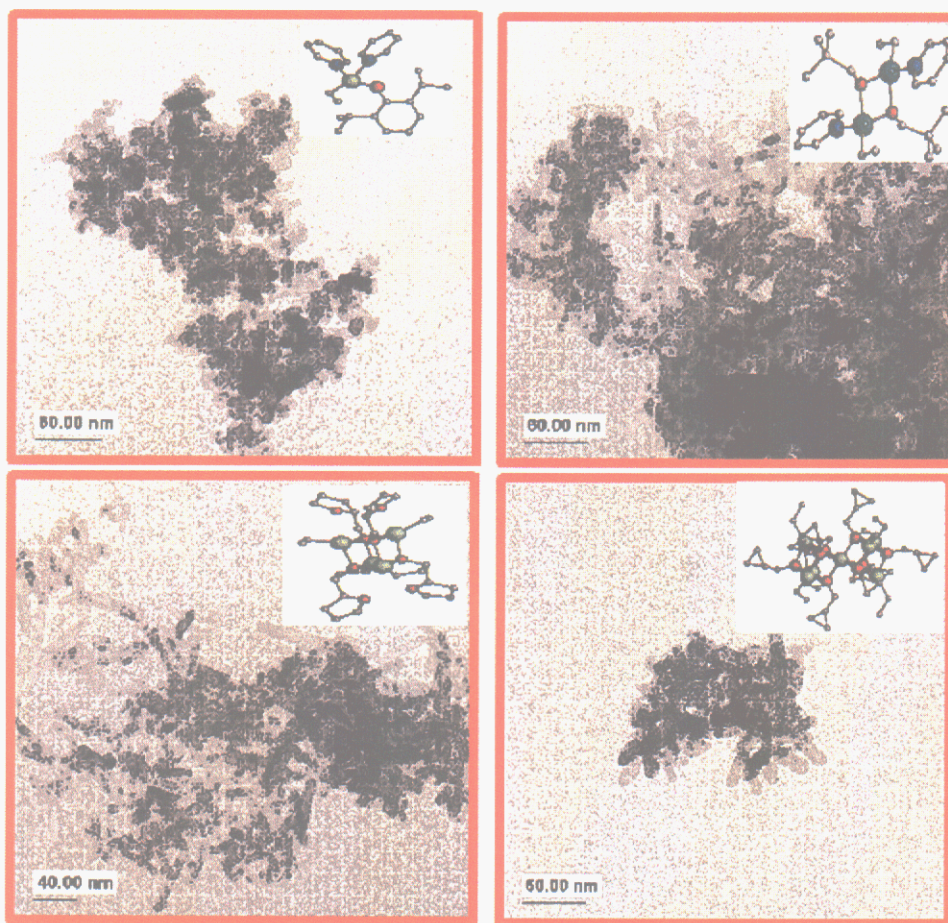


Figure 1. TEM micrographs of ZnO rods material generated from $[Zn(DIP)(Et)(py)]_2$, $[Zn(ONep)(Et)(py)]_2$, $[Zn(OTHF)(Et)]_4$, $Zn[Zn_3(OCH_2Pr^c)_4(Et)_4]_2$ (shown in the upper left corner). A solution of each precursor was dissolved in pyridine and then injected into a 1-methyl-imidazole: water (95:5) mixture heated to reflux temperatures. The reaction was heated for 1/2 h. and then allowed to cool to room temperature. The mixture was centrifuged and the insoluble material re-dispersed in hexanes and dropped onto a TEM grid. The figures shown were obtained from these deposits.

Oxidized Metal Powders for Mechanical Shock Safety Enhancers

T. J. Garino

Motivation: Weaklinks are a major element of nuclear weapons safety. A weaklink is a critical component in the firing sequence that will undergo an irreversible failure upon exposure to an abnormal environment brought on by, for example, an accident, thus dudding the weapon. The two most common attributes of abnormal environments are high temperature, due to a fire, and a mechanical shock, due to unintentional impact. An example of a weaklink is having the capacitor that stores the charge that fires the detonators be designed to fail above a certain temperature so that it is no longer able to store charge. If the component that fails is not an essential part of the firing sequence but can still dud the weapon in an abnormal environment, it is called a safety enhancer. A safety enhancer, while not as desirable as a weaklink, is nevertheless valuable especially when fielding a true weaklink is not possible. An example of a safety enhancer is a component that would be connected in parallel with the capacitor and acts as a resistor in normal environments but changes to a conductor when exposed to an abnormal environment.

Accomplishment: We have proposed and investigated a new concept for a mechanical shock safety enhancer based on the electrical characteristics of oxidized metal powders. When a powder consisting of electrically conducting metal particles each with a thin skin of thermally grown, electrically insulating native oxide is compacted, it's low voltage electrical resistivity changes by about seven orders of magnitude from a high value at low stress where the insulating oxides layers are intact, to a low value at high stress where the oxide layers have been broken. The transition from insulator to

conductor occurs over a narrow range of stress that can be in the range of a few MPa or less, as shown in Figure 1A for an oxidized aluminum powder. We have achieved the best results with tantalum and aluminum, two metal whose oxides are excellent insulators. Figure 2B shows breakdown strength behavior after application and removal of a stress for these metals. As shown, the initial breakdown strength of $\sim 5\text{kV/cm}$ decreases strongly at less than 1 MPa.

A conceptual design showing how an oxidized metal powder could be incorporated into a safety enhancer is shown in Figure 2. The powder is between a solid metal sphere and a metallic shell, which are connected to the electrodes of the capacitor. A mechanical shock causes the free-floating inner sphere to compact the powder in the region determined by the direction of the shock. Simple calculations show that a sphere 1 cm in diameter could produce a stress in excess of 1 MPa for a 1000g shock so that the entire device could be around 2 cm in diameter.

Significance: To date, a successful mechanical shock weaklink or safety enhancer has not been incorporated in any weapons system. All previous research in this area at Sandia National Laboratories has focused on fracture of brittle components. The oxidized metal powder concept has several advantages over brittle fracture including lower stress operation, omnidirectionality, and the fact that by going from an insulator to a conductor, they can short the capacitor so that charge cannot be stored as opposed to brittle fracture where a conducting path becomes an open and the stored charge could conceivably conduct to the detonators by some other path.

Contact: Terry Garino, Ceramic Materials Dept., 1843
Phone: (505) 845-8762
Fax: (505) 844-9781
E-mail: tjgarin@sandia.gov

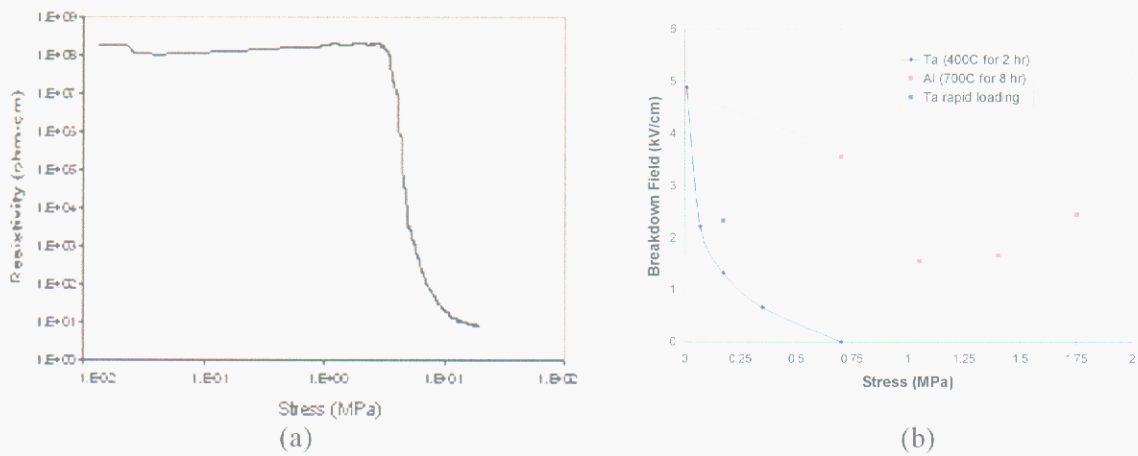


Figure 1. The electrical behavior of oxidized metal powders under compaction. (a) The low voltage resistivity of an aluminum powder during compaction. (b) The breakdown field strength of oxidized Al and Ta after the removal of the stress.

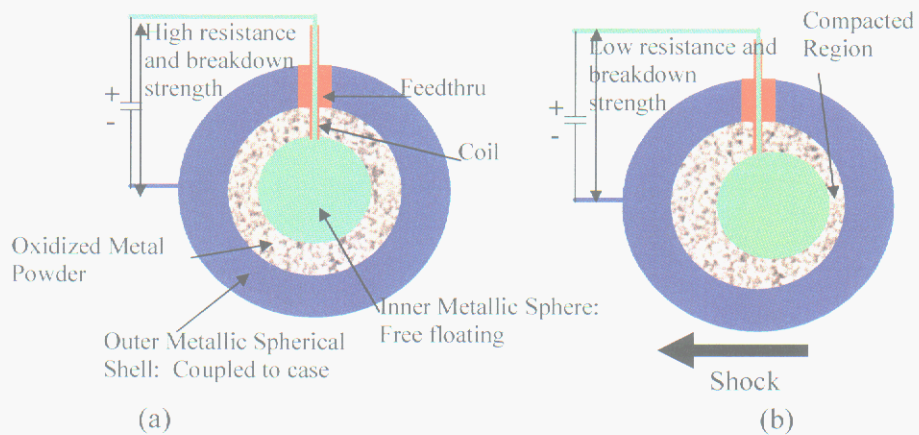


Figure 2. A conceptual design for a oxidized powder mechanical shock safety enhancer before (a) and after (b) the application of a shock.

Properties of Lanthanide Doped Lead Zirconium Titanate(PLnZT)

T. Boyle, J. Dawley, B. Tuttle, P. Clem, M. Rodriguez, G. Brenneka, T. Dunbar, W. Hammetter

Motivation: The incorporation of the appropriate dopants into lead zirconate titanate (PZT) materials is necessary to enable dielectric, electro-optic and piezoelectric device development. For PZT thin films, La doping has been shown to enhance fatigue resistance and increased breakdown strength at high temperatures (125 °C). We have further investigated the effects of doping PZT using the lanthanide (Ln) cation series. The Ln series is ideal to develop a science-based understanding of the impact of dopant ionic size since (the cation size systematically decreases from La⁺³ to Lu⁺³ by ~ 0.17 Å). Larger ions were shown by EPR analyses to preferentially occupy the A-site of the perovskite lattice and act as donors. As ionic size decreased, the Ln dopants become amphoteric, exhibiting both A and B site occupation. With further reduction in ionic size, the lanthanide ions preferentially occupied B-sites and acceptor behavior was exhibited. A primary reason for investigating this under explored material system is the possibility of synthesizing PZT based films with superior polarization (P_r), dielectric constants (ε), fatigue, retention and breakdown performance.

Accomplishment: Due to the flexibility of Sandia's patented BRP route, we utilized this method to fabricate PLnZT films using standard spin-pyrolysis methods. The fresh PLnZT (4/30/70) precursor solutions deposited onto Pt-Si wafers were single-phase perovskite by X-ray diffraction. EPR characterization of solution-derived, Gd doped PZT gel particles indicated

that these materials define the boundary of donor - amphoteric behavior. Electronic testing of these films revealed some unusual trends. For the A-site dopants, as the size of the cation decreases P_r increases, and ε decreases. From Gd - Er, which are truly amphoteric, P_r and ε remain similar. As Ln radius further decreases there is a decrease in P_r and an increase in ε that is consistent with B-site acceptor doping. The leveling effect was noted for the cations that can occupy either the A- or B-sites (aliovalent). The hysteresis loops of these PLnZT doped materials are very square with high P_r and ε values. Donor doping reduces the number of oxygen vacancies in the PZT system, which reduces the number of electron trap sites, that pin domain walls and thus reduces switchable P_r (fatigue). As expected, the amphoteric dopants have improved fatigue performance over pure acceptor dopants. The performance for the Dy doped film shows no fatigue over a range of 10¹⁰ switching cycles, a substantial improvement over PLZT films.

Significance: This study has led to a better materials understanding of the effects that dopants have on the atomic structure and the related macroscopic properties of PZT films. Improved properties of the PLnZT films will enable new piezoelectric and nonvolatile memory technologies.

Contact: Tim Boyle, Ceramic Materials Dept., 1843
Phone: (505) 272-7625
Fax: (505) 272-7336
E-mail: tjboyle@sandia.gov

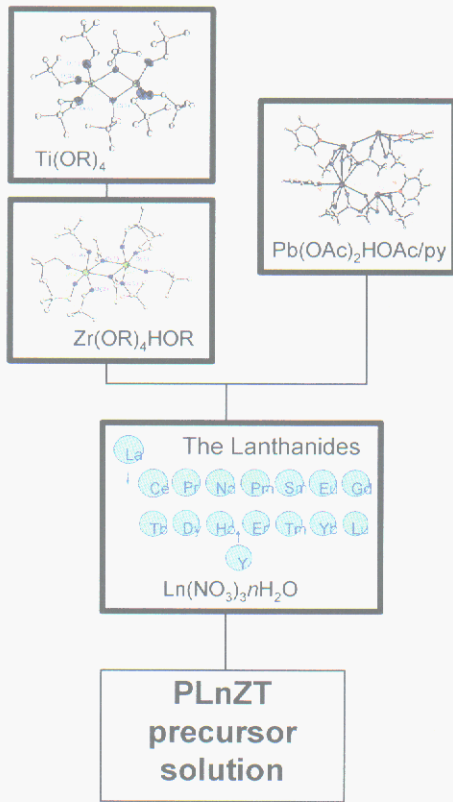


Figure 1. Schematic representation of BRP precursor solution synthesis.

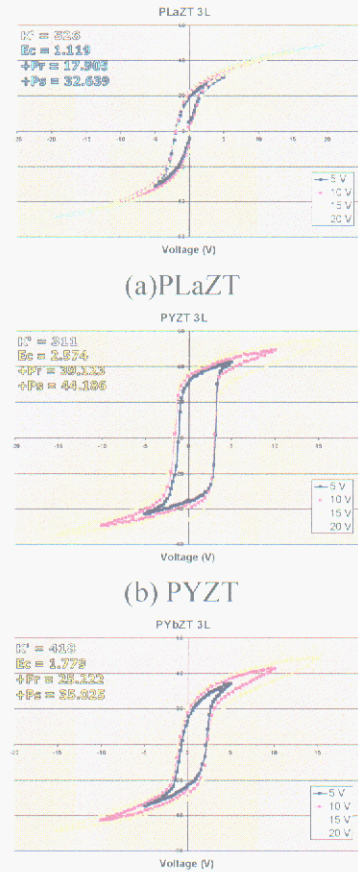


Figure 2. Hysteresis loops of various PZT materials.

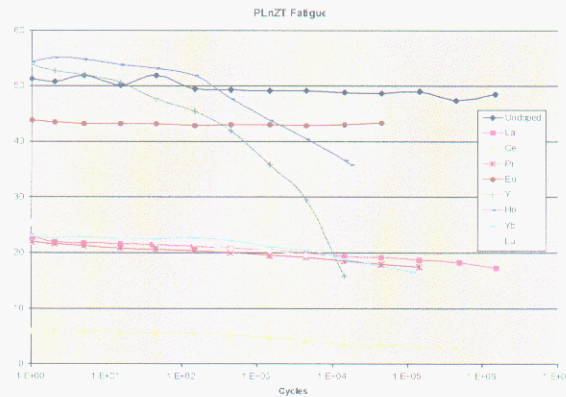


Figure 3. Fatigue testing results of aliovalent cation dopants.

Single-source Precursors to Nanoceramic Particles

M. R. Trujillo, T. J. Boyle, M. A. Rodriguez, T. J. Headley

Motivation: The study of complex nano-ceramic materials is of interest due to the unique physical properties expected for materials in this size regime. Ceramic oxide nanomaterials have a wide range of proposed applications. Simple ceramic systems have been extensively investigated but the more complex oxides have only recently been investigated. The routes to these complex nanoceramic materials are typically rather complex due to the necessary concurrent decomposition and similar solubility of the various precursors.

One way to circumvent these problems is to use a starting material that has the right cations in the appropriate stoichiometry. These single-source precursors will also greatly simplify in handling the starting materials. While there is a great deal of interest in these single-source precursors, little work has been proffered on using them to generate complex ceramic nanoparticles. This is most likely due to the difficulty in constructing controlled assemblages of alkoxides.

Accomplishment: We have synthesized and characterized a series of mixed metal alkoxide precursors using novel routes and compounds developed in our laboratory. We have used these precursors in a novel solution precipitation route developed in our laboratory to generate complex ceramic nanoparticles. The family of compounds developed have potential to be used for such systems as cathode materials such as LiCoO_2 and Li_5FeO_3 along with the dielectric materials BaTiO_3 , SrTiO_3 , $(\text{Ba,Sr})\text{TiO}_3$ (BST).

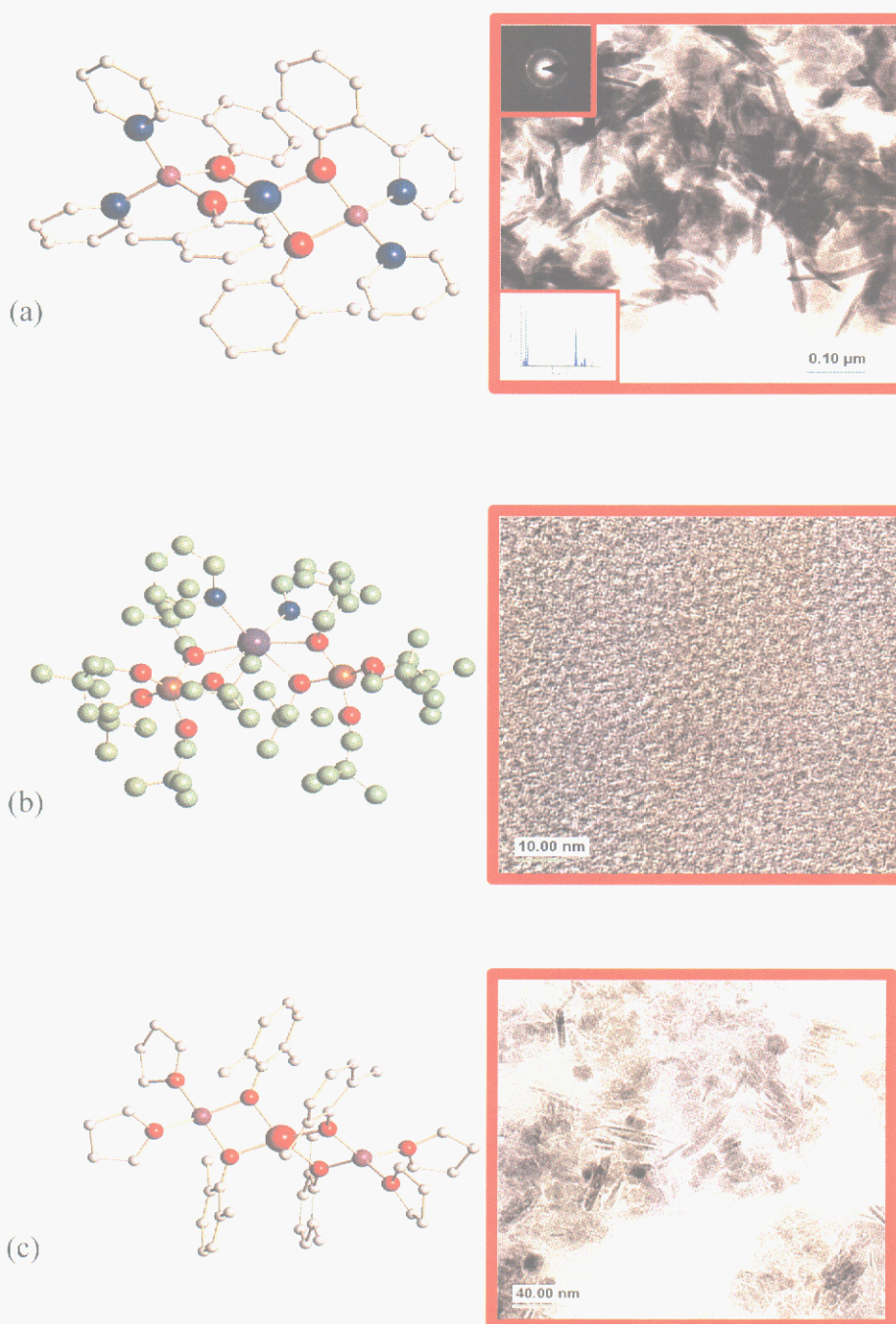
We have developed a novel solution mixture that utilizes the strong Lewis base, 1-

methylimidazole and water ($\text{MeIm:H}_2\text{O}$; 95:5) to act as the surfactant/oxidizer solution of a series of single-source precursors. Acceptable precursors are dissolved in a solvent (most often pyridine) and subsequently injected into a hot $\text{MeIm/H}_2\text{O}$ solution. We have been able to synthesize several families of novel mixed metal alkoxides which were used as precursors: (a) $[\text{CoLi}_2(\text{OAr})_4(\text{py})_2]$ (6 alternative aryloxide groups available), (b) $[\text{MTi}_2(\text{ONep})_{10}(\text{py})_2]$ ($\text{M} = \text{Sr, Ti}$), and (c) $[\text{Li}_2\text{Fe}(\text{OAr})_4(\text{THF})_4]$ (8 aryloxide derivatives available) for LiCoO_2 , BST-like, and Li_5FeO_3 -like materials. For (a) disk shaped 50 - 60 nm particles of $\text{Co}(\text{OH})_2$ were isolated, as verified by XRD, SAED, and TEM; For (b) 2-3 nm spherical particles were observed by TEM but were not crystalline (additional processing is necessary); (c) 15 -40 nm rods and disks were observed by TEM (additional characterization underway). Figure 1 shows the compounds and resultant nanoparticles.

Significance: We have demonstrated the utility of single-source precursors to produce nanoparticles of complex oxides. This will allow us to garner greater control over the final stoichiometry and simplify processing of complex ceramic oxide materials. This handle may allow us greater control over the crystallization behavior and morphology of the final material, necessary for the construction of nanodevices.

Contact: Tim Boyle, Ceramic Materials Dept., 1843
Phone: (505) 272-7625
Fax: (505) 272-7336
E-mail: tjboyle@sandia.gov

Figure 1. Ball and stick figures of single-source precursors: (a) $\text{Co}[(\mu\text{-oMP})_4\text{Li}(\text{py})_2]_2$, (b) $(\text{py})_2\text{Ba}[(\mu\text{-ONep})_4\text{Ti}(\text{ONep})_2]$, and (c) $\text{Fe}[\mu\text{-DMP}]_4\text{Li}(\text{THF})_2]_2$ that were dissolved in pyridine and then injected into a 1-methyl midazole:water (95:5) mixture at reflux temperatures. After 30 min., the reaction was allowed to cool to room temperature and then centrifuged. The insoluble fraction was re-slurried in hexanes and deposited onto a TEM grid. The images shown were obtained from these investigations.



Thin Film Dispenser Cathodes for Thermionic Micro-Devices

K. R. Zavadil

Motivation: Several technologies require a method of integrating a thin, electron emissive film into an energy conversion device. Examples include miniature thermionic diodes used as small-scale power sources, high frequency microwave generators (klystrons) for particle acceleration or directed energy applications, traveling wave tubes for space-based signal amplification, and high current, optically triggered switches. High flux, state-of-the-art emitters are dispenser-style structures based on BaO impregnation into a porous W matrix. This type of macro-cathode is not amenable to incorporation into a micro-device. This work focuses on developing methods for producing thin film cathodes that can be integrated into the fabrication of thermionic micro-devices.

Accomplishment: We demonstrate a method of producing electron emissive films that mimic the structure and properties of a macro-dispenser. These films are essentially micro-dispensers that are deposited as monolithic structures using radio frequency (rf) sputtering. These films are composed of alternating layers of tungsten and a BaO:CaO:Al₂O₃ ternary oxide, which show up as light and dark bands in the cross-section electron micrograph of Figure 1a. When a film is heated to temperatures as low as 630°C, the tungsten reacts with the ternary oxide forming free Ba and a tungstate phase. Voids are generated in the film as a result of this reaction and the coalescence of the tungsten layers into particles, as seen in the micrograph of Figure 1b. X-ray diffraction data, as see in Figure 2, shows the appearance and evolution of these bulk compositional changes with annealing.

Barium transport to the film surface is facilitated by these bulk film changes. The presence of barium results in a dipole, or positive locus of charge, extending from the surface that lowers the work function and results in electron emission. Placing an electrode opposite the heated film and applying a potential difference can study emission characteristics. The results of swept potential measurements are shown in Figure 3 in a Schottky format to highlight the characteristics of the cathode. The films show a sharp transition at low potentials to saturated current density indicating these films possess a uniform, low work function.

Our current work is aimed at tailoring film properties through the original film design. Sputter deposition allows a great deal of variability in bulk film constituents, layer thickness, deposition conditions and terminating constituents. We are studying the kinetics of phase coarsening and microstructural

Significance: Our work demonstrates that the mechanisms used for Ba generation and transport in macro-dispenser cathodes can also be built into thin film structures. These films will enable the monolithic fabrication of a variety of thermionic micro-devices.

Contact: Kevin R. Zavadil, Corrosion, Electrochemistry and Cleaning Dept., 1832
Phone: (505) 845-8442
Fax: (505) 844-7910
E-mail: krzavad@sandia.gov

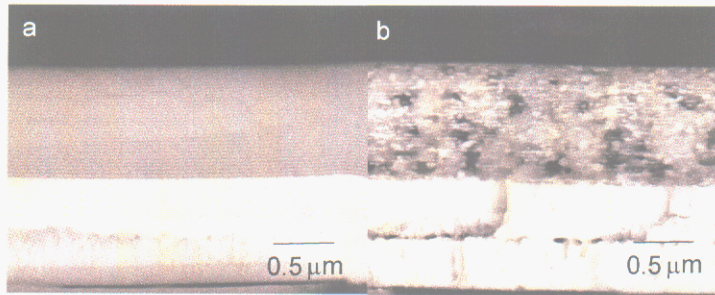


Figure 1. Backscattered electron images of a 1 μm thick compositionally modulated film: a) as-deposited and b) annealed to 1300 K. The film appears in the upper portion of the micrograph (banded region) and is comprised of alternating 10 nm W (light) and 20 nm BaCaAlO_x layers (dark) with a 3.5 nm Re/2 nm Sc₂O₃ terminating layer (not visible). The thick bright bands below the modulated film are the metal electrode layers.

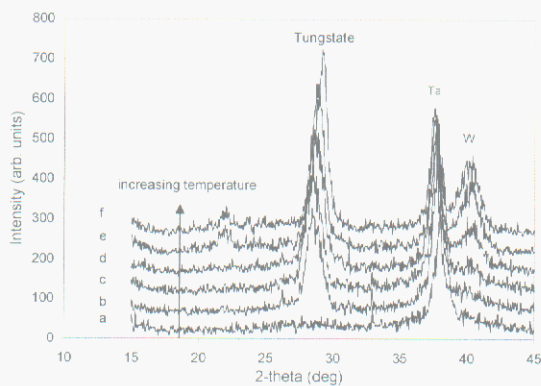


Figure 2. Grazing Angle (2°) Incidence X-ray Diffraction spectra of a 10 nm W/20 nm BaSrCaO_x modulated film as a function of annealing temperature – a) 298, b) 900, c) 1000, d) 1100, e) 1200, and f) 1300 K.

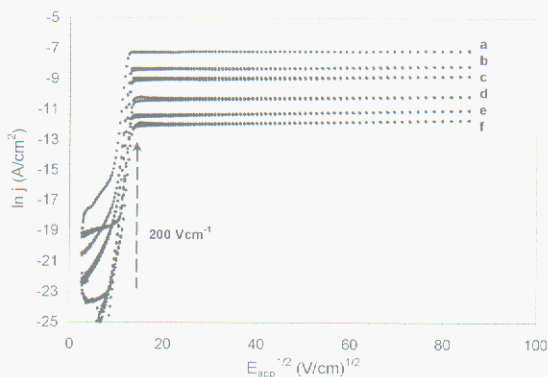


Figure 3. Schottky plot showing the variation in emission current from a 10 nm W/20 nm BaCaAlO_x modulated film with a 3.5 nm Re/2 nm Sc₂O₃ terminal layer as a function of applied field for various temperatures – a) 1061 K, b) 1003 K, c) 973, d) 939 K, e) 934 K and f) 921 K.

Automotive Lean-Burn NO_x Catalysis

J. E. Miller, T. J. Gardner, L. I. McLaughlin, D. L. Mowery, and R. S. Sandoval

Motivation: Lean-burn engines have been identified by U.S. automakers as the next major technological step in combustion engine design and fuel economy. By using more air during combustion, lean-burn engines yield better mileage and produce less carbon monoxide and unburned hydrocarbon pollutants than conventional gasoline engines. However, destruction of NO_x pollutants, which are produced by all engines, is more difficult in a lean-burn engine. Catalytic converters that were developed for conventional engines cannot be used for lean-burn engines. If a lean-burn engine is to become commercially viable, novel catalyst technologies are needed. Similar catalysts may also find application for compression ignition, direct injection (CIDI or diesel) engines, where highly oxidizing conditions in the exhaust stream demand similar advances in catalyst technology.

Accomplishment: Our initial goal was to develop hydrous metal oxide (HMO)-based catalysts to mitigate NO_x emissions in lean-burn engine exhaust. The flexibility of the HMO process chemistry allowed a wide variety of catalysts to be screened for activity in the selective catalytic reduction of NO_x via hydrocarbon reaction using materials in bulk powder form. We fabricated and tested promising catalyst compositions on small-scale cordierite monoliths using HMO coating and ion exchange techniques. The best HMO-supported catalyst systems were evaluated by scaling up the HMO-coating and ion-exchange processes to a full developmental size (110 cubic inch) catalytic converter (Figure 1). Tests of these prototype converters on a lean-burn engine dynamometer at Lockheed Martin Energy Systems Y-12 Plant showed that NO_x reduction activity rivaled a commercial benchmark catalytic converter. Total time from initial bulk screening to developmental

size catalytic converter fabrication was less than 2 years.

With the new Environmental Protection Agency (EPA) Tier II emission standards scheduled to be in place starting in 2004, we are now addressing new and potentially more efficient NO_x reduction options for lean-burn exhaust aftertreatment. We are investigating catalysts for use in the selective catalytic reduction of NO_x by urea (or NH₃). We are also engaged in more studies related to determining the mechanism of the selective catalytic reduction of NO_x over different catalyst materials with various reductants, and are conducting mixed catalyst and support studies designed to optimize lean-burn NO_x catalysts.

Significance: This effort involves a unique project team of multiple national laboratories, automakers, and catalyst suppliers. The overall program, which is sponsored by the DOE Office of Transportation Technologies, is facilitated by separate CRADAs between three national laboratories, Los Alamos, Oak Ridge, and Sandia National Laboratories, and the Low Emission Technologies Research and Development Partnership (LEP), which consists of General Motors, Ford, and DaimlerChrysler. The CRADA efforts are focused on the development and evaluation of new catalyst materials for reducing NO_x emissions.

This project received the 1996 Partnership for a New Generation of Vehicles Award for Technical Accomplishment. The Sandia project team also was awarded the 1999 National Laboratory CIDI R&D Award in recognition of outstanding achievement in R&D of lean NO_x catalysts for CIDI engine exhaust emission control. Three U.S. patents have been awarded for NO_x reduction by hydrocarbon technologies developed by Sandia.

Contact: James Miller, Chemical Synthesis and Nanomaterials Dept., 1846
Phone: (505) 272-7626
Fax: (505) 272-7336
E-Mail: jemille@sandia.gov

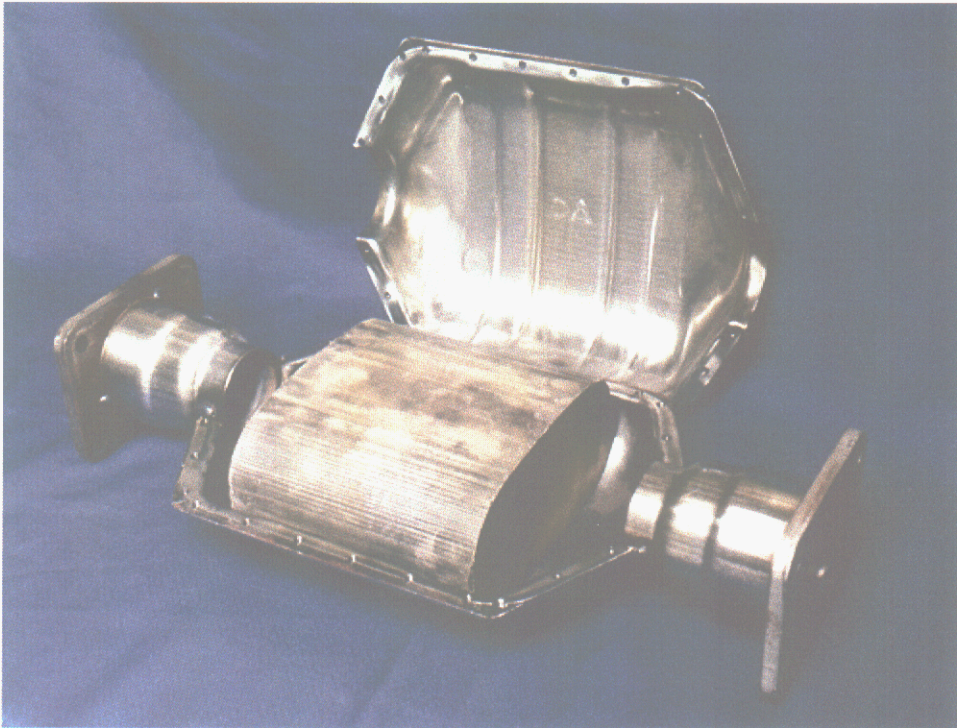


Figure 1. Sandia-fabricated full developmental size (110 cubic inch) catalytic converter in take-apart can assembly.

Homogeneous Catalysis Research at Sandia National Laboratories

R. A. Kemp, A.G. Hascall, and J. T. Moore

Motivation: The solutions to numerous catalytic problems lie in the rational design of very small arrangements of molecules. For example, the bulk metal catalysts used in many processes in the mid-1900's were inherently inefficient – due to their low surface areas only a small fraction of the metal was actually utilized. Chemists then invented supported catalysts, whereby small crystallites of the same metal were finely distributed upon high surface area supports. This process allowed a higher fraction of the metal to be used, thus improving activity and selectivity while reducing costs. Later, small molecular clusters of metal atoms were used in the deposition onto the catalyst support – this was a precursor to current nano-chemistry. Chemical promoters could then be added to these supported molecular clusters to improve catalyst performances further. However, it is possible to prepare even smaller architectures if one enters molecular design and control – the realm of homogeneous catalysis. In homogeneous catalysis, the active components of the catalyst are in solution, not in the solid phase. The design and control of the active site of the catalyst is limited only by a chemist's imagination and the ability to synthesize and isolate individual molecules.

Accomplishment: Sandia is a solid state-oriented laboratory and not normally associated with homogeneous catalysis. However, we have recently begun studies to understand two homogeneous processes of industrial interest. Firstly, we have been investigating the production of 1-alkenes via oligomerization of ethylene by inventing new catalysts for this reaction. We have isolated and

crystallographically characterized several new phosphine and carbene-coordinated nickel organometallic compounds (Figure 1). We anticipate the differences in steric and electronics around the active site will lead to altered catalytic chemistry, and particularly after deposition of these homogeneous catalysts onto a porous support - a different olefin distribution. This could significantly impact the economics of this world-scale process. Secondly, we are chasing a "Holy Grail" of catalysis – can we directly epoxidize 1-alkenes with oxygen in a catalytic homogeneous process that is environmentally friendly? We have postulated a possible catalytic cycle (Figure 2) in which all catalytic steps have literature precedence, albeit with different metal/ligand sets. Our task is to find a singular system that will perform every step of the reaction. In conjunction with Professor Karen Goldberg at Washington, we have initially chosen to prepare complexes of phosphine pincer-type ligands with late transition metals (platinum and rhodium) as we believe that early transition metals will prove too oxophilic for the cycle to occur.

Significance: We are adding homogeneous catalysis to the areas of chemical expertise within Sandia National Laboratories. If our projects are successful in these two areas of industrial interest, we will extensively impact Sandia's thrust area in energy science, as well as significantly impact the worldwide production of valuable commodity chemicals.

Contact: Rick Kemp, Chemical Synthesis and Nanomaterials Dept., 1846
Phone: (505) 272-7609
Fax: (505) 272-7336
E-mail: rakemp@sandia.gov

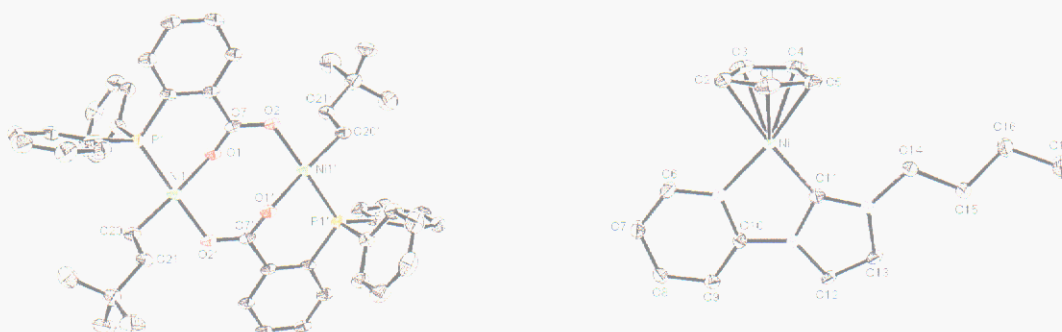


Figure 1. Thermal ellipsoid plots and molecular structures of Ni-based organometallics used as models for the commercial Ni-catalyst used in the production of 1-alkenes.

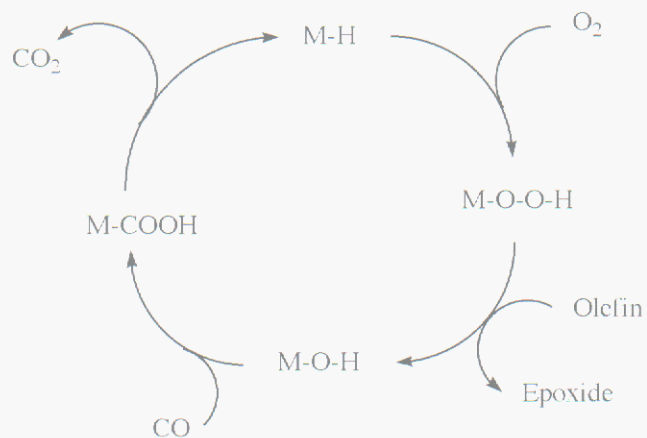


Figure 2. A possible catalytic mechanism for the direct epoxidation of alkenes beginning with a metal hydride catalyst. All steps have some level of precedence in the open literature; however, not using the same metal/ligand set.

Novel Monolithic Supports for Catalytic Combustion and Particulate Trapping

J.E. Miller, R.M. Ferrizz, J.N. Stuecker, J. Cesarano III

Motivation: Diesel particulate emissions (soot) have been recognized as a global problem, and current technologies cannot meet the projected U.S. regulations. Likewise, NO_x formation from methane combustion in gas-turbine electric power plants is becoming a significant environmental concern, especially considering estimates that 1900 additional power generating facilities will need to be brought on line in the U.S. through the next 20 years. Uniting these two problems is the fact that they can both be addressed through the use of state-of-the-art, in-line ceramic filters or supports incorporating an appropriate catalytic function.

We are utilizing a novel direct ceramic fabrication technique (robocasting) to produce 3-dimensional ceramic monoliths, e.g. meshes with controlled porosity in all dimensions but no line-of-sight pathways, that can function as catalyst supports for methane combustion, and self regenerating filters for diesel particulates. Compared to the traditional 2-dimensional "honeycomb" structured extrudates, our 3-dimensional structures can promote higher mass transfer rates to catalytic surfaces while maintaining high surface to volume ratios, predictable permeability and low pressure drop. In addition, robocasting allows for greater flexibility in materials, possibly alleviating problems related to thermal shock and chemical degradation.

Accomplishment: We have compared mass transfer in 2-D honeycomb geometries to 3 D geometries by combusting methane and CO over both Pt- and hexaaluminate-loaded monoliths as well as a monolith composed entirely of a catalytic hexaaluminate. Our 3 D supports have shown significant improvements in mass transfer with relatively small penalties in pressure drop. The 3-D structures consist of rods assembled in a face-centered-cubic (FCC) type arrangement

such that no direct line-of-sight pathways exist down the length of the monolith (Figure 1). Rod diameter and spacing were typically chosen such that the resultant monolith would have an identical geometric surface area to that of the 2-D sample.

A representative data set is presented in Figure 2. A considerable improvement in activity can be seen in the robocast sample (b), compared to the 2-dimensional sample (a). In fact, the measured conversion is almost identical to that predicted from kinetic data (i.e. no mass transfer limit) obtained from the powder sample. Conversely, the conversion is minimal in the straight-channel sample up to 800°C, when gas-phase reaction becomes significant. The difference in activity of the two samples is attributed to an increased turbulence in the flow resulting from the complex geometry of the robocast support. This conclusion is supported by computational-fluid-dynamics modeling of the flow field for straight-channel and FCC-like geometries. Curve (c) illustrates methane conversion for a robocast sample that was synthesized entirely from BaMn-hexaaluminate powder. This result seems very promising when one considers that this robocast hexaaluminate monolith can potentially be used as a support for other, more active combustion catalysts.

Significance: We are currently in the process of quantifying the improvements in mass transfer provided by turbulent flow in the 3-dimensional supports. These improvements could offer advantages such as maximizing conversions at high flow rates while minimizing the use of precious metals. The use of robocast lattices as diesel particulate filters is yet unproven, however, the incorporation of a catalyst for combustion of particulates may demonstrate another use for these three-dimensional lattice structures.

Contact: Jim Miller, Chemical Synthesis and Nanomaterials Dept., 01846
Phone: (505) 272-7626
Fax: (505) 272-7336
Email: jemille@sandia.gov

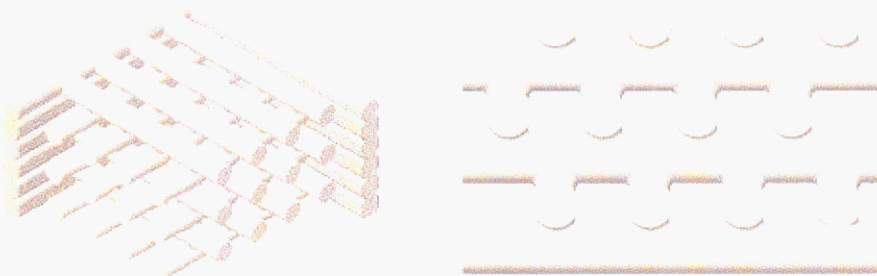


Figure 1. Isometric and side-view representations of FCC lattice structure.

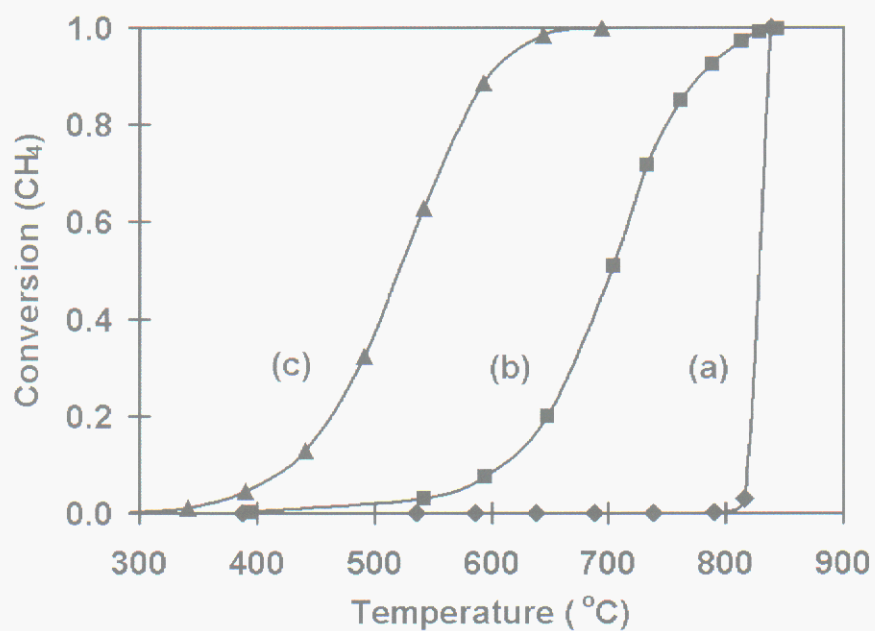


Figure 2. Methane conversion over (a) honeycomb and (b) robocast monoliths loaded with 0.4 g $\text{BaMn}_2\text{Al}_{10}\text{O}_{19-\alpha}$ (space velocity $\sim 10^4 \text{ hr}^{-1}$). Curve (c) is conversion over a robocast monolith fabricated from $\text{BaMn}_2\text{Al}_{10}\text{O}_{19-\alpha}$ (space velocity $\sim 2.4 \times 10^4 \text{ hr}^{-1}$).

Coinage Metal Nanoparticles from Mesityl Derivatives

S. D. Bunge, T. J. Boyle, T. J. Headley

Motivation: Developing a fundamental understanding of the processes that govern nanocrystalline growth, and organization, is necessary for the development of devices that exploit the unique properties that these materials promise. We have focused on a variety of ways to assemble these particles and the interactions that occur between similar and different nanoparticles. In order to realize this, it is necessary to generate high quality and monodispersed particles.

Chemical vapor deposition (CVD) is an area of research that has garnered a considerable amount of knowledge on the design of precursors for the formation of thin films. Since colloids can be considered as “soluble surfaces” it is reasonable to transfer the concepts used for CVD precursors to solution-based approaches (i.e., the synthesis of metal alkyls, metal alkoxides, metal amides, etc.).

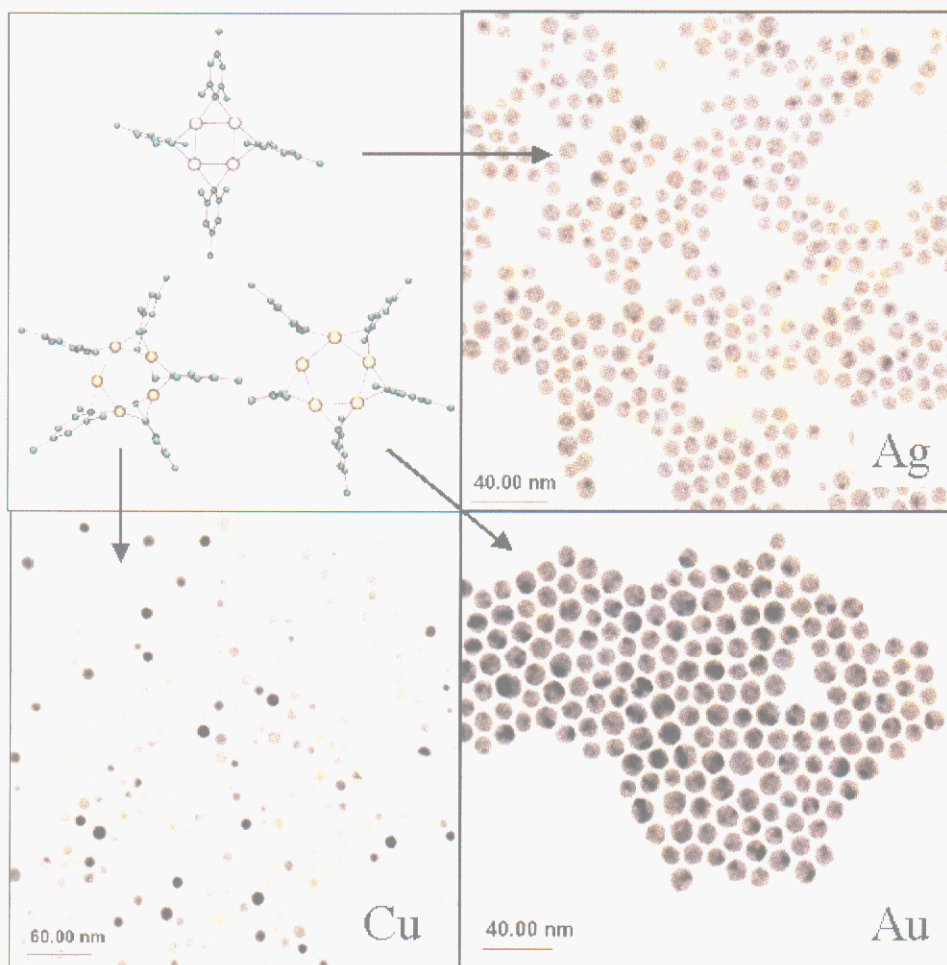
For our initial investigations, we designed a reaction system that utilized a coordinating solvent for the synthesis of nanoparticles via pyrolysis of a molecularly designed precursor. Of the available precursors, the mesityl (mesityl = 2,4,6-Me₃C₆H₂) derivatives are ubiquitous and appear to have the properties of interest. That is, they are easily synthesized, decompose cleanly at relatively low temperatures, and are soluble in standard solvent. This system not only takes advantage of the concepts of CVD, but offers control over both parameters that dictate the features of nanoparticles, the starting material, and reaction system.

Accomplishment: A novel anhydrous route for the synthesis of amine capped Cu⁰, Ag⁰, and Au⁰ nanoparticles was developed via the novel use of polynuclear mesityl derivatives. The structure of [Cu(μ-mesityl)]₅, [Ag(μ-mesityl)]₄ and [Au(μ-mesityl)]₅ were previously determined and are shown in Figure 1. All of the reaction processes were handled under an argon atmosphere to prevent any uncontrolled hydrolysis. The crystalline precursors were dissolved in octylamine and subsequently injected into a heated solution of hexadecylamine. The reaction was only heated for a short time and then rapidly cooled. The resulting solution was centrifuged and the insoluble material was redispersed in ethanol and deposited onto a TEM grid and allowed to dry (this was performed under an atmosphere of argon). The UV-Vis exciton peaks were in agreement with the size of the particles observed in the TEM images. The resulting nanoparticles generated were oxide-free as determined by XRD, SAED, and TEM.

Significance: This synthetic route greatly simplifies and improves the quality of coinage metal nanoparticles. The oxide free surface of Cu⁰ is typically difficult to obtain through other synthetic routes. With these clean coinage nanoparticles, we can now investigate functionalization for labeling studies, controlled construction of 3-D devices, and catalytic synergistic studies. Further we are exploiting this route to make alloys for studies concerning more complex nanoparticles.

Contact: Timothy Boyle, Ceramic Materials Dept., 1843
Phone: (505) 272-7625
Fax: (505) 272-7336
E-mail: tjboyle@sandia.gov

Figure 1. The mesityl (2,4,6-Me₃C₆H₂) derivatives of Cu⁰, Ag⁰, and Au⁰. Shown in the box on the left are dissolved in octylamine and then rapidly introduced into hexadecylamine at reflux temperatures. The resulting solution is centrifuged and the insoluble fraction re-dispersed in ethanol and dropped onto a TEM grid. The resulting TEM images are shown below.



Development of Low Temperature Conversion Silver Conductors for Deposition on Conformal Polymeric Surfaces

N. S. Bell

Motivation: The goals of the Mesoscopic Integrated Conformal Electronics (MICE) program sponsored by DARPA require the development of electronic materials (conductors, dielectrics) that can be deposited on polymeric substrates to form operating devices. This opens the door to a new class of material systems, which can be deposited as liquids or suspensions and reacted to give properties at temperatures below 400°C. Conventional Low Temperature Co-Fire materials are reacted at 850 to 1000°C.

Strategies for forming conductor elements for circuitry have focused on adding a silver salt precursor to a suspension of micron sized silver spheres. The approach uses the reaction of the silver salt at elevated temperatures to “weld” the particles into a conductive network. The detrimental factor in this approach relates to the material that can be deposited at the particle contacts and the interconnectivity of the particles. The neck region between surfaces acts as a bottleneck to conduction. Based on experimentally achievable levels of precursor and assuming a face centered cubic packing of uniform spheres, the best value of resistivity is expected to be 6x bulk.

We have taken the approach of adding nanoparticle silver to micron sized silver particles to achieve a conductive particle network at low temperature. The decreased in melting temperature caused by the presence of high curvature nanoparticles generates a low temperature reaction (necessary for writing on polymeric substrates). Particle interconnection is caused by reaction of nanoparticles to “weld” the micron-sized particles together.

$$T_m = T_{\text{planar}} - \frac{2\gamma V^s}{\Delta S} H$$

Accomplishment: Shown in the Figure are the micron size particles with nanoparticles concentrated at particle necks. This behavior indicates that the nanoparticles are dispersed in the liquid medium, and the capillary action of drying solvent draws the small particles to high curvature necks between the micron-sized particles. The benefit of this method is obvious – nearly all the reactive components are concentrated at particle junctions. At the reaction temperature (<325°C), these particles form strong necks between the larger particles to form a conductive network. The residual porosity stems from the particle packing of the micron sized spheres, and may be improved by using a higher solids loading. The conductive networks shown here have resistivities of ~ 3x bulk.

Significance: The use of nanoparticle silver as a reactive element has two primary benefits. First, the amount of silver that acts as a reactive element is significantly increased over the use of a silver salt precursor. Second, the reactive component is concentrated in regions of connectivity rather than distributed over the surface area of the particle assembly. The rheology, reactivity, conductivity and stress development at reactions for these compositions are being refined for direct writing applications.

Contact: Nelson Bell, Ceramic Materials Dept., 1843
Phone: (505) 844-6234
Fax: (505) 844-9781
E-mail: nsbell@sandia.gov

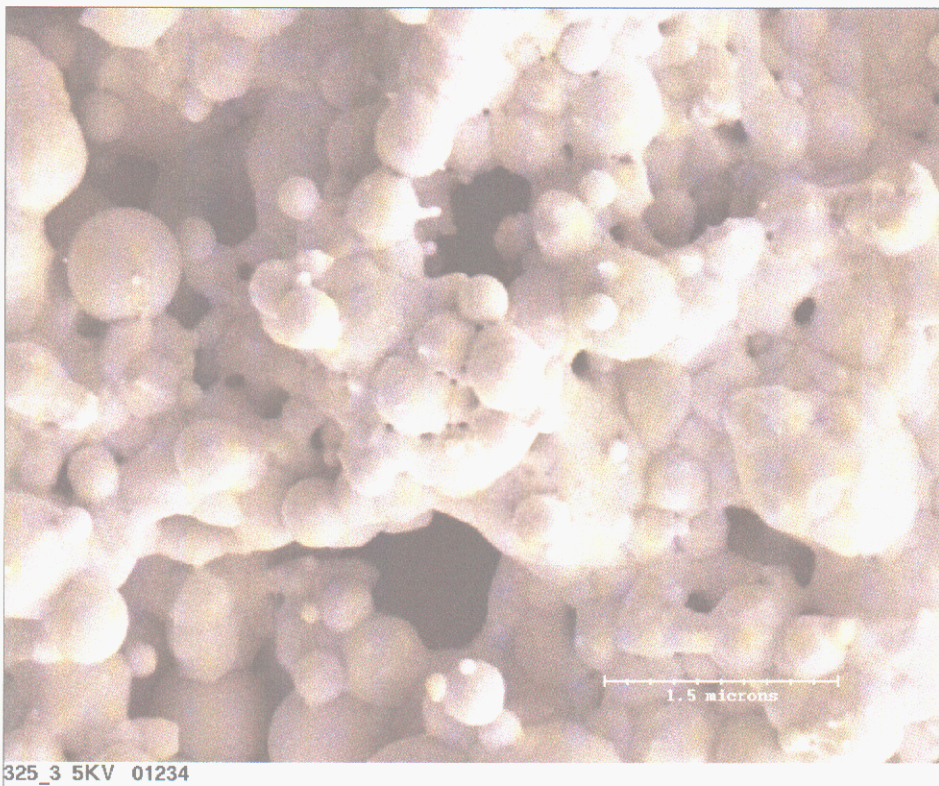
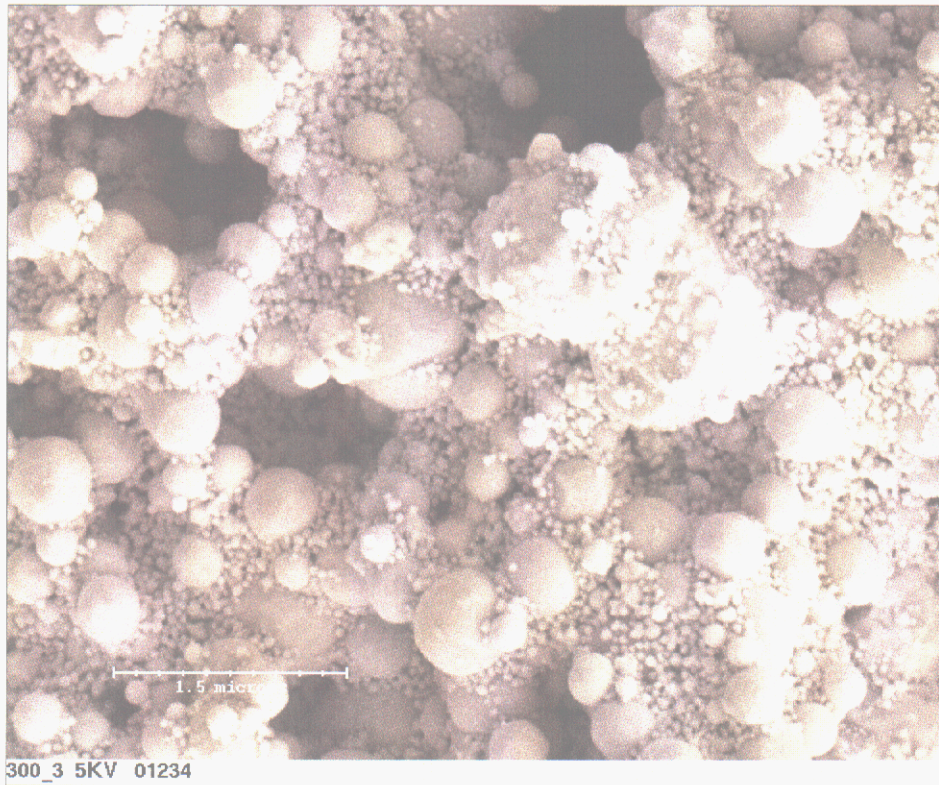


Figure 1. Paste microstructure after firing at 300 and 325 °C for 15 minutes.

Stagnation of Grain Growth in Polycrystalline Thin Films

E. A. Holm, A. L. Giermann, and G. N. Hassold

Motivation: Polycrystalline thin films are utilized in a variety of microelectronics applications. Although the microstructures of these films determine their properties, the mechanisms of microstructural formation are not understood. For example, in a wide variety of materials grain growth ceases when the average grain diameter approximates the film thickness. While grain stagnation has long been attributed to grain boundary grooving, recent experimental observations contradict the predictions of this model. In this study, we utilized computer simulations to test the classical grooving model, as well as alternate stagnation models.

Accomplishment: Grain growth was simulated using a three-dimensional kinetic Monte Carlo Potts model. The system was a film, periodic in the x and y dimensions and finite in thickness. Since stagnation is observed only in columnar grain structures, the initial microstructure was comprised of small, columnar grains. This system was evolved by grain growth incorporating various model assumptions.

When grain boundaries at the film surface have a low mobility due to thermal grooving, grain growth slows but does not stop, as shown in Figure 1(a). Because the growth rate scales simply with the average boundary mobility, no additional stagnation mechanisms become active as grooves slow. In agreement with experiments, boundaries form cylindrical sections and appear flat in cross-section; the catenoidal grain shapes predicted by theory do not occur, as shown in Figure 1(b). If grain triple junctions have low mobility due to grooving or other mechanisms, triple junction drag causes grain vertex angles to deviate from equilibrium. However, as shown in Figure 2, the curvature per grain boundary, thus the driving force for growth, remains constant, so

again stagnation does not occur. When grain triple junctions have a low energy due to a special crystallographic structure, the system may disorder to maximize triple junction formation. While grain growth formally stops in this case, the final ‘stagnant’ structure is fine-grained and equiaxed, not columnar as observed in experiments. Finally, if certain boundaries attain a low-energy crystallographic structure, these boundaries may be unable to move without disrupting that structure. Such ‘frozen’ boundaries can stagnate grain growth, as shown in Figure 3(a). However, the stagnant grain size exhibits a power law dependence on the probability of forming a frozen boundary [Figure 3(b)], which varies with both material system and with crystallographic texture. Thus, frozen boundaries are not likely to cause the universal stagnation behavior observed in experiments.

Significance: None of the tested models, including the classical grooving mechanism, could account for the experimentally observed characteristics of stagnated polycrystalline films. While this negative result creates uncertainty, it also provides opportunity. Thermal grooving, long the supposed stagnation mechanism, arises from intrinsic surface and interface energies, so cannot be eliminated. However, if stagnation actually arises from an extrinsic mechanism, such as solute drag, then grain growth can be controlled via process and materials design. By tailoring the stagnant grain structure, we may control the performance of metallic films in applications as diverse as microcircuit metallization lines and LIGA micromechanical components. [LIGA is a German acronym for lithography (Lithographie), electrodeposition (Galvanoformung) and molding (Abformung).]

Contact: Elizabeth Holm, Materials & Process Modeling & Computation Dept., 1834
Phone: (505) 844-9781
Fax: (505) 844-7669
E-mail: eaholm@sandia.gov

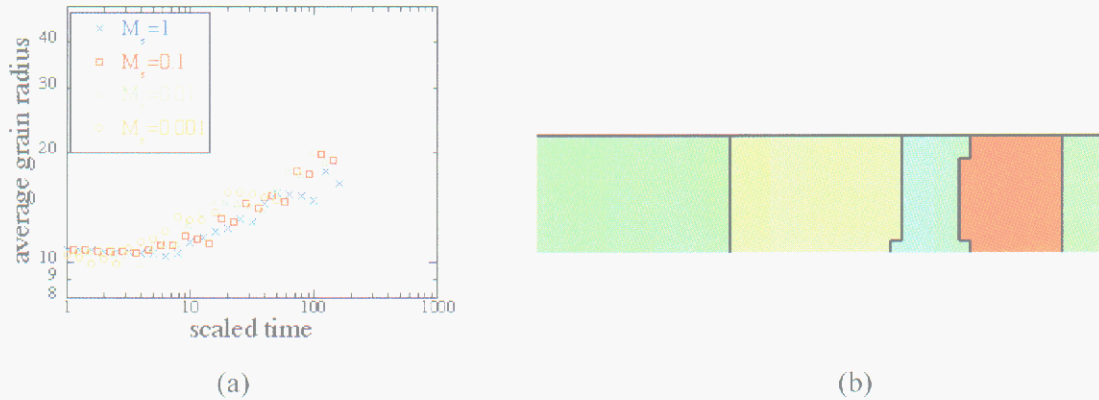


Figure 1. Grain growth in a thin, polycrystalline film when thermal grooving slows surface boundaries. (a) Contradicting classical theory, growth does not stagnate, and growth rate scales simply by average boundary mobility. (b) Cross-sections of films indicate that boundaries are cylindrical (not catenoidal) during grain growth.

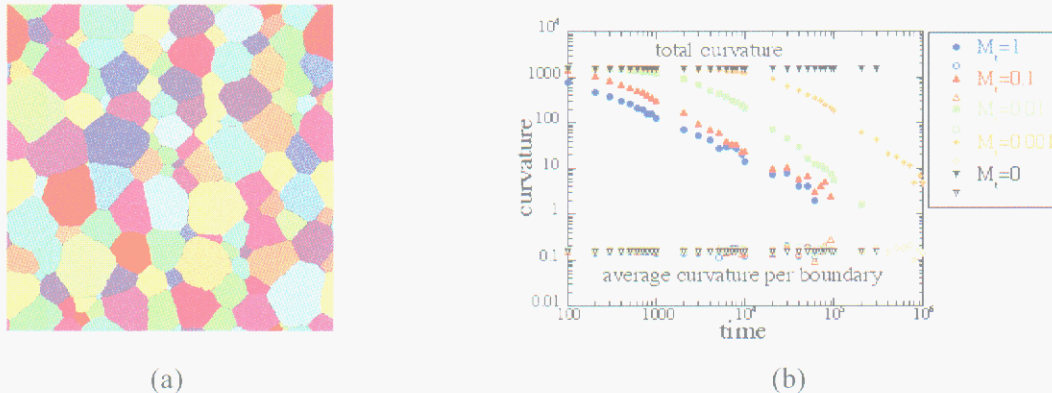


Figure 2. Grain growth in a thin, polycrystalline film when grain triple junctions have low mobility. (a) Plan-view of film microstructure appears normal, except that triple junction angles deviate from the 120° equilibrium angle. (b) While the total boundary curvature in the system (solid symbols) decreases as grains grow, the average curvature per boundary (open symbols), thus the driving force for growth, remains constant, so stagnation does not occur.



Figure 3. Grain growth in a thin, polycrystalline film when certain 'frozen' boundaries cannot move. (a) Plan-view of stagnant grain structure, with frozen boundaries shown as dark lines. (b) The stagnant grain size has a power-law dependence on the probability of forming a frozen boundary.

Superconducting Wires by Chemical Solution Deposition

P.G. Clem, J.T. Dawley, J.A. Voigt, D.L. Moore, M.P. Siegal, D.L. Overmyer

Motivation: A new architecture for high current density superconducting wires, termed 2nd generation coated conductors, has been developed under the Department of Energy's Superconductivity Program for Electric Systems. The ultimate goal of the program is fabrication of superconductor-based wires for high magnetic field (1-10 Tesla) and current density (10^4 - 10^6 A/cm²) applications, at a cost of \$10/kA-m, competitive with the cost of copper. The coated conductor wires possess performance advantages for a number of technologies, including higher resolution MRI and NMR machines, more efficient electric motors, and loss-free electrical power transmission. In the current work, metal tapes up to km lengths may be dip coated with solution precursors and annealed to deposit YBa₂Cu₃O₇ (YBCO) films with current densities up to 1.3 MA/cm² at liquid nitrogen temperature (77K). The method may find application for high throughput (1000 km/year) production of superconducting wires.

Accomplishment: Chemical solution deposition (a.k.a. sol-gel or metal-organic decomposition) has been used at Sandia to develop the first *all solution deposited* 1 MA/cm² current density coated conductor architecture: YBCO/SrTiO₃/Ni tape. The solution deposition method enables coating at 3-10 cm/s, or > 1000 km/year. Novel precursor chemistries have been developed to enable rapid film deposition, solvent removal and crystallization, toward industrial production rates.

In particular, methods of producing micron-thick YBCO coatings in fast (minutes) anneal times are under development. Currently, the processes are being scaled up in conjunction with Oak Ridge National Laboratories, and coated conductor technical details are being jointly studied in research projects with Oxford Superconducting Technologies, American Superconductor Corporation, and MicroCoating Technologies.

Significance: Solution deposition methods are a potentially low cost (~\$2/kA-m) and high throughput method of fabricating 2nd generation coated conductor wires. The current developments suggest promise for replacing existing metal and silver/BSCCO conductors in MRI, high current power conduits, and motor windings with a lower cost, higher-performance product.

Contact: Paul Clem, Microsystems Materials, Tribology & Technologies Dept., 1851
Phone: (505) 845-7544
Fax : (505) 844-9781
E-mail: pgclem@sandia.gov

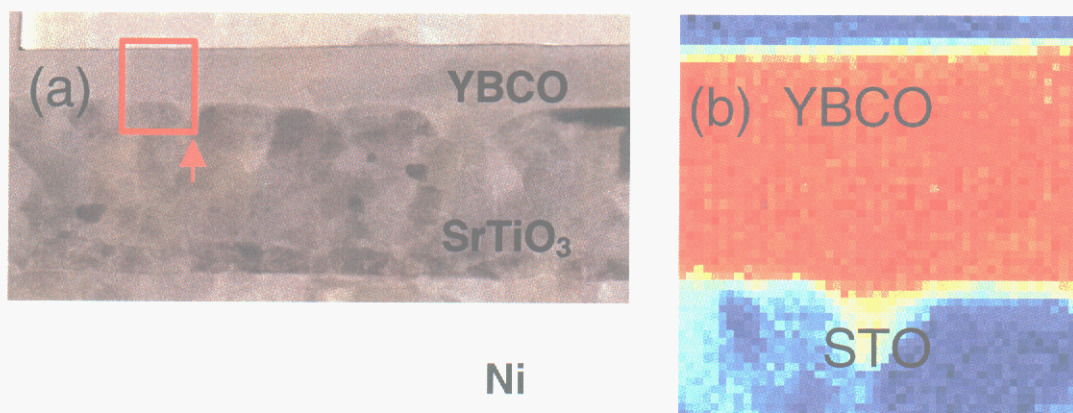


Figure 1. (a) Transmission electron microscope (TEM) image of YBCO/SrTiO₃/Ni superconducting composite, which demonstrates MA/cm² critical current density. (b) TEM compositional map at a ~1 nm² scale, showing YBCO compositional uniformity on an SrTiO₃ (STO) underlayer.

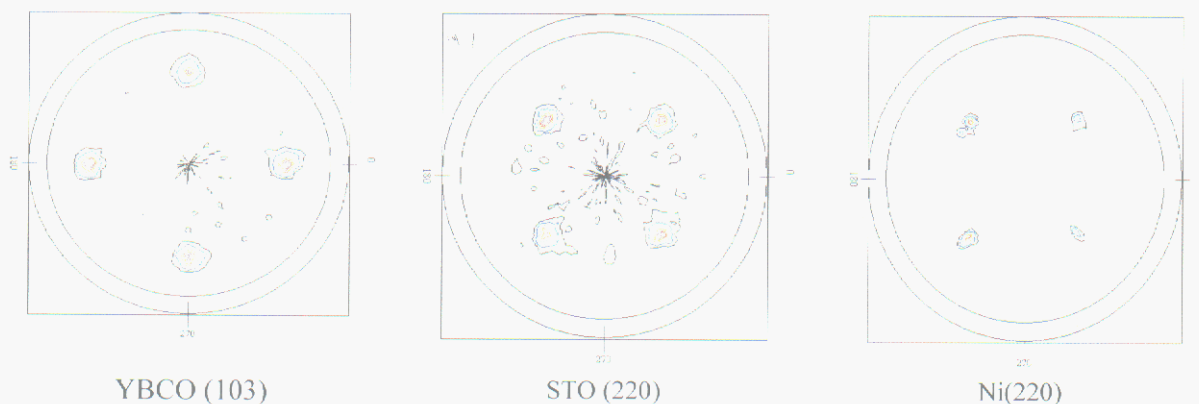


Figure 2. X-ray pole figures of the Ni substrate and solution deposited SrTiO₃ and YBCO coatings, demonstrating epitaxial deposition and biaxial alignment, necessary to achieve high superconducting current density. Development of such biaxial texture without need for vacuum deposition equipment may enable high throughput manufacturing.

Molecular Modeling of Polyolefins using Theory and Simulation

J. G. Curro and G. S. Grest

Motivation: Polyolefin polymers represent the largest and most important class of polymers in terms of volume of production. Even though these polymers consist of only single bonded carbon and hydrogen atoms, they have a wide range of properties that depend sensitively on the molecular architecture. Recent advances in polymer synthesis using metallocene catalysts now give the polymer chemist unprecedented control over the molecular weight, chain architecture, and stereochemistry of polyolefin macromolecules. We have developed computational tools that can help guide the synthesis of new polyolefins with optimized properties.

Accomplishment: Several years ago J. G. Curro and K. S. Schweizer developed a theoretical approach for describing the equilibrium structure and properties of amorphous polymers. This theory, the Polymer Reference Interaction site Model or PRISM theory, is based on an extension to polymers of liquid state methods originally developed for atomic and small molecule fluids. The essence of the theory is that the complex, multiple chain problem is replaced by the much simpler single chain problem. In this work we have written a general PRISM code that solves the PRISM nonlinear integral equations self-consistently with the single chain Monte Carlo simulation. This code gives a computationally tractable description of polymer liquids and polymer alloys using realistic models that reflect true chain architecture. In order to benchmark the accuracy of the ability of the theory to describe the packing of the macromolecules, we performed PRISM

calculations and exact Molecular Dynamics (MD) calculations for a range of polyolefin liquids using the same force fields and molecular architecture in both the theory and MD simulations. In Figure 1 we show a comparison between PRISM computations and MD simulation for the intermolecular packing of polyisobutylene, a polyolefin used extensively in o-rings and seals in Sandia applications. The packing is described by the six intermolecular pair correlation functions between CH₃, CH₂ and C groups making up the polyisobutylene macromolecules. It can be seen that the agreement of the theory, while not completely quantitative, certainly captures the essence of the intermolecular packing.

Significance: The PRISM code allows one to study a wide range of polyolefins with various molecular architectures. One can also study the miscibility and phase behavior of polyolefin alloys: a topic of considerable commercial interest. As an illustration, in Figure 2 we show the heats of mixing of two polyolefin blends calculated from PRISM theory. The positive heat of mixing seen for a blend of isotactic/syndiotactic polypropylene indicates a phase separating mixture suggested from experiment. The negative heat of mixing of head-to-head polypropylene and polyisobutylene indicates a miscible mixture observed from neutron scattering experiments.

Contact: John Curro, Materials & Process Modeling & Computation Dept., 1834
Phone: (505) 272-7129
Fax: (505) 272-7336
E-mail: jgcurro@sandia.gov

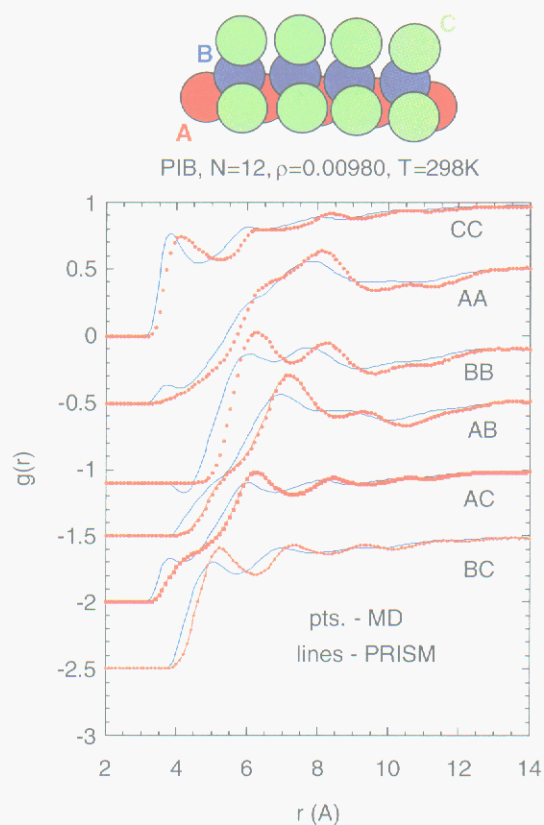


Figure 1. Comparison of PRISM theory and MD simulation for polyisobutylene (PIB) at 298 K.

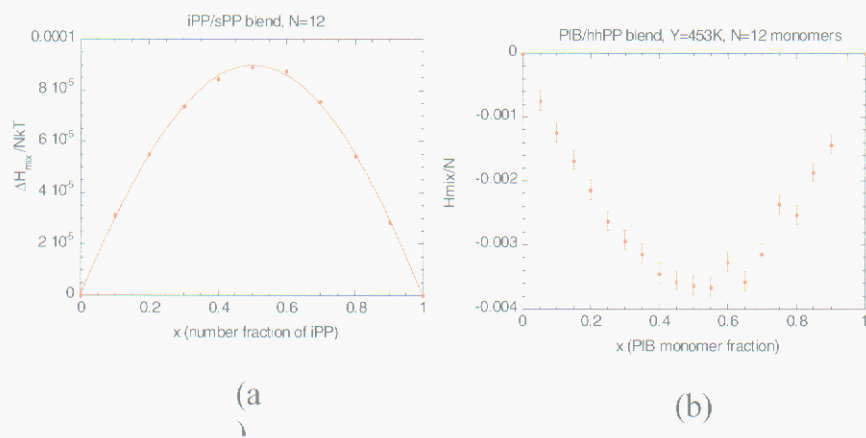


Figure 2. (a) Heat of mixing of the isotactic/syndiotactic polypropylene (iPP/sPP) blend. (b) Heat of mixing of the polyisobutylene (PIB) and head-to-head polypropylene (hhPP) blend.

Reformulated Sticky Foam for Non-lethal Deterrent and Access Delay Barriers

E. M. Russick

Motivation: Sticky Foam is a unique category of foam developed as a dispensable barrier to provide deterrence and access delay for DOE security applications. Sticky Foam can be dispensed through a nozzle or through the sudden rupture of a container to yield a very sticky foamed material that expands up to forty times its packaged volume. It is a tenacious, difficult to defeat non-lethal barrier which can be used to deter intruders and delay access to secure installations and equipment. Figure 1 shows a test where Sticky Foam is used as a deterrent to protect equipment from an intruder. Numerous classified and unclassified Sticky Foams have been developed for a variety of applications. An important Sticky Foam formulation used in some security applications contains a proprietary aromatic rubber processing oil that is no longer commercially available due to the supplier's decision to no longer supply aromatic processing oils primarily because of toxicity concerns. Due to the importance of this Sticky Foam formulation, a new processing oil had to be identified as a replacement material in a reformulated foam while providing the desirable properties of the original formulation.

Accomplishment: A new Sticky Foam formulation has been developed with a replacement for the commercially unavailable processing oil. The new formulation provides properties resulting in even greater access delay characteristics. A large number of processing oils were investigated including paraffinic, naphthenic, aromatic, and synthetic oils. Solubility of the oils with the other foam constituents, and material properties including foam stability, expansion ratio, modulus, and viscosity were used as criteria for selecting

potential replacement candidates. It was found that the paraffinic oils were not soluble in the other Sticky Foam ingredients and some of the naphthenic oils were marginally soluble. The best performing oil by far was a new aromatic rubber processing oil that will be commercially available indefinitely. The Sticky Foam resin with the replacement oil had virtually the same modulus as the original Sticky resin. A plot of shear modulus versus temperature for the resins is shown in Figure 2. With the new oil, the Sticky Foam had the same expansion ratio (i.e., foam density) as the original formulation and actually had significantly better foam stability which is a measure of the time that the foam structure remains intact before the cells coalesce resulting in the collapse of the foam. Additional testing is planned to further characterize the new Sticky Foam formulation for use as a non-lethal deterrent in important security applications.

Significance: This reformulation of Sticky Foam will allow for the continued production of the material for critical security applications in DOE. It has also resulted in a significant improvement in foam stability that will enhance the performance of the material as a non-lethal barrier to deter intruders from accessing secure installations and equipment. What has been learned about the enhancement of foam properties in this reformulation effort may assist in future reformulation efforts to bring about improvements in other Sticky Foam formulations. Sandia is currently in the process of transferring this new formulation to Honeywell, KCP and working with them to scale up to larger batch sizes and eventually for large scale production.

Contact: Ed Russick, Organic Materials Dept., 1811
Phone: (505) 844-4357
Fax: (505) 844-9624
E-mail: emrussi@sandia.gov



Figure 1. Test demonstrating the ability of Sticky Foam to delay an intruder's access to equipment.

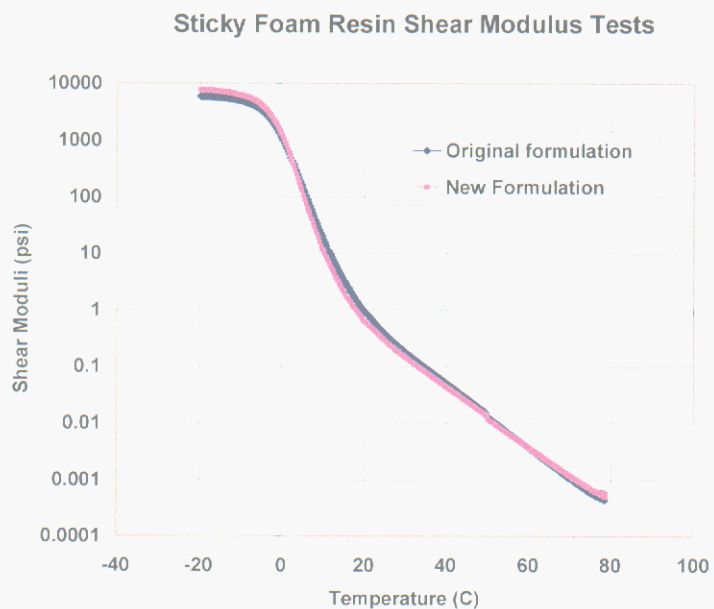


Figure 2. Plot of shear modulus versus temperature of the original Sticky Foam resin versus that of the new formulation with a replacement processing oil.

Removable Adhesives

J. H. Aubert

Motivation: There are a wide variety of adhesives used in the manufacture of complicated devices, such as weapons. They are customized for the specific materials to be joined and are chosen to hold parts together indefinitely. Normally, no thought is given to disassembly. Yet disassembly is becoming an increasingly important aspect of manufacturing as one is concerned with the cradle to grave aspect of materials for environmental and economic reasons. Future weapon systems are being planned so that they are more maintainable than in the past for repairing and upgrading of components. A critical enabling technology is that of removable adhesives. Easy disassembly allows for upgrading as new technology becomes available or rebuilding if any defects are discovered after deployment or during the original manufacturing.

Accomplishment: Adhesive removal is typically accomplished by heating an adhesive above its softening point and prying the materials apart. Our approach to a removable adhesive is new. It relies upon the use of a reversible chemistry that opens at elevated temperature and results in low molecular weight and low modulus constituents. The modulus can be many orders of magnitude lower than a conventional adhesive heated above its' glass transition temperature. The low force causes less collateral damage to electro-mechanical components when disassembled.

We are developing removable adhesives based upon thermally reversible Diels-Alder chemistry, Figure 1. The Diels-Alder adduct is formed between a furan and a maleimide at 60 °C or lower. At 90 °C, or higher, the adduct opens

forming the original furan and maleimide moieties. By incorporating these structures into reactive epoxy monomers, we are able to formulate elastomeric adhesives useful for the bonding of dissimilar metal pieces. An example of the bonding and debonding process for two metal pieces is shown in Figure 2. The adhesive is prepared as sheets of predetermined thickness. The adhesive sheet is then cut to size, applied to one surface to be bonded, and melted. The bond is made by bringing the melted adhesive into contact with the other metal surface and curing at 60 °C. The adhesive in this example has a removal temperature of 100 °C. The temperature at which the adhesive liquefies can be varied between 100 °C and 160 °C by the formulation and the mixture of bismaleimides utilized. To break the bond in this example, the component is heated to 100 °C, and the parts fall away from each other with only the force of gravity. At the removal temperature, the epoxy adhesive breaks apart into small molecules with a low modulus. Beside metals, removable adhesive technology has been applied to bond foams and some polymers.

Significance: Easily removable adhesive joints allow for versatile component assembly, easier and cheaper component repair, easy upgrading, and simplified dismantlement and recycle. By incorporating reversible Diels-alder chemistry into epoxy resins, we have formulated a range of removable elastomeric adhesives.

Contact: Jim Aubert, Organic Materials Dept., 1811
Phone: (505) 844-4481
Fax: (505) 844-9624
Email: jhauber@sandia.gov

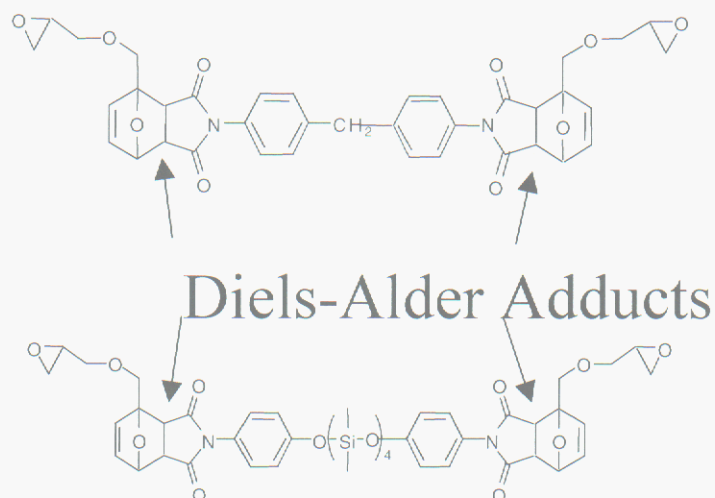


Figure 1. Two epoxy resins each contain two Diels-Alder adducts (top RR1, bottom RER1). The epoxy groups react with common diamine curatives resulting in crosslinked epoxy networks. The Diels-Alder adducts open above 90 °C, which then liquefies the adhesive for easy bond breaking. The exact liquefying temperature depends upon the formulation and can be varied between about 100 °C and 160 °C.

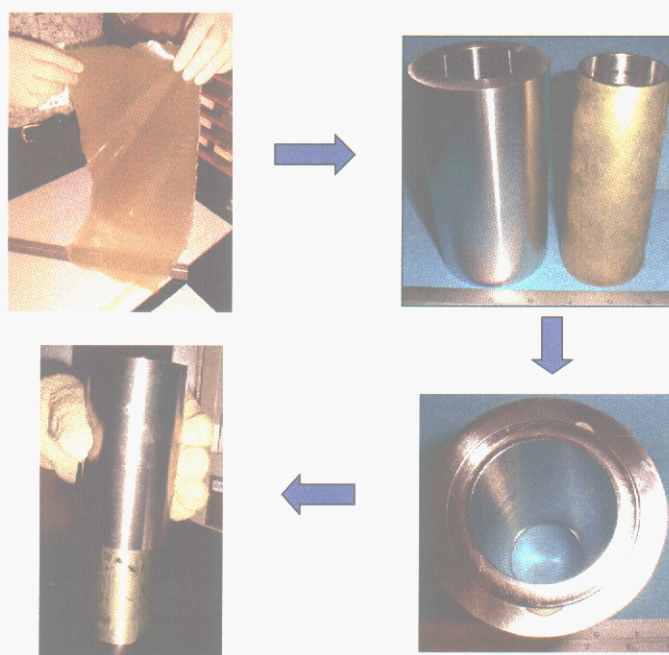


Figure 2. Adhesion and debonding process for two metal pieces: a) Sheet of adhesive is prepared to the desired thickness, in this case 10 mils, b) adhesive is cut to size and applied as a solid film to one surface to be bonded, c) bonding occurs by heating the metal above the adhesive melting point, 100 °C in this case, and then curing at 60 °C, d) debonding is accomplished by heating the assembly above 100 °C at which point the adhesive liquefies. No force other than gravity is required to separate the metal pieces.

Colloidal Self-Assembly and Nanointeractions

N. S. Bell, G. Jamison, and P.G. Clem

Motivation: Applications involving catalysts, chemical sensors, quantum confined materials, and photonic bandgap (PBG) architectures all require control and manipulation of the energetics of colloidal particles. Studies in self-assembly and nanoparticles focus on the surface chemistry modifications that allow for facile manipulation of aggregation stability and the development of novel structural arrangements. Remote routes for control of interparticle energetics give a new level of precision and control to the integration of nanoparticles into device technology.

Accomplishment: The assembly of mono-disperse spheres is a facile route to the formation of photonic bandgap materials (Figure 1.) The self-assembly process requires a phase transition initiated by an increase in particle volume concentration, and control of particle stability during the process to allow for the development of an ordered structure. Methods reported in the literature involve directed drying techniques on flat substrates (some of which are patterned), forced filtration, and electrophoretic deposition.

We are pioneering an alternative approach to control the formation of colloidal crystals that employs photosensitive organic moieties to manipulate particle-particle interactions so that crystallization can be remotely controlled by the application of laser wavelengths. The photo-controlled switching of surface groups creates the capability to remotely control the colloidal stability of particles via modulation of the particle surface polarity. Synthesis of azobenzene, spiropyran, and furyl fulgide organic moieties has been completed, and UV/VIS confirms photobleaching of UV-sensitive chromophores at low total fluences.

Modeling of the photo-response coupled with measurements of contact angle is being used to relate to colloidal stability. Modeling of surface energy utilizes the Fowkes formulation. Here the components of surface energy are separated into the dispersive and polar parts. Figure 2 shows the measured components for the switchable spiropyran films.

$$\sqrt{(\sigma_i^D)(\sigma_s^D)} + \sqrt{(\sigma_i^P)(\sigma_s^P)} = \frac{\sigma_i(\cos\Theta + 1)}{2}$$

The information determined by contact angle measurements and modeling of surface energy correlate well with molecular orbital calculations of the molecule dipole moment.

Direct force measurements of the strength of these interactions will also be determined utilizing the colloidal probe technique in an atomic force microscope. The measured adhesion and friction energies will relate to macroscopic rheological properties such as the elastic gel modulus. These parameters will be related to the microscopic observations of crystallization kinetics, and provide the potential to remotely remove defects, control crystallization direction, and lead to the integration of these photonic materials into MEMS scale microdevices.

Significance: Obstacles to the application of colloidal self-assembly to photonic networks and nanoparticulate processing are the generation of undesired defect states and uncontrolled registry of the network. Success in the use of particles for photonic networks requires control of crystallization, crystal orientation, and defect control. Non-invasive remote control of the self-assembly process can deposit and remove material repeatedly and enable the integration of PBGs into device architectures.

Contact: Nelson Bell, Chemical Synthesis & Nanomaterials Dept., 1846
 Phone: (505) 844-6234
 Fax: (505) 844-9781
 E-mail: nsbell@sandia.gov

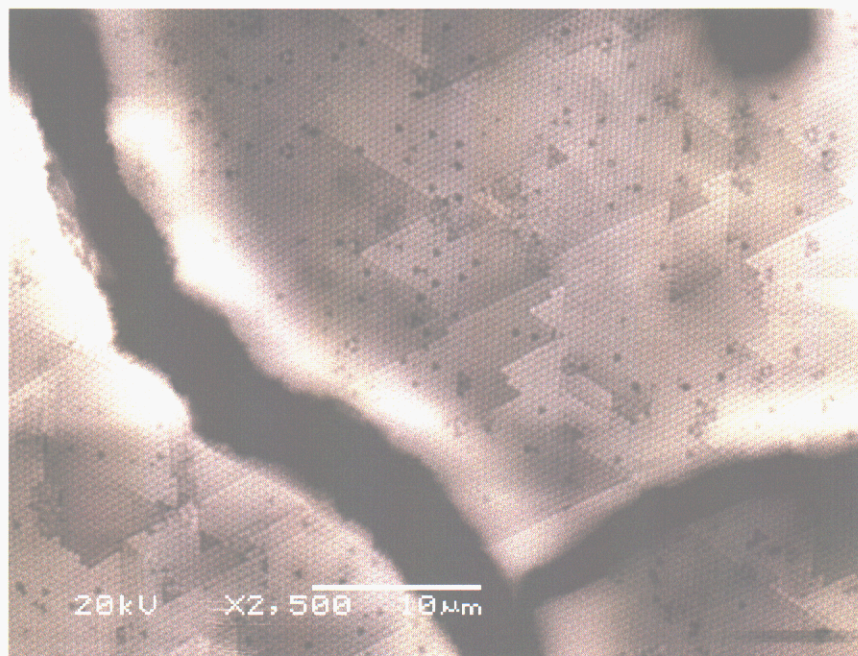


Figure 1. Scanning electron microscope image of monodisperse latex particles.

	Surface Energy	Disperse Component	Polar Component	Dipole Moment
Spiropyran	33.55 mN/m	25.07	8.48	4.422 Debye
Merocyanine	36.69 mN/m	24.89	11.80	9.652 Debye

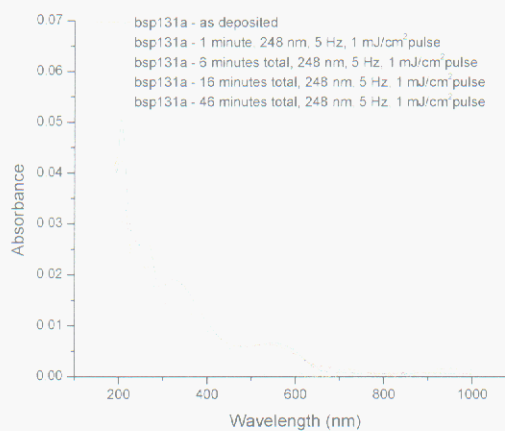
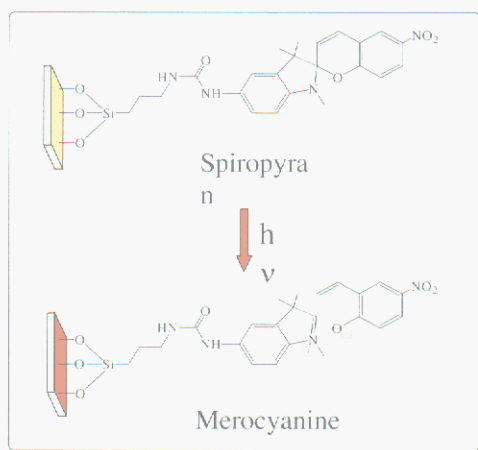


Figure 2. Contact angle modeling of surface energy switching and comparison with computational modeling of molecular dipole moment.

Friction between Self-Assembled Alkylsilane Monolayers

M. Chandross, G. S. Grest, B. Park, M. J. Stevens, and E. B. Webb III

Motivation: Self-assembled monolayers (SAMs) offer a unique means to alter and control the chemical nature of surfaces. The alkylsilanes are a particularly interesting type of SAM because they bond to oxide surfaces and are thus of use in silicon based micro-electromechanical systems (MEMS), which have a native oxide surface. While experimental measurements yield atomic scale force data, they do not produce the simultaneous structural characterization that can be deduced from molecular scale simulations. A predictive, molecular-level understanding of friction is the missing key to intelligently designing interfacial lubricants for MEMS.

Accomplishment: Molecular dynamics (MD) simulations are ideal for probing the properties of SAM coated surfaces, since they are able to produce both atomic scale force data as well as the underlying structural information. We have carried out extensive MD simulations of the adhesion and lubrication of SAM coated SiO₂ surfaces. We have studied the effects of chain length, system size, and shear velocity between pairs of SAMs covalently bonded to crystalline and amorphous SiO₂ surfaces. Snapshots of an ordered SAMs before and after compression are shown in Figure 1 for alkylsilane chains containing $n = 8$ backbone carbons. As the surfaces are brought into contact, there is a small region of attraction due to the van der Waals interaction, with a magnitude of about 150MPa for all chain lengths studied, $n = 6$ to 18. Further decrease in the distance between the surfaces leads to an increased compression, as the interactions become strongly repulsive. The relationship between load and distance between the surfaces is monotonically dependent on the chain length. Shorter chains are stiffer and have a

larger repulsion compared to longer chains. As seen in Figure 1a, the chains tilt in order to compress beyond the all trans contact configuration. Tilting allows the chains to accommodate smaller separations without introducing large repulsive van der Waals interactions.

Lubrication between pairs of SAMs in contact is studied by shearing the two surfaces relative to each other. The velocities that can be studied in a MD simulation are within the range of MEMS devices, typically on the order of a few cm/s, but large compared to those scanned by typical force probes. For all chain lengths and shear velocities studied, the shear stress versus time for ordered SAMs shows a stick-slip dynamics, Figure 2. Stick-slip dynamics requires commensurability of the two sliding surfaces, which ensures that the hills and valleys of the potential surfaces match in such a way that one SAM pushes against the hills of the other (stick) and then overcomes the barrier to quickly slide down (slip). A small percentage of defects break up this stick-slip dynamics for low loads but not for high loads. Simulations on a range of system sizes for $n=6$ show that larger system sizes result only in decreased noise.

Significance: MD simulations provide new insight into the atomic scale motion of SAMs, providing a picture of the molecular structure under shear and a detailed molecular level understanding of energy dissipation mechanisms. Future work on varying the end groups, including fluorocarbons and the introduction of water, will lead to a quantitative understanding of adhesion and friction as a function of chemical interactions and environmental exposure.

Contact: Mike Chandross, Materials & Process Modeling & Computation Dept., 1834
Phone: (505) 844-5081
Fax: (505) 844-9781
E-mail: mechand@sandia.gov

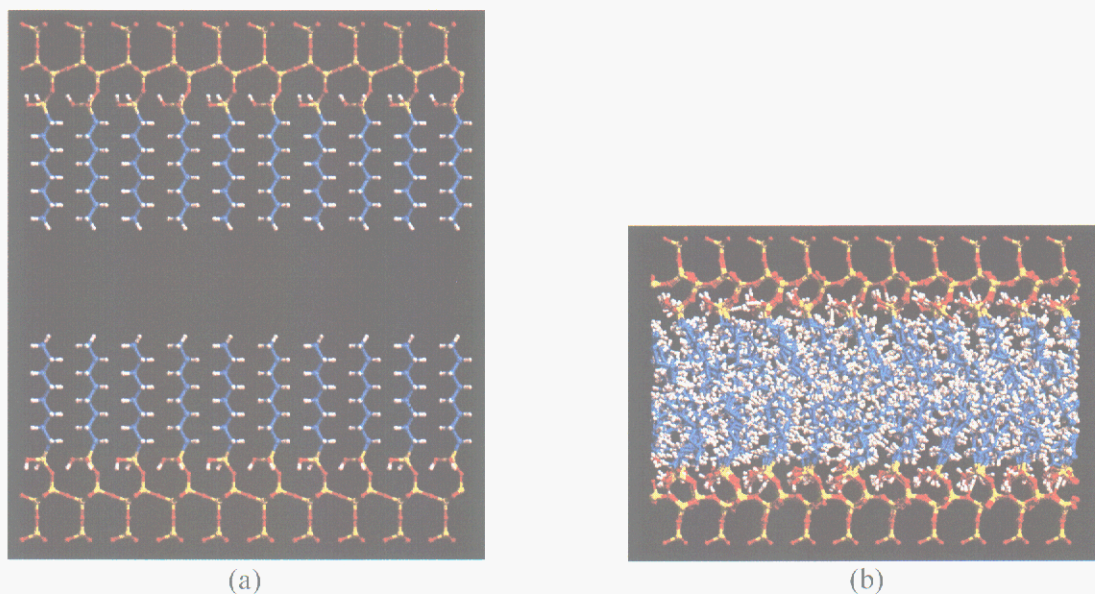


Figure 1. Snapshot of an $n=8$ ordered alkylsilane SAM before (a) and after (b) compression. Silicon atoms are red, oxygen atoms are yellow, carbon atoms are cyan and hydrogen atoms are white.

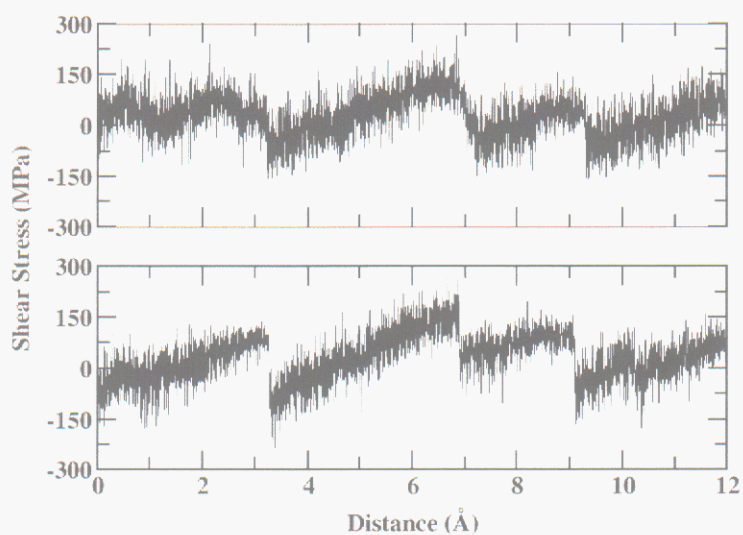


Figure 2. Shear stress σ_s as a function of distance sheared for $n=12$ (top) and $n=18$ (bottom) at a normal load of 0.2 GPa and relative shear velocity $v=0.2$ m/s. Results for 100 chains attached to each surface.

Controlled Sintering of Ceramics

K. G. Ewsuk and D. N. Bence

Motivation: More than fifty years of scientific studies have contributed to the development of sound atomic-scale sintering theory; however, it is still difficult or impossible to apply this fundamental scientific knowledge to commercial advantage (i.e., to understand and control macroscopic deformation and densification during sintering). A relatively new tool with the potential to predict/control macroscopic response in ceramic components, based on atomic-scale scientific understanding, is D.L. Johnson's master sintering curve, MSC [J. Am. Ceram. Soc., 79 [12] 3211-17 (1996)]. The MSC, which evolved from the combined stage sintering model that uses a single equation to describe all three stages of sintering [J. Am. Ceram. Soc., 75 [5] 1129-35 (1992)], is a tool that can be used to predict the density of a particulate body subjected to any arbitrary time-temperature excursion during sintering. Johnson's MSC theory was developed for solid-state sintering, and makes fundamental assumptions that have not yet been rigorously tested. The objectives of this work were to: 1) test MSC theory and its ability to predict densification behavior; and 2) extend MSC theory beyond solid-state sintering to a system that sinters with the aid of a liquid phase.

Accomplishment: Based on the works of Johnson, a simple experimental procedure was developed to characterize sintering and to determine the activation energy for sintering and to obtain the master sintering curve for a particulate ceramic body. MSC theory was applied to MgO-doped AKP53 alumina, and the ability to use MSC theory to predict density as a function of sintering time and temperature in this solid-state sintering system was verified. MSC

theory was extended to liquid-phase sintering systems by successfully applying it to the sintering of 94% alumina (6 wt. % glass). Furthermore, by generating comparable master sintering curves for 2 different 94% alumina powders, the second having been reverse-engineered to replicate the original powder, it was demonstrated that MSC theory can be used as a quality assurance tool to ensure process reproducibility (e.g., by ensuring that starting powders are virtually "identical" for processing). Figure 1 shows the MSC for MgO-doped AKP 53 alumina determined from the activation energy (Q) and the relationship between density and sintering time and temperature obtained from simple, constant-rate heating experiments. A dilatometer was used to measure the linear shrinkage of pressed powder compacts as a function of temperature during heating at 1-40°C/min.

Figure 2 shows the MSC-predicted density at different temperatures after heating at 10, 20, or 30°C/min. There is very good agreement between the MSC predictions and the dilatometer measured density-temperature curves for the same three heating rates.

Significance: The predictive capability of the MSC enables considerable flexibility to: 1) optimize a component's sintering schedule to achieve the desired density and performance; 2) predict densification behavior (i.e., sintering rate) to support numerical (FEM) modeling with only a small set of routine dilatometer sintering experiments; and 3) identify lot-to-lot variations in starting powders that could contribute to processing or component performance issues (i.e., for quality assurance).

Contact: Kevin Ewsuk, Ceramic Materials Dept., 1843
Phone: (505) 272-7620
Fax: (505) 272-7304
E-mail: kgewsuk@sandia.gov

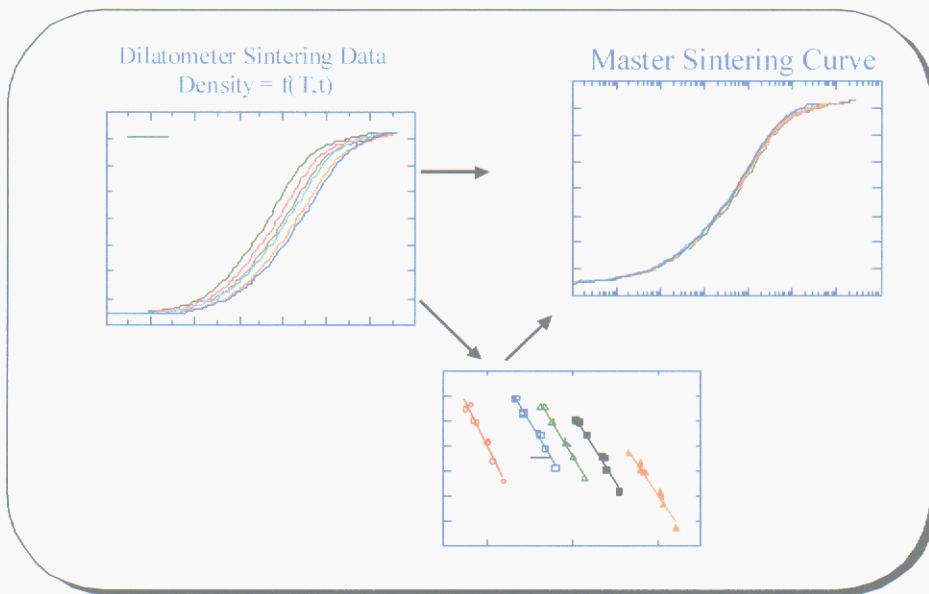


Figure 1. The master sintering curve (right) for MgO-doped AKP 53 alumina that was determined from the activation energy, Q , (bottom) and the relationship between density and sintering time and temperature (left) obtained from simple, constant-rate heating dilatometer sintering experiments.

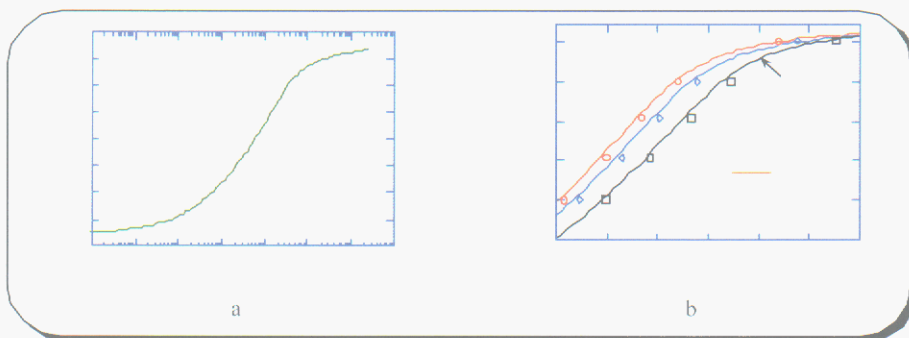


Figure 2. The a) MSC for MgO-doped AKP 53 Alumina, and b) MSC predicted density at different temperatures after heating at 10°C/min (circles), 15°C/min (diamonds), or 30°C/min (squares) in comparison to dilatometer measured density-temperature curves for those respective heating rates.

Freeform Fabrication of Photonic Band Gap Structures

J. E. Smay, J. Cesarano III, J. N. Stuecker, S. Y. Lin and J. A. Lewis

Motivation: Photonic band gap (PBG) materials exhibit a characteristic frequency domain in which the density of states for light propagation approaches zero. This behavior has great potential for efficient bending of light, increased efficiency of lasers by inhibiting unwanted modes, and a variety of other applications where control of photons is important. The length scale, symmetry, and dielectric constant contrast of the crystal structure define the domain and directionality of this band gap. Solution of the Maxwell equations for periodic dielectric structures reveals that the PBG scales with the feature size of the crystal. Thus, while the ultimate application of PBG's may lie at $1.5\mu\text{m}$ wavelengths, fabrication techniques that can create periodicity on the mm length scale can be used to rapidly screen new structures and materials with direct correlation to higher frequency applications. Our motivation was to demonstrate that a solid freeform fabrication technique, known as robocasting, could be used to rapidly produce PBG structures on a mm length scale. Robocasting was invented at Sandia National Labs to utilize colloidal ceramic slurries in the rapid fabrication of components.

Accomplishment: By carefully controlling interparticle forces, slurry rheology may be tailored. A weakly attractive interaction induces a rheology that is pseudoplastic with a yield stress. With this slurry, self-supporting, spanning lattices may be robocast. Here, we demonstrate the fabrication of periodic Al_2O_3 lattice PBG structures. Additionally, we demonstrate the ability to strategically inject defect states into the

band gap via line vacancies in the lattice. Preliminary measurements of the photonic band gap in the 80-110 GHz regime for two lattices, one containing periodic line defects, are described below.

Fig. 1 shows a schematic of the face centered tetragonal (FCT) macrostructure of our Al_2O_3 lattices. Fig. 2 and Fig. 3 show a defect-free FCT lattice and a FCT lattice with missing rods, respectively. These structures were characterized by measuring the attenuation of a transmitted microwave as a function of frequency from 80 to 110 GHz. The results in Fig. 4 reveal band gap measurements of 10 to 15 dB and a correlation of 12% bandwidth predicted by *a-priori* calculation. The presence of line vacancies changes the response of the PBG.

Significance: We have demonstrated that robocasting may be a versatile tool for fabricating prototype PBG structures and materials. Furthermore, we have demonstrated a technique for incorporating defects into lattices of rods to modify the band gap. Future work will be completed in an attempt to reduce the size scale of these structures to less than 75 microns and to incorporate non-linear optical materials. These structures may lead to novel switches for microwave and/or infrared communications.

Contact: Joe Cesarano, Ceramic Materials Dept., 1843
Phone: (505) 272-7624
Fax: (505) 272-7336
E-mail: jcesara@sandia.gov

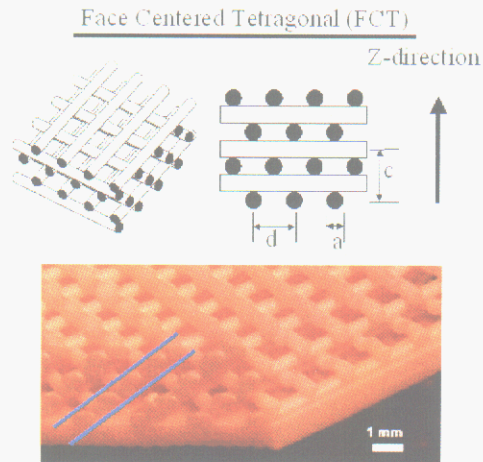


Figure 1. These drawings and photograph show a face centered tetragonal lattice of meshed rods. Robocasting was used to make these FCT structures out of alumina for prototype PBG's.

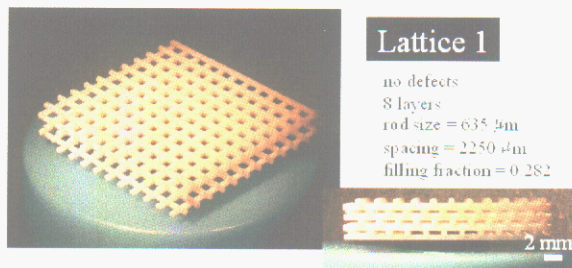
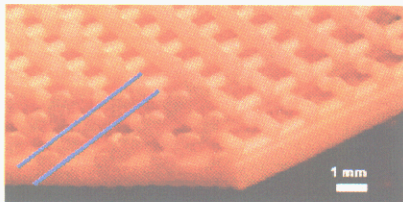
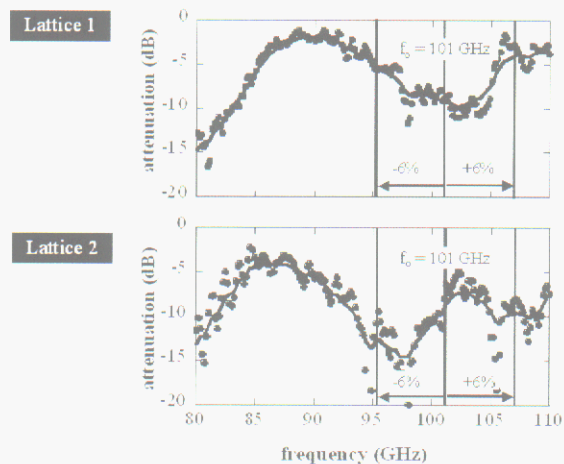


Figure 2. A defect-free alumina FCT lattice built to show a band gap in the 100 GHz range



Figure 3. An alumina FCT lattice designed and robocast with four line vacancies. The introduction of defects can modify the frequency response of PBG's.

Figure 4. Data showing how lattices 1 and 2 attenuate microwaves in the 100 GHz range. Microwaves are attenuated 10-15 decibels in the band gap region. Defects can modify and effectively narrow the gap.



Ceramic Joining

R. E. Loehman

Motivation: Ceramic joining is a technology that enables many other processes and products. Examples range from the exotic to the mundane. Commonplace uses of ceramic joining include attachment of cutting tool inserts, sealing of electrodes in sodium vapor lamps, and high power vacuum tubes. Examples of more advanced applications are joining of ceramics in next-generation heat engines, assembling solid oxide fuel cells, and the many connectors, feed thrus, and other devices used by Sandia in DP applications. There is no comprehensive science of ceramic joining. Systems are developed ad hoc. What is needed is a systematic approach to developing ceramic joining for arbitrary applications.

Accomplishment: Fundamental research on ceramic-metal interfaces and reaction is enabling us to develop an unequalled set of techniques for engineering ceramic-metal and glass-metal joints. Those results are combined with finite element models of interfacial stresses to predict whether a system that is chemically compatible will also have sufficient mechanical strength. Recently we have concentrated on understanding mechanisms of active element brazes used for joining. We have gone beyond the traditional Ti-containing brazes to include Zr, V, and Hf. They appear to work by promoting interfacial reactions, but the mechanisms appear to be very different for the various additives. In particular Hf is effective in small concentrations by promoting redox reactions at the ceramic interface. The reaction products are thin and finely dispersed, which may reduce inevitable interfacial stresses. Thus, Hf

may be a particularly useful ceramic braze additive.

Once favorable compositions have been identified Sandia's proprietary finite element modeling (FEM) codes and fast super computers can efficiently test component designs without the need to build prototypes.

Other research has concentrated on developing refractory glass compositions for high temperature ceramic-ceramic seals. This approach requires optimizing glass chemistry, glass-ceramic reactivity, and thermomechanical properties such as viscosity, thermal expansion and creep resistance. Recently we have been investigating borate-based glasses for making gas tight seals for solid oxide fuel cells. The most favorable compositions adhere strongly to fuel cell components and remain bonded through thermal cycles to 1000°C. Thermal expansion mismatch stresses are partly relieved by the very slight tendency of the glass to structurally relax at high temperatures. Long-term chemical compatibility is insured by choice of the glass components, guided by thermodynamic calculations.

Significance: Sandia's capability for developing novel ceramics, glasses and joining products and processes insures compatibility with candidate alloys and sealing glasses thus freeing component engineers from the constraints of current joining technology, and enabling the development of new products and devices with improved performance.

Contact: Ron Loehman, Ceramic Materials Dept., 1843
Phone: (505) 272-7601
Fax: (505) 272-7304
E-mail: loehman@sandia.gov



Figure 1. TEM image of the reaction interface resulting from heating 1at%Hf–Ag–Cu on 99.6% alumina for 30 min at 1000°C in gettered Ar. STEM analysis shows the interface contains small particles of HfO_2 that resulted from a redox reaction at the interface. The alloy adheres strongly to the ceramic. (TEM courtesy of Paul Kotula)

Elevated Temperature Properties of Braze Alloys

J. J. Stephens, M. K. Neilsen, F. M. Hosking, T. Buchheit, J. Gieske and D. Benceo

Motivation: The mechanical and physical properties of braze alloys used in metal/ceramic braze joints are of great interest from both a component design and reliability viewpoint. In particular, the elevated temperature creep and stress-strain behavior, coupled with braze joint geometry and thermal expansion properties, determine whether high residual stresses will exist in the ceramic which could lead to ceramic cracking and/or loss of hermeticity. Both conventional brazing alloys (i.e., brazed to metallized ceramic) and active metal braze alloys (alloys containing active metal additions which can wet bare ceramic) are of interest.

Accomplishment: During FY00, a PDP-funded effort was initiated to complete the matrix of physical properties for a number of conventional braze alloys. In years past we have generated constitutive models to represent the deformation behavior of a number of conventional braze alloys, but due to a shortage of resources we had not generated thermal expansion and dynamic modulus properties. We are generating physical properties for the following four braze alloys (compositions given in wt%): (a) 50Au-50Cu, (b) 47Au-50Cu-3Ni, (c) 62Cu-35Au-3Ni, and (d) 72Ag-28Cu.

Publications during FY00 have included a study of the high temperature mechanical properties of the 50Au-50Cu braze alloy. The 50Au-50Cu alloy is used for a number of conventional metal/ceramic braze joints in hermetic, high voltage component applications. The high temperature (450-850°C) creep behavior of annealed (2 hr./750°C/Water quenched) 50Au-50Cu alloy (see Figure 1) is well fit by the Garofalo sinh equation. At lower

temperatures, there is the possibility of ordering to a Cu_3Au structure, the in this alloy. A related X-ray diffraction study indicated that the ordering reaction is quite sluggish – requiring ~ 4 days at 375°C, followed by slow cooling to room temperature to realize an ordered Cu_3Au . The properties of the ordered 50Au-50Cu alloy at 250 and 350°C are compared to the disordered FCC structure in Figure 2. Note that the ordered alloy results in an approximately 20% increase in creep strength relative to the disordered alloy. Fortunately, the sluggish ordering kinetics in this alloy preclude the ordered structure for most brazing applications.

Previous publications have also included consideration of strengthening effects of active braze alloys relative to their conventional counterparts. The addition of Ti to the 72Ag-28Cu braze alloy results in a net strengthening effect, due to significant solid solution strengthening of the Cu-rich phase. By comparison, the active element addition of V to the 82Au-18Ni alloy results in a net weakening effect due to the stabilization of a weaker Ni-rich second phase, which is presumably not subject to the spinodal strengthening effects observed in the conventional 82Au-18Ni alloy.

Significance: Metal/ceramic brazing of high reliability components relies on a number of design and process capabilities. This properties-related effort has the overall goal of enabling prediction of brazing related residual stresses during the design phase of a component. High temperature properties have been generated for a wide variety of braze alloy compositions, and have proven useful to internal SNL component customers, DOD customers, and U. S. industry.

Contact: John J. Stephens, Joining and Coating Dept., 1833
Phone: (505) 845-9209
Fax: (505) 844-4816
E-mail: jjsteph@sandia.gov

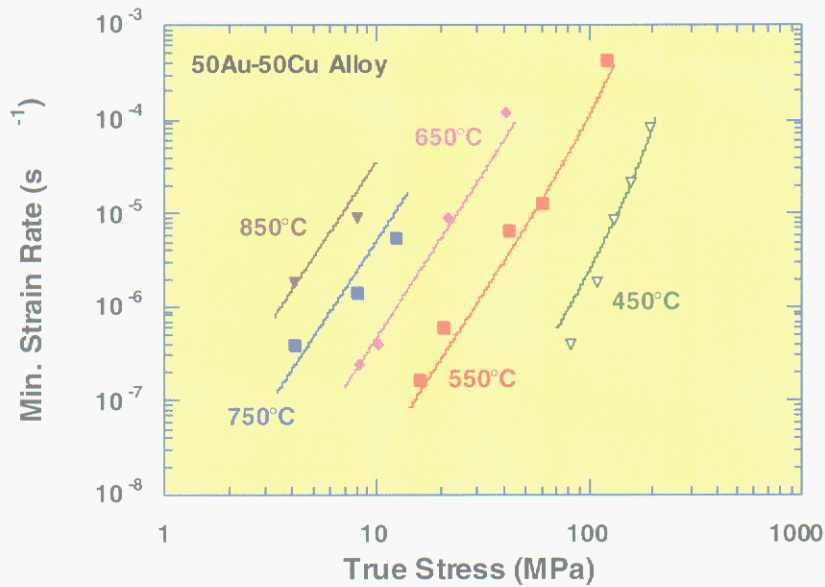


Figure 1. Elevated temperature creep properties of annealed 50Au-50Cu braze alloy over the temperature range 450-850°C.

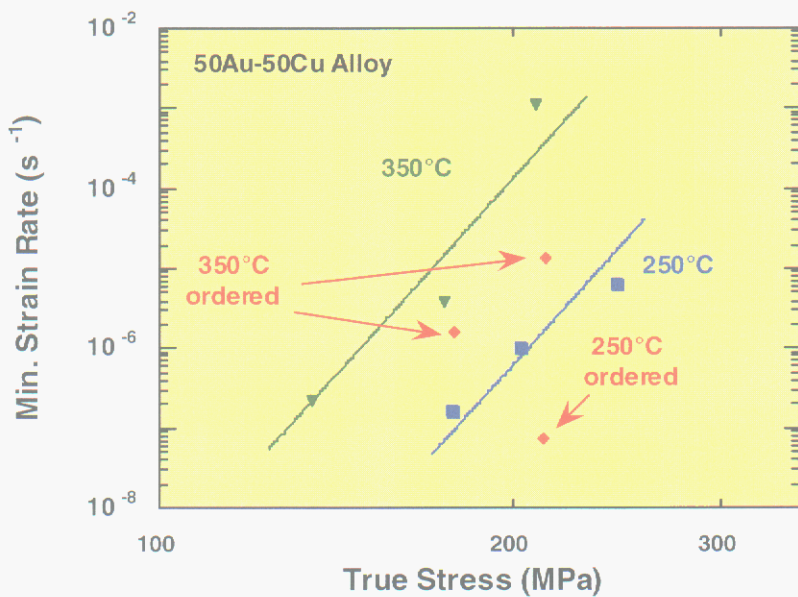


Figure 2. Comparison of creep properties for disordered and ordered (2 hr./750°C, 96 hr./375°C/slow cool) 50Au-50Cu alloy at 250 and 350°C.

Linking Atomistic Computations with Phase Field Modeling

J. J. Hoyt

Motivation: A number of components critical to the Sandia mission involve the process of metal joining, either soldering, brazing or welding. Therefore it is of interest to develop a modeling capability that can realistically capture the key features of alloy solidification. Modeling of the complex morphologies, which arise during solidification, is a formidable challenge. A major obstacle is the fact that the final microstructure depends critically on several materials parameters which are difficult, if not impossible, to measure experimentally. The goal of the present research is to utilize atomistic simulations to compute these key quantities.

Accomplishment: Three materials parameters are required to perform a continuum level (phase field) simulation of solidification: the liquid state diffusion coefficient, the solid-liquid interfacial free energy, and a kinetic coefficient which relates the velocity of a planar interface to the undercooling. Furthermore, it is well known that the shape and velocity of the growing dendrite depends critically on the small anisotropy of the latter two quantities. To date, we have had considerable success in computing all three parameters and our work has resulted in five publications in refereed journals, including two in the prestigious Physical Review Letters.

As an example, consider the interfacial free energy, γ , and its anisotropy. For a system at the melting point, the solid-liquid boundary is continually fluctuating and one can characterize the fluctuations by the Fourier space power spectrum averaged over many configurations, $\langle |A(k)|^2 \rangle$. From capillary theory it is known that $\langle |A(k)|^2 \rangle$ is proportional to k^{-2} with a proportionality constant proportional to $1/(\gamma+\gamma'')$, where γ'' is the second derivative of the interfacial energy as a function of crystallographic orientation angle of the interface, i.e. γ'' describes

the anisotropy. The sum $\gamma+\gamma''$ is known as the stiffness. The key to our recently developed capillary fluctuation method is the fact that the stiffness is an order of magnitude more anisotropic than γ itself. By monitoring the fluctuations of a boundary during a molecular dynamics simulation, one can extract the large anisotropy of the stiffness and, by assuming a proper functional form for γ , one can, in turn, derive the very small anisotropy in the interface energy itself.

Figure 1 shows a portion of the solid-liquid interface in the simulation cell color-coded such that yellow denotes atoms within the crystalline solid and red represents liquid atoms. A non-planar interface can clearly be seen. Plotted in Figure 2 is the reciprocal of the averaged power spectrum vs. k^2 for three different orientations of the solid-liquid boundary. The data shown is for pure Ni, and the embedded atom method has been utilized to describe the interatomic potential. The slopes of the lines in Figure 2 are proportional to the stiffness and the relatively large anisotropy is clearly seen. From these results we are able to predict an anisotropy in interfacial energy between the $\langle 100 \rangle$ and $\langle 110 \rangle$ orientations of just 1.8%. Furthermore, we compute an interfacial free energy for Ni of 326 mJ/m², in very good agreement with various empirical estimates.

Significance: The ability to accurately predict various thermodynamic and kinetic properties of solid-liquid interfaces means that realistic continuum level modeling of solidification is now possible in several important alloy systems. It is hoped that modeling of dendritic microstructures will lead to important insights into the processes of soldering, welding and brazing

Contact: Jeff Hoyt, Materials & Process Modeling & Computation Dept., 1834
Phone: (505) 284-5391
Fax: (505) 844-9781
E-mail: jjhoyt@sandia.gov

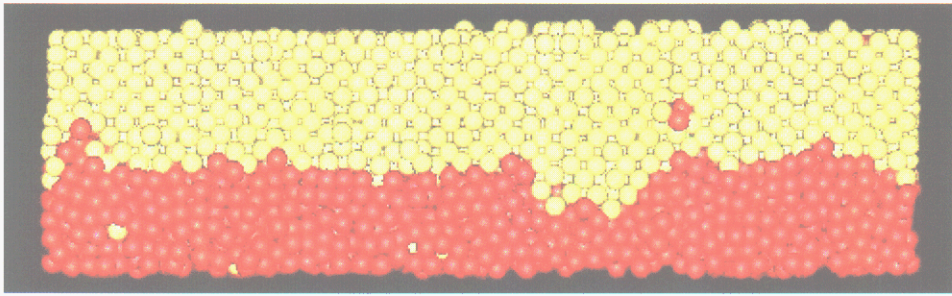


Figure 1. A portion of the solid (yellow)-liquid (red) interface in the molecular dynamics simulation of pure Ni using the embedded atom method.

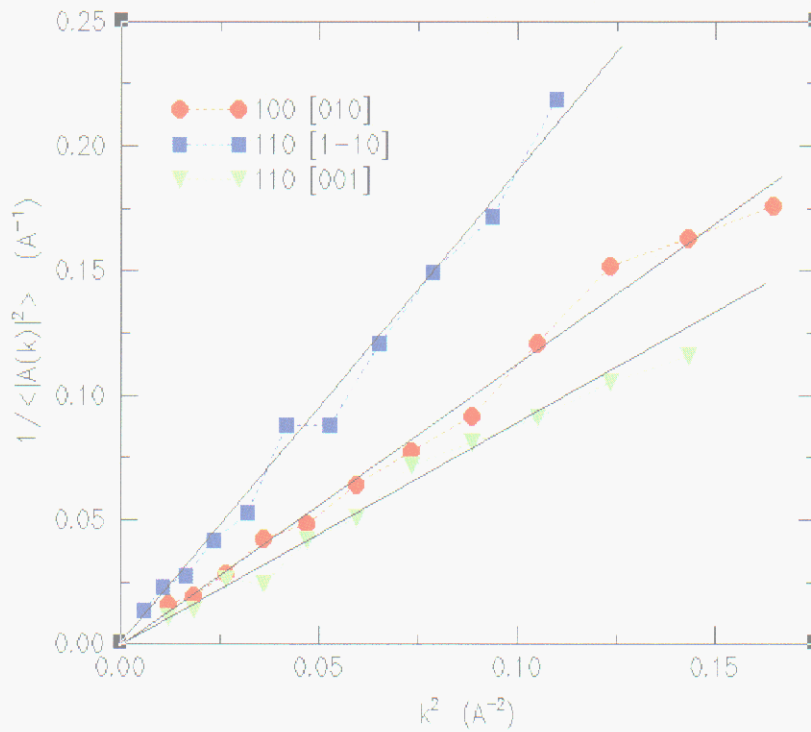


Figure 2. The inverse of the average power spectrum vs. k^2 for three different crystallographic orientations.

Molecular Dynamics Simulations of Reactive Wetting and Spreading

E. B. Webb III and G. S. Grest

Motivation: Formation of a robust joint between dissimilar metals or a metal and a ceramic is critical to a wide range of components. System requirements for material contacts can vary widely. Performance of metal-metal contacts is based on electrical conductivity for some applications and thermomechanical response for others. Ceramic seals on metal parts provide hermeticity in some systems or heat and corrosion resistance in others. While a joint's function can vary greatly, all applications depend on the relationship between microstructure and macroscopic properties realized. Chemistry at joint interfaces is complex and interfacial width can be of atomic dimension, making a detailed atomistic description desirable but often beyond the reach of experiment. This motivates our use of molecular dynamics (MD) modeling, coupled with experiment, to elucidate the nature of joint interfaces at an atomic level.

Accomplishment: Prior work has shown the feasibility of using classical atomistic modeling to perform large-scale, robust simulations of interface phenomena for metal-metal systems. Extending this work, we have conducted a series of MD simulations examining interface formation between a Ag(I) drop and the (100) single crystal surface of FCC Cu (Figure 1). Other attempts to model such systems have employed approximations that limited the ability to connect to experiment and application. For example, static substrates were used where substrate atoms were constrained to their initial positions throughout the simulation. This provides insight to wetting in the absence of reactions but the influence of reactions on wetting is exactly what we wish to examine. Computational restraints motivated such prior approximations; we have overcome this by employing a highly efficient parallel computer

code on CPlant™, a cluster-based supercomputer at Sandia. As such, Figure 1 portrays a drop 10 nm in diameter but our largest drop size simulated is roughly 20 nm.

Reactive wetting simulations have demonstrated the eutectic nature of the Ag/Cu system. As Figure 1 illustrates, a significant reaction zone is observed for temperature T below melting of pure Cu. For the short simulation shown (400 ps), lower T results in greatly suppressed reaction. Figure 2 shows density profiles of the interfaces, further illustrating the degree of mixing. We have analyzed the structural aspects of the reaction zone as a function of time, including atomic coordination and wetting angles, to establish the underlying kinetics. This analysis has been performed for a range in T allowing further description of kinetics. We are connecting to relevant experiments and have observed strong qualitative agreement between behavior in model systems and experiment. We are now examining the applicability of scaling rules to quantitatively connect predictions from MD models to larger length and time scales.

Significance: New capability exists to model reactive wetting and joining on an atomistic scale and to extract dynamic structural data from the simulations (stress distribution, local composition, contact angle, etc.). Such capability drives current efforts to more quantitatively connect to experiments on analogous systems as well as larger length scale modeling efforts. Through this collaboration, we hope to refine constitutive equations driving continuum models and thereby improve device design predictions from those models. We are also extending these studies to model Pb(I) wetting Cu, a material system relevant to solder joining.

Contact: Ed Webb III, Materials & Process Modeling & Computation Dept., 1834
Phone: (505) 284-6517
Fax: (505) 844-9781
E-mail: ebwebb@sandia.gov

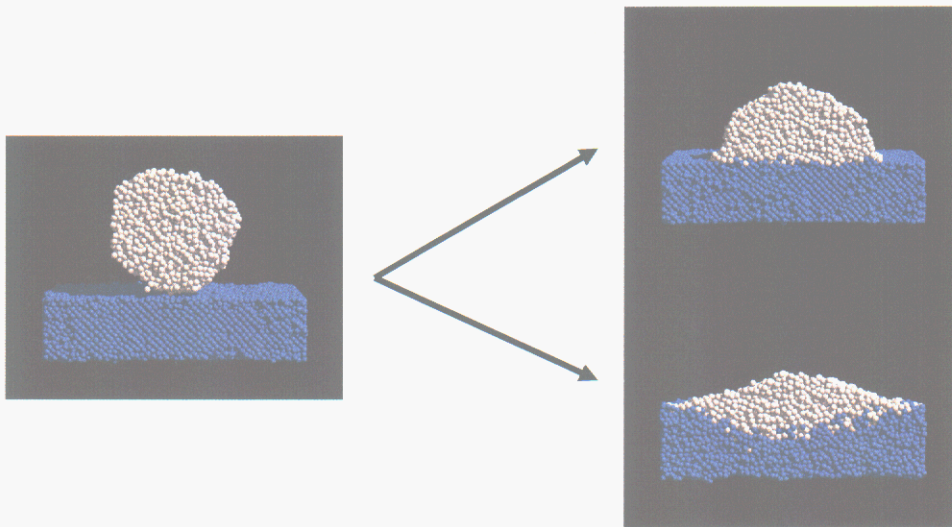


Figure 1. Snapshot of a simulation cross-section showing time evolution for the Ag drop (grey) on the (100) plane of face-centered-cubic Cu (blue). The top panel on the right shows the system at $T = 1000$ K and the bottom is at $T = 1275$ K; both systems have run for 100 ps.

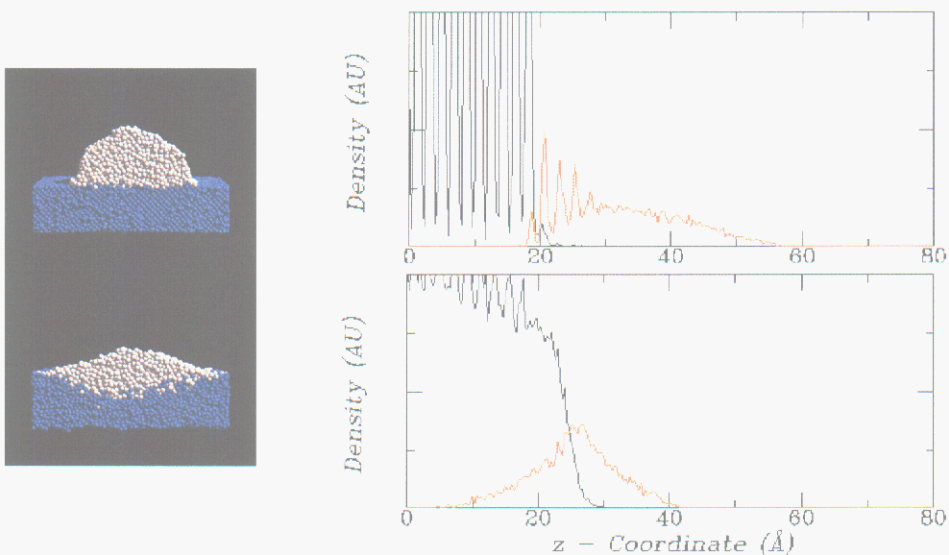


Figure 2. Density profiles for Cu (black curves) and Ag (red) through the interface, further illustrating the difference in reaction or mixing observed as a function of temperature. The top panel shows data for $T = 1000$ K while the bottom is for $T = 1275$ K. Distinct peaks in density in the top graph illustrate the Cu is still crystalline whereas this is not so in the bottom panel; mixing at higher T induces melting at the Cu surface.

Understanding Filler Metal Interactions Critical for Successful Use of Active Metal Braze Alloys in NT/NG Applications

P. F. Hlava and P. T. Vianco

Motivation: There is a continual need for improving and simplifying processing and production of critical weapons components (NT/NG) and nowhere is this more evident than in hermetic joining of metallic to ceramic parts. Metallization techniques, while effective, require successful completion of a large number of steps and thus are time intensive and fraught with problem areas. The development of an effective active-metal braze process would drastically reduce processing steps thereby improving the product while saving time, money, and resources.

Accomplishment: Active metal brazes function by reaction of the active metal with the ceramic (usually alumina) side of the joint, producing an active-metal oxide, which bonds strongly to both the ceramic and metallic sides of the joint. (The reduced aluminum diffuses into the braze alloy). But active metals can also react with the metallic portion of the joint, scavenging up most or all of the active metal at the expense of the oxide phase. This produces a poor, non-hermetic joint. This very scenario occurs when a Cu-Ag-Ti ABA braze alloy is used on a Kovar/alumina joint. The Ti reacts with Ni, Co, and Fe to produce a lace-work of $(\text{Ni, Co, Fe})_3\text{Ti}$ within the alloy at the expense of the desired oxide. Some TiO_2 is produced but not enough to form a hermetic seal. In depth understanding of filler metal/braze alloy reactions with the Fe-Co-Ni system is necessary for successful use of such a system.

An electron microprobe study was conducted in order to determine which of the Kovar metals was causing the problem. Test samples were made using the normal Cu-Ag-Ti ABA braze

alloy and the normal alumina ceramic but with a washer of pure Fe, pure Co, or pure Ni. These were processed in the usual way and analyzed with the electron microprobe. This study revealed that only Fe did not react with Ti from the filler metal. Consequently, a good Ti_xO_y reaction layer was formed at the Cu-Ag-Ti/ceramic interface and the Cu-Ag-Ti/Fe braze joints met hermeticity requirements. Minimal reaction was observed between Co and Ti, with the formation of TiCo_3 particles that scavenged a limited amount of Ti from the filler metal. Only a small number of these joints failed hermeticity. A significant reaction was observed between Ni and Ti, producing an extensive lace-work of the TiNi_3 phase within the filler metal field. As a result, there was a resounding absence of Ti_xO_y phase at the Cu-Ag-Ti/alumina interface and none of the test joints was hermetic.

Significance: This study identified, not only the significant elemental reactions to be expected between Cu-Ag-Ti ABA and Fe-Ni-Co base alloys, but also a criterion by which to select alternative base alloys and/or the use of coatings that would provide a suitable braze joint for nuclear component applications.

Contact: Paul Hlava, Materials Characterization Dept., 1822
Phone: (505) 844-1890
Fax: (505) 844-2974
E-mail: pflava@sandia.gov

Figure 1. "Lace-work" structure of Co_3Ti in the pure Co sample that morphologically appears essentially identical to the intermetallic compound (IMC) in the Kovar sample. (SEM 2107)

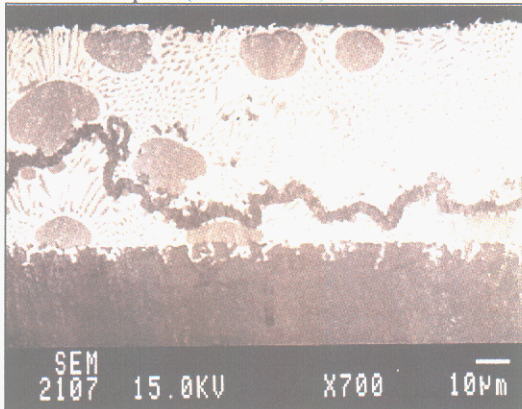


Figure 2. The Ni_3Ti "lace-work" has broken up into individual grains floating in the braze alloy. Evidence of a most intense reaction. (BSE 2163)

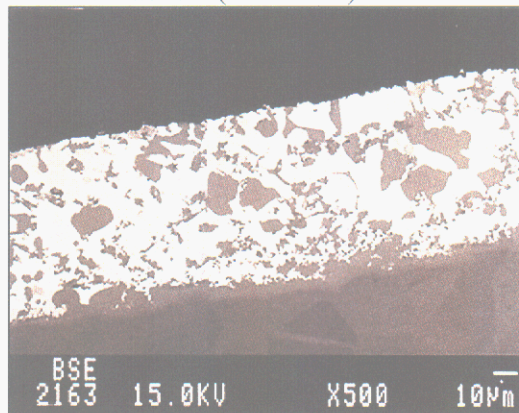
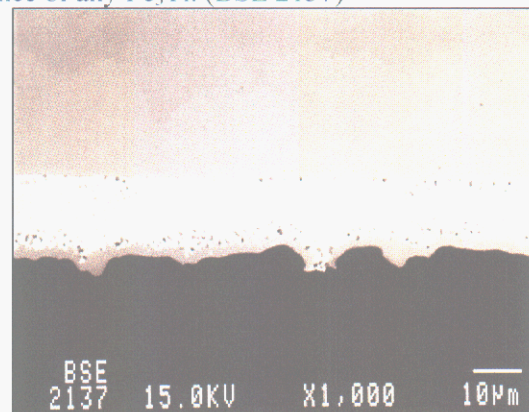


Figure 3. Well-developed reaction layer of TiO_x but no evidence of any Fe_3Ti . (BSE 2137)



Weld Visualization for Investigation of Solidification

A. C. Hall, C. V. Robino, G. Knorovsky, and J. Brooks

Motivation: Understanding the solidification behavior of metals continues to be an important challenge. Conventional experimental techniques for investigating the solid-liquid interface in a metal involve rapidly quenching a partially solid sample (e.g. by quenching in liquid Sn or brine) and examining its microstructure. These techniques, based on rapidly quenched samples, can only provide a “snapshot” of the solid-liquid interface; they cannot provide information about the interface motion or its evolution with time. Until recently, direct measurements of dendrite growth velocities could only be obtained by viewing solidification phenomenon in transparent polymeric systems that are metal solidification analogues.

Accomplishment: Last year we demonstrated that high-speed video microscopy can be used to directly view the solid-liquid interface in a gas tungsten arc weld. Dendrite motion and evolution with time were observed. This year's efforts have focused on improving our video technique and developing methods for automating data extraction from the video clips we have obtained. Improvements to our video techniques have centered on implementing a new high-speed, high-resolution digital camera. The CCD chip in this new camera contains four times more pixels than the camera we used initially. This increase in pixel density results in a fundamental improvement in the spatial resolution of each image. Figure 1 shows two typical high magnification images of the solid-liquid interface, one taken with the old camera and one taken with our new camera. High spatial resolution is critical for the extraction of quantitative information from these experiments. Using commercially available image analysis

software (National Instruments Lab View and IMAQ Vision) we have developed a group of programs capable of processing thousands of images and extracting coordinated spatial and temporal information from each image. This has allowed us to measure the position and velocity of the solid-liquid interface with spatial and temporal resolutions of microns and microseconds! Figure 2 contains a few examples of this data. The interface velocity associated with a rippling weld is shown, as is the interface velocity profile associated with a solidifying spot weld. The weld ripple data has been associated with microstructural features present in the weld and has helped us to better understand the origins of this phenomenon. The spot weld data is a preliminary experiment associated with verification of solidification-based laser welding models. Data from experiments like this will allow us to validate the thermal boundary conditions in these models.

Significance: An increased understanding of solidification phenomena in welds is critical for their use in high-consequence nuclear weapon safety and security applications. High-speed, high-resolution, video microscopy allows the solid-liquid interface to be accessed in ways never before possible. Quantitative information about solid-liquid interfaces in engineering materials can now be gathered under actual welding conditions. This technique has led to new insights about dendrite growth, and has provided a tool that can be used to generate valuable quantitative data.

Contact: Aaron C. Hall, Joining and Coating, Dept., 1833
Phone: (505) 284-6964
Fax: (505) 844-4816
E-mail: achall@sandia.gov

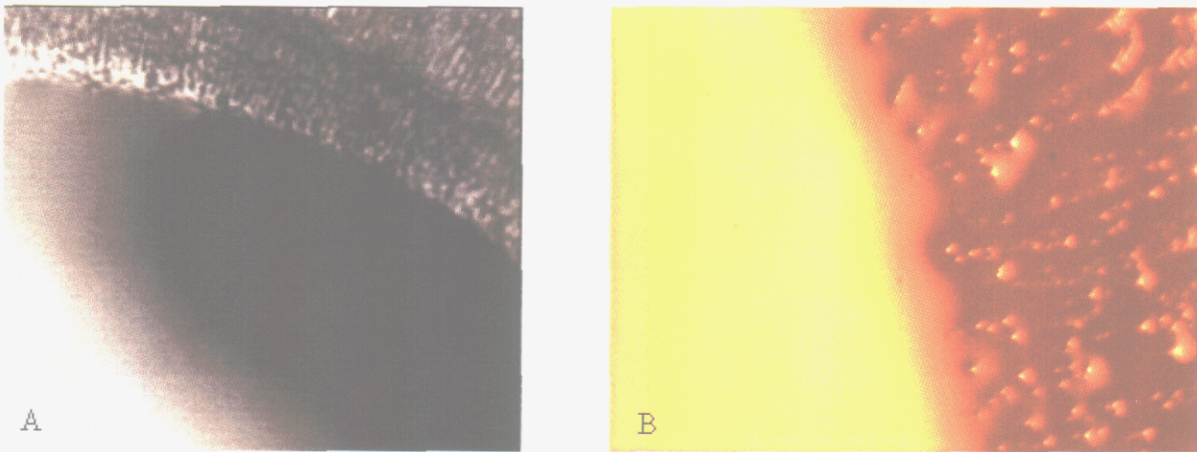


Figure 1. The image on the left (A) contains 45,000 digital pixels, the image on the right (B) contains 196,000 digital pixels and is a color image. To machine vision software image B is a data set with 400% more information than image A. The increase in size of the image data set results in a direct improvement in the spatial resolution of the experiment.

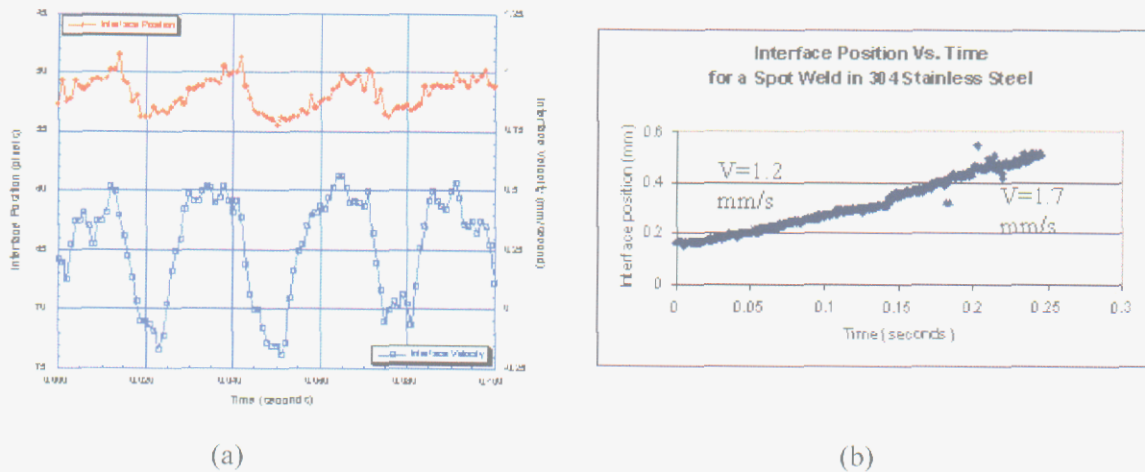


Figure 2. Data extracted from videos of the solid-liquid interface. (a) shows interface position and velocity versus time for a rippling weld in stainless steel. (b) shows the interface velocity profile for a solidifying spot weld. Data from experiments like this can be used to verify solidification-based laser welding models.

An Investigation of Droplet Transfer Mechanisms for Micro-Wire Welding

P.W. Fuerschbach, L.A. Bertram, D.L. Luck, R.A. Anderson

Motivation: An alternative to laser beam welding is desired because workpiece beam absorption is extremely sensitive to variations in surface condition and joint geometry. Despite the robustness and metallurgical advantages of conventional wire arc welding, it is not a good substitute because the scale of the resulting welds is too large. In order for a wire arc to be feasible for miniature weld applications, consistent droplet detachment and precise workpiece heating must be achieved. Problems with smooth melt-in of a small wire arc are expected to be overcome with the assistance of a fiber delivered laser beam. Diagnostic experiments to understand droplet detachment are a necessary first step in the development of a new laser assisted micro wire arc process.

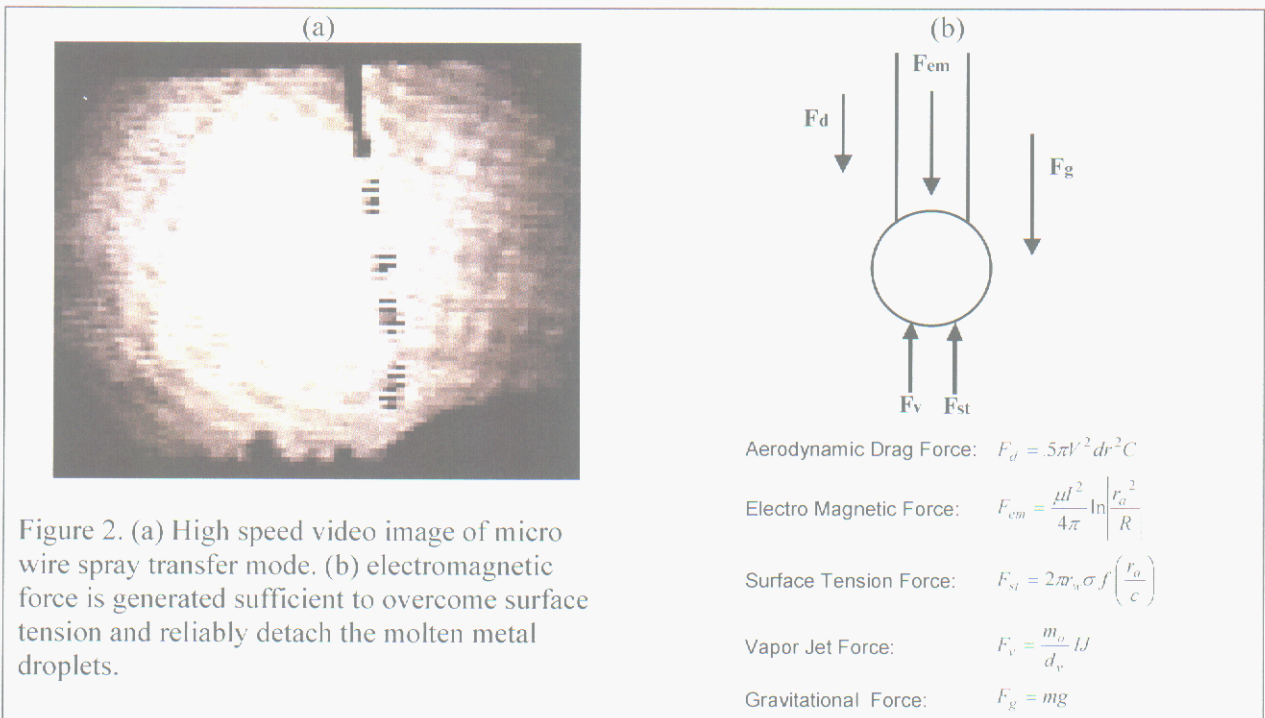
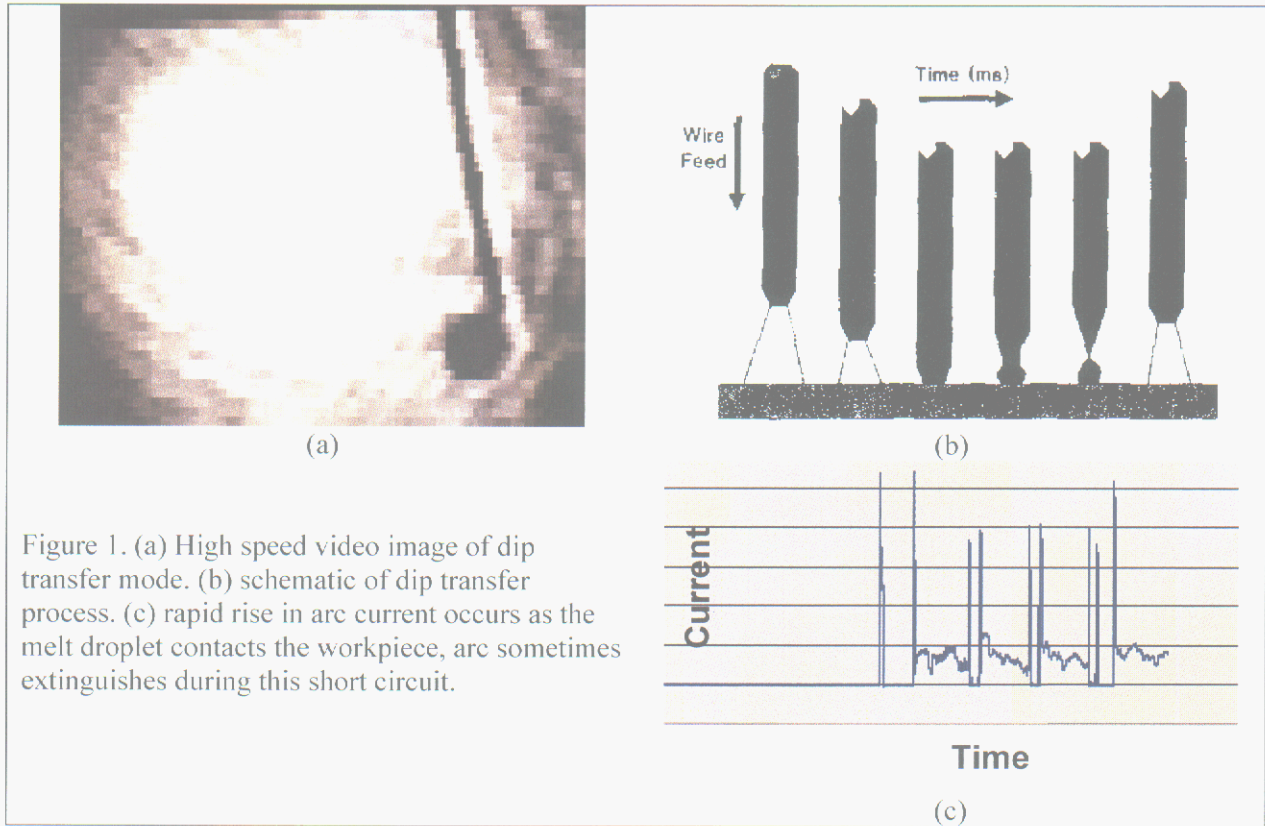
Accomplishment: Imaging of the extremely active and luminous arc interaction zone allows one to obtain diagnostic measurements of metal arc transfer. We have assembled a high-speed video system with laser back-lighting and filtering to obtain clear observation of droplet detachment in the metal arc. Several distinct micro-wire arc transfer modes have been photographed and analyzed. In dip transfer (Figure 1(a,b)), the droplet is detached by strong surface tension forces. Inconsistencies in droplet detachment occur because of rapid fluctuations in arc current, and therefore heating. The arc is often extinguished (Figure 1(c)), when the short circuit event occurs. In globular transfer, the droplet forms at the tip of the electrode several millimeters above the workpiece and is sporadically transferred to the workpiece by combined gravitational and electromagnetic forces at the wire tip. In spray transfer (Figure

2(a,b)), the current density on the tip of the electrode is sufficient to detach the droplet in a steady stream, but excessive heating of the base metal makes this mode impractical for miniature welding applications. High currents are required in order to develop sufficient electromagnetic and vaporization forces on the droplet to achieve detachment.

A remarkable effect was observed with laser-assisted micro-wire welding in globular transfer. As propelled metal droplets are impacted by the focused laser beam, they are either repelled 180° or their path is significantly altered. This phenomenon is believed to be due to vapor recoil arising from significant vaporization from the face of the molten droplet as it is impacted by the focused laser beam. It is thought to be the same vaporization force that maintains a stable vapor cavity or keyhole in deep penetration laser and electron beam welding.

Significance: All of the modes feature large arcs, with broad bands of cathode spot travel, far bigger than the wire cross section, suggesting that very large arc heating areas persist even with micro-scale wire. This is a fundamental impediment to true miniature arc welding. Common to all of the modes examined, consistent detachment of the droplet appears to be difficult and unstable enough to require a supplemental mechanical detachment force before an entirely successful union with the laser beam can be achieved. A more revolutionary rather than evolutionary approach to micro-wire welding appears to be required, and is now envisioned.

Contact: Phil Fuerschbach, Joining and Coating Dept., 1833
Phone: (505) 845-8877
Fax: (505) 845-9659
E-mail: pwfuers@sandia.gov



Integrated Science-Based Understanding of Fundamental Brazing Reactions

F. M. Hosking, C. H. Cadden, P. G. Kotula, R. L. Loehman, J. J. Stephens, E. B. Webb III

Motivation: New ceramic-metal assembly designs are simplified through the use of active metal brazing. The joining process eliminates the need for ceramic metallization and related processing steps. The fundamental interfacial reactions that occur between the active constituents in the filler metal and the ceramic are typically complex. A more science-based approach to characterize and optimize these reactions is necessary for the active brazing process to produce reliable results and be widely accepted.

Accomplishment: We have established an integrated brazing research program that utilizes fundamental experimental, analytical, and computational tools to understand the critical reaction mechanisms at the braze-ceramic interface (Figure 1). We have analyzed the wetting behavior and interfacial reactions for silver and gold-based active brazing alloys (ABA's) containing titanium, vanadium, zirconium, and hafnium. Results from these fundamental experiments suggest that the active element segregates to the ceramic interface, with substantially different bonding reactions for each "active" element. Titanium, zirconium and hafnium produce well-defined reaction layers, while the vanadium reaction is difficult to resolve. Vanadium is particularly sensitive to the silica glassy phase that is used to bind the polycrystalline alumina grains. The vanadium-containing ABA forms a stronger, hermetic bond as the glassy phase is increased (i.e., lower purity alumina grades). We have modified the surface of high purity alumina with silicon/silica and mullite (alumina-silica) to enhance joint strength. We are also investigating other ABA systems that take advantage of the relatively low melting

temperature (950-1000°C) of reactive intermetallic compounds.

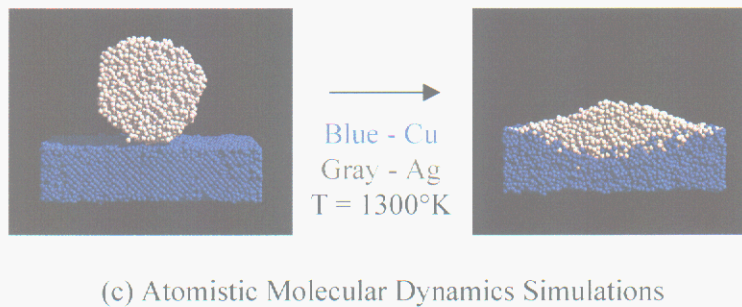
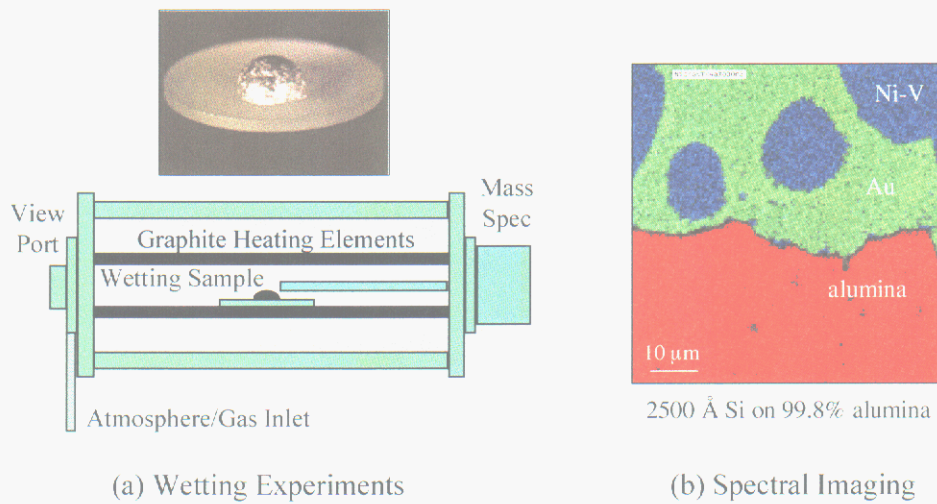
The microstructural features are being characterized by automated x-ray spectral image analysis and information extraction. The technique collects an entire elemental spectrum for each sample image. Unique chemical phases and their distributions are then resolved for analysis. This new analytical tool is particularly useful in characterizing reactions between alumina and the vanadium-containing ABA. The reaction layer is very thin (≤ 10 nanometers), discrete and generally difficult to prepare using traditional SEM/TEM sample preparation techniques. Spectral imaging allows more flexibility in the selection and identification of the principal reaction phases at the ceramic interface.

We are also developing atomistic-to-molecular length-scale models for predicting interfacial reactions. The computations depend on the accuracy of the interatomic potentials and the ability to apply both metallic and ionic bonding mechanisms. The potentials for simple metal-ceramic reactions are being initially determined to simulate the relevant titanium-alumina brazing reaction.

Significance: Improvements to critical Nuclear Weapons brazing materials and processes will be enabled by this science-based approach that leverages new experimental, analytical, and modeling tools. The integrated research package will also enable better control and optimization of the brazing process, which will result in more simple, improved component designs and greater manufacturing yields.

Contact: Mike Hosking, Joining and Coating Dept., 1833
Phone: (505) 845-8401
Fax: (505) 844-4816
E-mail: fmhoski@sandia.gov

Figure 1. Integrated, science-based approach for determining complex, interfacial reactions between ceramics and metal systems: (a) fundamental wetting experiments, (b) spectral imaging and information extraction, and (c) atomistic, molecular dynamics (MD) predictions.



Qualification of Processes to Clean Kovar Parts

E.P. Lopez

Motivation: An important process associated with the manufacture of neutron tubes at Sandia involves the proper cleaning of various metals and ceramic parts. Cleaning of Kovar parts using an aqueous alkaline solution in a 40 KHz ultrasonic bath manufactured by NEY had been previously qualified. Recently, a 40 KHz CREST ultrasonic cleaner was incorporated into the production line. Specification requirements call for an aqueous alkaline solution temperature range of 130°F ±5°. The CREST ultrasonic cleaners are incapable of maintaining the temperature range as specified and, in fact, exceed the required temperature range by more than 15°F. As a result, re-qualification at the higher temperature range was necessary to ensure the proper level of cleaning was being attained.

Accomplishment: A re-qualification plan was developed to compare the cleanliness produced with the NEY ultrasonic cleaners with that from the CREST ultrasonic cleaners. The test matrix included cleanliness verification of Kovar using goniometer/contact angle measurements and surface contamination analysis with auger electron spectroscopy. Surface finish was determined by visual observation and surface profilometry.

The contact angle results indicate that the higher temperature CREST process produces a slight improvement in cleaning effectiveness (Figure 1). In general, the lower the tangent angle, the cleaner the surface. In this case, the as-received contact angle was 98° as compared to 48° at 135°F and 41° at 152°F. The auger electron spectroscopy results correlated with the contact angle measurements (Figure 2). For example, the amount of surface carbon was significantly reduced from an average of ~67

atomic % for the as-received surface to ~36 atomic % for coupons cleaned at 135°F and ~32 atomic % for coupons cleaned at 152°F. As the carbon levels are reduced, more bare metal is exposed and the relative amounts of Fe, Co, and Ni increase. For example, the Fe atomic % values increase from an average of ~4 for the as-received coupons as compared to ~14 at 135°F and ~12 at 152°F.

Surface roughness measurements were taken with a DekTak 8000 profilometer and the results are shown in Figure 3. The measurements were taken using a 2-micron stylus traversed over a 4 mm distance perpendicular to the roll marks on the Kovar. The results indicate a noticeable change in surface roughness between the as-received coupons and the coupons cleaned at the higher temperatures. The average surface roughness for the as-received surfaces was 3.7 µin as compared to 3.1 at 135°F and 3.0 at 152°F. Not only are the surfaces smoother after cleaning at the higher temperatures but also more uniform as indicated by the tighter standard deviations. The smoothing effect is probably due to increased microetching of the surface related to the higher temperatures used. No visual differences were seen between the two higher temperature cleans.

Significance: Completion of the re-qualification plan verified previously reported data showing that the higher temperature associated with ultrasonics was not a problem. These results enabled re-starting the neutron tube manufacturing line, which had not been operational and brought the cleaning specification back into compliance.

Contact: Eddie Lopez, Corrosion Electrochemistry and Cleaning Dept., 1832
Phone: (505) 845-9181
Fax: (505) 844-9624
E-mail: eplopez@sandia.gov

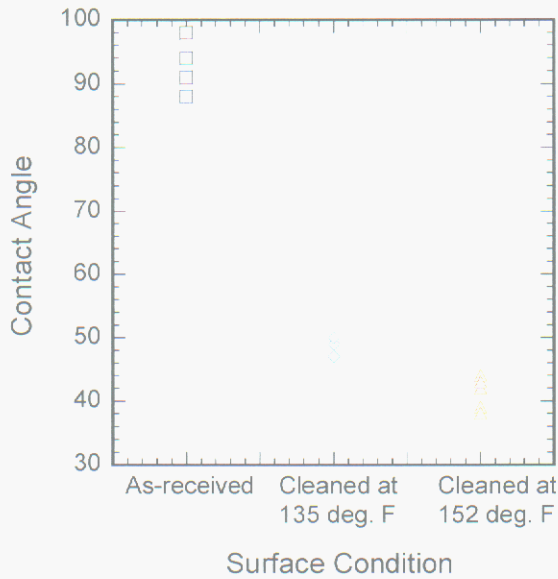


Figure 1. Contact angle as a function of surface preparation. Cleaning efficiency increases with increasing temperature.

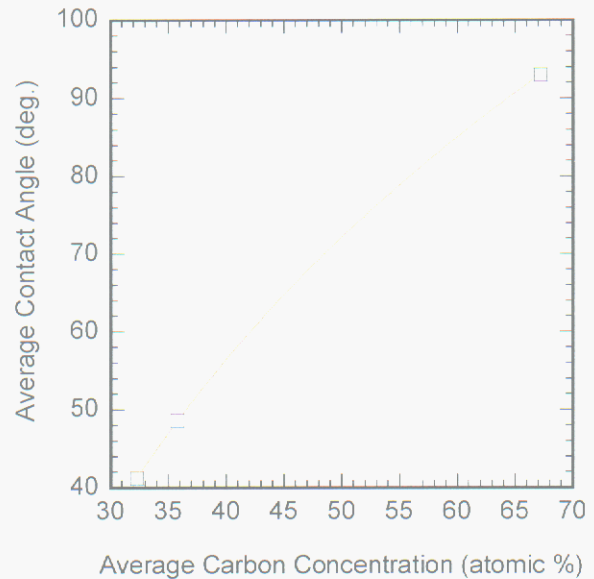


Figure 2. Relationship between contact angle and surface carbon concentration. Lower carbon correlates to a cleaner surface and lower contact angle.

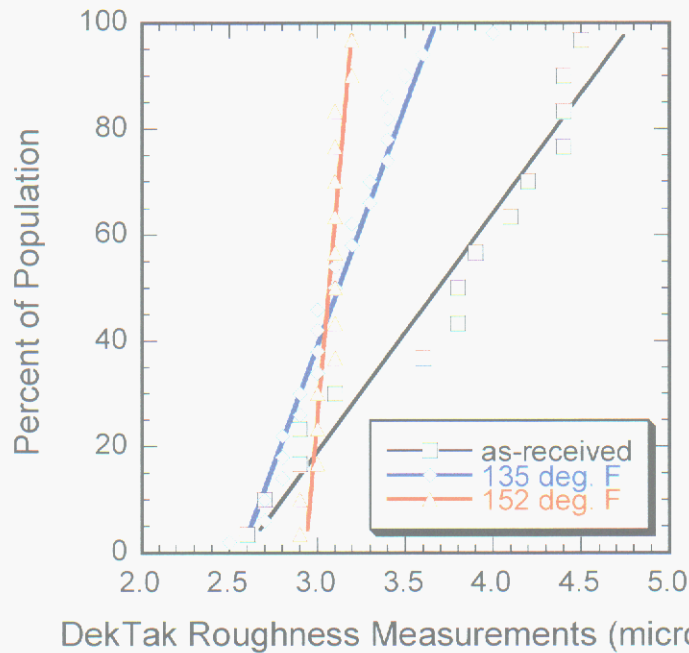


Figure 3. Surface roughness distributions as a function of cleaning process. Cleaning decreases average surface roughness and improves uniformity.

Segregation of Alloying Elements to Grain Boundaries

S. M. Foiles

Motivation: The addition of alloying elements and the presence of impurities has a profound effect on the properties of metals including microstructural evolution, diffusion and mechanical properties. In fact, the addition of alloying elements to control final properties is one of the standard tools of an alloy designer. While in many cases, there is an empirical understanding of the role of various alloy additions; there is often much less mechanistic understanding. The present work is aimed at furthering the mechanistic understanding of how impurities modify grain boundary properties such as boundary mobilities and boundary diffusivities.

Accomplishment: The present work is a computational examination of the segregation of Cu to a high symmetry Al grain boundary. The choice of Cu in Al was motivated by the observed reduction of electromigration-induced failures in Al microelectronic interconnect lines as a result of the addition of Cu. The choice of a high symmetry boundary enables detailed comparisons to high-resolution microscopy based experiments on the same boundary. These density-functional electronic structure calculations find the structure and energy of an Al $\Sigma 5$ (310) symmetric tilt boundary, both with and without Cu impurities. The calculations were performed using the Vienna Ab Initio Simulation Package (VASP).

The first panel of Figure 1 shows the computed lowest energy structure of this boundary. This is consistent with previous calculations. Initially, the energy associated with various substitutional locations for a Cu impurity

was computed. The second panel of Figure 1 shows the Cu locations expected in that case. Finally, interstitial positions for the Cu atoms were considered. Note that the boundary in the pure case has a relatively large interstitial site in the center of the boundary. The calculations indicated that the interstitial site is strongly favored over the substitutional site.

Plitzko, Campbell and King at LLNL fabricated this boundary in a diffusion-bonding machine both with and without Cu additions. Figure 2 shows the high-resolution electron microscopy image of this boundary. The second frame shows a simulated image based on the computed structure with the Cu located at the interstitial site. The good agreement between the experimental and simulated image demonstrates that this is the correct structure.

Significance: The current work demonstrates that defect types not present in bulk material may well be present at grain boundaries. In particular, an impurity that is substitutional in the bulk metal is shown to occupy an interstitial site at the boundary. Recognition of the relevant defect types is an essential first step in the development of a mechanistic understanding of macroscopic properties. In this case, the detailed mechanism of diffusion will be strongly altered by the presence of the interstitial Cu. Future work will determine the detailed diffusion mechanism for this boundary and how it is altered by the presence of the interstitial Cu. In addition, this boundary can now be used to understand how the presence of impurities might modify the mechanisms of boundary motion.

Contact: Stephen Foiles, Materials & Process Modeling & Computation Dept., 1834

Phone: (505) 844-7064

Fax: (505) 844-9781

E-mail: foiles@sandia.gov

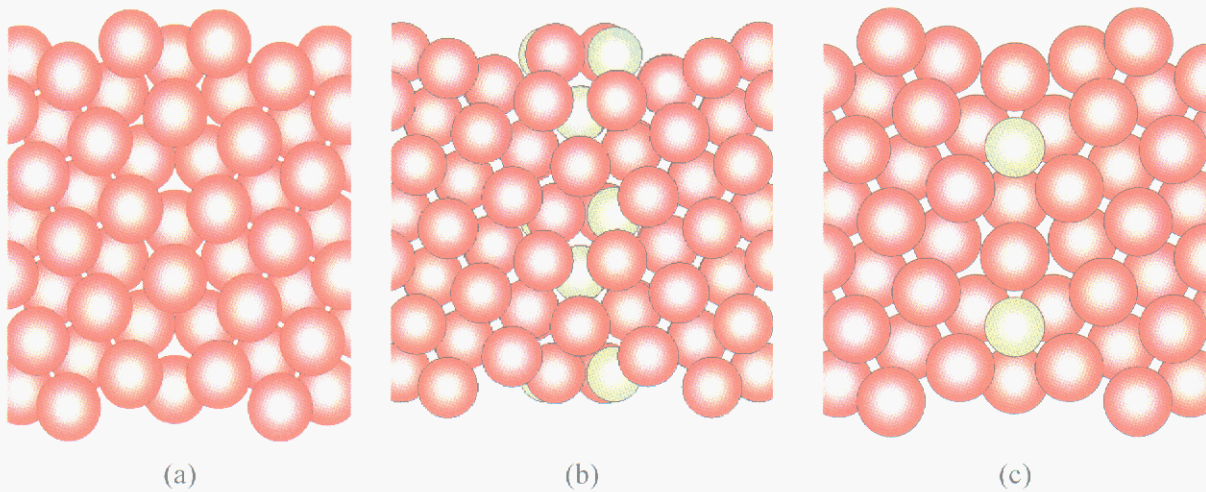


Figure 1. Computed structures of the Al $\Sigma 5$ (310) symmetric tilt boundary. The first figure shows the structure for pure Al. The second frame shows the prediction for Cu (green atoms) segregated to the boundary assuming only substitutional sites at the boundary. The third frame shows the predicted structure with the Cu located at an interstitial site in the boundary.

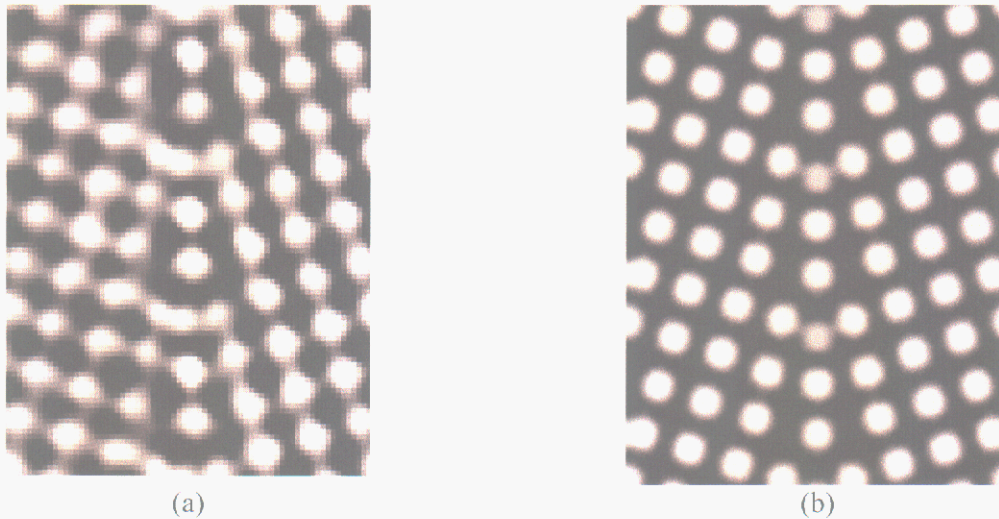


Figure 2. The first frame is a high-resolution electron microscopy image of the Al $\Sigma 5$ (310) symmetric tilt boundary with segregated Cu. (Work of J. Plitzko, G. Campbell, and W. King, LLNL) The second frame is the simulated image based on the structure computed for Cu located in the interstitial site.

Control of Casting Rate During Vacuum Arc Remelting

R. L. Williamson, D. K. Melgaard and G. J. Shelmidine

Motivation: Vacuum arc remelting is a casting process used widely in the specialty metals industry for the production of large ingots of nickel-base superalloys and aerospace titanium alloys. It is important to carefully control casting rate in this process in order to produce high quality, homogeneous castings that are free of solidification defects. This requires a method of controlling the electrode melting rate, a process parameter that is dependent on melt power as well as the temperature distribution in the electrode tip. Effectively controlling melting rate requires a means of continuously estimating the thermal distribution in the electrode and sensing changes in the distribution in real time.

Accomplishment: A VAR casting rate controller has been developed and tested; it is depicted schematically in Figure 1. The controller employs a Kalman filter based VAR Estimator. The estimator uses a dynamic process model to predict values for process variables and compares them with measured values to form optimal estimates. Those variables used to characterize the state of the VAR process are electrode position, electrode mass, electrode gap, process efficiency, electrode area ratio, and electrode thermal boundary layer (TBL). No measurement of TBL is available and a measure of electrode mass is available only on some industrial VAR furnaces. The filter produces estimates of these variables that are consistent with the physical constraints inherent in the process model and measurements. The estimated variables are used to control melting current and electrode feed rate. Estimated process efficiency is used as a disturbance variable to correct the process inputs when melting is faster or slower than the physical

model expects. The electrode area ratio is also used as a disturbance variable. Its estimated value is used to correct for variations in electrode density due to "pipe" or other types of casting voids.

The nonlinear controller was developed specifically for VAR of Ti-6Al-4V because of the very wide range of melt rates employed from start-up through hot-top in an industrial melt. Excellent melt rate control has been demonstrated during industrial tests with this material. The controller has also been successfully tested melting Alloy 718, 15-5PH and 304 stainless steels, and U-6Nb alloy. The controller successfully produces linear melt rate ramps and steps over a wide range of melting conditions. Note that this requires nonlinear current ramps because the TBL requires 1-3 hours to reach its steady-state value depending on electrode size and material. Additionally, the controller automatically compensates for process disturbances caused by abnormal heat conduction. Common causes of such disturbances are transverse electrode cracks and melting near the end of the electrode.

Significance: A melting tool has been developed that allows VAR process engineers to implement the optimized melt rate schedules spanning very large ranges. Melt rate control is maintained through welds, cracks and during start-up and end effect melting. This technique also makes possible active melt rate control when no electrode mass measurement is available, a capability that is presently unavailable to the industry. This technology is protected under U.S. Patent #6,115,404.

Contact: Rod Williamson, Metal Processing Dept., 1835
Phone: (505) 284-8223
Fax: (505) 845-3430
E-mail: rodwill@sandia.gov

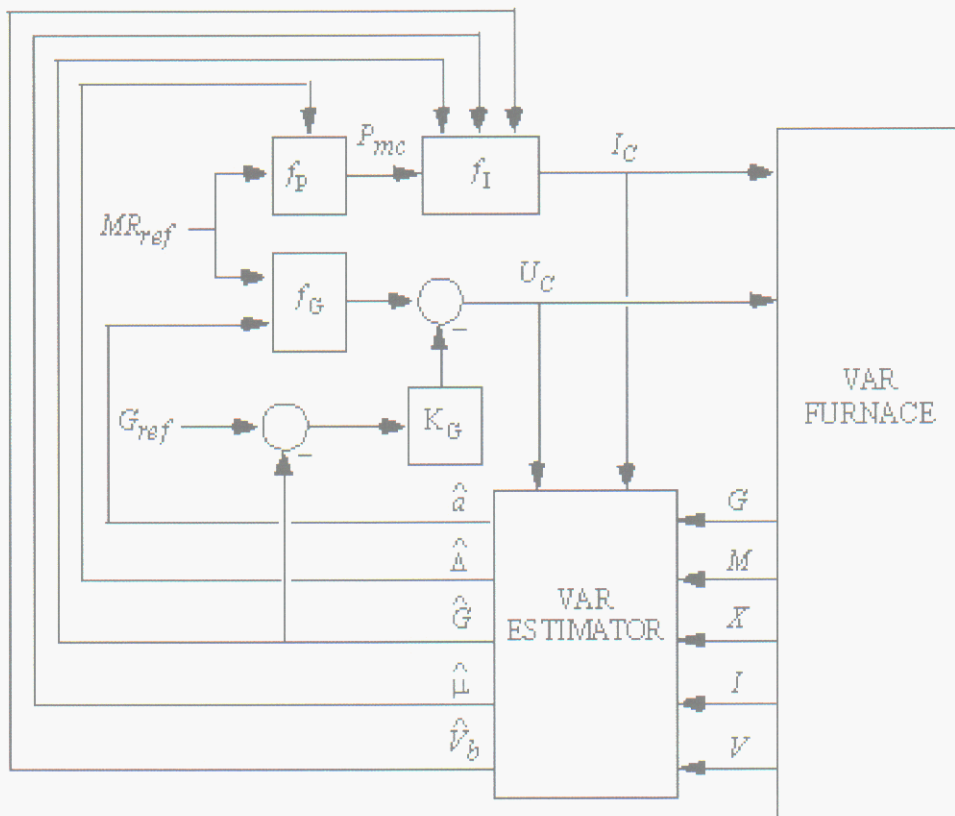


Figure 1. Schematic depiction of the VAR casting rate controller. Key: MR_{ref} = electrode melting rate reference; G_{ref} = electrode gap reference; P_{mc} = commanded melt power; I_c = commanded melting current; U_c = commanded electrode feed rate; G = estimate of electrode gap based on voltage measurement model; M = measured electrode mass; I = measured current; V = measured process voltage; X = measured electrode position; \hat{a} is the estimated area ratio parameter; $\hat{\Delta}$ = estimated thermal boundary layer; \hat{G} = estimated electrode gap; $\hat{\mu}$ = estimated process efficiency; \hat{V}_b is the estimated voltage bias; K_G = feedback gain. f_p , f_I and f_G are nonlinear functions describing key elements of the process.

Immersion Depth Control of the Electroslag Remelting Process at Shallower, More Consistent Levels

D. K. Melgaard and G. J. Shelmidine

Motivation: The electroslag remelting (ESR) process is used extensively to produce clean, fully dense ingots of high quality steel and nickel-based superalloys with applications throughout the aerospace industry. Due to the critical nature of these applications, the quality standards for these materials are becoming more stringent. The immersion depth is a crucial control parameter for producing high quality material. The depth has direct impact on the surface quality and the solidification structure of the ingot. No direct technique is available to determine its value, so rather subjective methods for inferring the depth have been used with varying results. The need for a more consistent, direct approach is clearly apparent.

Accomplishment: During ESR, a metal electrode is melted by immersing it into a molten slag bath, which has been resistively heated above the melting temperature of the metal. The electrode melts, coalescing into droplets which eventually fall through the slag and collect in a molten metal pools below the slag in a water-cooled mold. The mold extracts the heat causing the liquid metal to solidify, but since the slag is also in contact with the mold, a small portion solidifies on the surface (see Figure 1). The heat balance of the process requires that the electrode be immersed about 5mm into the slag because at greater depths the slag becomes too cool, and more of the slag solidifies against the mold, causing the surface quality of the ingot suffers. Conversely at shallower depths, arcing often occurs, resulting in deleterious oxidizing reactions. Since the protuberances on the electrode tip are about 5 mm in magnitude, maintaining a consistent immersion depth at that level is difficult. Current practice uses a voltage

variance algorithm to estimate the depth, but that approach requires the electrode to be translated up and down in the slag. That practice is inherently contrary to the goal of holding the electrode at a consistent depth but also for stability, requires that the melting is conducted at a greater depth. A multitude of experiments have been conducted at the Liquid Metals Processing Laboratory to develop a control method, which reduced the depth variation. As the variation was reduced during those experiments, a voltage signature was discovered (Figure 2). As the electrode melts, the impedance of the process periodically spikes. The level of the spikes is directly related to the immersion depth. Using this information, a new control algorithm has been developed which monitors the spikes and adjusts the electrode drive speeds based on the results. The algorithm is currently under evaluation on industrial scale furnaces, and the preliminary results indicate a measurable improvement in ingot surface quality. In addition, the amount of movement in the electrode has been significantly reduced.

Significance: The new control algorithm has been demonstrated to operate at more consistent immersion depth, resulting in improved surface quality of ESR ingots. This improved quality will translate into higher yields and a reduction in slag entrapment defects. Equally as important is the reduction in variability in the electrode immersion depth, which has direct implications for the solidification structure of the ingot. Perturbations or transients in the process may initiate solidification defects. By reducing these, the homogeneity of the grain structure in the resulting ingots will be improved as well

Contact: David Melgaard, Meltal Processing Dept., 1835

Phone: (505) 844-1022

Fax: (505) 845-3430

E-mail: dmelga@sandia.gov



Figure 1. Slag skin in unique split mold available only at Sandia which makes skin thickness and melt conditions possible.

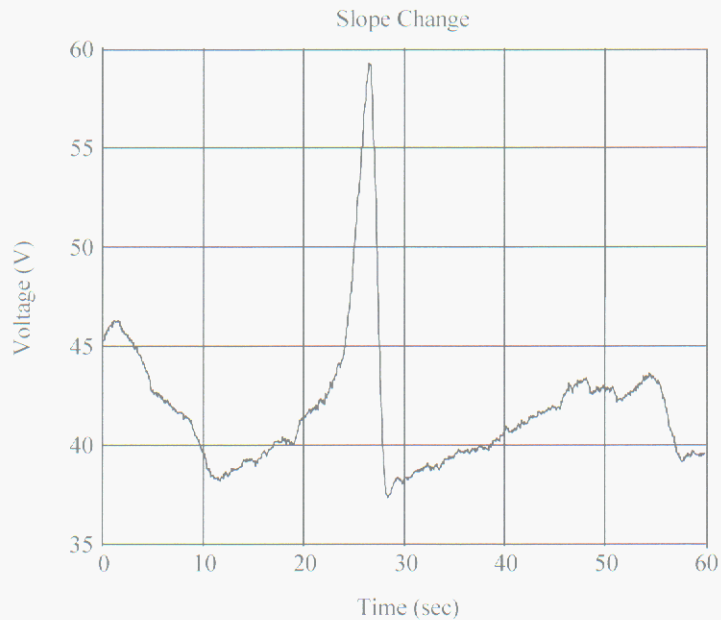


Figure 2. The unique voltage signature indicative of shallow immersion depths. The data was taken from during the melting of a 15 cm electrode into a 20 cm mold.

Nonlinear Viscoelasticity of Curing Thermosets

D. B. Adolf and R. S. Chambers

Motivation: As epoxies cure, stresses develop due to competition between cure shrinkage, thermal expansion mismatches, and viscoelastic relaxation. Our prior work on predicting these cure stresses used a linear viscoelastic framework that proved quantitative for cures where the increasing epoxy glass transition temperature did not hover near the cure temperature for prolonged periods. While this held true for our historical stockpile encapsulants, the new non-carcinogenic replacements cure faster and severely vitrify during cure. This complication requires an intrinsically nonlinear viscoelastic formulation, which has been implemented in our finite element codes this year.

Accomplishment: For the past several years, we have been developing a nonlinear viscoelastic formalism for cured glassy epoxies that is capable of predicting the wide variety of complicated phenomena these materials exhibit. As an epoxy is cooled below its glass transition temperature (T_g), the relaxation times increase enormously and become comparable or longer than the characteristic processing times which, in turn, leads to a host of interesting effects: physical aging, volume recovery, and enthalpy relaxation. While several approaches in the literature have been able to capture many of these effects, they have been unable to predict concurrently any mechanical yielding under high loads in the glassy state. Our efforts have focused on developing a comprehensive and quantitative formalism capable of predicting all these phenomena including yield.

The resulting theory has quantitatively predicted all experimental data to engineering

accuracy (20%) on a variety of filled and unfilled epoxies. The underlying physical picture builds on the historical polymer lore, which states that, above T_g , increasing temperature increases the relaxation rates. We have generalized this picture so that increasing the thermodynamic energy increases the relaxation rates. Since energy includes mechanical work, our formalism predicts that applied stresses also increase the relaxation rates thereby enabling yield.

We have extended the formalism to account for epoxy curing. Curing affects the internal energy and therefore the relaxation rates. Interestingly, the formalism gives a clear physical interpretation for the increase in T_g with cure that is consistent with polymer lore. Specifically, T_g increases due to the energy of reaction and the measurable decrease in the step change in heat capacity at T_g . The formalism has been validated on a series of tests with imbedded strain gauges and thermocouples.

Significance: With this formalism we are now able to predict stresses accurately in our new, fast curing encapsulants, which enable optimization of cure schedules. Moreover, since this is the only formalism capable of calculating stresses and strains in a curing epoxy as it cycles through T_g , we are in a position to address critical industrial problems. As a specific example, the dimensional tolerances on large aerospace composite components are incredibly tight and cure-induced warpage leads to costly, iterative mold re-design. A predictive capability could minimize the number of mold iterations or lead to a cure schedule that reduces the overall warpage.

Contact: Doug Adolf, Organic Materials Dept., 1811
Phone: (505) 844-4773
Fax: (505) 844-9624
E-mail: dbadolff@sandia.gov

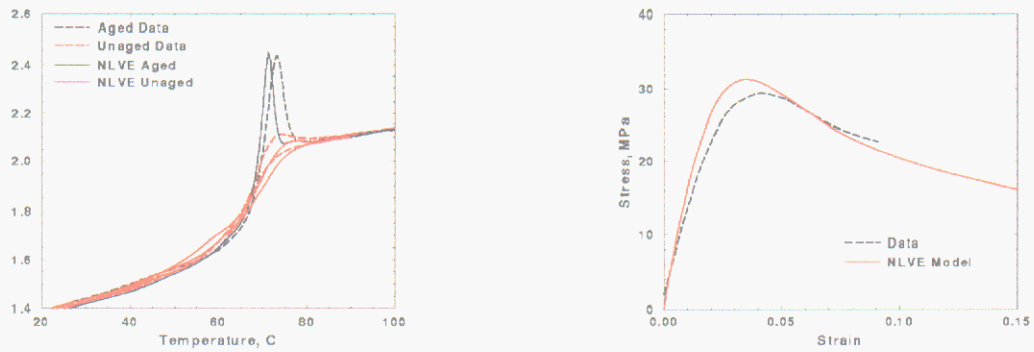


Figure 1. Examples of the level of quantitative agreement between predictions and experimental data for a fully cured epoxy. The left figure shows heat capacity as a function of temperature as the sample is heated and cooled through T_g . The “aged” sample sat 20°C below T_g for 90 minutes before reheating. Notice the spike upon reheating. The right curve shows yield in tension again 20°C below T_g .

DISTRIBUTION

MS&T external review panel: 1 copy each					
	Dr. William A. Baeslack III Dean, School of Engineering Jonsson Engineering Center – 3002 Rensselaer Polytechnic Institute 110 Eighth St. Troy, NY 12180-3590				Dr. David J. Bishop Vice President of Optical Research Bell Laboratories Lucent Technologies 700 Mountain Ave. – Rm 1A-264 Murray Hill, NJ 07974
	Dr. Harry Saxton 11257 Golden Chestnut Place Las Vegas, NV 89135				Dr. Alan Taub, Executive Director – Science General Motors R&D Center 30500 Mound Rd. MC 480-106-EX1 Warren, MI 48090-9055
	Dr. Steven Wax, Deputy Director Defense Sciences Office DARPA/DSO 3701 N Fairfax Dr. Arlington, VA 22203-1714				Professor John H. Weaver, Department Head Materials Science & Engineering University of Illinois 1304 W Green Urbana, IL 61801
	Dr. Thomas Zacharia Oak Ridge National Laboratory PO Box 2008 MS-6232 Oak Ridge, TN 37831-6232				
1	MS 0102	J. B. Woodward, 2	1	MS 0886	N. B. Jackson, 1812
1	MS 0112	F. A. Figueroa, 10000	1	MS 0887	M. J. Cieslak, 1800
1	MS 0121	C. M. Hart, 1200	1	MS 0888	R. L. Clough, 1811
1	MS 0130	J. Polito, 2800	1	MS 0889	J. W. Braithwaite, 1832
1	MS 0132	J. L. Martinez, 14000	1	MS 0889	M. F. Smith, 1833
1	MS 0134	R. J. Detry, 9700	1	MS 0889	R. J. Salzbrenner, 1835
1	MS 0139	M. O. Vahle, 9900	1	MS 0889	J. S. Custer, 1851
1	MS 0139	P. J. Wilson, 9902	1	MS 0918	M. L. Jones, 7000
1	MS 0151	T. O. Hunter, 9000	1	MS 0960	C. L. Adkins, 14100
1	MS 0185	D. L. Goldheim, 1300	1	MS 1079	M. W. Scott, 1700
1	MS 0186	D. H. Blanton, 3000	1	MS 1190	J. P. Quintenz, 1600
1	MS 0429	J. S. Rottler, 2100	1	MS 1221	J. A. Tegnalia, 15000
1	MS 0437	C. L. Knapp, 2120	1	MS 1231	A. D. Romig, 5000
1	MS 0457	J. H. Stichman, 2000	1	MS 1349	W. F. Hammetter, 1843
1	MS 0503	D. W. Plummer, 2330	1	MS 1411	H. E. Fang, 1834
1	MS 0509	M. W. Callahan, 2300	1	MS 1411	J. Liu, 1846
1	MS 0511	J. R. Fellerhoff, 1020	1	MS 1427	J. M. Phillips, 1100
1	MS 0511	C. E. Meyers, 1010	1	MS 1630	W. D. Williams, 1400
1	MS 0513	J. P. Vandevender, 1000	1	MS 9005	R. G. Miller, 2820
1	MS 0724	R. J. Eagan, 6000	1	MS 9401	G. D. Kubiak, 8702
1	MS 0865	D. L. Cook, 1900	1	MS 9402	K. L. Wilson, 8703
1	MS 0868	K. G. McCaughey, 14400	1	MS 9403	J. M. Hruby, 8700
1	MS 0885	D. B. Dimos, 1801			
1	MS 0885	G. S. Heffelfinger, 1802	1	MS9018	Central Technical Files, 8945-1
25	MS 0885	C. L. Porter, 1801	2	MS0899	Technical Library, 9616
1	MS 0886	R. P. Goehner, 1822			